Université Fédérale
Toulouse Midi-Pyrénées

THÈSE

En vue de l'obtention du

DOCTORAT DE L'UNIVERSITÉ DE TOULOUSE

Délivré par :

Université Toulouse 3 Paul Sabatier (UT3 Paul Sabatier)

Présentée et soutenue par :
Andreas GAVRIELIDES
le mardi 28 novembre 2017

Titre :

Modélisation du poly-époxy DGEBA-EDA et de sa réactivité vis à vis du cuivre: approche expérimentale et numérique
Modelling the DGEBA-EDA poly-epoxy and its reactivity towards copper: experimental and numerical approach

---

École doctorale et discipline ou spécialité :
ED SDM : Sciences et génie des matériaux - CO034

Unité de recherche :
CIRIMAT UMR CNRS 5085

Directeur/trice(s) de Thèse :

Pr. Corinne LACAZE-DUFAURE
Dr. Thomas DUGUET

Jury :
Dominique COSTA, Directrice de Recherche, Chimie ParisTech, Paris, Rapporteur
Tzonka MINEVA, Directrice de Recherche, Institut Charles Gerhardt, Montpellier, Rapporteur
Patrice RAYNAUD, Directeur de Recherche, LAPLACE, Toulouse, Examinateur
Frederic MERCIER, Chargé de Recherche, Université Grenoble Alpes, Examinateur
Corinne LACAZE-DUFAURE, Professeur, CIRIMAT, Toulouse, Directrice de thèse
Thomas DUGUET, Chargé de Recherche, CIRIMAT, Toulouse, Co-directeur de thèse
Yohann LEDRU, Ingénieur Docteur, MECANO-ID, Toulouse, Invité

Acknowledgements

I would like to start by expressing my sincere gratitude to my supervisors Professor Corinne Lacaze-Dufaure and Dr. Thomas Duguet who trusted me with these project and gave me the opportunity to work with them. They are both great scientific minds and excellent characters and truly passionate about anything they are involved and the advancement of science. They were always there for me and without our valuable discussions and their dedication to the success of this project, this thesis would not have been feasible. The knowledge they have instilled in me will stay forever and I am grateful for the supplies they have provided for the open road that lies ahead of me. They have not only provided the knowledge but also the skills necessary to achieve my dreams. I will cherish our moments and hope in the future that our roads will once again converge.

I would like to thank Professor Paul S. Bagus for his enormous help with the Hartree-Fock ΔSCF calculations which are a part of this thesis and for providing us with some very interesting results on the calculation of XPS spectra.

Professor Doros Theodorou and PhD student Mr. Orestis Ziogos had a big impact on this project as our discussions both in Athens (National Technical University of Athens) as well as following discussions after returning back to France helped us accelerate the calculations on the Molecular Dynamics front.

To both Professor Theodorou and Professor Andreas Boudouvis, I would like to say a big thank you for directing me in the path of executing a PhD thus giving me three of my best years.

I would also like to thank the members of the SURF team of which I was a proud member during my 3-year PhD course and would like to extend special thanks to Dr. Maëlenn Aufray for our very helpful discussions and Mr. Jérôme Esvan for his valuable help in the experimental XPS spectra acquisition as well as the mounting of the metal evaporator on the UHV chamber. I am also lucky to have met and discussed with Dr. Constantin Vahlas in numerous occasions. Through our discussions I managed to change my character in a way I am sure will help me for years to come.

My PhD thesis could not have been executed if not for my two wonderful parents Kleanthis and Marina which were there for me from the beginning and continue to support me until this very day. I owe them everything and they have shaped me throughout the years. My two brothers Pavlos and Alexandros were also there when I needed them and I am sure they will grow to be excellent.

To my grandparents Pavlos, Virginia, Andreas and Alexandra I need to express my gratitude which cannot be contained in words as they are pillars of my life and have been there in all of my moments even from a distance. They have sacrificed a lot for me and this PhD is dedicated to their memory.

Finally I would like to thank all of my friends that were right beside me, from my childhood years, to the 5 wonderful years in Athens and the 3 amazing years in France. They have stood by me in every moment, both good and bad and without them there would be no point in anything.

This PhD thesis is finally dedicated to everyone who is not afraid to pursue their dreams no matter how impossible they may seem. I want you to know that if you put your mind on anything you can do it and even if you fail, persist and you can only win. Things will come around even in unpredictable ways.

As far as the financial support of this thesis is concerned I would like to thank the French Ministère de l’Enseignement supérieur et de la Recherche for providing the funds for the execution of this thesis.

Table of Contents

Introduction générale

Les composites à matrice polymère sont de plus en plus utilisés en tant que matériaux de structure, et en tant que substituts pour des composants métalliques, notamment dans le domaine aéronautique et spatial[1]. Ils réduisent le poids des assemblages et abaissent la consommation de carburant des avions ou des lanceurs spatiaux. Ils étaient jusqu'alors seulement utilisés pour des pièces « secondaires » comme certains morceaux de carlingue ; mais la gamme d'application s'est maintenant largement étendue à des composants fonctionnels, tels que les revêtements d'aile et de fuselage, le train d'atterrissage, ou encore les réservoirs de réfrigérant de satellite.

La mise en forme des pièces composites est relativement avantageuse. Ces dernières peuvent adopter des formes complexes qui, pour des pièces métalliques, nécessiteraient de l'usinage et de l'assemblage, par exemple. De plus, leur utilisation réduit le nombre de fixations et de joints – qui sont des points de défaillance potentielle - que ce soit pour les aéronefs ou pour les satellites. Les matériaux composites permettent donc d'abaisser les coûts, en réduisant le nombre de composants, et en procédant à des conceptions uni-pièce chaque fois que cela est possible.

Cependant, le remplacement des pièces métalliques par des polymères nécessite souvent une fonctionnalisation de surface afin de retrouver des propriétés optiques, électriques, magnétiques, biomédicales, esthétiques ou chimiques[2]. Le principal inconvénient quand il s'agit de recouvrir ou de greffer la surface des composites à base de polymère provient de l'énergie de surface très faible de ces derniers. Il en résulte une mouillabilité et des forces d'adhésion faible lorsque du métal y est déposé. Les efforts consentis jusqu'à présent pour pallier ce phénomène reposent exclusivement sur des études empiriques. Nous pensons que le manque de simulations et de modèles est un obstacle à un développement technologique efficace. Le développement d'un modèle précis pour la surface des polymères peut aider à la conception de surfaces sur mesure avec un bon contrôle sur la réactivité chimique, et donc sur les processus de fonctionnalisation subséquents. La portée de ce travail n'est donc pas limitée à la seule métallisation des composites.

Nous choisissons de réaliser une étude à la fois expérimentale et théorique de la surface d'un polymère époxy et de sa métallisation en lien avec des projets applicatifs en cours dans notre groupe de recherche (*Surfaces : Réactivité et Protection,* du CIRIMAT, Toulouse). L'objectif principal est de développer un modèle de surface qui soit utilisable comme *template* pour l'étude de mécanismes élémentaires, tels que l'adsorption/désorption, la germination/croissance, ou le greffage chimique.

Les simulations numériques sont l'outil choisi afin d'obtenir des informations sur la surface, et sur les mécanismes d'adsorption et de germination-croissance des films métalliques. L'échelle de temps que l'on veut simuler, la taille du système étudié et les propriétés qui doivent être calculées conduisent au choix de deux méthodologies spécifiques. D'une part, nous réalisons des calculs statiques (qui ne tiennent pas compte de l'évolution du système avec le temps) dans le cadre de la théorie de la fonctionnelle de la densité (DFT)[3]. L'échelle concerne ici des phénomènes quantiques et des systèmes de dimensions de l'ordre de quelques nanomètres. La DFT est utilisée pour déterminer avec précision les paramètres structurels et les propriétés électroniques de molécules et de solides modèles. Nous cherchons alors à simuler les spectres XPS du polymère poly-époxyde à l'aide d'un dimère modèle formé d'une molécule de diglycidylether de biphénol A (DGEBA) connectée à une molécule d'éthylène diamine (EDA). Cette petite molécule permet de prendre en compte toutes les liaisons possibles du polymère réticulé réel, mais en conservant un faible nombre d'atomes (61 atomes) pour faciliter les calculs. En utilisant deux méthodes de calcul (Hartree-Fock[4,5], ΔSCF[6], DFT et uGTS[8–10]), nous tentons d'améliorer les connaissances générales à propos de cette surface et de sa réactivité. D'autre part, nous effectuons des calculs qui tiennent compte de l'évolution temporelle du système dans le cadre de la dynamique moléculaire (MD) classique. Ces simulations numériques concernent des systèmes plus grands (jusqu'à l'échelle micrométrique) et pour différentes échelles de temps (jusqu'à quelques ns)[11,12]. Ils permettent de déterminer des propriétés structurales (distribution de distances interatomiques intra- et inter- moléculaire, par ex.), physico-chimiques (température de transition vitreuse, ...), ou encore mécaniques (Module d'Young, ...) de grands ensemble de particules ou de molécules. Ici, nous utilisons la dynamique moléculaire avec trois objectifs: (i) équilibrer et calculer les propriétés physiques et structurales des liquides (DGEBA et EDA) réactifs purs et de leur mélange, (ii) simuler le processus de polymérisation[13,14] qui crée le réseau poly-époxyde à partir du mélange liquide de nos monomères, et (iii) obtenir les propriétés du polymère.

Pour la partie expérimentale, nous avons développé un protocole de synthèse d'une surface poly-époxyde de faible rugosité ($R_a < 1$ nm), homogène et présentant peu de défauts. Une telle surface « modèle » est souhaitée car il faut être en mesure d'observer les nano-îlots et les clusters métalliques clairement, sans qu'ils soient confondus avec les aspérités de surface, et que la germination ne doit pas être exclusivement hétérogènes (sur les défauts) ; auxquels cas les modèles simples sur lesquels reposent les calculs seraient faux. Les caractérisations volumiques du polymère (taux de polymérisation et température de transition vitreuse) sont conduites par FTIR et DSC. La surface non métallisée est caractérisée par AFM et XPS et est ensuite métallisée à température ambiante par évaporation sous ultravide. Cette technique permet une adsorption sans énergie cinétique et correspond donc mieux aux calculs quantiques d'adsorption. La surface métallisée est aussi caractérisée par AFM et XPS afin de déterminer la réactivité du polymère vis-à-vis du métal, la formation des liaisons interfaciales du métal avec le polymère, et observer la croissance des films de Cu.

Ce manuscrit de thèse est organisé de la manière suivante. Dans le chapitre 1, nous allons détailler les théories sur lesquelles reposent les calculs quantiques et classiques, et comment ils nous aiderons dans le développement d'un modèle de surface. Dans le chapitre 2, nous montrerons le protocole expérimental choisi pour la formation des surfaces de poly-époxydes modèles, ainsi que les caractérisations volumique et de surface, avant et après métallisation. Dans le chapitre 3, nous allons détailler les différentes méthodes qui peuvent être utilisées pour simuler les spectres XPS de la surface vierge et métallisée grâce à l'utilisation d'une molécule dimère modèle. Enfin, dans le chapitre 4, nous démonterons les capacités de la dynamique moléculaire dans la simulation des propriétés physiques et structurales des liquides purs (réactifs) et de leur mélange. Enfin, nous montrerons comment, avec l'utilisation d'un code multi-étapes développé pendant la thèse, nous créons un polymère modèle, dont les propriétés physiques et structurelles sont comparables aux résultats de la bibliographie.

Bibliographie

1. Aerospace materials — past, present, and future. *Aerospace Manufacturing and Design* Available at: http://www.aerospacemanufacturinganddesign.com/article/amd0814-materials-aerospace-manufacturing/. (Accessed: 25th September 2017)
2. E. Sacher (ed.). *Metallization of Polymers 2*. (Plenum Publishers, 2002).
3. Hohenberg, P. & Kohn, W. Inhomogeneous Electron Gas. *Phys. Rev.* **136,** B864–B871 (1964).
4. Bagus, P. S., Ilton, E. S. & Nelin, C. J. The interpretation of XPS spectra: Insights into materials properties. *Surf. Sci. Rep.* **68,** 273–304 (2013).
5. Bagus, P. S., Freeman, A. J. & Sasaki, F. Prediction of New Multiplet Structure in Photoemission Experiments. *Phys. Rev. Lett.* **30,** 850–853 (1973).

6. Ziegler, T., Rauk, A. & Baerends, E. J. On the calculation of multiplet energies by the hartree-fock-slater method. *Theor. Chim. Acta* **43,** 261–271 (1977).
7. Janak, J. F. Proof that θE/θni=εi in density-functional theory. *Phys. Rev. B* **18,** 7165–7168 (1978).
8. Endo, K., Kaneda, Y., Okada, H., Chong, D. P. & Duffy, P. Analysis of X-ray Photoelectron Spectra of Eight Polymers by deMon Density-Functional Calculations Using the Model Oligomers. *J. Phys. Chem.* **100,** 19455–19460 (1996).
9. Motozaki, W., Otsuka, T., Endo, K. & Chong, D. P. Electron Binding Energies of Si 2p and S 2p for Si- and S-containing Substances by DFT Calculations Using the Model Molecules. *Polym. J.* **36,** 600–606 (2004).
10. Otsuka, T., Endo, K., Suhara, M. & Chong, D. P. Theoretical X-ray photoelectron spectra of polymers by deMon DFT calculations using the model dimers. *J. Mol. Struct.* **522,** 47–60 (2000).
11. Alder, B. J. & Wainwright, T. E. Studies in Molecular Dynamics. I. General Method. *J. Chem. Phys.* **31,** 459–466 (1959).
12. Andersen, H. C. Molecular dynamics simulations at constant pressure and/or temperature. *J. Chem. Phys.* **72,** 2384–2393 (1980).
13. Jang, C., Sirk, T. W., Andzelm, J. W. & Abrams, C. F. Comparison of Crosslinking Algorithms in Molecular Dynamics Simulation of Thermosetting Polymers. *Macromol. Theory Simul.* **24,** 260–270 (2015).
14. Sirk, T. W. *et al.* High strain rate mechanical properties of a cross-linked epoxy across the glass transition. *Polymer* **54,** 7048–7057 (2013).

Chapter 1: Objectives and methods

1.1 Introduction

In this chapter, our objective is to describe in details the aims of the project and to give some insight into the methods used for the computational studies which are further analyzed in Chapters 3 and 4. We present elements of quantum and classical methods, together with the computational tools. Concerning the experimental work, methods and technics are included together with the state of the art in Chapter 2.

1.2 Why poly-epoxy polymers and what is the benefit of their surface metallization?

Poly-epoxy polymers are widely implemented in three families of applications: adhesives, paints, and composite materials[1] . The latter, such as epoxy/C fibers composites, is increasingly found in a wealth of devices and parts in the fields of leisure (skis, rackets, boats, golf clubs, etc.), or transports, aeronautics and space (cars, aircrafts, satellites, etc.), to name but a few. These composite materials possess stiffness and Young's modulus that compare well with metallic alloys but with a much lower chemical reactivity and density. Therefore, they allow mass reduction and a large increase of parts durability. Replacement of metallic parts by polymers often requires surface functionalization in order to acquire optical, electrical, magnetic, biomedical, aesthetic, or chemical properties. The main drawback of the coating or grafting of the surface of polymer-based composites comes from the very low surface energy of such materials once polymerized. This leads to a poor wettability rendering painting or gluing difficult, and resulting in poor adhesion. The surface energy of poly-ether ether ketone (PEEK) or poly-epoxy is approximately 40-50 mJ/m^2 to be compared to approximately 500 mJ/m^2 for aluminum. Moreover, the polar component (due to H bonding) is as low as 6-7 mJ/m^2 which inhibits the use of simple functionalization protocols[2–4]. Hence, the reactivity of poly-epoxy surfaces is of major concern regarding functionalization pretreatments and/or treatments. The lack of simulations and models is an obstacle to an efficient technology development which nowadays relies on empirical studies, exclusively. Therefore, the development of an accurate model for the surface of poly-epoxies can help in the design of tailored surfaces with a good control on chemical reactivity, and therefore on subsequent metallization processes. Until now very few attempts have been made[5–8], whereas this family of materials is strategic in many industrial sectors. A metallization model should include a polymer surface model, which could be used to study adsorption/desorption of metallic atoms, the nucleation and growth of the metallic coating.

The early stages of polymer metallization are far from thermodynamic equilibrium conditions since isolated metals atoms are adsorbed on the polymer surface. After deposition the metal atoms may diffuse on the surface or into the polymer. Metal atoms encountering each other form clusters at the surface and in the polymer bulk. These clusters are stable if their size exceeds the size of a critical radius (a minimum number of atoms). At higher coverages metal atoms increasingly form a thin film with a more or less 3-dimensional aspect.[9] This is true when nucleation is homogeneous and not driven by defects/traps. Actually, there are two possibilities: preferential nucleation where metal atoms are trapped at preferred sites or defects, and homogeneous nucleation where nuclei are formed by metal atoms random encounters. Both processes have been observed in polymer metallization and they usually rely upon the specific reactivity of the metal towards the polymer surface[10]. Two opposite examples are given below with Al and Cu.

The adsorption energy of Cu on polyimide, 0.6±0.1 eV is surprisingly high. The activation energy for surface diffusion is lower (e.g. 0.2±0.05 eV).[9] Cu will thus diffuse to long distances before nucleation. This absence of chemical reactivity with polyimide is supported by experiments where Cu migrates inside the polyimide films to form copper agglomerates that are nearly spherical in shape.[11] Davis *et al.*[12] assumed that copper does not react with polyimide at low coverages but that there is a change in bond order of the polyimide carbonyl groups induced by the copper at higher coverages. Bond order is the number of bonding pairs of electrons between two atoms. In the case of a covalent bond between two atoms, a single bond has a bond order of one, a double bond a bond order of two and so on. They found, however, no evidence for copper in an oxidized state. It is correct that Cu is not very reactive towards the polyimide surface, and largely less reactive than Al. However, other studies have shown the preferential adsorption of Cu on hydroxyls of the polyimide surface[13–16], counter arguing Davis *et. al.* hypothesis. The story is different with Al that interacts strongly with the polyimide surface, the C=O group being the preferential site for metal bonding.[17] Another illustration of the higher reactivity of Al with polymers is found in fundamental studies of the Al/ Poly(ethylene terephthalate) interfacial bonding. PET is widely used for packaging.

Unfortunately its diffusion barrier properties are insufficient and an aluminum metallization layer is required. A theoretical study[18] (supported by previous experiments[19] has been performed by calculating atomic orbitals for monomers in interactions with an Al atom. In the XPS core level data, the C1s component corresponding to the C=O group is strongly affected by Al adsorption, with a large modification of the electronic charge distribution on that site. Al atoms are also found to bind covalently to the phenyl rings; however the corresponding complexes are significantly less stable than those involving Al–ester bonding. Overall, the first step of deposition of Al on PET proceeds by the saturation of the C=O sites, followed by an increasing number of Al-Al interactions which favor the formation of dense Al layers. It is unclear whether Al does adsorb on phenyls or not, because once C=O have been attacked, phenyls electronic density is strongly modified, to the detriment of Al/phenyl bonding.

Finally, the adhesion of the metallization layer to the polymer substrate is strongly affected by the above-mentioned mechanisms of adsorption, nucleation and growth. Various theories or mechanisms of adhesion exist but those responsible for metal-polymer adhesion are mechanical locking or interlocking, chemical and electrostatic interactions. Whereas the majority of the thesis work concerns chemical bonding, we introduce these mechanisms briefly.

> *Mechanical locking or interlocking.* In this mechanism the roughness of the substrate provides a mechanical locking if the deposited film covers the whole surface uniformly. Additionally, a larger surface area is available for bonding. It becomes counterproductive if there is no intimate contact between the film and the substrate, with uncoated areas and voids weakening the polymer/metal interface. In the case of electroless deposition[20], polymer surfaces are etched before, so as to create an extensive network of fine shallow "holes" on the surface and/or to create deep channels that connect with each other inside the polymer surface layer. These "holes" and channels provide attachment points for the electroless metal.
>
> *Chemical.* According to this theory, bonds are actually formed between the polymer and the metal. The presence of such chemical bonds should provide a high force of adhesion and be resistant to moisture and/or ambient ageing or mechanical stress. In case of electroless deposition of metals on polymers there are many examples where this specific mechanism of adhesion has been suggested.[17,21,22] Examples of Cu and Al covalent bonding presented above, illustrate this theory.

> *Electrostatic.* This theory support the fact that if two dissimilar materials come in contact, then a charge transfer takes place and a double layer is thus formed. The two layers created can be compared to a capacitor and work is consumed in the separation of these two layers. Derjaguin *et al.*[23], who are the main developers of this theory have given strong arguments in its favor based on their work of removing a polymer film from metal surfaces. Skinner *et al.*[24] have also contributed in proving the value of electrostatic contribution to adhesive performance. Specifically their calculations show that only if charge densities approach $10^{21} electons/cm^3$, then electrostatic interactions will have an important contribution to adhesion.

Chapter 1 is organized as follows. First, we discuss why calculations are performed on polymers with examples from the bibliography. Then we proceed to describe basic concepts involved in quantum calculations, and we finish with elements of classical calculations and what settings we choose for these calculations.

1.3 Calculations on polymers:

Computer simulations can be chosen rather than experiment with the real system for several reasons: (i) the system we want to study does not exist yet (ii) experiments for the system is expensive or too time consuming (or too dangerous…) (iii) all the necessary information for the understanding of a process is not available from experiments. Our project falls in this latter case. The time scale one wants to simulate, the size of the system studied and the properties that need to be calculated lead to the choice of a specific methodology. Additionally, simulations can model both static and dynamic situations. Static calculations refer to calculations that do not take into account the evolution of the system with time. For instance, quantum calculations such as standard density functional theory (DFT), can be performed for systems up to a few nanometers, and can be used to accurately determine structural parameters and electronic properties of molecules and solids. And if there is no need to get electronic properties from the computations, static molecular mechanics simulations can be done for larger systems up to hundreds of nanometers.

Dynamic calculations refer to calculations that take into account the time evolution of the system. Numerical simulations such as Monte-Carlo (MC) calculations and Molecular Dynamics (MD), can be performed in the framework of quantum methods or classical mechanics and can thus be used for larger systems (up to the μm scale) and for various time scales (up to ns). The choice between MC and MD is dictated by the phenomenon in study.

In the literature, classical molecular simulations, and particularly atomistic ones track the evolution of model systems for times up to a few tens of ns[25] . It thus allows to extract dynamic properties of polymers. But it used to be (and it is already) problematic since it requires very long simulations and thus stability of the integrator algorithms for very long times. To overcome this problem for polymeric systems, several approaches have been proposed over the last decades. First, parallelization techniques and computer sciences made possible the use of a large number of processors[26] for the calculations. Moreover, for large time scales, new algorithms involving a multiple time step approach[27] were developed for the integration of equations of motion. They allowed to simulate longer times than the conventional algorithms. But these technical solutions showed limitations and alternative models of the systems had to be developed. One consists in the abandon of chemical details of all-atom models and their substitution by coarse-grained models[28,29]. These models are simplified representations of the molecules. “Pseudo-atoms” replace the group of atoms. Much longer simulation times can be studied than with atomistic models leading to many more realistic network architectures. But to study properties that depend on the detailed chemical structure, a reverse mapping back to the original atomistic description is needed.

In our case, we want to develop a model of a poly-epoxy polymer and its metallization. We need to get information at the atomic level on the electronic structure of the polymer. But we also need to know how the polymer chains move at different temperatures and times. Using a combination of quantum calculations (Hartree-Fock and DFT methods for the results presented in Chapter 3), and classical simulations (atomistic classical Molecular Dynamics in Chapter 4), we will demonstrate our ability to simulate systems of various sizes and to calculate various properties (XPS spectra, polymer density…).

1.3.1 Quantum calculations

In this section we present some concepts of quantum chemistry.

1.3.1.1 The Schrödinger’s equation

The Schrödinger’s equation is the basis of any non-relativistic quantum calculations. It essentially describes the changes over time of a system taking into account quantum effects. This equation although written for changes over time, also includes a formulation that does not take into account time (time-independent equation) and therefore simplifies calculations. This formulation is given by Equation 1:

$$\widehat{H}\psi = E\psi \; (1)$$

where $\widehat{H}$ is the Hamiltonian operator, Ψ is the wavefunction and E is the energy of the state Ψ.

Wavefunctions are mathematical depictions of the quantum state of the system. They represent all the information of the system (position in space of the particles, momenta of particles etc…). The square modulus of a wave-function is a real number which gives the range of probabilities for a particle to be at a given spatial position.

The non-relativistic Hamiltonian operator can be expressed, for a system of N nuclei and n electrons, in atomic units, as:

$$\widehat{H} = -\sum_{I}^{N}\frac{1}{2M_I}\nabla_I^2 - \sum_{i}^{n}\frac{1}{2}\nabla_i^2 - \sum_{I}^{N}\sum_{i}^{n}\frac{Z_I}{r_{Ii}} + \sum_{J>I}^{N}\frac{Z_I Z_J}{R_{IJ}} + \sum_{j>i}^{n}\frac{1}{r_{ij}} \; (2)$$

The first two terms represent the kinetic energy of the nuclei and the electrons respectively. The third term expresses the electrostatic attraction between electrons and nuclei and the two last represent the nuclei/nuclei and electron/electron repulsions respectively. In Equation 2, M_I is the mass of the nucleus I and Z_I is its charge, the distance r_{Ii} is the distance between an electron and a nucleus, R_{IJ} is the distance between two nuclei I and J, and r_{ij} is the distance separating two electrons i and j.

1.3.1.2 The Born-Oppenheimer approximation

The physical basis for the Born-Oppenheimer approximation, is that nuclei move much slower than electrons due to their relative size. This in turn leads to the assumption that the motion of the atomic nuclei and electrons in a molecule are independent. We can then say that the nucleus can be considered stationary and thus its kinetic energy is negligible.

Mathematically this means that the wavefunction of a molecule is a cross multiplication of the wavefunction of electrons and the wavefunction of nuclei as given by Equation 3:

$$\psi_{molecule}(\vec{r_i}, \vec{R_J}) = \psi_{electrons}(\vec{r_i}, \vec{R_J}) \times \psi_{nuclei}(\vec{R_J}) \; (3)$$

where $\vec{r_i}$ and $\vec{R_J}$ are the positions of electrons and nuclei respectively.

The Schrödinger's equation can be reduced to the electronic Schrödinger's equation that gives access to the electronic wavefunction:

$$\hat{H}_{electrons}\ \psi_{electrons}\left(\vec{r_i},\overrightarrow{R_J}\right) = E_{electrons}\ \psi_{electrons}\left(\vec{r_i},\overrightarrow{R_J}\right)\ (4)$$

And using the non-relativistic theory, the electronic Schrödinger's equation for a single electron in a potential $V_{Ne}(\vec{r})$ is given by Equation 5:

$$\left[-\frac{\nabla^2}{2m} + V_{Ne}(\vec{r})\right]\psi(\vec{r}) = E\psi(\vec{r})\ (5)$$

If there are multiple electrons (what is known as a many-body problem) Schrödinger's equation becomes:

$$\left[\sum_{i}^{n}\left(-\frac{{\nabla_i}^2}{2m} + V_{Ne}(\vec{r}_i)\right) + \sum_{i<j} V_{ee}\left(\vec{r}_i,\vec{r}_j\right)\right]\psi\left(\vec{r}_{1,}\vec{r},\ldots,\vec{r}_n\right) = \mathrm{E}\psi\left(\vec{r}_{1,}\vec{r}_2,\ldots,\vec{r}_n\right)\ (6)$$

where *n* is the number of electrons, $V_{Ne}(\vec{r}_i)$ is the potential from the nuclei and $V_{ee}\left(\vec{r}_i,\vec{r}_j\right)$ is the electron-electron interaction.

The expression of the external potential generated by the nuclei is:

$$V_{Ne}(\vec{r}_i) = \sum_{I}\frac{Z_I}{\left|\vec{r}_i - \overrightarrow{R_I}\right|}\ (7)$$

where the sum on *I* concerns all the nuclei in the system (with charge $Q_I = Z_I e$) and position $\overrightarrow{R_I}$.

For a Coulombic system we have the electron-electron interaction:

$$\sum_{i<j} V_{ee}\left(\vec{r}_i,\vec{r}_j\right) = \sum_{i<j}\frac{1}{\left|\vec{r}_i - \vec{r}_j\right|}\ (8)$$

There is no analytical solution to the Schrödinger equation for systems containing more than one electron. This difficulty is caused by the fact that the existence of multiple electrons and their interactions over-complicate the solution to the Schrödinger equation. Therefore, an approximate, numerical solution has to be found.

1.3.1.3 The Hartree-Fock method

Slater introduced a general method to solve Schrödinger's equation. It was based on the independent works of Heisenberg and Dirac that proposed that the sign of a wavefunction changes and becomes the opposite if two electrons are exchanged. Let's consider the exchange of two electrons. The Hamiltonian operator is not modified by exchanging their coordinates:

$$\hat{H}(\overrightarrow{r_1},\overrightarrow{r_2}) = \hat{H}(\overrightarrow{r_2},\overrightarrow{r_1}) \; (9)$$

By substituting in Equation 1 we have

$$\hat{H}(\vec{r_i},\vec{r_j})\psi(\vec{r_j},\vec{r_i}) = E\psi(\vec{r_j},\vec{r_i}) \; (10)$$

We can replace the positions of two electrons with the exchange operator $\widehat{P_{ij}}$ and this operator can exchange positions with the Hamiltonian operator without changing the result (they are commutative). This leads to Equation 11:

$$\hat{H}(\vec{r_i},\vec{r_j})\,\widehat{P_{ij}}\psi(\vec{r_j},\vec{r_i}) = \widehat{P_{ij}}\hat{H}(\vec{r_i},\vec{r_j})\,\psi(\vec{r_j},\vec{r_i}) \; (11)$$

Which transforms into

$$[\hat{H},\widehat{P_{ij}}]\psi = (\hat{H}\widehat{P_{ij}} - \widehat{P_{ij}}\hat{H})\psi = 0 \; (12)$$

Showing that the Hamiltonian and the exchange operator have similar eigenstates. The positions of two electrons are reverted by two exchanges leading to the value of $\widehat{P_{ij}}^2 = 1$. This means that the eigenvalues of $\widehat{P_{ij}}$ are ±1. Thus there are two wavefunctions corresponding to the exchange operator. The first for +1 being:

$$\psi^{(S)}(\vec{r_i},\vec{r_j}) = \frac{1}{\sqrt{2}}\left[\psi(\vec{r_i},\vec{r_j}) + \psi(\vec{r_j},\vec{r_i})\right] \; (13)$$

and the antisymmetric for the -1 eigenvalue

$$\psi^{(A)}(\vec{r_i},\vec{r_j}) = \frac{1}{\sqrt{2}}\left[\psi(\overrightarrow{r_{i,j}}) - \psi(\vec{r_j},\vec{r_i})\right] \; (14)$$

where the $\frac{1}{\sqrt{2}}$ is the normalization constant. If we consider the Hartree wavefunction which is essentially the Hamiltonian operator expressed as the product of different electronic wavefunctions:

$$\psi\left(\vec{r_i},\vec{r_j}\right) = \phi_i(\vec{r_i})\phi_j\left(\vec{r_j}\right) \;(15)$$

where ϕ_i is the one-electron wavefunction, we obtain Equation 16 and 17 that represent the symmetric and antisymmetric functions:

$$\psi^{(S)}\left(\vec{r_i},\vec{r_j}\right) = \frac{1}{\sqrt{2}}\left[\phi_i(\vec{r_i})\phi_j\left(\vec{r_j}\right) + \phi_i\left(\vec{r_j}\right)\phi_j(\vec{r_i})\right] \;(16)$$

$$\psi^{(S)}\left(\vec{r_i},\vec{r_j}\right) = \frac{1}{\sqrt{2}}\left[\phi_i(\vec{r_i})\phi_j\left(\vec{r_j}\right) - \phi_i\left(\vec{r_j}\right)\phi_j(\vec{r_i})\right] \;(17)$$

From these wavefunctions, only the antisymmetric one is in accordance with Pauli's exclusion principle. This is due to the fact that for the case the same electron occupies the same orbital the wavefunction must be 0, that is $\overrightarrow{r_1} = \overrightarrow{r_2}$. This leads to the conclusion that electronic motions have antisymmetric functions. The antisymmetric wavefunction of Equation 17 can be written as a determinant in the following manner:

$$\psi(\overrightarrow{r_1},\overrightarrow{r_2}) = \frac{1}{\sqrt{2}}\begin{vmatrix} \phi_1(\vec{r}_1) & \phi_1(\vec{r}_2) \\ \phi_2(\vec{r}_1) & \phi_2(\vec{r}_2) \end{vmatrix} \;(18)$$

To respect these rules, at the simplest level, the wave function can be represented by a single Slater determinant, an antisymmetrized product of one-electron wave functions for n electrons as presented in Equation 19:

$$\psi(\overrightarrow{r_1},\overrightarrow{r_2},\dots,\overrightarrow{r_n}) = \frac{1}{\sqrt{n!}}\begin{bmatrix} \phi_1(\vec{r}_1) & \cdots & \phi_1(\vec{r}_n) \\ \vdots & \ddots & \vdots \\ \phi_n(\vec{r}_1) & \cdots & \phi_n(\vec{r}_n) \end{bmatrix} \;(19)$$

Using this formulation for the wavefunction, the Hartree-Fock method allows to solve the Schrödinger equation with a variational method and a set of n-coupled monoelectronic equations. The Hartree-Fock approach defines a term of Coulomb interaction between an electron and the mean electron distribution (mean Hartree potential). But the exchange potential that contributes to the energy does not take into account the correlation effects between the movements of electrons.

1.3.1.4 Density functional theory (DFT) calculations

The electronic density, $\rho(\vec{r})$, represents the number of electrons per unit volume at a position in space, $\vec{r}$. In the framework of the density functional theory, the n-electron wavefunction $\Psi(\overrightarrow{r_1}, \overrightarrow{r_2}, \overrightarrow{r_3}, \ldots, \overrightarrow{r_n})$ is replaced by the electronic density. Hohenberg and Kohn (HK)[30] established two theorems which constitute the foundation of DFT.

First HK theorem (a.k.a The existence theorem)[30]

This theorem states that all the properties of a system in a ground electronic state are determined by the ground state electron density $\rho_0(x, y, z)$. This means that if $\rho_0(x, y, z)$ is known, one can calculate any ground state property.

The theorem generalizes the calculation of any ground state property of a system as a functional of the ground state electron density function, for example the energy can be mathematically calculated by

$$E_0 = F[\rho_0] = E[\rho_0] \; (20)$$

Mathematically speaking the term "functional" describes a function whose argument is itself a function. Some quantities are simultaneously functionals and functions.

Second HK theorem (a.k.a The variational theorem)[30]

This theorem states that any trial electron density function will give an energy higher than (or equal to, if the true electron density function is calculated), the true ground state energy. So the electronic density of the ground state can be calculated using a variational method. Although the original Hohenberg-Kohn theorems were proved for non-degenerate ground states they have been proved to work for degenerate ground states too.

The Kohn-Sham approach

The basic ideas behind the Kohn-Sham[31] approach are:

(1) To express the energy as a sum of terms with only one, a relatively small term, that is the unknown to the equation functional.

(2) To use an initial guess of the electron density ρ in the Kohn-Sham (KS) equations to calculate an initial guess of the KS orbitals and energy levels.

(3) To use this initial guess to iteratively refine these orbitals and energy levels, in a manner similar to that used in the HF-SCF method. At every iteration the KS orbitals are used to calculate an electron density and the energy.

The way to deal with this issue is to separate the electronic energy of our molecule into a portion which can be calculated accurately, and a relatively small term which requires the functional.

The electronic energy of a real system is the sum of the electron kinetic energies, the nucleus-electron attraction potential energies, and the electron-electron interaction energies as shown in Equation 21:

$$E[\rho] = T[\rho] + E_{Ne}[\rho] + E_{ee}[\rho] \ (21)$$

The nucleus-electron potential energy, $E_{Ne}[\rho]$ is the sum over all n electrons of the potential corresponding to attraction of an electron for all the nuclei *I*:

$$E_{Ne}\ [\rho] = \int \rho(\vec{r}).v_{Ne}(\vec{r})d\vec{r} \ (22)$$

$$with \quad v_{Ne} = \sum_{i=1}^{n}\sum_{I=1}^{N} -\frac{Z_I}{\vec{r}_{iI}} \ (23)$$

$\frac{Z_I}{\vec{r}_{iI}}$ is the potential energy due to the interaction of electron *i* with nucleus *I* at a given distance $\vec{r}_{iI}$

This leads to Equation 24:

$$E = T[\rho] + \int \rho(\vec{r})\ v_{Ne}(\vec{r})\ d\vec{r} + E_{ee}[\rho] \ (24)$$

The middle term is a classical electrostatic attraction potential energy expression. A problem that arises is that there is no way to know the functionals for the kinetic and potential energies for the other two terms, $T[\rho]$ and $E_{ee}[\rho]$, making the equation unsolvable.

Kohn and Sham thus assumed a reference system of non-interacting electrons which gives the same ground state electron density distribution as the real system ($\rho_{ref} = \rho_0$). The difference in "behavior" between the reference system and the real system can be accounted into a term that we call "the exchange and correlation functional".

This non-interacting system has a kinetic energy $T[\rho]_{ref}$. First in respect to the electronic kinetic energy, the quantity $\Delta T[\rho]$ is defined: $\Delta T[\rho] \equiv T[\rho]_{real} - T[\rho]_{ref}$.

Next, for the electronic potential energy calculation, the term ΔVE_{ee} is defined as the deviation of the real electron-electron repulsion energy from a classical charge-cloud coulomb repulsion energy. The classical electrostatic repulsion is calculated from pairs of infinitesimal densities $\rho(\vec{r}_1)d\vec{r}_1$ and $\rho(\vec{r}_2)d\vec{r}_2$ (in a classical, non-quantum cloud of negative charge) separated by a distance $\vec{r}_{12}$(multiplied by ½ so that the repulsion energy is not counted twice). It leads to Equation 25:

$$\Delta E_{ee}[\rho] = E_{ee}[\rho]_{real} - \frac{1}{2}\iint \frac{\rho(\vec{r}_1)\rho(\vec{r}_2)}{\vec{r}_{12}} d\vec{r}_1 d\vec{r}_2 \quad (25)$$

One can thus write:

$$E = \int \rho(\vec{r}) v_{Ne}(\vec{r}) d\vec{r} + \frac{1}{2}\iint \frac{\rho(\vec{r}_1)\rho(\vec{r}_2)}{\vec{r}_{12}} d\vec{r}_1 d\vec{r}_2 + \Delta E_{ee}[\rho] + \Delta T[\rho] + T[\rho]_{ref} \quad (26)$$

The two "delta terms" which have been placed next to each other, present the main problem with DFT, that is the sum of the kinetic energy deviation from the reference system and the electron-electron repulsion energy deviation from the classical system, also called the exchange-correlation energy. This exchange-correlation energy is a functional of the electron density function:

$$E_{XC}[\rho] \equiv \Delta E_{ee}[\rho] + \Delta T[\rho] \quad (27)$$

Thus Equation 26 becomes:

$$E = T[\rho]_{ref} + \int \rho(\vec{r}) v_{Ne}(\vec{r}) d\vec{r} + + \frac{1}{2} \iint \frac{\rho(\vec{r}_1)\rho(\vec{r}_2)}{\vec{r}_{12}} d\vec{r}_1 d\vec{r}_2 + E_{XC}[\rho] \ (28)$$

The Kohn-Sham equations

The KS equations can be derived by differentiating the energy with respect to the KS orbitals that are used to generate the electronic density. The electron density distribution is exactly the same for the non-interacting reference system as that of the ground state of our real system. That is expressed by Equation 29:

$$\rho = \rho_{ref} = \sum_{i=1}^{n} \left|\psi_i^{KS}\right|^2 \ (29)$$

where ψ_i^{KS} are the Kohn-Sham orbitals.

The Kohn-Sham equations are one-electron equations:

$$\left[-\frac{1}{2}\nabla_i^2 - \sum_I \frac{Z_I}{\vec{r}_{1I}} + \int \frac{\rho(\vec{r}_2)}{\vec{r}_{12}} d\vec{r}_2 + v_{XC}(1)\right] \psi_i^{KS}(1) = \epsilon_i^{KS} \psi_i^{KS}(1) \ (30)$$

where ϵ_i^{KS} are the Kohn-Sham levels and $v_{XC}(1)$ is the exchange-correlation potential.

This can be rewritten using the Kohn Sham operator:

$$\hat{h}^{KS}(1)\psi_i^{KS}(1) = \epsilon_i^{KS}\psi_i^{KS}(1) \ (31)$$

The exchange correlation potential v_{XC} is a functional derivative of the exchange correlation energy described above $E_{XC}[\rho]$. And thus:

$$v_{XC}[\rho] = \frac{\delta E_{XC}[\rho(\vec{r})]}{\delta \rho(\vec{r})} \ (32)$$

The Kohn-Sham energy equation is exact, but it would give an exact energy only if the electronic density function $\rho(\vec{r})$ and the functional for the exchange-correlation energy $E_{XC}[\rho]$ are known exactly.

Approximation of exchange-correlation energy functional

Creating a good functional $E_{XC}[\rho(\vec{r})]$ is the main problem in density functional theory. Some of the functionals used widely are presented now by increasing sophistication: (a) the local density approximation (LDA), (b) the local spin density approximation (LSDA), (c) the generalized gradient approximation (GGA) and (e) the hybrid functionals.

The local density approximation (LDA)

At the beginning, much of the popularity of DFT was due to the introduction of an exchange and correlation energy $E_{XC}[\rho]$ that can be reasonably approximated by a local functional of the density. The LDA tells us that at every point in the system the energy density has the value that would be given by a homogeneous electron gas which had the same electron density ρ at that point. The energy density is the energy per electron. Within the LDA approximation any system is locally treated as an electron gas. The exchange-correlation energy for a homogeneous electron gas can be written as in Equation 33,

$$E_{xc}^{LDA} = E_x^{LDA} + E_c^{LDA} \ (33)$$

The first term E_x^{LDA} is the Dirac exchange energy with the analytic form shown in Equation 34

$$E_x^{LDA} = -\frac{2}{3}\left(\frac{3}{4\pi}\right)^{\frac{1}{3}} \int [\rho(\vec{r})]^{\frac{4}{3}}\, d\vec{r} \ (34)$$

The correlation term E_c^{LDA} in Equation 33 does not have a known analytic form. However, the correlation part can be obtained by using[32,33] the results of Monte Carlo simulations[34].

Typically the LDA has a good accuracy in reproducing experimental structural and vibrational properties of strongly bound systems. It usually overestimates bonding energies and underestimates bond lengths[35,36]. LDA was the first generation of exchange-correlation functionals. An extension of the method is the local spin density approximation (LSDA) where electrons of α and β spin are assigned to different spatial KS orbitals $\psi_\alpha^{KS}$and ψ_β^{KS}, from which different density functions ρ^α and ρ^β follow. LSDA geometries, frequencies and electron-distribution properties tend to be reasonably good, but the dissociation energies, including atomization energies are very poor. Examples of these functionals are functionals developed by Vosko-Wilk-Nusair[33] (VWN) or Perdew-Zunger[32] (PZ81). But they are nowadays largely replaced by an approach that uses not only the electron density but also its gradient.

The Generalized Gradient Approximation (GGA)

A large number of DFT calculations nowadays use exchange-correlation energy functionals E_{XC} that utilize both the electron density and its gradient, the first derivative of ρ with respect to position as shown by Equation 35:

$$\left(\frac{\partial}{\partial x}+\frac{\partial}{\partial y}+\frac{\partial}{\partial z}\right)\rho = \nabla\rho \ (35)$$

These functionals are called gradient-corrected or said to use the generalized-gradient approximation. The exchange correlation energy functional can be written as the sum of an exchange-energy functional and a correlation-energy functional:

$$E_{xc}^{GGA} = E_{x}^{GGA} + E_{C}^{GGA} \ (36)$$

with $|E_x|$ being much bigger than $|E_C|$. One of their most important advantage is that they reduce the bond dissociation energy error and lead to improved bond lengths and angles but are more computationally expensive than LDA functionals. For 4d-5d transition metals the improvement of GGA over LDA functionals is not clear depending on each particular case examined.

Examples of gradient-corrected correlation energy are the Lee-Yang-Par[37] (LYP), Perdew 1986[32] (P86), Perdew 1991[38] (PW91) and Perdew, Burke, and Enzerhof[39] (PBE), amongst others.

The Hybrid Functionals

Hybrid functionals are functionals (of the GGA level or higher) that contain HF exchange, the correction energy to the classical Coulomb repulsion. The percentage of HF exchange energy to use is a main characteristic of the various hybrid functionals. Some hybrid methods base the HF percentage not on experimental parametrization ("parameter-free" hybrid methods), but on theoretical arguments. This however does not give them superior performance[40]. These functionals are very expensive computationally due to the long-range interactions that are taken into account. However they can estimate better than simple DFT functionals the vibrational and magnetic properties as well as band gaps in semiconductors. Examples of such hybrid functionals are the Becke[41] (B3) and the Heyd, Scuseria and Ernzerhof[42] (HSE).

The Kohn-Sham equations solution and the deMon2k code

Density functional calculations were performed with the deMon2k code[43] based on the PhD work of A. St-Amant at the *Université de Montréal*[44]. It is based on the linear combination of Gaussian type orbitals (LCGTO). In this framework, standard strategy for solving the KS equations is thus to expand the KS orbitals in terms of atomic orbital basis φ_S (built from contracted Gaussians):

$$\psi_i^{KS} = \sum_s c_{si}\varphi_s \quad (37)$$

where C_{si} is a molecular orbital coefficient.

The same basis functions are often used in the solution of KS equations as well as in the wavefunction theory, although as in all calculations designed to capture electron correlation, sets with smaller than split-valence should not be used. This guess is usually a non-interacting atoms guess, obtained by summing mathematically the electron densities of the individual atoms of the molecule, at the initial molecular geometry.

Auxiliary Density Functional Theory (ADFT)

One of the main reasons the deMon2k code was selected is that it executes calculations much faster than other DFT codes, by making use of the auxiliary density functional theory[45] (ADFT): the direct calculation of the four-center electron repulsion integrals is not necessary because an auxiliary function basis for the variational fitting of the Coulomb potential is introduced[46–48]. ADFT makes use of an auxiliary function density, which is an approximate density, $\tilde{\rho}$ given by Equation 38:

$$\tilde{\rho}(\overrightarrow{r}) = \sum_{\tilde{k}} x_{\tilde{k}}\tilde{k}(\vec{r}) \quad (38)$$

where $\tilde{k}(\vec{r})$ are the primitive Hermite Gaussians[49] which are centered on atoms and $x_{\tilde{k}}$ is the auxiliary function fitting coefficient. More details are given in references [50–52].

By applying ADFT, the approximate density is also used for the calculation of the exchange-correlation energy. Differences between ADFT and standard DFT geometries and bond energies are usually in the range of the accuracy of the exchange-correlation functional. Using ADFT might introduce noise in the geometry optimization and in higher energy derivatives but the gain in computational time is high.

Pseudopotential calculations with deMon2k

All-electrons and effective core potentials (ECPS) calculations can be performed with *deMon2k*. The use of Effective Core Potentials (ECPs) have the purpose to replace the core electrons in a calculation with an effective potential. This makes the need for core basis functions obsolete and saves computational time . Thus only the valence electrons are treated explicitly and valence wavefunctions are sensitive to the effects of core states. The separation between valence and core electrons is a difficult task which is only directed by experimental data and all-electron calculations previously executed. DeMon2k offers a library containing the ECPs from Stuttgart-Dresden[53] and from Los Almos National Laboratory[54].

1.3.2 Classical Calculations

1.3.2.1 Molecular Mechanics (MM) basics

In addition to our quantum calculations, we also perform classical MD simulations to study the evolution with time and temperature of several systems, i.e. the reactants for the synthesis of the poly-epoxy (pure liquids and stoichiometric mixture) as well as different polymerized phases. We derive various physical and structural properties from these computations (presented in Chapter 4).

We introduce now some molecular mechanics basics to understand how the total energy of the system is calculated through the various interactions that exist in such systems. The mathematical description of these types of interactions are detailed below. It includes equations and parameters. In a force field, the parameters can be derived from quantum calculations regarding intra- and inter- molecular interactions and the calculation of the total energy or from the fitting of experimental data. These parameters are specific of a given interaction between specific atoms. All the equations and parameters that account for the bonded and non-bonded interactions are called a force field. In the bibliography we can find a great variety of force fields:

- Classical force fields: Class I force fields are the simplest force fields that include parameters for the molecular mechanics bond, angle, dihedral and van der Waals interactions mentioned in this chapter. Class II force fields take into account intra-molecular interactions at larger distances between atoms. This fact gives them the ability to evaluate the total energy of the system in a more precise, but computationally expensive way. The other problem that occurs is that for many molecules all the parameters cannot be found and require further calculations.
- Polarizable force fields[55] which add point dipoles on some or all atomic sites and are used to study systems located inside mediums affected by electrical fields and demonstrate dielectric polarization.
- Reactive force fields[56] that employ a bond length/bond order relationship, i.e. in every iteration after every connection with the reactive pairs the bond orders (single, double or triple) are updated. The use a charge calculation scheme that takes into account geometry. They include valence angles allowing connectivity and change of bond order. They calculate non-bonded interactions between all atom pairs.
- Coarse-grained force fields[57] that reduce the computational cost of calculations by reducing the degrees of freedom in a system allowing for longer time and larger system size simulations.

We use the Generalized Amber Force Field (GAFF)[58], that is a Class I force field, for the classical molecular dynamics in Chapter 4. We chose this force field as it was greatly used in previous studies for poly-epoxy polymerizations. GAFF is freely available for download[59] together with the AmberTools[59] program that is used for the calculation of atomic charges. The force field parameters used with the atom types are included in Annex A.

In the following section, we present the equations implemented in GAFF for the calculation of the energy of the bonded and non-bonded interactions[58]. In GAFF, the bonded interactions are summed in three basic types:

- Bond stretching
- Bond bending
- Bond torsional

The non-bonded interactions, on the other hand, are distinguished in two main types:

- Inter- and intra-molecular van der Waals interactions
- Inter- and intra-molecular Coulombic interactions

The GAFF equations are detailed below.

***Bond stretching interactions**:* they are described by an oscillatory potential that refers to the distance variations around the equilibrium distance, $\vec{r_0}$ between two bonded atoms:

$$U_{str}(\vec{r}) = \frac{1}{2}k_{str}(\vec{r} - \vec{r_0})^2 \ (39)$$

Here k_{str} is the spring constant and $\vec{r}$ is the distance between the two atoms.

***Bond bending interactions**:* these interactions are also modeled by an oscillatory potential. It represents the angle variations between three bonded atoms around the equilibrium angle θ_0:

$$U_{bend}(\vec{r}) = \frac{1}{2}k_{bend}(\theta - \theta_0)^2 \ (40)$$

Here k_{bend} is the spring constant and θ is the angle formed by the three atoms.

Dihedral interactions: They relate to the variation of the dihedral angle φ formed by the rotation of the second bond between four consecutive bonded atoms.

$$U_{dih}(\varphi) = \sum_{i}^{k} C_i cos^i(\varphi) \ (41)$$

where k is the maximum number of terms that will be added, and C_i the multiplier of each power term for each cosine in the summation using a Fourier transform.

Electrostatic potential: By assuming that charges on atoms are described as point charges, the electrostatic (or Coulomb) potential describes the interaction between these point charges along an imaginary line, given by $\vec{r}_{ij}$ and connecting the two charges. It is modeled by the following equation:

$$U_{el}(\vec{r}_{ij}) = -\frac{q_i q_j}{4\pi\varepsilon_0 \overrightarrow{r_{ij}}} \ (42)$$

where ε_0 is the vacuum permittivity with value 8.85418782×10^{-12} F/m, and q_i and q_j the charges of atoms i and j, respectively. Due to the fact that electrostatic forces are of infinite range in nature, we need to add a cut-off distance for our calculations and take into account the electrostatic forces up to a specific region for each pair.

Due to their very long range nature, in addition to their description by the force field, Coulombic interactions must not be limited only to the atoms contained in the simulation box in periodic conditions. The strength of these interactions decline and we usually consider that it becomes negligible at distances larger than three or four times the simulation box. Many methods have been proposed for the calculation of long range Coulombic interactions. The most accurate method is Ewald summation[60], but it is very demanding in CPU and therefore seldom applied. Other methods that can be used alternatively are the spherical truncation[60] and the Particle-Particle Particle-Mesh Ewald (PPPM)[61] methods.

Dipole-Dipole interaction: A Lennard-Jones potential analyzes the hardcore repulsion occurring at close distances due to the overlap of electron orbitals, and long-range attraction at greater distances due to van der Waals interactions. It describes interactions between atoms along the same chain that are separated by three bonds and more, or between non-bonded atoms that are distant. A typical expression is:

$$U_{LJ}(\overrightarrow{r_{ij}}) = \begin{cases} 4\epsilon\left[\left(\frac{\sigma}{\overrightarrow{r_{ij}}}\right)^{12} - \left(\frac{\sigma}{\overrightarrow{r_{ij}}}\right)^{6}\right], & \overrightarrow{r_{ij}} < \overrightarrow{r_c} \\ 0, & \overrightarrow{r_{ij}} \geq \overrightarrow{r_c} \end{cases} \quad (43)$$

where ϵ denotes the well depth (how strongly the two atoms attract each other), σ is the distance at which the Lennard-Jones potential between the two particles becomes zero. σ gives a measure of how close two non-bonded atoms can get and is also called the van der Waals radius. Both parameters are strongly dependent on the type of atoms involved in the interaction. $\overrightarrow{r_{ij}}$ is the distance between particles i and j, and $\overrightarrow{r_c}$ is the potential cutoff. By potential cutoff we mean the distance up to which we choose to take into account the dipole-dipole interactions.

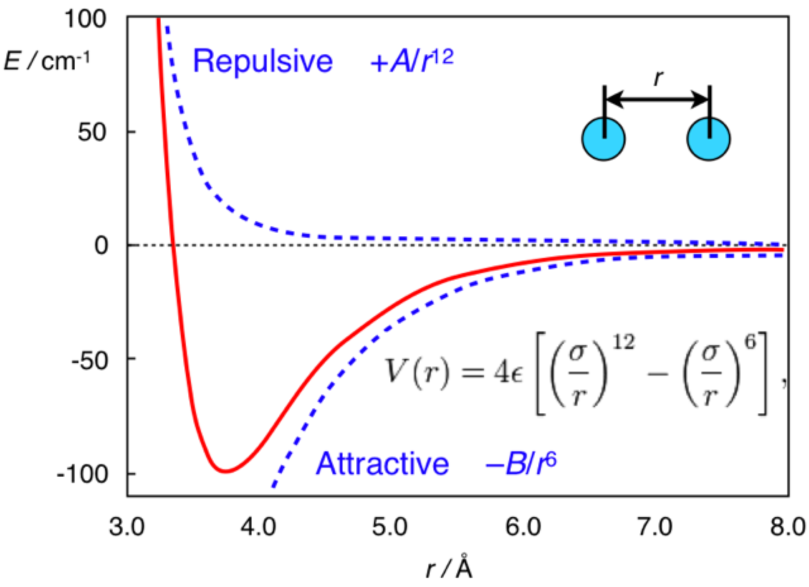

Figure 1. The Lennard-Jones 12-6 pair potential plotted that shows both the repulsive and attractive parts. Adapted from Ref.[62].

Figure 1 shows a plot of the Lennard-Jones potential function (solid line, red) exhibiting the repulsive and attractive contributions (dotted lines). The $\left(\frac{\sigma}{r}\right)^{12}$ term is used to describe the short-range repulsion caused by to the overlap of electron clouds and the $\left(\frac{\sigma}{r}\right)^{6}$ term is used to describe the attraction between atoms (induced dipole-dipole interactions).

With classical molecular mechanics, one can performed static calculations. But molecular simulations taking into account time and temperature are needed to calculate properties that can be compared to experimental counterparts. Additionally, it would help to describe mechanisms at a microscopic scale, which are not often totally identified with experiments. There are two main technics of molecular simulations: Molecular Dynamics (MD) and Monte Carlo[63] simulations (MC). Classical MD simulations solve the equations of motions of Newton to predict the time evolution of a system either by taking into account temperature and pressure or relaxing the system in a given time. MC simulations are a rigorous tool to extrapolate multiple configurations of a system by using the Boltzmann distribution at a given temperature and to get large and realistic samplings. MC methods are often used in conjunction with MD by creating a large number of configurations and by choosing the most stable we can then use in the MD context to simulate a real system[64].

1.3.2.1 The molecular Dynamics (MD) method

An MD simulation can reproduce the general behavior of matter in gas, liquid, and solid states. MD is performed within a specified ensemble[65]. The ensemble name refers to the quantities that are fixed by the users and held constant during calculations, i.e. the number of particles (N), the volume (V), the temperature (T), the energy (E) and the pressure (P). The MD simulation can be done for a system in the *microcanonical* NVE ensemble. The system is thus isolated because there is no exchange (matter, heat, work) with the environment. Nevertheless, energy is not a variable that can be regulated in real life experiments. Many experimental observations are done at constant pressure and temperature, such that the system is no longer isolated from its environment. Therefore, simulations are also often performed in the *canonical* ensemble (NVT), and in the *isothermal-isobaric* ensemble (NPT), and in a variety of other ensembles depending on the knowledge that is targeted. Other quantities that can be fixed include enthalpy (H), and chemical potential (μ). Although these ensembles are the most common, this list is not exhaustive.

In Molecular Dynamics simulations the time evolution of a set of interacting particles is followed via the solution of Newton’s equations of motion:

$$m_i \frac{\partial^2 \overrightarrow{r_i(t)}}{\partial t^2} = -\nabla E_p(\vec{r_i}) = F_i \ (44)$$

Where $\vec{r_i}$ are the positions, m_i the mass of one particle i, $E_p(\vec{r_i})$ the potential energy function between the particles in the system and F_i is the force on each particle in the system. F_i is calculated from the potential energy function.

MD trajectories are defined by both positions and velocity vectors (or momenta of the particles) and they describe the time evolution of the system. Accordingly, the positions and velocities are propagated with a finite time interval using numerical integrators (described below). The velocities determine the kinetic energy and temperature in the system and averaged properties are provided from the trajectories.

Any quantity that can be expressed in terms of the positions and momenta associated with the movement of the particles can be calculated. For instance, each particle (in a 3D simulation) has its kinetic energy related to temperature through:

$$\frac{1}{2} m |\vec{v}|^2 = \frac{3}{2} k_B T \ (45)$$

where k_B is the Boltzmann constant. The instantaneous of the pressure is calculated as:

$$P = \frac{N k_B T}{V} + \frac{1}{3V} \sum_{i=1}^{N} \vec{r_i} \cdot \vec{F_i} \ (46)$$

where V is volume, and $\vec{r_i}$ and $\overrightarrow{F_i}$ are the position and force acting on particle i.

For our dynamics simulations, we chose the code LAMMPS and we had thus to select one algorithm for the integration of the equations of motion and the thermostat and barostat algorithms. These options are detailed below.

Integration Scheme

In the present work, Newton’s equations of motion are integrated by using an algorithm called the ‘velocity-Verlet’ integration scheme[66]. The position and velocity of each particle of the system are updated from time *t* to time $t + \Delta t$ using an intermediate half-time step at $t + \frac{1}{2}\Delta t$:

$$\vec{r}(t + \Delta t) = \vec{r}(t) + \vec{v}(t)\Delta t + \frac{1}{2}\vec{a}(t)\Delta t^2 \ (47)$$

where $\vec{a}(t)$ is the acceleration of a particle at a time t. It is calculated from the force acting on the particles divided by their mass. Δt is the timestep.

The velocities and positions are updated at half time step and at time step:

$$\vec{v}\left(t+\frac{1}{2}\Delta t\right)=\vec{v}\left(t-\frac{1}{2}\Delta t\right)\Delta t+\vec{v}(t)\Delta t \ (48)$$

$$\vec{r}(t+\Delta t)=\vec{r}(t)+\vec{v}\left(t+\frac{1}{2}\Delta t\right) \ (49)$$

Using the updated positions and velocities each time, the force $\vec{F}(t+\Delta t)$ is further evaluated.

At t = 0 the initial velocities are given to the particles by using a Maxwell-Boltzmann distribution corresponding to the fixed temperature. This integrator is fast, simple and stable. The step-by-step execution of the algorithm is given in Annex B.

The timestep in the simulations needs to be validated by preliminary computations. In our work, the choice of the timestep depends on the time required to observe the microscopic evolution of the system (movements of molecules and chains). So it should be large enough to capture the dynamics of the system. On the other hand, a very large timestep (e.g. 1 ns) will lead to the immediate destruction of the simulation box as the forces developed for a time evolution of this magnitude will cause overlaps of atoms.

Periodic conditions

We perform periodic computations in order to simulate a polymer bulk phase. It is thus essential to choose periodic boundary conditions that mimic practically an infinite sample of the material. The volume containing the N particles is treated as the primitive cell of an infinite periodic lattice of identical cells. A given particle from the primitive cell interacts with all other particles in this infinitely periodic system, i.e., with all other particles in the same periodic cell and all particles (including its own periodic image) in all other cells. Also, as a molecule leaves the central box, one of its images will enter through the opposite face. There are no walls at the boundary of the central box, and no surface molecules. Of course, since the poly-epoxy material is amorphous, one must check that periodicity does not add order to the system that would bias calculated properties.

Thermostat Algorithms

An algorithm that maintains a periodic simulation box at a fixed temperature is called a thermostat algorithm[65,67,68]. A thermostat can be used to: (i) match experimental conditions (most condensed-phase calculations are performed under temperature); (ii) study temperature dependent processes (e.g., determination of thermal coefficients, determination of glass transition temperature etc.) and (iii) enhance the efficiency of a conformational search (e.g., high-temperature dynamics, simulated annealing). The use of a thermostat requires the definition of an instantaneous temperature. This temperature will be compared to the reference temperature T_o of the heat bath to which the system is coupled. A good thermostat should reproduce the required temperature at our given timescale at least qualitatively.

We choose the Nosé-Hoover thermostat[65] for our NPT and NVT simulations because this thermostat is deterministic and time-reversible. It will always satisfy the same dynamic equations as when the system started to evolve.

The Nosé-Hoover thermostat works through the following equations:

$$\vec{r_i} = \frac{\vec{p_i}}{m_i} \quad (50)$$

$$\vec{p_i} = \vec{F_i}(\vec{r_1}, \dots, \vec{r_1}) - \zeta \vec{p_i} \quad (51)$$

$$\dot{\zeta} = \frac{1}{Q}\left[\sum_i \frac{\vec{p}_i^2}{2m_i} - 3Nk_BT\right] \quad (52)$$

where ζ is a thermodynamic friction coefficient that allows the heat exchange between the thermostat and our system. Q determines the strength of the thermostat. The thermostat by using these equations allows us to acquire the statistical evolution of the system in the canonical ensemble. Although comparing whether one thermostat leads to a better description of the dynamics compared to another one is empirical, it seems reasonable to assume that: (i) thermostats that allow the temperature to oscillate are more likely to represent the dynamics correctly compared to thermostats fixing the temperature at a given value; (ii) thermostats with temperature fluctuations are more likely to represent the dynamics correctly when these fluctuations occur in the duration of a simulation and when the dynamics is smooth (continuous velocity trajectory).

Barostat Algorithms

An extension of the MD method to systems not described by the *microcanonical* NVE ensemble was presented by Andersen[67] in 1980. Andersen proved that by modifying the Lagrangian of the system, a constant external pressure could be added in the MD simulation of a system. Specifically for a system in which a constant external pressure P is imposed, the system volume V is a dynamic variable that fluctuates in order to maintain mechanical equilibrium between the external and system pressures. The system is then exposed to a barostat, whereby an analogy of a "piston" of arbitrary "mass" as given by textbooks, controls the dynamics of the volume. While ensemble averages are independent of the piston mass, the fictitious mass does affect the response time for volume fluctuations.

Andersen's approach was later modified to simulate systems in contact with a thermostat[67]. Nosé[65] and Hoover[69,70] proposed another isothermal-isobaric (NPT) MD algorithm using a modification of Andersen's piston method for maintaining constant pressure and the thermostating method of Nosé. Later, other algorithms were developed and the choice is again subjective to the results observed a given system. In general the barostat will have much larger oscillations than a thermostat (a characteristic that we also observed in the present work).

Our choice for a barostat is the Nosé-Hoover barostat[69]. It allows the volume of the system to fluctuate under constant pressure. This algorithm drives the system to the state where the average internal pressure is equal to the applied external pressure. It follows an approach analogous to the Nosé-Hoover thermostat using a separate set of variables.

The LAMMPS simulation software

In this section, a description of the LAMMPS[26] code is given, because this is the code employed in the present MD simulations. The basic features and advantages of this code can be summarized as follows:

- LAMMPS is a classical molecular dynamics code. The acronym stands for Large-scale Atomic/Molecular Massively Parallel Simulator.
- LAMMPS integrates Newton's equations of motion for collections of atoms, molecules, or macroscopic particles that interact via short- or long-range forces with a variety of initial and/or boundary conditions. The integration of the equations of motion can be done either with the velocity Verlet[66] or the rRESPA[71] algorithm.
- It contains many potential functions in its libraries both for soft (biomolecules, polymers) and solid-state (metals, semiconductors) materials, as well as for coarse grained or mesoscopic systems. The Coulombic interactions are addressed by many different methods such as the Ewald and the particle-particle-particle-mesh (PPPM) methods.
- LAMMPS proposes minimization algorithms such as steepest descent[72] (SD), Conjugate Gradient[73] (CG), and Hessian Free-Truncated Newton[74] (HFTN).
- For NVT and NPT molecular dynamics simulations, the temperature is kept constant either with the Berendsen[68] or the Nosé-Hoover[65] thermostats and the pressure is kept constant with the Nosé-Hoover barostat[65].
- The biggest advantage of LAMMPS though, is that it is optimized in order to work as efficiently as possible on parallel machines. LAMMPS uses spatial decomposition techniques to partition the simulation domain into small 3D subdomains, each one assigned to a different processor. Processors communicate by using the message passing method via the MPI libraries.
- Finally it is freely available and has an enormous community upon which someone can rely for any troubleshooting that may occur.

1.4 Computational Facilities

Calculations were executed on the EoS supercomputing cluster which belongs to the Scientific Grouping CALMIP (Computations in Midi-Pyrénées[75]). EoS (Bull SA) comprises 12240 cores and a total of 612 nodes for utilization by the users (612 nodes * 20 cores each). The processors are Intel Xeon E5-2680v2 10C 2.8GHz which have 10 cores each with the ability to hyperthread doubling the number of cores available in each node. It uses the Intel Math Kernel Library and utilizes MPI (Message Passing Interface) and has Intel FORTRAN Compilers.

The deMon2k software suite was compiled using the MPI protocol on EoS in order to have the capability to perform calculations using multiple cores and nodes thus increasing calculation speed.

LAMMPS was build using the MPI protocol for parallelization allowing the use of multiple cores and the g++ compiler available on EoS. For using special features (such as the PPPM method) additional packages were installed that exist in the .tar file of LAMMPS.

1.5 Conclusion

We have seen in this chapter some basic elements of both quantum and classical theories that are the basis of our calculations. We are going to analyze the results of our computations and show how joining both quantum and classical approaches can lead to accurate simulation of the XPS spectra of both the pristine and metalized surface as well as the bulk of our model poly-epoxy polymer, in the following Chapters 3 (quantum simulations) and 4 (classical dynamics).

But first, Chapter 2 will introduce the experimental counterpart of the project. The synthesis and characterization of poly-epoxy polymers and their surface metallization are presented together with methods and techniques used.

Bibliography

1. Pascault, J. P., Sautereau, H., Verdu, J. & Williams, R. J. . *Thermosetting Polymers*. (CRC Press, 2002).
2. Petrie, E. M. *Handbook of Adhesives and Sealants*. (McGraw-Hill, 2007).
3. Gooch, J. W. *Encyclopedic dictionary of polymers*. (Springer, 2010).
4. Petrie, E. M. *Epoxy adhesives formulation*. (McGraw-Hill, 2006).
5. Charbonnier, M. & Romand, M. Polymer pretreatments for enhanced adhesion of metals deposited by the electroless process. *Int. J. Adhes. Adhes.* **23,** 277–285 (2003).
6. Baum, T. H., Miller, D. C. & O'Toole, T. R. Photoselective catalysis of electroless copper solutions for the formation of adherent copper films onto polyimide. *Chem. Mater.* **3,** 714–720 (1991).

7. Yoon, S., Choi, H.-J., Yang, J.-K. & Park, H.-H. Comparative study between poly(p-phenylenevinylene) (PPV) and PPV/SiO2 nano-composite for interface with aluminum electrode. *Appl. Surf. Sci.* **237,** 451–456 (2004).
8. Woo, T.-G., Park, I.-S. & Seol, K.-W. Effects of various metal seed layers on the surface morphology and structural composition of the electroplated copper layer. *Met. Mater. Int.* **15,** 293–297 (2009).
9. E. Sacher (ed.). *Metallization of Polymers 2*. (Plenum Publishers, 2002).
10. Kanzow, J. *et al.* Formation of a metal/epoxy resin interface. *Appl. Surf. Sci.* **239,** 227–236 (2005).
11. LeGoues, F. K., Silverman, B. D. & Ho, P. S. The microstructure of metal–polyimide interfaces. *J. Vac. Sci. Technol. A* **6,** 2200–2204 (1988).
12. Davis, G. D., Rees, B. J. & Whisnant, P. L. Chemical evaluation of Cu–polyimide interfaces. *J. Vac. Sci. Technol. A* **12,** 2378–2387 (1994).
13. Pertsin, A. J. & Pashunin, Y. M. An XPS study of the in-situ formation of the polyimide/copper interface. *Appl. Surf. Sci.* **47,** 115–125 (1991).
14. Bébin, P. & Prud'homme, R. E. Comparative XPS Study of Copper, Nickel, and Aluminum Coatings on Polymer Surfaces. *Chem. Mater.* **15,** 965–973 (2003).
15. Wolany, D. *et al.* Combined ToF-SIMS/XPS study of plasma modification and metallization of polyimide. *Surf. Interface Anal.* **27,** 609–617 (1999).
16. Haight, R., White, R. C., Silverman, B. D. & Ho, P. S. Complex formation and growth at the Cr– and Cu–polyimide interface. *J. Vac. Sci. Technol. Vac. Surf. Films* **6,** 2188–2199 (1988).
17. Bartha, J. W., Hahn, P. O., LeGoues, F. & Ho, P. S. Photoemission spectroscopy study of aluminum–polyimide interface. *J. Vac. Sci. Technol. Vac. Surf. Films* **3,** 1390–1393 (1985).
18. Travaly, Y., Bertrand, P., Rignanese, G.-M. & Gonze, X. Theoretical Modeling of the Nucleation and Growth of Aluminium Films Thermally Evaporated onto Poly(ethylene terephthalate) Substrate. *J. Adhes.* **66,** 339–355 (1998).
19. Travaly, Y. & Bertrand, P. Static SIMS investigation of metal/polymer interfaces. *Surf. Interface Anal.* **23,** 328–334 (1995).
20. Siau, S., Vervaet, A., Degrendele, L., Baets, J. D. & Calster, A. V. Qualitative electroless Ni/Au plating considerations for the solder mask on top of sequential build-up layers. *Appl. Surf. Sci.* **252,** 2717–2740 (2006).
21. Sykes, J. M. & Hoar, T. P. Role of polymer oxidation in the adhesion of polyethylene to metals. *J. Polym. Sci. [A1]* **7,** 1385–1391 (1969).
22. Mittal, K. L. Adhesion aspects of metallization of organic polymer surfaces. *J. Vac. Sci. Technol.* **13,** 19–25 (1976).
23. Derjaguin, B. V. & Smilga, V. P. Electronic Theory of Adhesion. *J. Appl. Phys.* **38,** 4609–4616 (1967).
24. Skinner, S. M., Savage, R. L. & Jr, J. E. R. Electrical Phenomena in Adhesion. I. Electron Atmospheres in Dielectrics. *J. Appl. Phys.* **24,** 438–450 (1953).
25. Binder, K. *Monte Carlo and Molecular Dynamics Simulations in Polymer Science*. (Oxford University Press, 1995).
26. Plimpton, S. Fast Parallel Algorithms for Short-Range Molecular Dynamics. *J. Comput. Phys.* **117,** 1–19 (1995).
27. Kalé, L. *et al.* NAMD2: Greater Scalability for Parallel Molecular Dynamics. *J. Comput. Phys.* **151,** 283–312 (1999).
28. Rudd, R. E. & Broughton, J. Q. Coarse-grained molecular dynamics and the atomic limit of finite elements. *Phys. Rev. B* **58,** R5893–R5896 (1998).
29. Padding, J. T. & Briels, W. J. Time and length scales of polymer melts studied by coarse-grained molecular dynamics simulations. *J. Chem. Phys.* **117,** 925–943 (2002).
30. Hohenberg, P. & Kohn, W. Inhomogeneous Electron Gas. *Phys. Rev.* **136,** B864–B871 (1964).
31. Kohn, W. & Sham, L. J. Self-Consistent Equations Including Exchange and Correlation Effects. *Phys. Rev.* **140,** A1133–A1138 (1965).
32. Perdew, J. P. & Zunger, A. Self-interaction correction to density-functional approximations for many-electron systems. *Phys. Rev. B* **23,** 5048–5079 (1981).
33. Vosko, S. H., Wilk, L. & Nusair, M. Accurate spin-dependent electron liquid correlation energies for local spin density calculations: a critical analysis. *Can. J. Phys.* **58,** 1200–1211 (1980).

34. Ceperley, D. M. & Alder, B. J. Ground State of the Electron Gas by a Stochastic Method. *Phys. Rev. Lett.* **45,** 566–569 (1980).
35. Kohanoff, J. Electronic Structure Calculations for Solids and Molecules: Theory and Computational methods. *Cambridge University Press* Available at: http://www.cambridge.org/fr/academic/subjects/physics/condensed-matter-physics-nanoscience-and-mesoscopic-physics/electronic-structure-calculations-solids-and-molecules-theory-and-computational-methods. (Accessed: 15th October 2017)
36. Jacobsen, H. & Cavallo, L. Directions for Use of Density Functional Theory: A Short Instruction Manual for Chemists. in *Handbook of Computational Chemistry* (ed. Leszczynski, J.) 95–133 (Springer Netherlands, 2012). doi:10.1007/978-94-007-0711-5_4
37. Lee, C., Yang, W. & Parr, R. G. Development of the Colle-Salvetti correlation-energy formula into a functional of the electron density. *Phys. Rev. B* **37,** 785–789 (1988).
38. Perdew, J. P. *et al.* Atoms, molecules, solids, and surfaces: Applications of the generalized gradient approximation for exchange and correlation. *Phys. Rev. B* **46,** 6671–6687 (1992).
39. Perdew, J. P., Burke, K. & Ernzerhof, M. Generalized Gradient Approximation Made Simple. *Phys. Rev. Lett.* **77,** 3865–3868 (1996).
40. Csonka, G. I., Perdew, J. P. & Ruzsinszky, A. Global Hybrid Functionals: A Look at the Engine under the Hood. *J. Chem. Theory Comput.* **6,** 3688–3703 (2010).
41. Becke, A. D. Density-functional thermochemistry. III. The role of exact exchange. *J. Chem. Phys.* **98,** 5648–5652 (1993).
42. Heyd, J., Scuseria, G. E. & Ernzerhof, M. Hybrid functionals based on a screened Coulomb potential. *J. Chem. Phys.* **118,** 8207–8215 (2003).
43. Kostar, A. M. *et al. A.M. Koster, G. Geudtner, P. Calaminici, M.E. Casida, V.D. Dominguez, R. Flores-Moreno, G.U. Gamboa, A. Goursot, T. Heine, A. Ipatov, F. Janetzko, J.M. del Campo, J. U. Reveles, A. Vela, B. Zuniga-Gutierrez, and D.R. Salahub, deMon2k, Version 3.0.6, The deMon developers, Cinvestav, Mexico City (2011).* (2014).
44. St-Amant, A. deMon, un programme LCGTO-MCP-DF, et une etude théorique de l’adsorption de l’hydrogène sur les monomères et dimères de Ni, Rh, et Pd. (Université de Montréal, 1992).
45. Eichkorn, K., Treutler, O., Öhm, H., Häser, M. & Ahlrichs, R. Auxiliary basis sets to approximate Coulomb potentials. *Chem. Phys. Lett.* **240,** 283–290 (1995).
46. Dunlap, B. I., Connolly, J. W. D. & Sabin, J. R. On first-row diatomic molecules and local density models. *J. Chem. Phys.* **71,** 4993–4999 (1979).
47. Mintmire, J. W. & Dunlap, B. I. Fitting the Coulomb potential variationally in linear-combination-of-atomic-orbitals density-functional calculations. *Phys. Rev. A* **25,** 88–95 (1982).
48. Mintmire, J. W., Sabin, J. R. & Trickey, S. B. Local-density-functional methods in two-dimensionally periodic systems. Hydrogen and beryllium monolayers. *Phys. Rev. B* **26,** 1743–1753 (1982).
49. Köster, A. M. Hermite Gaussian auxiliary functions for the variational fitting of the Coulomb potential in density functional methods. *J. Chem. Phys.* **118,** 9943–9951 (2003).
50. Geudtner, G. *et al.* deMon2k. *Wiley Interdiscip. Rev. Comput. Mol. Sci.* **2,** 548–555 (2012).
51. Calaminici, P. *et al.* Auxiliary Density Functional Theory: From Molecules to Nanostructures. in *Handbook of Computational Chemistry* 575–610
52. Salahub, D. R., Goursot, A., Weber, J., Köster, A. M. & Vela, A. Chapter 38 - Applied density functional theory and the deMon codes 1964–2004. in *Theory and Applications of Computational Chemistry* (eds. Dykstra, C. E., Frenking, G., Kim, K. S. & Scuseria, G. E.) 1079–1097 (Elsevier, 2005). doi:10.1016/B978-044451719-7/50081-0
53. Institute for Theoretical Chemistry | Institut für Theoretische Chemie | University of Stuttgart. Available at: http://www.uni-stuttgart.de/theochem/. (Accessed: 29th September 2017)
54. Schuchardt, K. L. *et al.* Basis Set Exchange: A Community Database for Computational Sciences. *J. Chem. Inf. Model.* **47,** 1045–1052 (2007).
55. Halgren, T. A. & Damm, W. Polarizable force fields. *Curr. Opin. Struct. Biol.* **11,** 236–242 (2001).

56. van Duin, A. C. T., Dasgupta, S., Lorant, F. & Goddard, W. A. ReaxFF: A Reactive Force Field for Hydrocarbons. *J. Phys. Chem. A* **105,** 9396–9409 (2001).
57. Barnoud, J. & Monticelli, L. Coarse-Grained Force Fields for Molecular Simulations. in *Molecular Modeling of Proteins* (ed. Kukol, A.) **1215,** 125–149 (Springer New York, 2015).
58. Wang, J., Wolf, R. M., Caldwell, J. W., Kollman, P. A. & Case, D. A. Development and testing of a general amber force field. *J. Comput. Chem.* **25,** 1157–1174 (2004).
59. *D.A. Case, D.S. Cerutti, T.E. Cheatham, III, T.A. Darden, R.E. Duke, T.J. Giese, H. Gohlke, A.W. Goetz, D. Greene, N. Homeyer, S. Izadi, A. Kovalenko, T.S. Lee, S. LeGrand, P. Li, C. Lin, J. Liu, T. Luchko, R. Luo, D. Mermelstein, K.M. Merz, G. Monard, H. Nguyen, I. Omelyan, A. Onufriev, F. Pan, R. Qi, D.R. Roe, A. Roitberg, C. Sagui, C.L. Simmerling, W.M. Botello-Smith, J. Swails, R.C. Walker, J. Wang, R.M. Wolf, X. Wu, L. Xiao, D.M. York and P.A. Kollman (2017), AMBER 2017, University of California, San Francisco.*
60. Del Buono, G. S., Figueirido, F. E. & Levy, R. M. Dielectric response of solvent surrounding an ion pair: Ewald potential versus spherical truncation. *Chem. Phys. Lett.* **263,** 521–529 (1996).
61. Hockney, R. & Eastwood, J. Particle-Particle-Particle-Mesh (P3M) Algorithms. in *Computer simulation using particles* 267–304
62. Lennard Jones Potential Equation - Jennarocca. Available at: http://jennarocca.com/lennard-jones-potential-equation/. (Accessed: 4th September 2017)
63. Metropolis, N. & Ulam, S. The Monte Carlo Method. *J. Am. Stat. Assoc.* **44,** 335–341 (1949).
64. Chiu, S. W., Jakobsson, E., Subramaniam, S. & Scott, H. L. Combined Monte Carlo and Molecular Dynamics Simulation of Fully Hydrated Dioleyl and Palmitoyl-oleyl Phosphatidylcholine Lipid Bilayers. *Biophys. J.* **77,** 2462–2469 (1999).
65. Nosé, S. A unified formulation of the constant temperature molecular dynamics methods. *J. Chem. Phys.* **81,** 511–519 (1984).
66. Verlet, L. Computer 'Experiments' on Classical Fluids. I. Thermodynamical Properties of Lennard-Jones Molecules. *Phys. Rev.* **159,** 98–103 (1967).
67. Andersen, H. C. Molecular dynamics simulations at constant pressure and/or temperature. *J. Chem. Phys.* **72,** 2384–2393 (1980).
68. Ryckaert, J.-P., Ciccotti, G. & Berendsen, H. J. C. Numerical integration of the cartesian equations of motion of a system with constraints: molecular dynamics of n-alkanes. *J. Comput. Phys.* **23,** 327–341 (1977).
69. Hoover, W. G. & Holian, B. L. Kinetic moments method for the canonical ensemble distribution. *Phys. Lett. A* **211,** 253–257 (1996).
70. Alder, B. J., Hoover, W. G. & Young, D. A. Studies in Molecular Dynamics. V. High-Density Equation of State and Entropy for Hard Disks and Spheres. *J. Chem. Phys.* **49,** 3688–3696 (1968).
71. Plimpton, S., Pollock, R. & Stevens, M. Particle-Mesh Ewald and rRESPA for Parallel Molecular Dynamics Simulations. in *In Proceedings of the Eighth SIAM Conference on Parallel Processing for Scientific Computing* (1997).
72. Goldstein, A. On Steepest Descent. *J. Soc. Ind. Appl. Math. Ser. Control* **3,** 147–151 (1965).
73. Ajiz, M. A. & Jennings, A. A robust incomplete Choleski-conjugate gradient algorithm. *Int. J. Numer. Methods Eng.* **20,** 949–966 (1984).
74. Chapelle, O. & Erhan, D. Improved preconditioner for hessian free optimization. in *In NIPS Workshop on Deep Learning and Unsupervised Feature Learning* (2011).
75. CALMIP. Available at: https://www.calmip.univ-toulouse.fr/. (Accessed: 29th September 2017)

Chapter 2: Experimental formation of model poly-epoxy surfaces and characterizations

2.1 Introduction

Poly-epoxy polymers are of tremendous interest in various industrial sectors and are involved in various ongoing researches for their surface or bulk functionalization. Examples of applications are found in the leisure industry, or the aerospace and military industry[1–4]. Poly-epoxies are traditionally used as adhesives, sealants, or paints, and as the matrix in composites because of their superior thermal and mechanical properties when compared to other polymers. In fact, poly-epoxies cover 80% of the general demand of polymers for high performance composites[5]. Main reinforcements are carbon fibers. But for the latter application, it may be necessary to proceed to a metallization as in the present project.

Epoxy resins used as commercial products contain aliphatic, cycloaliphatic or aromatic backbones. Their molecular weights can be adjusted from a few hundreds to tens of thousands. The most widely used epoxy resins are the glycidyl ether derivatives of bisphenol A (more than 75% of total resin sales), such as the diglycidylether of bisphenol A (DGEBA) of the present study. The epoxy rings of DGEBA can react with a wide variety of curing agents. Here, we use ethylene diamine (EDA) which is the smallest liquid amine.

As we described in the previous chapter, poly-epoxy surfaces we form are intended to be metallized at ambient temperature under ultrahigh vacuum (UHV) conditions. Metallized polymers have a great variety of applications (e.g. in the microelectronics sector)and thus the analysis of the chemical bonds formed and reaction at these interfaces have a great interest[6–8]. In our works, we are interested in analyzing the poly-epoxy/metal interface[9–11]. In the literature, Wagner *et al.*[12] investigated the reactivity of Fe, Ni, Cu, and Au evaporated in UHV on 3 different N-containing polymers (Nylon 6 which contains C=O and C-N functionalities, N-PE with different C-N, and CN-SAM which only exhibits C≡N nitriles). Overall it is shown that the reactivity order Fe>Ni>Cu>Au follows the affinity of the metals for O and N.

A very important tool to aid us in our objective is the polymer/metal X-Ray Photoelectron Spectroscopy used for surface chemical analysis. Our aim is to get an insight in the mechanisms of formation of polymer/metal interfaces, which depend on three main features[13,14]: (i) the availability of reactive functional groups at the polymer surface, (ii) the nano- and microstructure of the surface, and (iii) the valence of the metal adsorbate(s). Metals that easily form oxides, such as Al, Cr, Fe, or Ni, will form stable metal (M-)O-C covalent bonds[12,15–17]. On a poly-epoxy that is similar to the one of the present work, observations of condensation coefficients, bonding, and diffusion of Al, Cu, Ag, and Au show the same trend for reactivities: Al >Cu>Au>Ag[18]. Al oxidizes and forms a dense layer, whereas Cu, Au, and Ag form clusters. Diffusion towards the bulk is negligible, even above glass transition temperature, in contrast with metal/thermoplastics interfaces. Finally, when the adsorption is accompanied by a degradation of the polymer chain by scissions, the most reactive metals (e.g. Cr or Ni) form carbides or phosphides[15].

Chapter 2 is organized as follows: Section 2 is dedicated to the presentation of the synthesis and characterization of the poly-epoxy polymer bulk as well as the pristine surface. The synthesis protocol is presented, followed by the FTIR and DSC measurements. The surface is also characterized by AFM and XPS measurements. Following, in section 3, we describe the protocol of the deposition of a Cu film on the poly-epoxy surface. AFM measurements are executed for the calibration of the time of deposition through metallization of Si wafers in different times and for the determination of the thickness of the Cu film deposited on the poly-epoxy surface. Lastly XPS measurements give us a first indication for the mechanism of reaction of the Cu atoms with the surface functions.

2.2 Pristine (non-metallized) poly-epoxy surface

2.2.1 Synthesis protocol of a pristine low-roughness poly-epoxy surface

The first step is to be able to accurately and reproducibly create a surface with very low roughness (R_a<1 nm) so that we are able to observe nano-clusters and nano-islands formation without any prevention or confusion with roughness existing on the surface. Another reason for a surface with a low defect density is to ensure that heterogeneous nucleation will not take place in these defects. Finally, our samples must be chemically homogeneous since chemical homogeneity is assumed in calculations. At the end of a period of tedious research (described in section 2.2) we have finally developed a safe protocol that ensures all samples of a batch to be close to full polymerization (~ 93%).

The protocol involves the following steps:

- ✓ The Si wafer substrates along with any disposable and non-disposable tools that will be used are thoroughly cleaned and dried with ethanol and/or acetone depending on the material.
- ✓ After everything is dried it is carefully placed in the load-lock chamber of an Ar glovebox for overnight pumping.
- ✓ In the Ar glovebox, we mix 0.86 g of EDA and 10 g of DGEBA (stoichiometric 2DGEBA:1EDA mixture).
- ✓ The liquid mixture is stirred manually using a plastic or wooden stirrer for 7 minutes for a homogeneous stirring.
- ✓ Then, small droplets are deposited on the clean Si wafers. They are left for 48h in the Ar glovebox in order to reach approx. 80% conversion rate.
- ✓ After the 48h period, an electric heater is used for post-curing (2h, 140°C).

In section 2.2.2.1 we describe bulk properties and how we determine the polymerization rate based on Fourier-transform infrared spectroscopy (FTIR), and how we determine the glass transition temperature (T_g) by differential scanning calorimetry (DSC). We also ensure that the surface has the required low roughness using atomic force microscopy (AFM) and obtain surface chemical composition by analyzing X-Ray photoelectron spectra (XPS).

2.2.2. Characterizations

2.2.2.1 Bulk Characterizations

Introduction to Fourier Transform Infrared (FTIR) spectroscopy

Fourier Transform Infrared (FTIR) spectroscopy is a very useful analytical tool. It is a technique in which we obtain an infrared spectrum of absorption or emission of a material in any phase (gas, liquid or solid). For our project we need to analyze solid (our final polymers) and liquid (initial mixture of DGEBA and EDA). We will speak briefly about the methodology and functionality of FTIR spectroscopy before showing our results.

Generally speaking, an absorption spectroscopy technique (such as FTIR, UV-Vis (ultraviolet-visible), photoemission spectroscopy etc.) outputs a spectra that shows the ability of the material to absorb light at a great number of wavelengths. The simplest way to do this is to use a monochromatic light source at a given sample and then repeat for various wavelengths.

Fourier-transform spectroscopy accelerates this procedure by the use of a polychromatic source and records the percentage of the beam that is either absorbed or transmitted, depending on the modes the user selects or the material nature (e.g. how transparent the material is). The beams emitted are of certain bandwidths and thus one can scan a large range of frequencies. We use transmission IR spectroscopy in the Near Infrared (NIR) spectrum. The apparatus is the Perkin Elmer Frontier and Spotlight NIR/MIR spectrometer.

In order to calculate the conversion rate ($X_{e,NIR}$), we use Equation 1:

$$X_{e,NIR} = 1 - \frac{\left(\frac{A_{epoxy}}{A_{reference}}\right)_t}{\left(\frac{A_{epoxy}}{A_{reference}}\right)_{t=0}} \quad (1)$$

As indicated in the equation we extract spectra in the near infrared (NIR) area of the spectrum. The terms A_{epoxy} and $A_{reference}$ refer to the area of the peak of the epoxy bond located in the 4530 cm^{-1} band, and the area of the reference band (combination of the aromatic C=C (1625 cm^{-1}) and aromatic C-H (3000 cm^{-1}) bond) located at 4623 cm^{-1}.[19,20] We obtain background spectra by using two empty microscope glass slides.

Results of FTIR characterizations

In our project, FTIR spectroscopy is useful to ensure that the reaction of polymerization takes place, and enables the determination of the conversion rate (%). It is important that all samples are close to 100% polymerization. The reason is not only the relevance with DFT and Molecular Dynamics calculations but also the compatibility of the samples with UHV. They will be introduced in the XPS apparatus (10^{-9} mbar) and in the evaporation chamber (10^{-10} mbar) for metallization. If samples are not completely solid then the UHV chambers will be contaminated.

In order to have a rigorous polymerization protocol, results from previous works are used[21] to help us determine the time needed for the samples to stay in the Ar gloves box until the maximum conversion rate has been reached in ambient temperature. The findings of this work described in Figures 1 and 2 indicate that the minimum time the samples need to stay in ambient temperature under Ar atmosphere is 48h. After the 48h period there is no significant change in the conversion rate and a post-curing at higher temperatures is needed. Figure 1 shows the superposition of 6 FTIR spectra acquired from t=0 to t > 8 days.

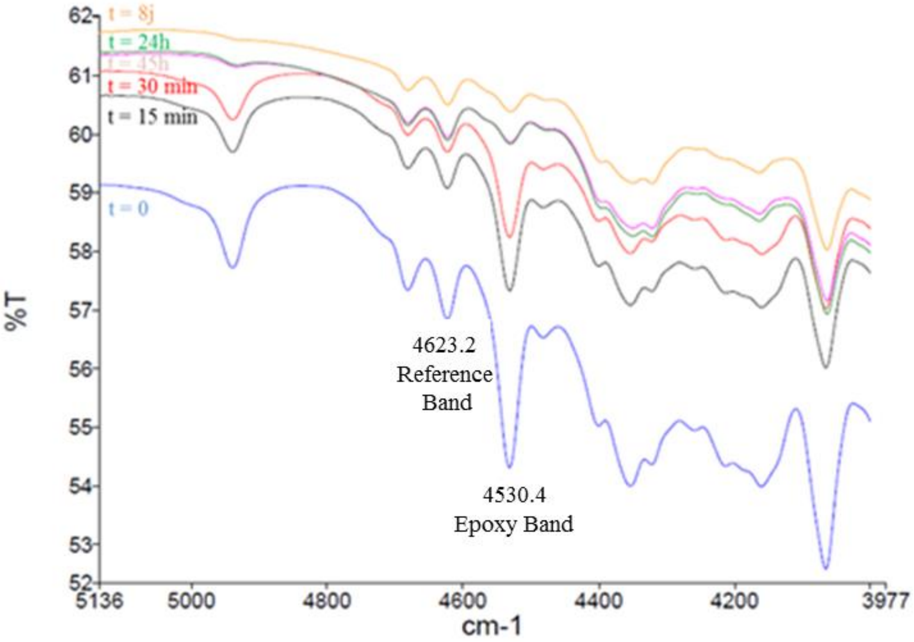

Figure 1. Polymerization monitoring by the use of FTIR adapter from Ref.[22]

The time of the initial mixing of the DGEBA and EDA reactants is denoted as t=0. For each time period, that the spectra are extrapolated in this study, it can be seen that while the reference band remains constant, the epoxy band is continually lessened. Between the 24h spectrum and the 8 days spectrum the epoxy band does not have a significant difference in peak size. The conversion rate has reached a plateau between this timespan. The spectra acquired demonstrate the minimum amount possible of noise and the bands of interest can be clearly identified. For each spectrum obtained, the areas of the bands are used as constants for the subsequent calculations of $X_{e,NIR}$ through Equation 1. The results of the study concerning this parameter are given in Figure 2.

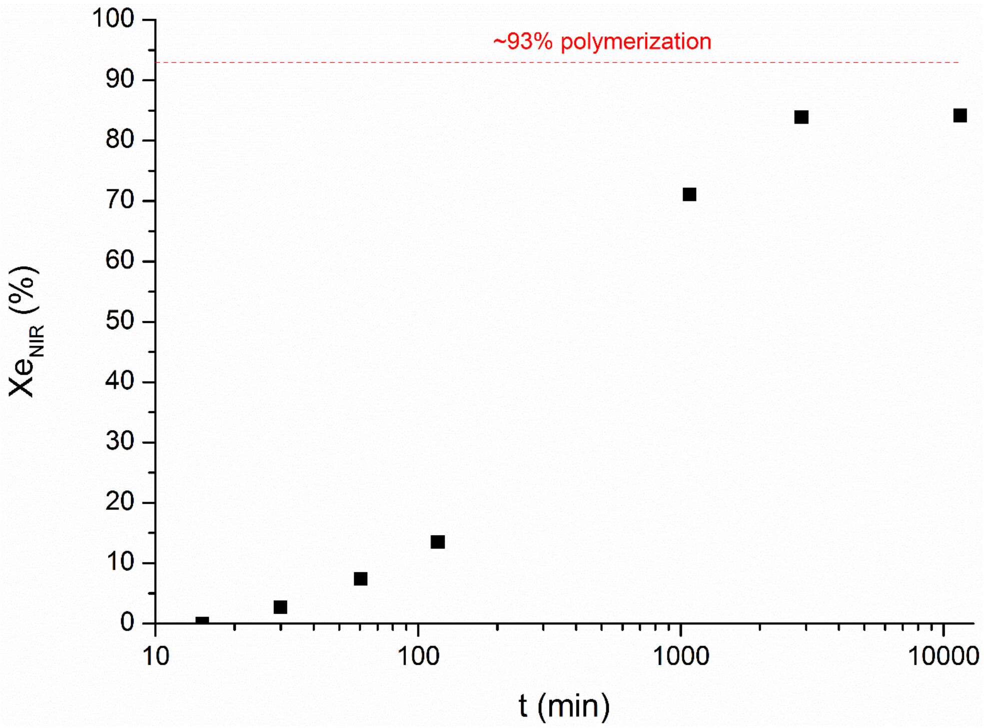

Figure 2. Epoxy group conversion rate as a function of polymerization over an 8-day period of time. The dashed line indicates that the polymerization is complete after post-curing at 140 °C for 2h. Adapted from Ref.[21].

Figure 2 shows the increase of $X_{e,NIR}$ with time. The Xe_{NIR} is increased continuously until the 48h mark, where the conversion rate reaches a plateau. The conversion rate in this plateau is 84%. The study indicates that for an above 90% polymerization a post-curing treatment at 140 °C for 2h is needed. By using the same protocol we were able to arrive at high conversion rates (~ 93%) for all of our samples. This protocol when applied in all sample batches gives reproducible results.

The next step is to analyze each batch of polymers by FTIR before any further characterization takes place due to the sensitivity of the other methods to the introduction of a liquid (even partially) sample. Figure 3 shows one of many (typical for a fully polymerized sample) FTIR spectra.

The time t=0 refers to the spectrum that is obtained as soon as our two monomers are mixed. To do this we trap the two liquids between two microscope glass slides and acquire the spectrum. The spectrum obtained for t=0 and t = 48h after post-curing is presented in Figure 3.

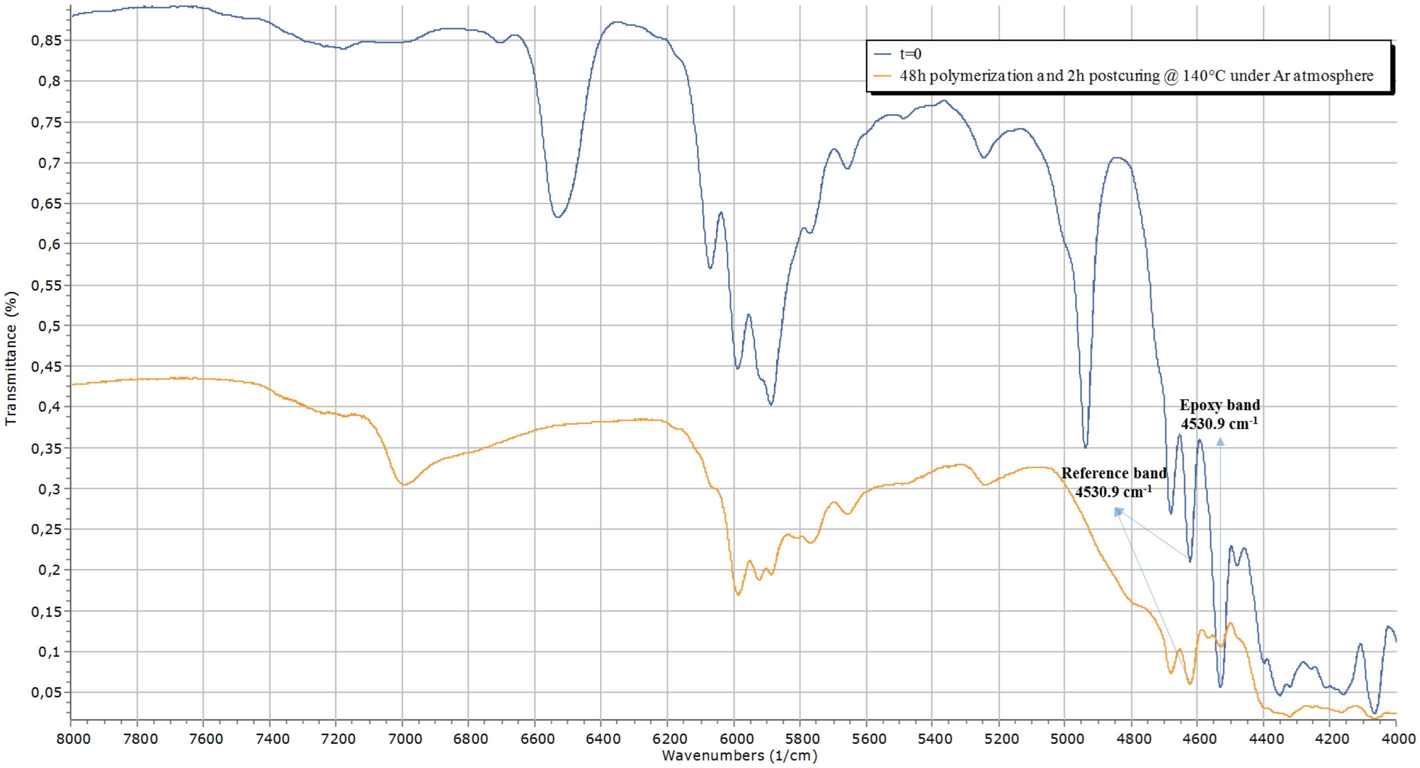

Figure 3. FTIR Transmission Spectra in the NIR region for t = 0 (blue) and t = 48h + 2h post-curing (orange) polymerization.

The epoxy band is clearly lessened for the post-cured final polymer indicating that our sample is highly cross-linked. We need to be certain that our protocol is reproducible and gives high conversion rates for us to be able to study and metallize the poly-epoxy surface.

Before the protocol reached its final form we performed a variety of tests with atmospheric conditions and post-curing procedures. These efforts are summarized in Table 1, along with data extracted from FTIR analyses, and the final conversion rates.

The reason why the initial polymerization is performed inside the Ar Glove Box, is because EDA is highly volatile and oxidizes heavily if left in a non-inert atmosphere. It results in the consumption of EDA, and in the creation of a high density of defects. The deviation from a stoichiometric composition leads to a poor polymerization rate, while defects result in the formation of a rough surface.

It is to be noted that for all of these substrates, polymerization parameters are also tweaked (such as time of stirring, quantities of monomers from 5g of DGEBA and 0.43g of EDA to 10g of DGEBA and 0.86g of EDA to increase the volume of stirring) as well as various post-curing times and temperatures.

Table 1. Polymerization results obtained by FTIR spectroscopy using different experimental conditions for the polymerization environment. $X_{e,NIR}$ is the conversion rate and the quantities A_{epoxy} and $A_{reference}$ refer to the areas of the epoxy and reference peaks.

Sample	A_{epoxy}	$A_{reference}$	Ratio	X_{eNIR}
Post-curing in ambient conditions	-17.04	-17.14	0.99416569	0.70
Post-curing in ambient conditions	-28.5	-22.16	1.28610108	0.61
Post-curing in ambient conditions	-22.81	-22.77	1.0017567	0.70
Post-curing in ambient conditions	-24.67	-25.24	0.9774168	0.71
Post-curing in ambient conditions	-9.03	-11.38	0.79349736	0.76
Post-curing under vacuum (brief air transfer)	-10.88	-17.2	0.63255814	0.81
Post-curing under vacuum (brief air transfer)	-1.16	-2.89	0.40138408	0.88
Post-curing under vacuum (brief air transfer)	-7.76	-11.68	0.66438356	0.80
Post-curing under vacuum (brief air transfer)	-16.47	-27.71	0.59437026	0.82
Post-curing under vacuum (brief air transfer)	-2.2	-4.09	0.53789731	0.84
Post-curing under vacuum (brief air transfer)	-8.35	-14.41	0.57945871	0.83
Post-curing under vacuum (brief air transfer)	-10.2	-25.83	0.39488966	0.88
Post-curing under Ar atmosphere	-5.99	-26.07	0.22976601	0.93
Post-curing under Ar atmosphere	-7.07	-21.43	0.32991134	0.90
Post-curing under Ar atmosphere	-0.75	-3.66	0.20491803	0.94
Post-curing under Ar atmosphere	-7.17	-23.28	0.30798969	0.91
Post-curing under Ar atmosphere	-24.33	-84.35	0.28844102	0.91
Post-curing under Ar atmosphere	-8.62	-37.63	0.22907255	0.93
Post-curing under Ar atmosphere	-24.76	-100.48	0.2464172	0.93
Post-curing under Ar atmosphere	-47.82	-163.74	0.29204837	0.91
Post-curing under Ar atmosphere	-53.06	-181.93	0.29165063	0.91

In an Ar environment, the conversion rate equals 92±2% and it is reproducible over various batches. In contrast with the other methods tested, under non-inert conditions this rate is at the range of low values between 61-76%. The post-curing under vacuum seems to yield better results than air post-curing but is lower that the Ar atmosphere, giving a conversion rate of 84±4%.

We thus have a robust protocol if all steps are performed in the Ar Glove Box. It ensures a conversion rate above 90%. Then, we must verify the glass transition temperature and check if it is in good accordance with bibliography. For this purpose, we use differential scanning calorimetry (DSC).

Introduction to Differential Scanning Calorimetry (DSC)

DSC is a thermal analysis technique which measures the heating power absorbed or produced by a sample when it is submitted to a heating or cooling profile. With a known mass of material, DSC can determine heat capacity (c_p) changes with temperature.

The glass transition temperature (T_g) is a characteristic temperature of poly-epoxies. T_g, is the temperature for which the polymer changes from its glassy (low T) state to a rubbery (higher T) state, accompanied by a significant change of its heat capacity (c_p). Below T_g, the cross-linked chains are very rigid and no mobility is permitted because of Van der Waals (VdW) intermolecular interactions. At $T>T_g$ the chains have enough energy to break VdW bonds and to enter the rubbery state.

After weighting the required quantity of polymer, we seal it in an Al capsule using a pastille maker. We also prepare a reference capsule that remains empty. The DSC apparatus measures the heat flow of the two capsules and calculates the extra heat necessary to heat the polymer-filled capsule at every temperature step so that the two capsules heat flows remain constant. Through this method, we can calculate c_p using Equations 2-4. In these equations Φ is the heat flow, q represents heat, t is the time and ΔT is the variation of the temperature for time t. We use a Netzsch DSC 204 apparatus to perform DSC experiments.

$$\Phi = \frac{q}{t} \, (2)$$

$$\frac{temperature\ variation}{time} = \frac{\Delta T}{t} \ (3)$$

$$\frac{\frac{q}{t}}{\frac{\Delta T}{t}} = \frac{q}{\Delta T} = C_p \ (4)$$

Glass transition temperature of the poly-epoxy

Figure 4 shows the DSC plot obtained with the following procedure. 11.8 mg of poly-epoxy are placed in the capsule. Then, the chamber is heated from -10 to 250 °C, at a heating rate of 10 °C/min. Reactions take place in an inert atmosphere composed of nitrogen which has a high heat conductivity ($0.026\ \mathrm{W/m \cdot K}$) allowing the even distribution of heat in the sample chamber. Argon is also a very good candidate although more expensive and is preferred for high temperatures which is not needed for our polymer.

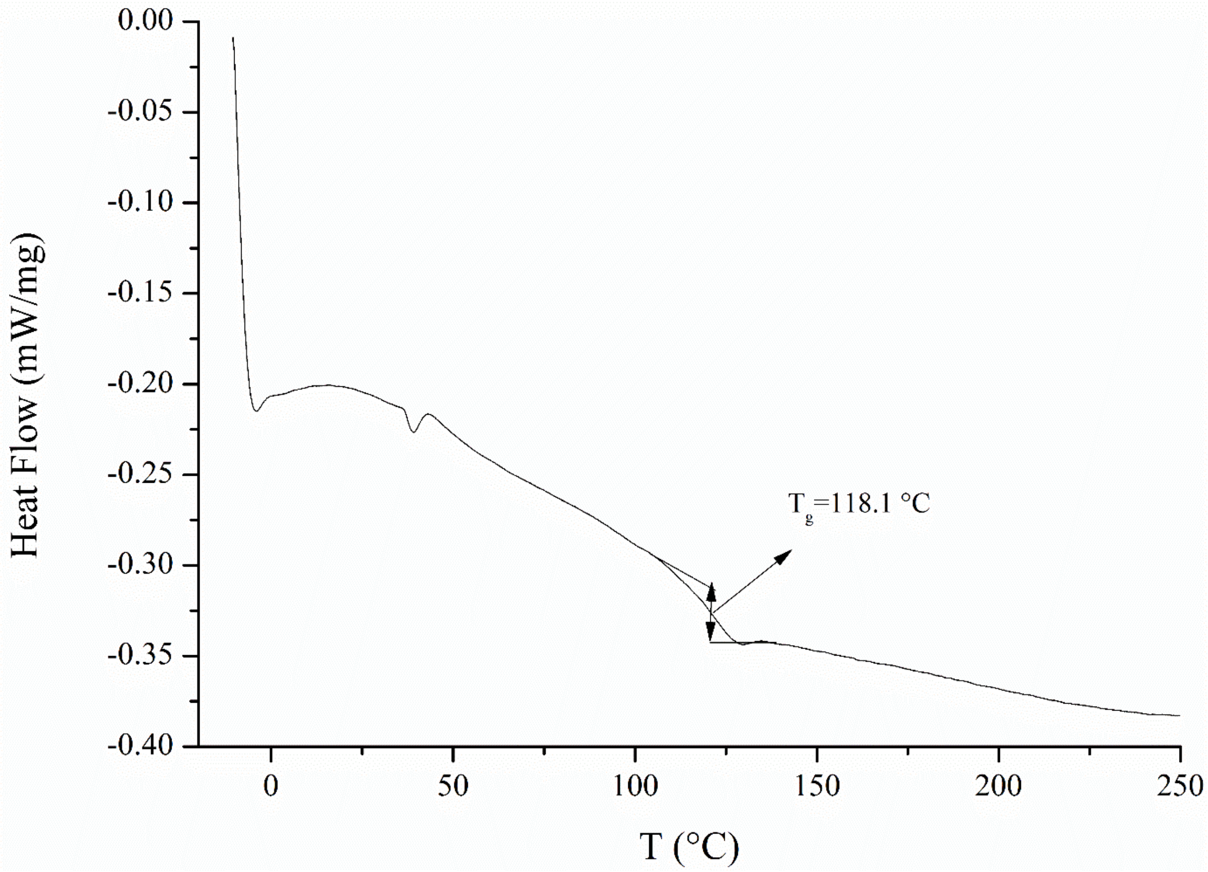

Figure 4. DSC plot of a 93% polymerized poly-epoxy polymer.

In Figure 4, we observe an exothermic process, i.e. a decrease of the power injected in the reactor chamber to maintain the temperature. The onset, midpoint and endpoint of the transition are determined by post-processing; through the drawing of the tangents of the glassy and rubbery regions. . We choose the mid-point temperature 118±1 °C (391±1 K) as a T_g, because it is usually preferred in the bibliography[23]. The T_g presented in Figure 4 is obtained on 2 samples, with a margin of error of ±1 °C (the margin of error for the Indium Response Ratio, used for calibration is ±0.5 °C and we have added a user error of fitting at ±0.5 °C). The results are in accordance with bibliography.[23,24]

After verifying the T_g of our polymers, and being sure that we have well polymerized samples, we move on to the surface analysis of pristine surfaces using AFM and XPS.

2.2.2.2 Surface Characterizations

Introduction to Atomic Force Microscopy (AFM)

AFM is based on the interactions between a sharp tip and a surface. The probed interactions are, from far to close tip, the electrostatic forces, the surface tension, and the coulombic repulsion.

AFM has the advantage over scanning tunneling microscopy that it can give results for both conducting and insulating surfaces, and measurements can be performed in ambient air, liquid or vacuum. An example of application is the measurement of force-distance curves.

There has been a great variety of scientific works in the last years whose aim was to determine the viscoelastic behavior and the glass transition temperature T_g by the use of force-distance curves. One example is the work of Marti *et al.*[25] who used polystyrene samples of different weights at different temperatures. They were able to measure the tip-sample adhesion and found a large increase of adhesion above a specific temperature which they assume to be $T_{g.}$ Tsui et al[26] examined force-distance curves at various temperatures on poly(t-butyl acrylate) and showed the good agreement between the shift factors (correcting the force-distance curves taking into account temperature) obtained using AFM and rheological measurements (fracture mechanics at unloading) made on the bulk polymer. The technical principles of AFM are described in Figure 5. The main component is the cantilever. At its end, it has a sharp micro fabricated tip, with a radius of only a few nanometers. The cantilever is usually made out of silicon or silicon nitride. The cantilever's back side (the side not in contact with samples) is covered with a thin metallic layer (e.g. Au) in order to enhance its reflectivity. There, a laser beam is reflected toward a 2-dimensional photodetector. When the cantilever moves because of tip-surface interactions, then the reflection of the laser beam moves within the photodetector area. Lateral movements correspond to tip flexion (i.e. friction) whereas vertical movements correspond to z-motion (topography and/or repulsive/attractive interactions).

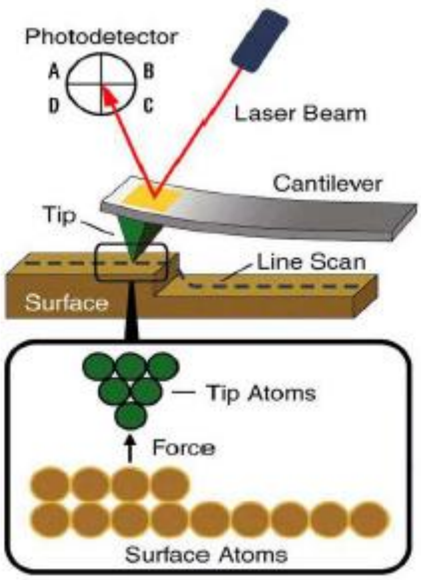

Figure 5. Principle of Atomic Force Microscopy. Image adapted from the manual for the PicoPlus AFM/STM model 5500 by Agilent Industries located in CIRIMAT.

The other end of the cantilever is fixed to a piezo-electric motion controller. For the user to be able to obtain topographic 2-D images the cantilever scans the surface for several μm with a high z-resolution (1 Å per line). A feedback mechanism then keeps the tip-sample distance stable by adjusting the deflection or the oscillation amplitude (depending on the mode we choose) and thus prevents the degradation of the tip and the sample. A controller is also used to collect and process all data and to drive the piezoscanner. The atomic force microscope we use is the Agilent Technologies Model 5500, shown in the photo in Figure 6.

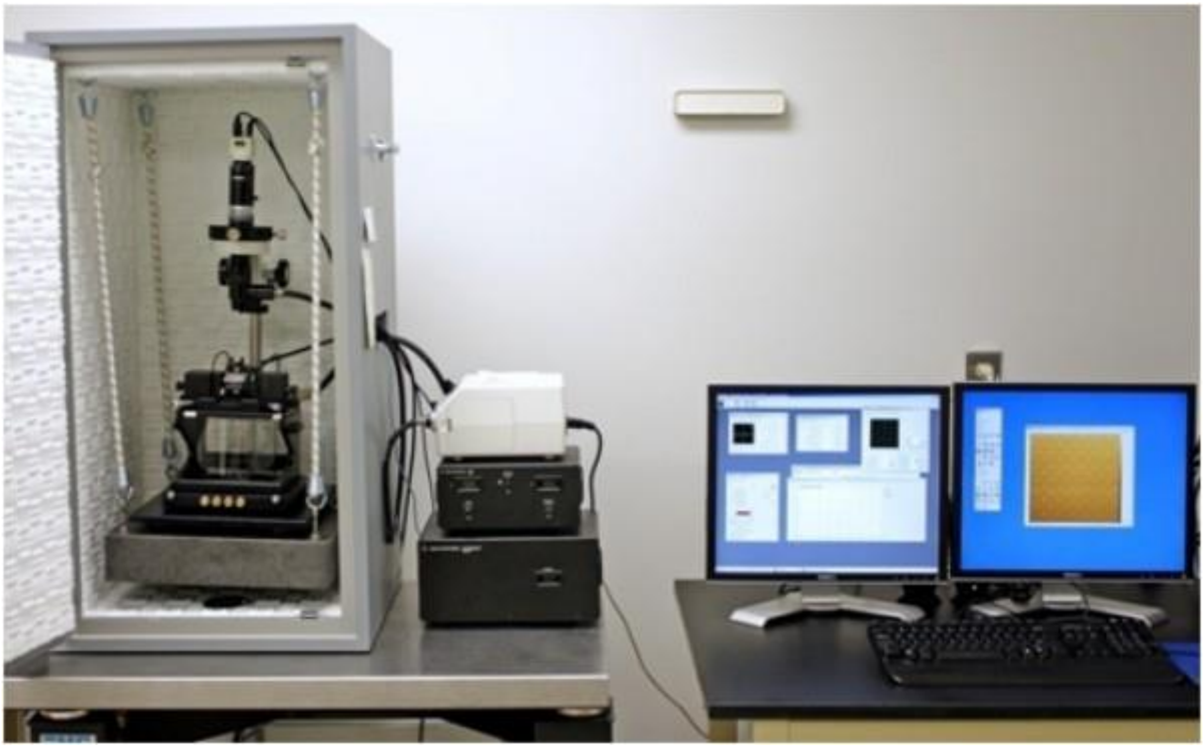

Figure 6. The Agilent Technologies Model 5500 AFM apparatus located at ENSIACET (INPT, Toulouse).

Modes of operation

AFM can be operated in various modes to measure the interaction forces as a function of the tip position over the entire scanned area. Each mode differs in relation to the force between the tip and the sample. These modes are shown in Figure 7. We describe only 3 modes, though AFM is very versatile and there actually exist many more modes that will not be discussed here.

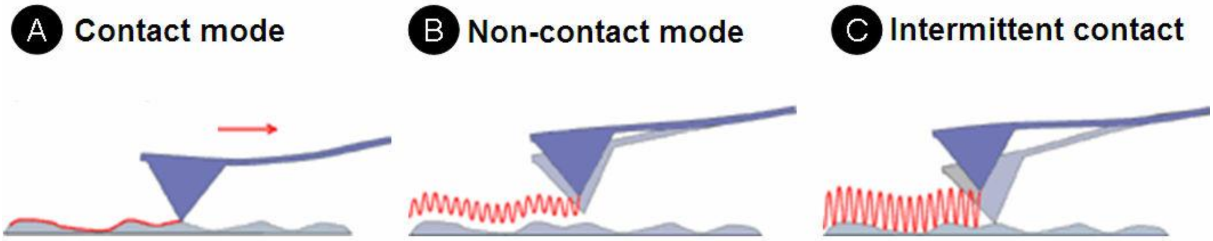

Figure 7. Contact (panel A), non-contact (panel B) and intermittent contact (panel C) modes of operation. Figure adapted from Ref.[27]

Contact Mode

This is the basic mode of operation of AFM. As the tip is scanned across the surface, it is deflected as it moves on the surface as shown in Figure 7a. In constant force mode, the tip is constantly adjusted using the feedback mechanism to maintain a constant deflection, and therefore constant height above the surface. The changes in the feedback signal required to maintain the force constant are used to reconstruct the topography. As the tip is in hard contact with the surface, the stiffness of the cantilever needs to be less than that of the effective spring constant holding atoms together, which is on the order 1-10 nN/nm. Most contact mode levers have a spring constant of <1 N/m so that soft materials are not damaged.

In addition, a large class of materials (such as semiconductors and insulators), can trap electrostatic charge. This charge can lead to additional attractive forces between the probe and sample. All of these forces combine to define a minimum normal force that can be controllably applied by the probe to the sample. This normal force creates a substantial frictional force as the probe scans over the sample. It appears that these frictional forces are far more destructive than the normal force and can damage the sample, the tip, and corrupt the resulting data. An attempt to avoid this problem is the Non-contact Mode.

Non-contact mode

This mode relies on the use of an oscillating cantilever. A stiff cantilever oscillates in the attractive regime, meaning that the tip is quite close to the sample, but not touching it as shown in Figure 7b. The forces between the tip and the sample are quite low, in the order of pN. The oscillation amplitude, phase and resonance frequency are modified by tip-sample interaction forces. These changes in oscillation with respect to the forced reference oscillation provide information about several properties of the samples. The detection is based on measuring changes to the resonance frequency or amplitude of the cantilever.

Intermittent Contact Mode

In intermittent contact mode (a.k.a “Tapping Mode^{TM}”) of operation, a stiff cantilever oscillates closer to the sample than in non-contact mode. Part of the oscillation extends into the repulsive regime, so the tip intermittently touches or “taps” the surface. Very stiff cantilevers are typically used, as tips can get “stuck” in the water layer absorbed on the sample surface, if any exists. The major advantage of tapping the surface is the improved lateral resolution on soft samples. Typical Tapping Mode^{TM} operation is carried out using amplitude modulation detection with a lock-in amplifier. For the purposes of our project we use the Contact and Tapping^{TM} modes for the analysis of the polymer surfaces. Following in the next section are AFM results for the pristine poly-epoxy surface.

AFM results

After testing both Contact and Tapping^{TM} modes for analyzing our samples we verified that we obtained better results using the Tapping^{TM} mode. Actually, in contact mode there is presence of shear forces that deform and modify the polymer surface and the tip suffers from wear or any adherence the surface may present. It is thus essential to use Tapping^{TM} mode for better image quality. The surface analysis of two of our polymer samples is shown in Figure 8.

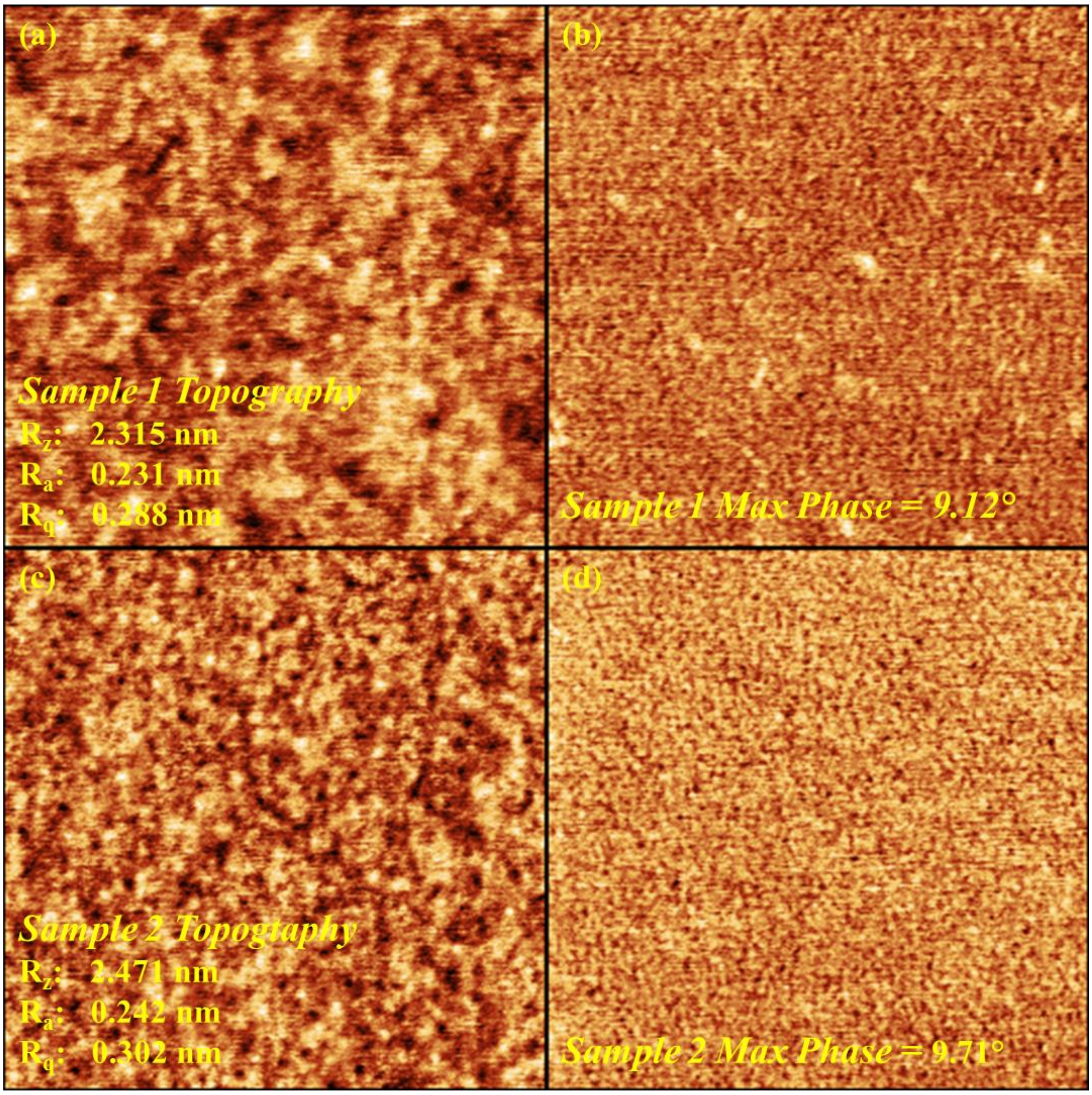

Figure 8. 1µm x 1µm AFM images of two pristine poly-epoxy surfaces.

The topography and phase contrast images were extracted using the Gwyddion®[28] software and after a polynomial of degree 1 and 2 background removal (tilt and curvature corrections). We take into account three statistical quantities for the roughness of the poly-epoxy surface specified by the ISO 25178 protocol[29]. The R_z parameter corresponds to the height between the minimum and maximum points. The R_a parameter is the mean arithmetical roughness which is the parameter we are more interested in having a <1nm value as mentioned in Section 2.1. The R_q parameter is the root mean squared (RMS) deviation of the surface profile. The R_a value of these 1µm x 1µm surface areas are 0.231 and 0.242 nm respectively. This roughness fulfills the criterion we set for the non-metallized surface required to observe the first steps of growth of Cu clusters. Figures 8b and 8d show the phase contrast imaging. Since the phase contrast remains below 10°, we assess that the viscoelastic properties are constant over the micrometric surface area. Therefore we assume that the surface is chemically homogeneous. We can also observe that although the surface roughness is low there are some blobs and troughs of up to 2.5 nm-high/deep.

<u>Introduction to X-Ray Photoelectron Spectroscopy</u>

X-Ray Photoelectron Spectroscopy (XPS) is a surface analysis technique which allows the determination of the elemental composition of a surface (from a few Å up to 10 nm-deep), the contamination level, the local bonding of atoms, or the oxidation states. XPS is achieved by irradiating a sample with soft X-Rays and by analyzing the energy of the electrons emitted by the surface layer. When the photon source emits photons at a high-enough frequency, then electrons of the core-level of atoms are ejected (and called photoelectrons). The kinetic energy that remains on these photoelectrons carries intrinsic information, such as the binding energy of the electron in its atomic core-level. Electrons binding energies are element and bond specific, and thus identifications can be performed. The equation in PES is given by Equation 5.

$$BE = hv - KE - \varphi_{sample} \ (5)$$

where hν is the energy of the incident photon, KE is the kinetic energy of the emitted electron, BE is the binding energy of the photo emitted electron, and φ is the work function of the sample. Actually, since the sample and spectrometer are electrically connected, their Fermi levels are equal.

Therefore, the photoelectrons are submitted to an electric field caused by the difference ($\varphi_{sample} - \varphi_{spec}$) of both work functions. The complete equation now writes:

$$BE = h\nu - KE - \varphi_{sample} + (\varphi_{sample} - \varphi_{spec}) = h\nu - KE - \varphi_{spec} \quad (6)$$

φ_{spec} is a constant that is determined by calibration of a given apparatus.

Theoretically, the XPS process is described in a two-step model, with two distinct states called the initial (before ionization) and the final (the pot-electron is in vacuum) states. They are depicted in Figure 9. The initial state is the real state of the matter that we should like to characterize, whereas the final state is an artefact that is intrinsically related to the measurement principle. Unfortunately, the photoelectrons carry both initial and final state contributions. Final states can have comprehensive effects on the XPS spectra. For instance, the new core-level hole will be screened by surrounding electrons and thus modify the electric field crossed by the photoelectron. Its kinetic energy will be affected, and so its apparent binding energy. Consecutively, simulations of XPS spectra performed with initial state calculations are likely to lead to fundamental discrepancies. We will show two different calculation methods in Chapter 3 where final state effects are taken into account.

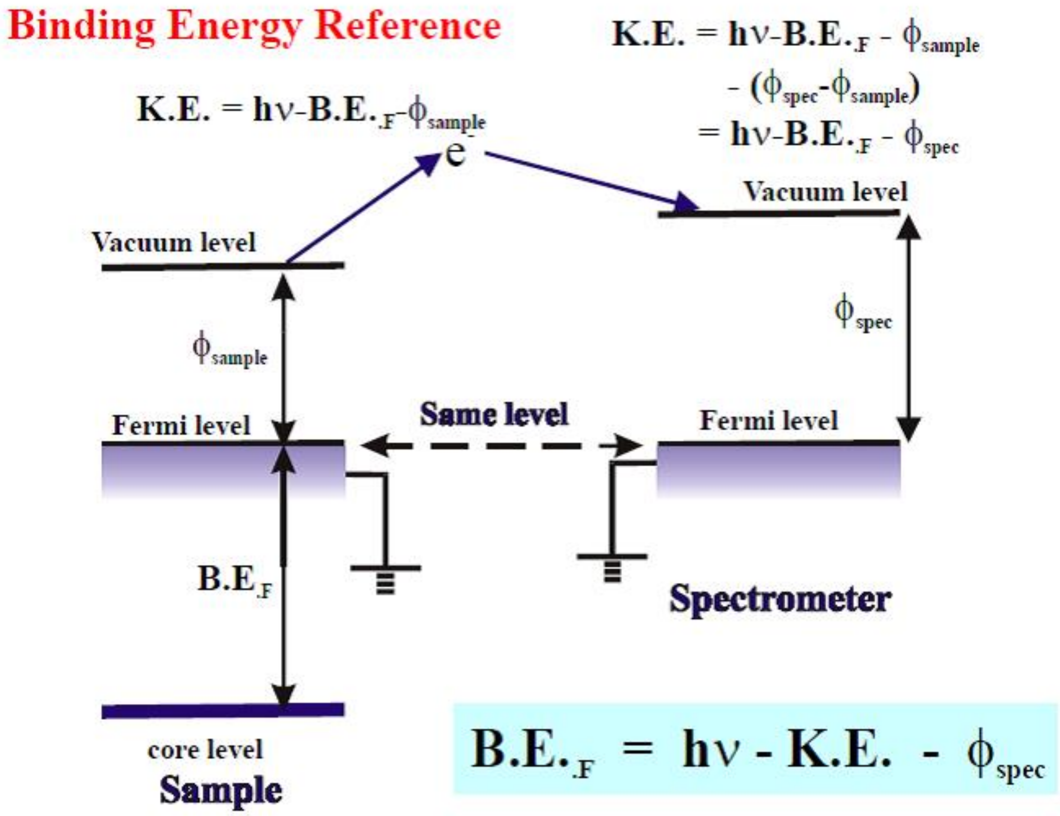

Figure 9. Principles of measurements in XPS adapted from Ref[30].

An X-Ray photoelectron spectrometer consists of the following components: (i) a vacuum system that ensures a high or ultrahigh vacuum that is necessary to maximize the electrons diffusion towards the detector, (ii) the X-Ray source, (iii) an electron-energy analyzer, and (iv) a PC that both controls the spectrometer and processes the spectra. The apparatus we use at our laboratory is the ThermoScientific XPS Kalpha as shown in Figure 10. It is equipped with a monochromatic Al Kα source (hν = 1486.6 eV). At a pass energy of 30 eV the FWHM is 0.7 eV on the $Ag3d_{5/2}$ peak of a silver standard. The FWHM of the Ag peak is commonly taken as providing an estimate of the experimental resolution of the XPS spectra.

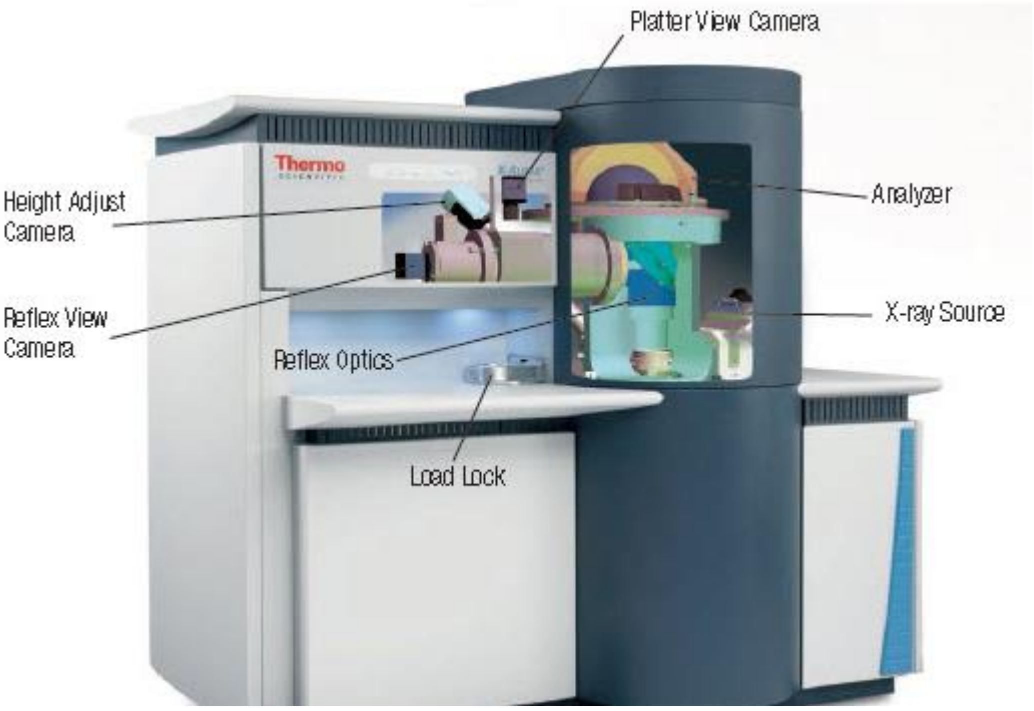

Figure 10. The Thermoscientific K-Alpha XPS aparatus (image provided by the vender's site).

Results of X-Ray Photoelectron Spectroscopy

An XPS spectra that is representative of our 2DGEBA:1EDA poly-epoxy polymer is shown in Figure 11.

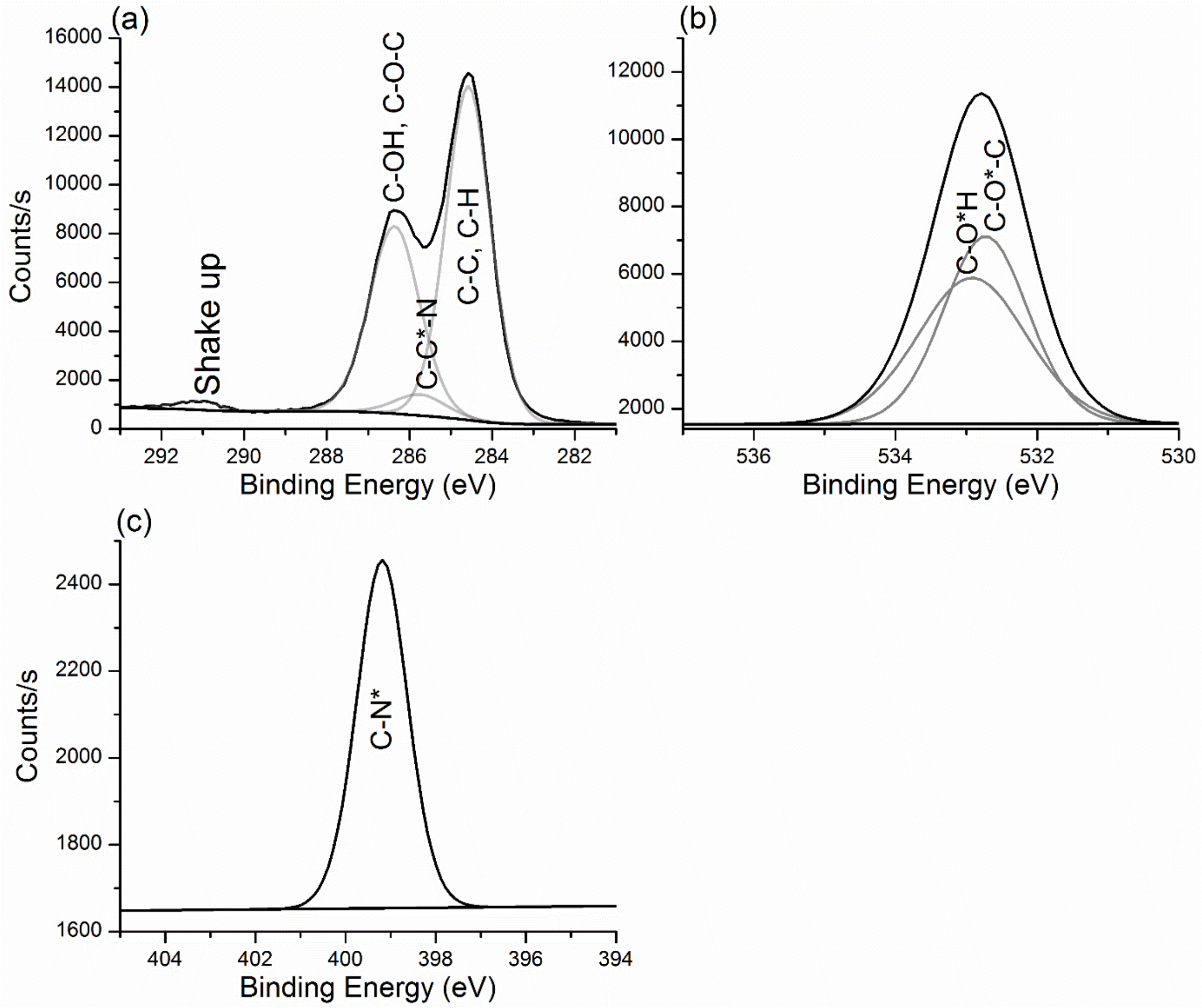

Figure 11. Experimental XPS spectra for the (a) C1s, (b) O1s and (c) N1s core levels of a pristine poly-epoxy (2DGEBA:1EDA) surface.

Figure 11 shows the experimental results with an empirical peak decomposition based on literature data, experience, and knowledge about the polymer composition. After the fitting procedure, a fair assessment of the poly-epoxy surface is possible with 3 contributions plus the shake-up satellite for the C1s, 2 contributions for the O1s and only 1 contribution for the N1s spectra. These 3 contributions for the C1s spectrum correspond to C-C/C-H ($BE = 284.6\ eV$), C-N ($BE = 285.4\ eV$), and oxygenated bonds ($BE = 286.4\ eV$) which cannot be separated with the experimental resolution. For the O1s spectrum the contributions correspond to C-O-H ($BE = 532.9\ eV$) and C-O-C ($BE = 532.4\ eV$) bonds and for the N1s we can only identify the C-N ($BE = 399.2\ eV$) contribution. Whereas it is correct in terms of composition and chemical shifts, the accuracy is limited for the description of the surface chemistry; i.e. peaks are broad (e.g. 1.6 eV FWHM for the C-O-C, C-OH peak) and hide finer details. After extracting information for the pristine surface we advance our work towards the metallization of the surface using pure Cu.

2.3 Metallized poly-epoxy surface

2.3.1 Protocol for metallizing a poly-epoxy surface in ambient temperature with Cu

The next step is the characterization of the surface after metallization means of AFM and XPS. Our first choice as a metal to test is Cu. The reason is that copper metallization has many applications in the industrial and leisure sector[13] and is currently studied in the research group, specialized in Chemical Vapor Deposition (CVD). CVD cannot be used for our system due to the fact that the temperature used for Cu deposition in the CVD reactor is greater than the T_g of the polymer. Preferably metallization of the surface should be performed at ambient temperature.

Hence we purchased a metal evaporator namely the M-EV Mini e-beam Evaporator from Mantis Deposition LTD. Its schematics are shown in Figure 12. This metal evaporator works only under Ultra High Vacuum (<10^{-9} mbar). It is mounted on the existing Microlab 350 AUGER chamber.

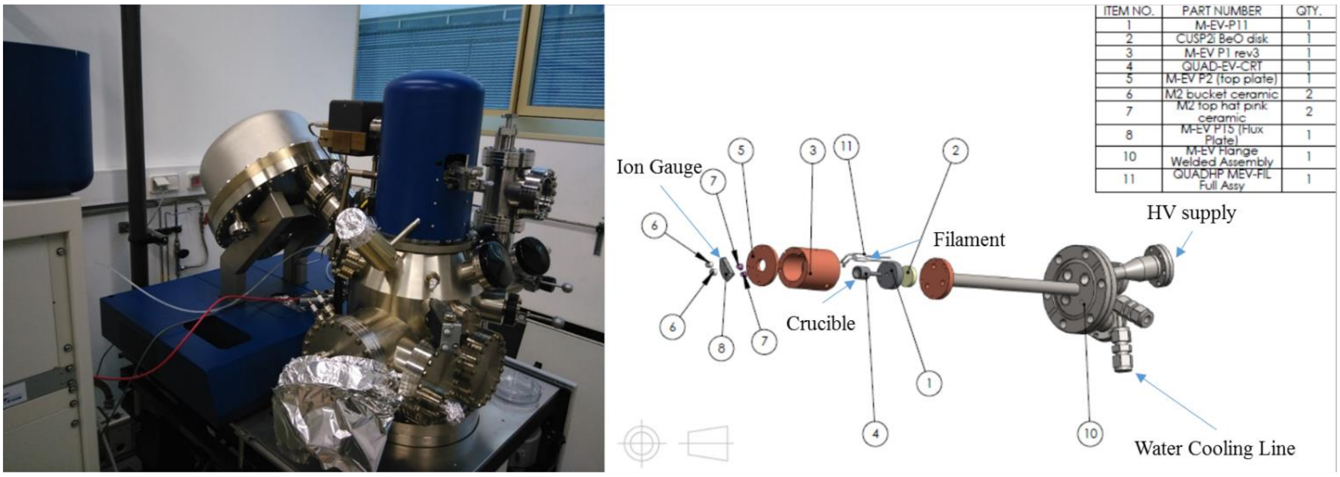

ITEM NO.	PART NUMBER	QTY.
1	M-EV-P11	1
2	CUSP2i BeO disk	1
3	M-EV P1 rev3	1
4	QUAD-EV-CRT	1
5	M-EV P2 (top plate)	1
6	M2 bucket ceramic	2
7	M2 top hat pink ceramic	2
8	M-EV P15 (Flux Plate)	1
10	M-EV Flange Welded Assembly	1
11	QUADHP MEV-FIL Full Assy	1

Figure 12. LEFT: The UHV chamber used for Cu evaporation. RIGHT: The schematics of the metal evaporator provided by MANTIS.

The protocol for the metallization involves the following steps:

Initial outgassing (of the empty source)

Melting the source material

Our source material is a 5N purity copper (99.999% pure, Goodfellow). The source material must first be melted before the evaporation can take place, in order to complete the outgassing of the bulk.

The power obtained at a given filament current will be dependent upon the gap and subsequent field gradient between filament and evaporation source. We then construct a plot of power as a function of the filament current in order to decide which is the ideal power setting for the evaporation as shown in Figure 13.

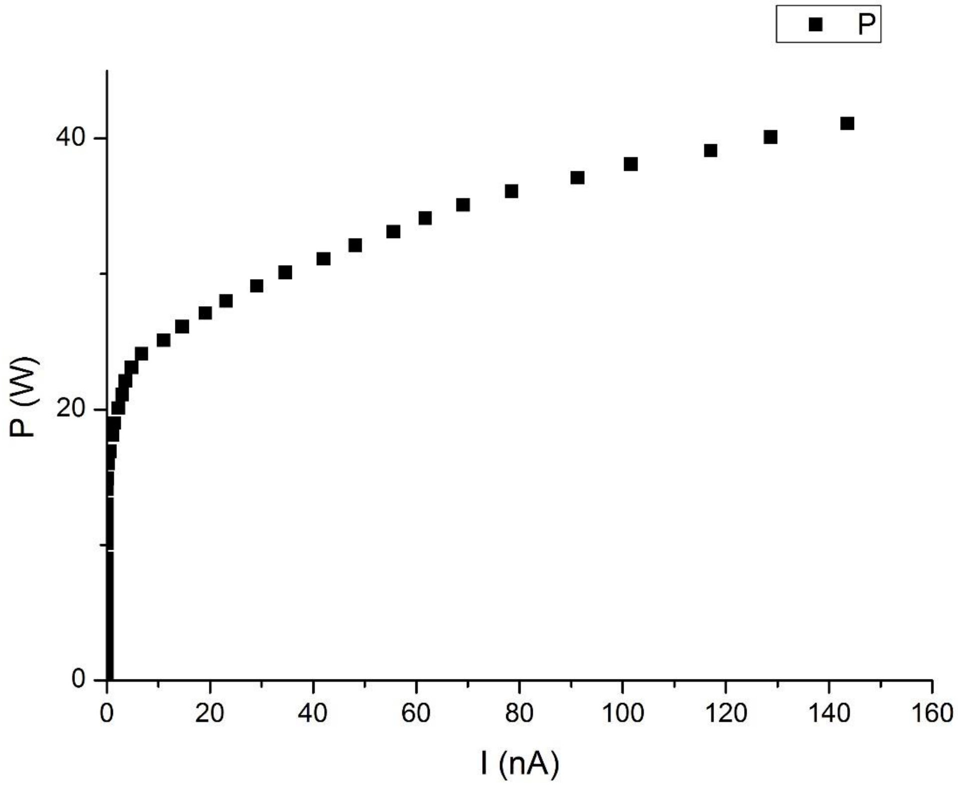

Figure 13. Filament power as function of the current to determine the starting point for power for evaporization of Cu

The initial power to start the evaporation is 25W corresponding to the inflexion of the curve. This initial power corresponds to a flux of 23.2 nA. The metallization takes place under UHV conditions at ambient temperature at a pressure of 1.1x10^{-8} mbar. We performed depositions of Cu on Si wafers at various durations (2, 4 and 6 min) in order to decide the time needed to bury the metal/epoxy interface. By burying the interface we protect it from the necessary exposure to air during the transfer from the evaporation chamber to the XPS chamber. Then, if the thickness is low enough, we can observe modifications of the C1s core-level of the interface upon Cu deposition. In order to determine if the film covers the Si wafers entirely we perform AFM imaging. Following are the AFM results for the metallized poly-epoxy polymer surface.

2.3.2 AFM results

Figure 14 shows the AFM images obtained from depositions of Cu on Si wafers for the 3 deposition durations.

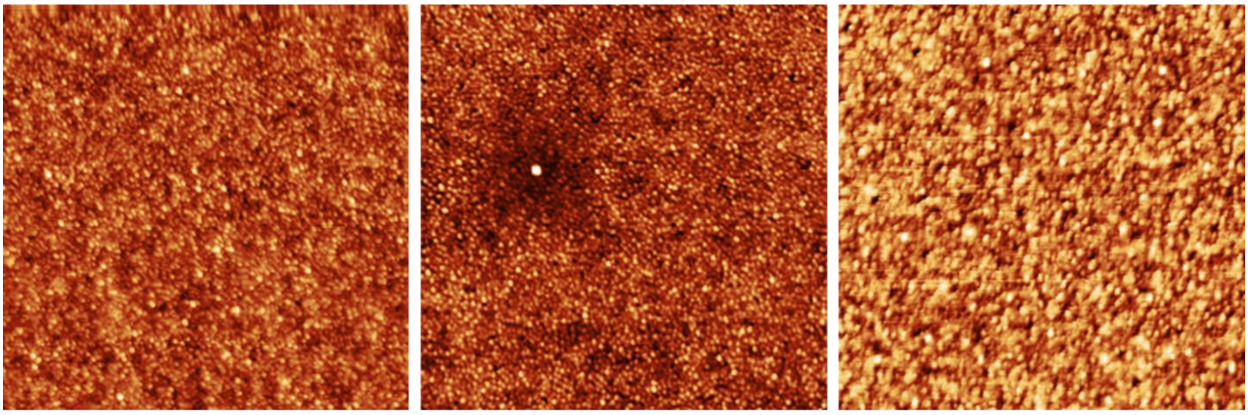

2 min. deposition of Cu
on an Si wafer @ 23.2 nA flux

$R_z = 3.076$ nm
$R_a = 0.436$ nm
$S/S_{projected} = 1.0097$

4 min. deposition of Cu
on an Si wafer @ 23.2 nA flux

$R_z = 3.660$ nm
$R_a = 0.605$ nm
$S/S_{projected} = 1.0201$

6 min. deposition of Cu
on an Si wafer @ 23.2 nA flux

$R_z = 4.120$ nm
$R_a = 0.705$ nm
$S/S_{projected} = 1.0196$

Figure 14. AFM images of 1μm x 1μm area of test deposits of Cu on Si wafers under UHV conditions.

We calculate the R_z and R_a parameters to monitor the metallization of the Si surfaces and determine if the interface is buried. The maximum amplitude and mean arithmetic roughness increase linearly for increasing deposition time. This is due to a 3D growth mode of the Cu which forms large clusters. The surface is then rough with the formation of open porosity and troughs, illustrated by the high R_z. Nevertheless, even after 6 min deposition, the equivalent film thickness is < 4.12 nm, i.e. > 3x Inelastic Mean Free Path ($\lambda = 1.8$ -1.9 nm) of electrons in Cu.[31] The thickness is then low enough to allow electrons from the interface to be detected in XPS. Therefore, while lower deposition durations (2 and 4 minutes) might be enough to cover the surface, we conservatively choose the 6 min deposits for XPS. The poly-epoxy surface is then metallized and AFM imaging is performed. The results for the Cu covered surface are shown in Figure 15.

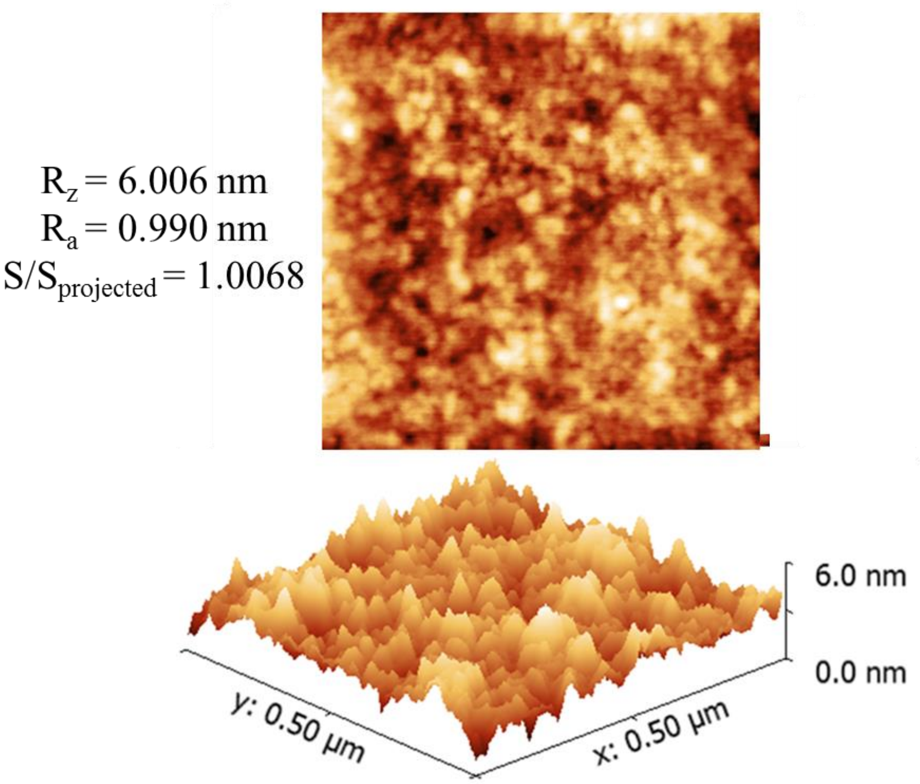

Figure 15. AFM results for a poly-epoxy surface fully covered with Cu.

The maximum amplitude is 6 nm. The 3D growth mode of the Cu on the poly-epoxy surface is significantly different from the 3D growth on the Si wafer. Due to the difference in nucleation density, the R_a of the Cu films on the poly-epoxy surface is larger than that on the Si wafer surface. That is an effect of the low reactivity of the poly-epoxy surface that doesn't promote Cu/epoxy interactions to the benefit of Cu/Cu interactions and thus create less number of nuclei/nm^2.

2.3.3 XPS results

Figure 16 shows the comparison between the C1s XPS spectra of the pristine and the metallized poly-epoxy surface. It must be noted that for XPS, we should complete the analysis with the Auger peaks of Cu that may demonstrate Cu oxidation. But, since the metallic Cu contribution is in large excess compared to the Cu contribution of the interface, no features are found in the Cu LMM spectrum that would differ from a bulk Cu.

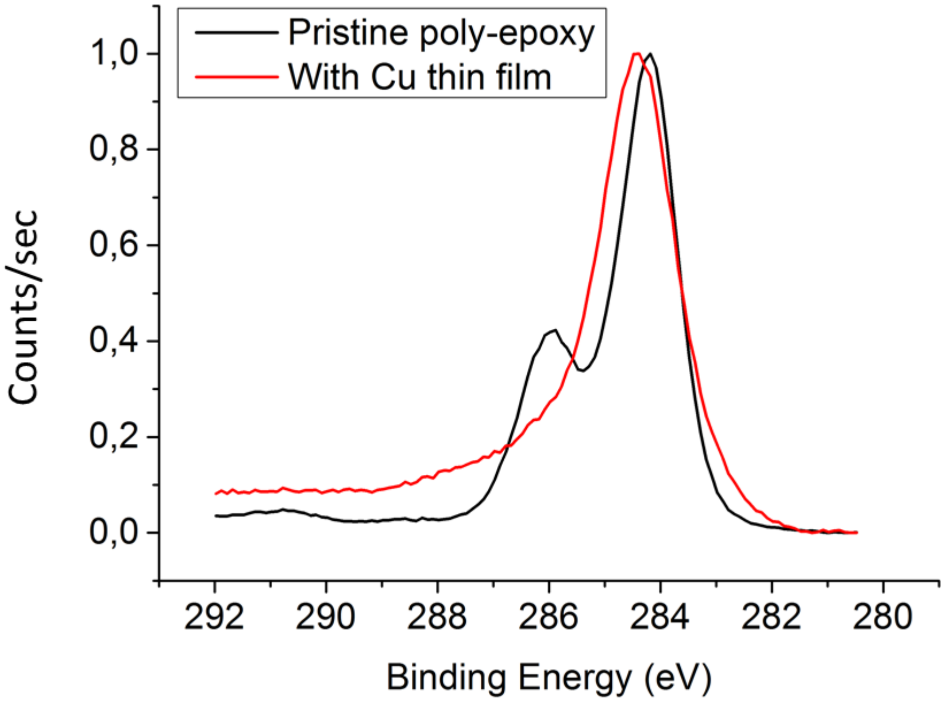

Figure 16. Comparison between the pristine and metallized poly-epoxy surface at a specific range of BE's

Nevertheless, we observe that the shoulder corresponding to C-OH, C_{ph}-O-C has disappeared when the surface is covered with the Cu thin film, leading to the conclusion that the adsorption likely occurs preferentially on these groups. Calculations are performed in Chapter 3 in order to identify the mechanism of adsorption.

2.4 Conclusion

In the present chapter we demonstrate the experimental counterpart of our work. We show how a reproducible protocol can be used to form polymer samples that exhibit a low surface roughness and are fully polymerized. Through DSC measurements we derive the T_g of our polymer (118 °C) which will be used later on for comparison with the T_g calculated by MD. Atomic force microscopy measurements show a low surface roughness (<1nm). The XPS C1s spectrum of the pristine surface is decomposed empirically showing 3 contributions. The surface is then metallized with pure Cu in UHV conditions at ambient temperature. To deduce the best metallization duration, test metallizations are performed showing that the optimum time is 6 minutes in order to obtain a covering thin film. The thickness is lower than 6 nm, below 3λ meaning that the surface is fully buried while allowing us to perform XPS characterizations of the interface. XPS measurements on the metallized poly-epoxy surface show that the C-OH, C_{ph}-O-C shoulder of the C1s peak disappears, giving first hints about the

Cu adsorption mechanism. This study is deepened in Chapter 3 where we will demonstrate how different approaches in quantum calculations can be used to gain better understanding on the XPS spectra of the pristine and metallized surfaces.

Bibliography

1. Aerospace materials — past, present, and future - Aerospace Manufacturing and Design. Available at: http://www.aerospacemanufacturinganddesign.com/article/amd0814-materials-aerospace-manufacturing/. (Accessed: 25th September 2017)
2. Flosbach, C. & Fugier, R. Epoxy Functional Acrylic Polymers for High Performance Coating Applications. in *Epoxy Polymers* (eds. Pascault, J.-P. & Williams, R. J. J.) 39–54 (Wiley-VCH Verlag GmbH & Co. KGaA, 2010). doi:10.1002/9783527628704.ch3
3. Gandini, A. Epoxy Polymers Based on Renewable Resources. in *Epoxy Polymers* (eds. Pascault, J.-P. & Williams, R. J. J.) 55–78 (Wiley-VCH Verlag GmbH & Co. KGaA, 2010). doi:10.1002/9783527628704.ch4
4. Chandrasekhar, P. *et al.* Conducting Polymer (CP) infrared electrochromics in spacecraft thermal control and military applications. in *Synthetic metals* **135–36,** 23–24 (Elsevier, 2003).
5. Feldman, D. & Barbalata, A. *Synthetic Polymers: Technology, Properties, Applications*. (Springer Netherlands, 1996).
6. Zaporojtchenko, V. *et al.* Formation of metal–polymer interfaces by metal evaporation: influence of deposition parameters and defects. *Microelectron. Eng.* **50,** 465–471 (2000).
7. Ho, P. S. *et al.* Chemical bonding and reaction at metal/polymer interfaces. *J. Vac. Sci. Technol. Vac. Surf. Films* **3,** 739–745 (1985).
8. Burrell, M. C. *et al.* Characterization of Surface Modifications during Metallization of Polyetherimide. in *Metallized Plastics 1* 223–233 (Springer, Boston, MA, 1989). doi:10.1007/978-1-4899-0879-7_15
9. Bébin, P. & Prud'homme, R. E. Comparative XPS Study of Copper, Nickel, and Aluminum Coatings on Polymer Surfaces. *Chem. Mater.* **15,** 965–973 (2003).
10. Zaporojtchenko, V., Behnke, K., Thran, A., Strunskus, T. & Faupel, F. Condensation coefficients and initial stages of growth for noble metals deposited onto chemically different polymer surfaces. *Appl. Surf. Sci.* **144,** 355–359 (1999).
11. Bou, M., Martin, J. M., Le Mogne, T. & Vovelle, L. Chemistry of the interface between aluminium and polyethyleneterephthalate by XPS. *Appl. Surf. Sci.* **47,** 149–161 (1991).
12. Wagner, A. J., Wolfe, G. M. & Fairbrother, D. H. Reactivity of vapor-deposited metal atoms with nitrogen-containing polymers and organic surfaces studied by in situ XPS. *Appl. Surf. Sci.* **219,** 317–328 (2003).
13. E. Sacher (ed.). *Metallization of Polymers 2*. (Plenum Publishers, 2002).
14. Travaly, Y., Bertrand, P., Rignanese, G.-M. & Gonze, X. Theoretical Modeling of the Nucleation and Growth of Aluminium Films Thermally Evaporated onto Poly(ethylene terephthalate) Substrate. *J. Adhes.* **66,** 339–355 (1998).
15. Friedrich, J. F., Koprinarov, I., Giebler, R., Lippitz, A. & Unger, W. E. S. Reactions and Intermediates at the Metal-Polymer Interface as Observed by XPS and NEXAFS Spectroscopy. *J. Adhes.* **71,** 297–321 (1999).
16. Wolany, D. *et al.* Combined ToF-SIMS/XPS study of plasma modification and metallization of polyimide. *Surf. Interface Anal.* **27,** 609–617 (1999).
17. Rastomjee, C. S. *et al.* Aluminium metallisation of argon and oxygen plasma-modified polycarbonate thin film surfaces. *Appl. Surf. Sci.* **136,** 280–297 (1998).
18. Kanzow, J. *et al.* Formation of a metal/epoxy resin interface. *Appl. Surf. Sci.* **239,** 227–236 (2005).
19. Infrared Spectroscopy - Materials Science, Engineering and Technology. Available at: https://www.intechopen.com/books/infrared-spectroscopy-materials-science-engineering-and-technology. (Accessed: 26th September 2017)
20. Nikolic, G. *et al.* Fast Fourier Transform IR Characterization of Epoxy GY Systems Crosslinked with Aliphatic and Cycloaliphatic EH Polyamine Adducts. *Sensors* **10,** 684–696 (2010).

21. Duguet, T. *et al.* Toward a computational and experimental model of a poly-epoxy surface. *Appl. Surf. Sci.* **324,** 605–611 (2015).
22. Bessaguet, C. *Synthèse de polymères thermodurcissables modèles et caractérisation de leur surface par XPS et AFM, Rapport de stage Master 2*. (Institut National Polytechnique de Toulouse, 2013).
23. Bliznyuk, V. N., Assender, H. E. & Briggs, G. A. D. Surface Glass Transition Temperature of Amorphous Polymers. A New Insight with SFM. *Macromolecules* **35,** 6613–6622 (2002).
24. Bermejo, J. S. & Ugarte, C. M. Influence of Cross-Linking Density on the Glass Transition and Structure of Chemically Cross-Linked PVA: A Molecular Dynamics Study. *Macromol. Theory Simul.* **18,** 317–327 (2009).
25. Marti, O., Stifter, T., Waschipky, H., Quintus, M. & Hild, S. Scanning probe microscopy of heterogeneous polymers. *Colloids Surf. Physicochem. Eng. Asp.* **154,** 65–73 (1999).
26. Tsui, O. K. C., Wang, X. P., Ho, J. Y. L., Ng, T. K. & Xiao, X. Studying Surface Glass-to-Rubber Transition Using Atomic Force Microscopic Adhesion Measurements. *Macromolecules* **33,** 4198–4204 (2000).
27. Funes, D. 2.2. Atomic force microscope (AFM).
28. Nečas, D. & Klapetek, P. Gwyddion: an open-source software for SPM data analysis. *Cent. Eur. J. Phys.* **10,** 181–188 (2012).
29. ISO 25178-2:2012 - Geometrical product specifications (GPS) -- Surface texture: Areal -- Part 2: Terms, definitions and surface texture parameters. Available at: https://www.iso.org/standard/42785.html. (Accessed: 15th October 2017)
30. XPS Summary (Sylvia Natividad, Arena Holguin, and Gabriel Gonzalez) - Sylvia Natividad - Confluence. Available at: https://wiki.utep.edu/pages/viewpage.action?pageId=51217510. (Accessed: 15th October 2017)
31. Powell, C. J. & Jablonski, A. *NIST Electron Inelastic-Mean-Free-Path Database - Version 1.2, National Institute of Standards and Technology, Gaithersburg, MD.* (2010).

Chapter 3: HF and DFT computations for the simulation of XPS spectra

3.1 Introduction

Our goal is to create numerical models of the poly-epoxy surface. In this chapter and in the next one, we propose two models, each one adapted to part of our studies. As it will be explained in the perspectives of the manuscript, the proposal of an integrated model will be the next objective, beyond this PhD work.

The first model that we study is a molecular model: one DGEBA molecule connected to one EDA molecule. This model, called the 'dimer model' in the following, is used to simulate the XPS spectra for the pristine surface. Thanks to these results, we are able to analyze the experimental spectrum more accurately than with the exclusive use of experiments and literature. This dimer model is also used to study the mechanism of the metallization process with copper by the determination of Cu adsorption energies on the dimer. The most stable adsorption sites can then be determined and XPS spectra of the molecular model of the metallized surface are simulated and compared with the experimental counterpart.

3.2 General introduction to XPS

As explained in Chapter 2, in X-Ray Photoelectron Spectroscopy (XPS), photons emitted by a monochromatic source (photons of fixed energy hv) are absorbed by an atom and this can lead to the emission of an electron and the ionization of the atom. With XPS, core-levels are analyzed (while ultraviolet photoelectron spectroscopy (UPS) probes valence levels).

The kinetic energy distribution of the emitted photoelectrons is therefore measured by an electron energy analyzer. The binding energy of the photoelectron in the atom is then given by Equation 1:

$$BE_k = hv - KE - \varphi_{spec} \; (1)$$

where hν is the energy of the incident photon, KE is the kinetic energy of the emitted electron, BE_k is the binding energy of the electron removed from orbital k, and φ_{spec} is the known work function of the electron analyzer.

The BE of an electron can also be defined as the difference between the energies of the initial un-ionized state (E^n) and the final ionized state (E^{n-1}):

$$BE_k = E^{n-1} - E^n \quad (2)$$

A positive binding energy refers to a bound state.

The emission of a core electron leads to several phenomena, therefore the photoelectron energy corresponds to both the initial state binding energy and that due to final state effects (after ionization). Initial state corresponds to the emission of one electron from an atom (containing n electrons). It results in the change of its electronic structure (n-1 electrons and a core-hole). The final state effects refer to the response of the atom to the emission of the photoelectron, i.e. core-hole polarization (electrostatic and magnetic effects that are instantaneous) and core-hole rearrangement with electronic relaxation[1] and following processes such as fluorescence and the emission of Auger electrons. These effects are described in Figure 1.

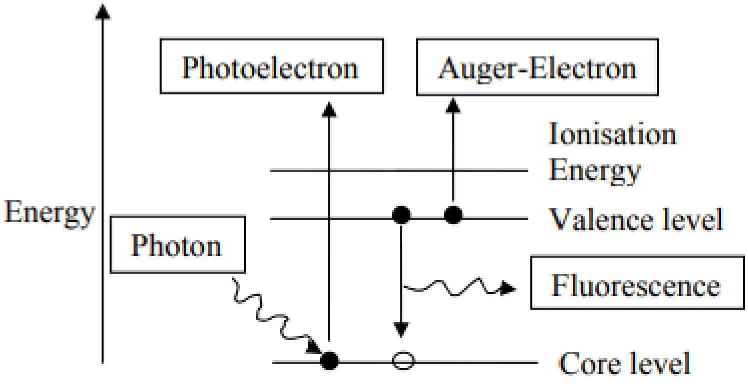

Figure 1. Core-level ionization, electronic relaxation and following phenomena.

BEs of core-electrons are specific to each element and by the use of relative BEs that are calculated relatively to a reference (in our case the lowest binding energy of core-level electrons for one given element), we can identify chemical bonding: the core-level BE of an atom is shifted in different chemical and physical environments. This is attributed to valence electron transfers between the atom and its environment[2].

In an experimental XPS spectrum, peaks can be decomposed into several components if a given element is found in different bonds and environment. We showed in chapter 2 that this can be achieved thanks to the literature and to rigorous databases. But quantum calculations can help for an even more accurate interpretation of the spectra. Simulations of XPS spectra can be done at several levels of theory: (i) at the Hartree-Fock level of theory with the use of the Koopmans' theorem[3] and the ΔSCF theory[4] , (ii) and in the framework of the density functional theory using the Generalized Transition State theory (GTS)[5]. We present now the main methodologies for the calculation of XPS spectra.

3.3 Calculation of XPS spectra

3.3.1 Hartree-Fock calculations

At the simplest level, Koopmans' theorem[3] provides a straightforward method to make a rough evaluation of the valence and core binding energies. Koopmans's theorem states that "the negative of the eigenvalue of an occupied orbital from a Hartree-Fock calculation is equal to the vertical ionization energy to the ion state formed by removal of one electron from that orbital, provided the distributions of the remaining electrons do not change". Thus BEs can be calculated by:

$$BE_k = -\varepsilon_k \ (3)$$

where ε_k is a molecular orbital energy resulting from a Hartree-Fock calculation on the neutral parent molecule.

This method gives results that shift away from the experimental values (up to a difference of 10-20 eV)[6] because it does not take into account final state effects.

Various alternatives can be used to compute core-electron BEs. One is the HF-ΔSCF method that includes the initial state contributions due to the charge distribution in the ground state and the final state contributions due to the electronic relaxation in response to the core-hole. In the ΔSCF method, the BEs are taken as the difference in the HF Self-consistent field, SCF, energies of the ground state (E_{SCF}^{n}) and the core-ionized state (E_{SCF}^{n-1})[7]:

$$BE_k = \Delta E = E_{SCF}^{n-1} - E_{SCF}^{n} \ (4)$$

It is necessary to include the final state effects since the electronic relaxation may be different for the ionization of different inequivalent atoms[8]. The quality of the results then depends on the theoretical treatment used in both SCF calculations but the accuracy of the HF-ΔSCF method was adequate for our purposes. This adequacy has been documented in the review of Ref.[7] and in three recent papers[8–10] where the XPS BEs have been studied for a large number of molecules containing C, N, and O atoms.

An advantage of using HF wavefunctions is that they provide a way to determine the relative intensities, I_{rel}, of the main peaks. In our calculations, the XPS intensities for these main peaks were determined on the basis of the Sudden Approximation, SA[11]. The SA is based on several assumptions:

- The final state wavefunction of the system (containing n electrons) after ionization can be expressed as an anti-symmetrized product of one wavefunction including (n-1) electrons Ψ_k^{n-1} and a one electron continuum orbital
- At the time of the photoionization, Ψ_k^{n-1} is given “by suddenly removing one electron”[7] to the orbital number k without allowing any electronic relaxation. This wavefunction, called a frozen orbital (FO) wavefunction, is thus determined from the orbitals that were calculated for the neutral molecule ground state.

This Ψ_k^{n-1} wavefunction is not solution of the (n-1) electron Hamiltonian H^{n-1}. To compute energies, Ψ_k^{n-1} needs thus to be expressed from (n-1) electron wavefunctions that are eigenfunctions of H^{n-1} :

$$H^{n-1}\,\Psi_\alpha^{n-1} = E_\alpha^{n-1}\,\Psi_\alpha^{n-1} \quad (5)$$

$$\Psi_k^{n-1} = \sum_\alpha C_{k,\alpha}\,\Psi_\alpha^{n-1} \quad (6)$$

For a peak corresponding to the ionized molecule wavefunction Ψ_α^{n-1}, the relative intensity is the probability for the system to be in this state:

$$I_{rel}(k,\alpha) = |\langle \Psi_k^{n-1} | \Psi_\alpha^{n-1} \rangle|^2 (7)$$

This is the square of the overlap of the (n-1) electron FO wavefunction with the ΔSCF wavefunction where the removed C1s electron has been fully screened.

Since the orbitals of the set optimized for the hole-states are not orthogonal to the orbitals of the set optimized for the ground state, GS, it is necessary to use a sum over overlap integrals times a minor of the overlap determinant between the GS and the core-hole orbitals.[12]

3.3.2 Density Functional Theory calculations

In the framework of the density functional theory, final state effects have also to be taken into account to accurately simulate XPS spectra. Methods developed to include initial and final state effects are based on the Slater's transition-state (TS)[13], first generalized by Williams *et al*[5], and later slightly modified by Chong *et al*[14,15]. This latter development is known as the unrestricted Generalized Transition State theory (uGTS). The idea, based on the Taylor series expansion of the energy in terms of the shell occupation, is to remove a fraction of electron from the molecular orbital of interest.

The aim of Slater's transition state is the accurate evaluation of electronic excitation energies of finite molecular systems. The excitation energy ΔE is defined as the difference in the total energy of the electronic system in study before and after excitation:

$$\Delta E = E_{final} - E_{initial} \text{ (8)}$$

The transition state concept was combined with an expression of the total energy of the system as an analytic function of the occupation numbers n_i of orbitals $\{\psi_i(\vec{r})\}$:

$$E = E(n_1, n_2, \dots, n_i) \quad \text{(9)}$$

And then, it could be used to determine ionization energies, for instance core-ionization energies:

$$\Delta E = E_{final} - E_{initial} = E(0,1,1,\dots,1) - E(1,1,1,\dots,1) \text{ (10)}$$

The analytic expression of the total energies allows their Taylor series expansion. If both the initial energy $E_{initial}$ and final energy E_{final} are expanded about the common point in n space $\{n_i\}$ defined below:

$$\{n_i\} = \left(\frac{1}{2}, 1,1,\dots,1\right) \quad \text{(11)}$$

then, all the even order terms in the expansion in powers of δn_1 are zero and finally it can be written:

$$\Delta E = \frac{\partial E}{\partial n_1} + terms\ of\ order\ (\delta n_1)^3 \quad \text{(12)}$$

In the Slater's transition state method, only the first term in Equation 12 is kept and $n_1 = \frac{1}{2}$.

Moreover, using the Janak's[16] theorem, $\frac{\partial E}{\partial n_1}$ is equal to the opposite of the energy ε_1 of the orbital number 1 with the occupation number n_1. Then:

$$\Delta E = -\varepsilon_1\left(\frac{1}{2}\right) (13)$$

Later Williams *et al.*[5] demonstrated that the core-ionization energy can be more accurately calculated as:

$$\Delta \mathrm{E} = -\frac{1}{4}\,\varepsilon_k(1) - \frac{3}{4}\varepsilon_k\left(\frac{1}{3}\right) (14)$$

Chong[14,15] and Endo *et al.*[6, 19–21] later demonstrated that the most accurate results are obtained when the calculation with an occupation number of $\frac{1}{3}$ is performed as an unrestricted computation. We now present the results of our studies using both HF-ΔSCF and DFT-uGTS methodologies.

3.4 Poly-epoxy pristine polymer surface

In Chapter 2, we presented an experimental XPS spectrum for the pristine poly-epoxy surface. The analysis of the experimental spectrum, obtained by the exclusive use of experiments and literature, was good but could be more accurate thanks to simulations of the XPS spectrum of the polymer by quantum calculations. We present now the results of our simulations.

We first optimized the geometry of the dimer model with DFT calculations. The optimized geometry was then used to simulate the XPS spectrum of the pristine surface at the Hartree-Fock level of theory. In a second time, we performed additional DFT computations to simulate the XPS spectra of the pristine and metallized surfaces in the uGTS framework.

3.4.1 Geometry Optimization Calculations

The first step consists to determine the most stable geometry for the monomer (DGEBA), the cross-linker (EDA) and the dimer shown in Figures 2 and 3 respectively.

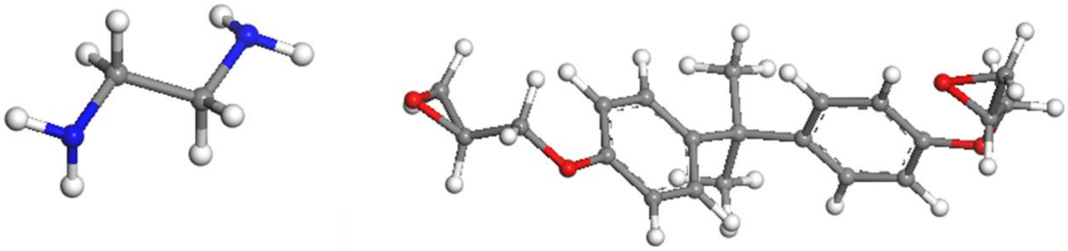

Figure 2. The EDA (left) and DGEBA (right) molecules. We use blue balls for nitrogen atoms, grey balls for carbon atoms, red balls for oxygen atoms and white balls for hydrogen atoms.

The dimer shown in Figure 3 is selected for XPS calculations because we are limited by the number of atoms. With this dimer, we are able to extract information about the –OH and C-N bonds that are formed after the opening of the epoxy ring of the DGEBA molecule and the branching of the amine molecule during the polymerization reaction (described in chapter 2).

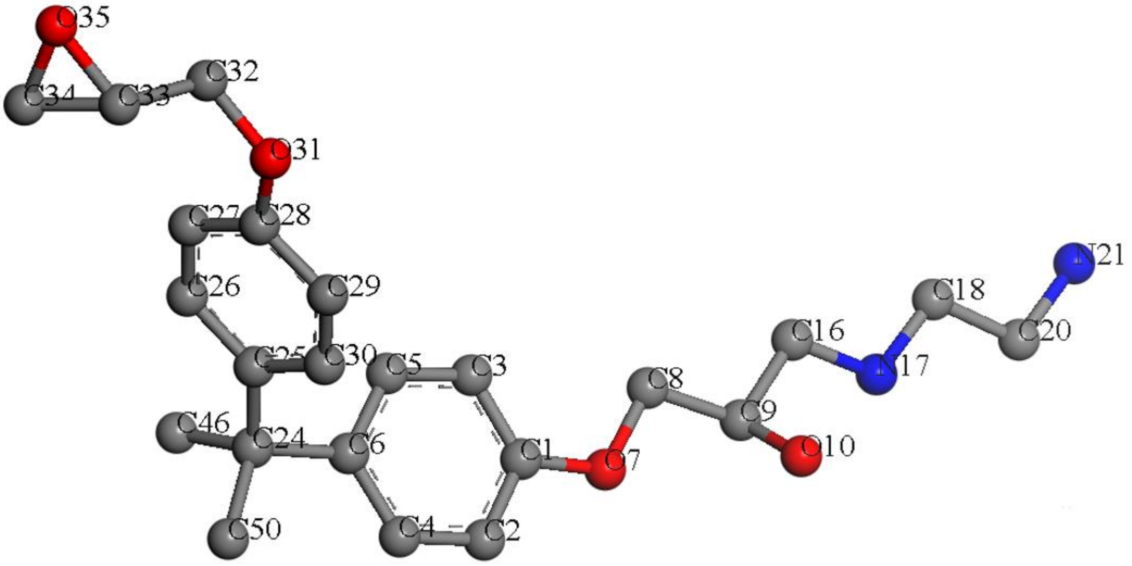

Figure 3. The dimer molecule. The ball colours represent the same atoms as in Figure 2.

The different basis sets and functionals used for the optimization of the geometry of the dimer molecule are summarized in Table 1. The SCF Tolerance was set at 10^{-8} and the optimization tolerance was 10^{-6}.

Table 1. Computational conditions for the optimization of the dimer molecule.

Test	Exchange-Correlation Functional	Orbital Basis Set
1	B88-LYP	DZVP
2	B88-LYP	TZVP
3	B88-PW91	TZVP

The orbital basis sets that are chosen for comparison are the double zeta polarization basis set (DZVP) and the triple zeta polarization (TZVP) basis set[21,22]. By using a polarization basis set we take into account the fact that as atoms are brought closer, their charge distribution causes a polarization effect (the positive charge is drawn to one side while the negative charge is drawn to the other) which distorts the shape of the atomic orbitals, making our calculations more accurate. We compare the optimized structures of the dimer molecule in the different computational conditions. The results are given in Annex C. We conclude that for all the functional/basis set combinations, the calculated bond lengths are in good agreement with experimental values. Taking into account studies[23,24] on the functional dependence of calculated core energies, we decide for a better accuracy to choose the B88-PW91/TZVP optimized geometry for the XPS HF simulations.

Concerning the other parameters for the DFT optimization, we tried to optimize the geometry of the dimer using auxiliary basis sets to save computational time. Unfortunately when very high optimization tolerances were chosen (e.g. $1x10^{-06}$), no convergence was achieved. Tests also showed no significant difference in results by variation of the grid from FINE to EXTRA FINE, so the use of an ADAPTIVE FINE grid was decided. An ADAPTIVE FINE grid means that more points are taken into account when calculating various properties and thus accounts for a larger sampling of the 3D space. To have a great accuracy in results the tolerance of the grid was raised to 10^{-9} μHartree[25]. We used a value of 0.1 (scalar quantity) for the mixing parameter that regulates the Hartree damping[26] of the coefficients that determine the fitting of the charge density.

3.4.2 XPS calculations using Hartree-Fock theory

We first chose the Hartree Fock level of theory and initiated a close collaboration with Prof. Paul Bagus at the North Texas University. He performed all the calculations of the XPS hole-states (ΔSCF method) and SA intensities on the dimer model using the CLIPS program.[27]

The HF energies of the ground state (GS) and the core-ionized state[7] are calculated with a modest basis set that is slightly more extended than double zeta, DZ+[28]. The basis set is made with contracted Cartesian Gaussian functions. For the C, N, and O atoms, the basis set is based on the 9s and 5p basis set of van Djinevelt[29] contracted to 4s and 3p functions, (9,5/4,3). For the H atoms, the basis set is (4,1/2,1) where the s basis function exponents are taken from van Djineveldt[29] supplemented by a p function with exponent 1.0. Calculations of Hartree-Fock wavefunctions are performed for the ground state of the molecule and for configurations where the 1s shell of each of the C atoms was singly occupied. Convergence to the hole-states where the singly occupied orbital had the proper localized 1s character is ensured by selecting the occupied orbitals at each SCF iteration according to a criterion of maximum overlap with the starting guess for that iteration.[30] However with an overlap criterion for selecting occupied orbitals, there is a danger of converging to an excited state, especially if the changes from the initial trial guess are large. When this occurs, it is necessary to change the order of the occupied and virtual orbitals, perhaps in several steps, until one converges to the lowest energy state for the core-hole configuration. This is an arduous manual procedure. A procedure to avoid this manual effort is implemented to insure automatic convergence to the desired state. In the spirit of Jolly's equivalent core approximation[31], the C atom to be core ionized is replaced with a N atom and we determine the HF ground state orbitals for the closed shell positive ions for this equivalent core molecule where it is not necessary to use the overlap criterion to select the occupied orbitals. For the calculations on this equivalent core molecule, the same basis set as for the real molecule of interest is used so that the orbitals for the fictitious molecule can be used as the initial trial functions for the calculations on the core-hole state of the real molecule. For these latter calculations, it is only necessary to specify that the 1s orbital centered on the equivalent core atom is singly occupied. Since the equivalent core orbitals are a good approximation to the orbitals of the lowest core-hole state,[30] there is no difficulty in converging to the desired state without manual intervention except for the preparation of the input files.

The left frame of Table 2 shows results obtained from the ΔSCF calculations. C1s orbitals can be identified from the atom numbering of the first column derived from the model dimer shown in Figure 3. Chemical shifts (ΔBEs) are all obtained from the orbital with the lowest energy (C6), fixed at 0 eV. The third column shows the theoretical intensities calculated in the framework of the SA. The relative SA intensities range between 0.65 and 0.75 meaning that, depending on the C atom, 25% to 35% of the XPS intensity is lost from the main peak to shake satellites. These data are used to build the theoretical C1s spectrum by computing a Voigt convolution for each individual contribution. The Voigt convolution consists in the convolution of a Gaussian and a Lorentzian function[32], with full-width at half maximum (FWHM) of 0.9 eV and 0.1 eV[33,34], respectively. The spectrum envelope is the sum of all contributions.

Table 2. LEFT: Calculated chemical shift (ΔBE) and intensities for each orbitals of the dimer molecule shown in Figure 1. CENTER: Functional group identification (the orbital of interest belong to atoms marked with a *). RIGHT: The number and relative concentration of C1s orbitals in the solid poly-epoxy from the stoichiometric ratio 2DGEBA:1EDA. Greyed rows correspond to orbitals which are present in the model dimer, but no longer present in the fully-polymerized solid.

Model dimer				*Poly-epoxy (2 DGEBA + 1 EDA)*	
Orbitals ID	ΔBE(ΔSCF) (eV)	Calculated relative intensity	Functional groups	Number of C1s orbitals	Relative composition
C6	0,00	0,68	C_{ph}*-C_{quater}	2	9,1%
C25	0,03	0,68	C_{ph}*-C_{quater}	2	
C2	0,04	0,67	C_{ph}	2	36,4%
C29	0,08	0,68	C_{ph}	2	
C5	0,14	0,67	C_{ph}	2	
C30	0,16	0,67	C_{ph}	2	
C4	0,22	0,68	C_{ph}	2	
C26	0,24	0,67	C_{ph}	2	
C3	0,25	0,68	C_{ph}	2	
C27	0,25	0,68	C_{ph}	2	
C50	0,26	0,74	CH_3	2	9,1%
C46	0,28	0,74	CH_3	2	
C24	0,82	0,74	C_{quater}	2	4,5%
C18	1,00	0,75	N-C-C*-N	2*	4,5%
C20	1,20	0,75	N(H2)-C*-C-N	0	n/a
C16	1,25	0,75	N-C*-C(OH)	4	9,1%
C1	1,89	0,65	C_{ph}*-O-C	2	9,1%
C28	1,92	0,65	C_{ph}*-O-C	2	
C9	2,09	0,74	C-OH	4	9,1%
C8	2,36	0,73	C*-O-C_{ph}	4	9,1%
C34	2,58	0,73	epoxy	0	n/a
C33	2,59	0,73	epoxy	0	n/a
C32	2,65	0,74	epoxy-C*-O-C_{ph}	0	n/a

Figure 4a shows the experimental result, presented in chapter 2, with an empirical peak decomposition based on literature data, experience, and knowledge about the polymer composition. After the fitting procedure, a fair assessment of the poly-epoxy surface is possible with 3 contributions plus the shake-up satellite, only. ΔBE (ΔSCF) and SA results are presented in Figure 4b with the comparison of the experimental (grey full line) and simulated (black full line) spectra. It helps distinguishing 9 contributions instead of 3 as the “empirical case”, hence it provides more information than is obtained from the imperfect resolution of the XPS experimental data. In this Figure 4b, a Tougaard background[35] is subtracted from the experimental spectrum and the simulated spectrum is positioned by applying a rigid shift until the maximum intensity matches the maximum experimental intensity (normalized to 1.0). The agreement between the experiment and the theory is rather good. The most serious limitation is that the theoretical energy of the second peak at approx. 2.3 eV is too high with respect to experiment by 0.3 eV. The intensity of this peak is also too low by 25%. Finally, there is a difference at the leading, low BE edge of the spectra.

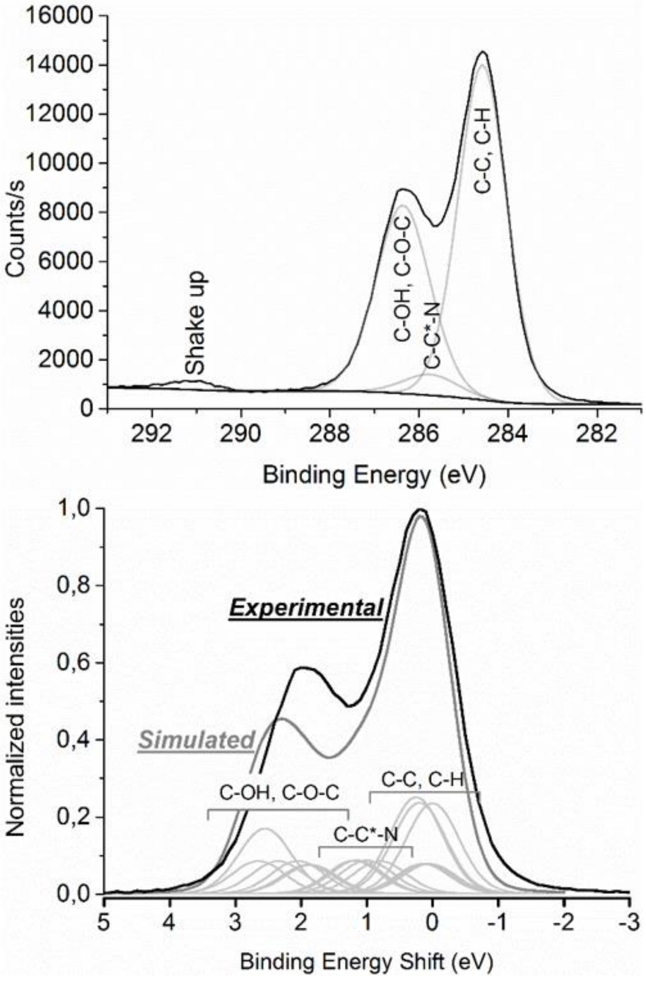

Figure 4. (a) Experimental C1s spectrum decomposed empirically. (b) Comparison of the experimental (grey full line) and simulated (black full line) C1s spectra obtained from the sum of the calculated contributions of each orbitals.

The identification of the bond responsible of the chemical shift of the atomic orbitals BE’s is shown in the central column of Table 2. Some mixing was present for the C1s orbitals in the initial, GS, state calculations where some of these orbitals were not localized exclusively on a single C atom but were distributed over a few of the C atoms; this occurred especially when the C1s orbital energies were nearly degenerate. However, the singly occupied C1s orbitals of the ionic state HF wavefunctions were all localized on a single C atom. The fact that the initial state C1s orbitals were sometimes not localized was taken into account in our calculation of the SA relative XPS intensities. Nine different environments can be identified from the data in Table 2 and the model molecule (the relevant C atom orbital is marked with a *), with the following method.

1. C_{ph}*-C_{quater}: C6 and C25 of the phenyl ring bonded to the unique quaternary carbon, C24.
2. C_{ph}: C atoms of the 2 phenyl rings (C2-5, C26, C27, C29, and C30).
3. CH_3: C46, C50.
4. C_{quater}: quaternary C (C24).
5. N-C-C*-N: C-N bond within the EDA molecule (C18). C20 is discarded because it is bonded to a primary $N(H_2)$ which shifted its 1s electron BE by +0.2 eV as compared to C18, whereas it is absent of the real surface. As a consequence C18 is counted twice (C18 + “actual” C20).
6. N-C*-C(OH): C-N bond of the DGEBA molecule (C16) somehow shifted by the neighboring C-OH.
7. C_{ph}*-O-C: C atoms of the phenyl rings (C1 and C28) bonded to O (O7 and O31).
8. C-OH: C9.
9. C*-O-C_{ph}: C atom from the DGEBA chain (C8). C32 is discarded because the neighboring epoxy ring shifts its 1s electron BE by 0.29 eV as compared to C8, whereas it is absent of the actual surface.

Therefore a first consequence of using theoretical modeling is that it offers the possibility to decompose the XPS spectra with many contributions that are guaranteed by the theory. In that sense the 3 broad contributions of Figure 4a now decompose into:

- C-C, C-H → phenyls C (ΔBE = +0–0.25 eV) + CH_3 (ΔBE = +0.26–0.28 eV)).
- C-C*-N → C-C*-N within EDA (ΔBE = +1.00 eV), C-C*-N within DGEBA (ΔBE = +1.25 eV), and an additional non-negligible quaternary C atom contribution (ΔBE = +0.82 eV).
- C-O-C, C-OH → C-O-C (ΔBE = +1.89–2.36 eV), C-OH (ΔBE = +2.09 eV).

Therefore, to finely decompose the XPS experimental details of the C1s peaks of a polymer composed of similar bonds, acquired in similar conditions (e.g. pass energy and apparatus resolution), it may be appropriate to use a small FWHM broadening for localized contributions (such as CH_3, C-C*-N, quaternary C, and C-OH), and a larger broadening when an *apparently similar environment* allows a modest variation of the BE shifts from these C atoms as, for example, for the phenyls and the C-O-C, in the present work. We describe such variation of the ΔBE as a Δ(ΔBE). Overall, from the interpretation of both spectra in 4a and b, we state that the assignment of each bond at specific ΔBE is correct and can be used to describe the poly-epoxy surface.

But if we consider in details the Figure 4b, we observe discrepancies between experiment and theory in terms of position of the higher-BE peak, relative intensities, and at the low-BE edge of the spectra. Improvement to the HF calculations could improve the agreement, for instance using larger basis sets than the DZ+ basis sets we have used which may be responsible for the positioning of the second peak at a too high BE. Another possible limitation is that HF calculations do not include static electron correlation effects; such static correlation effects, especially those involving promotion from occupied bonding pi orbitals to unoccupied anti-bonding pi orbitals could change energies and intensities. Another improvement of the fit could be the use of a different Voigt function with a larger Gaussian width. Anyway, before any of the theoretical parameter is modified, there is another limitation that surpasses all the others which is the size of the dimer model: although it allows a correct description of the chemistry of the system, it is not correct for the estimation of intensities because it does not respect the actual stoichiometry. Supporting evidence for this assertion is shown in Figure 5 where the C1s peak decomposition is obtained by using ΔBE(ΔSCF) corrected from the stoichiometric composition obtained by dividing the number of orbitals in a particular family (see Table 2, LEFT) over the total number of C1s orbitals, 44, in the bulk solid.

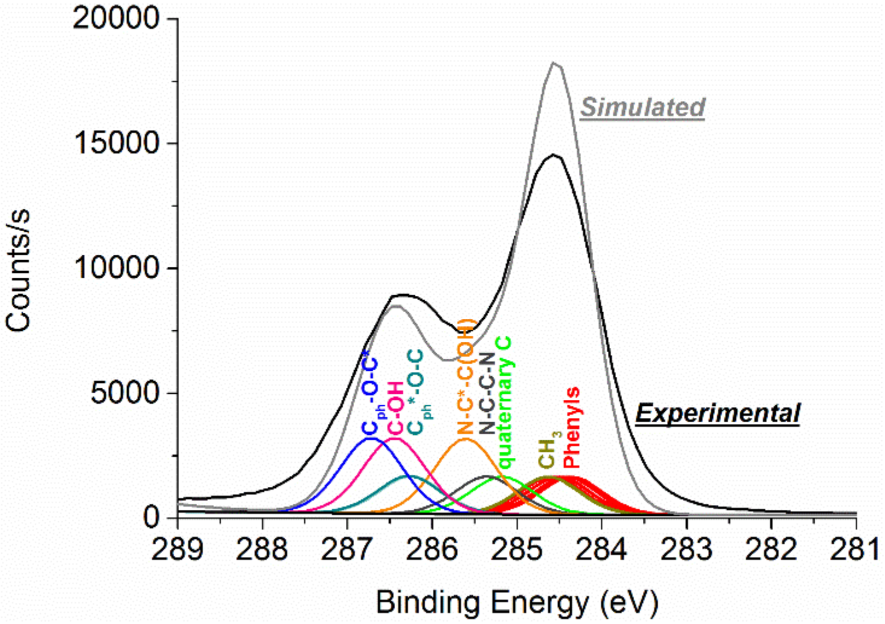

Figure 5. C1s spectra decomposed using the ΔBE(ΔSCF) results along with the actual stoichiometry.

We observe a better positioning of the second peak at about 286.5 eV but discrepancies remain in the BE region between 285.5 and 286 eV, and at the leading low-BE edge of the spectra. Additionally, the total intensity of the phenyls and CH_3 contributions is higher than experiment by about 20%. Nevertheless, intensities corrected from stoichiometry indicate that the poly-epoxy surface is close to a bulk truncation. The surface may be enriched in oxygenated species since the second higher-BE peak relative intensity is higher in experiment than in theory.

The only way to further improve our results would be to start from a different model that could take into account neighboring chains and the presence of vacuum; i.e. moving towards a semi-infinite model mimicking a *surface* instead of a *molecular* model. This is the objective of chapter 4.

3.4.3 XPS calculations using DFT theory

We now calculate core-electron binding energies (BEs) with the unrestricted Generalized Transition State theory (uGTS)[36,5]. To use this method with the deMon2k code, the following steps are executed:

- The geometry is optimized using the PBE96-PBE (Original Perdew, Burke and Ernzerhof GGA exchange from 1996[37] - Original Perdew, Burke and Ernzerhof GGA correlation from 1996[37]), relativistic valence basis set and relativistic Stuttgart pseudopotentials[38] for all the atoms except for the H atoms (DZVP). We apply GEN-A2 auxiliary functions.

- We then remove the pseudopotential on the atom of interest (to calculate the energy of the 1s orbital for this atom). We apply the large AUG-CC-pVTZ[39] orbital basis set to this atom to take all final state effects into account.
- We perform a single point calculation of the energy on the neutral molecule and we then extract the energy $-\varepsilon_k$ of the 1s orbital for the atom of interest.
- We perform a single point calculation of the energy on the ionized molecule, with 0.33 electron on the 1s orbital for the atom of interest. We obtain the energy $-\varepsilon'_k$ of the 1s orbital.
- We then apply the equation: $\mathrm{BE} = \frac{1}{4}[-\varepsilon_k + 3(-\varepsilon'_k)]$ and compose the simulated spectra accordingly.

3.4.3.1 Simulation of the XPS spectrum for the pristine polymer

The results of our calculations within the uGTS framework are summarized in Table 3. Left frame of Table 3 shows ΔBEs. C1s orbitals can be identified from the atom numbering of the first column derived from the model dimer shown in Figure 3. Chemical shifts (ΔBE) are all obtained from the orbital with the lowest energy (C6), fixed at 0 eV. These data are used to build the theoretical C1s spectrum by computing a Voigt convolution for each individual contribution. The Voigt convolution consists in the convolution of a Gaussian (G) and a Lorentzian (L) function, with full-width at half maximum (FWHM) of 0.9 eV and a L/G mix of 30%. The spectrum envelope is the sum of all contributions.

Table 3. LEFT: Calculated chemical shift (ΔBE) of the dimer molecule shown in Figure 4. CENTER: Functional group identification (the orbital of interest belong to atoms marked with an *). RIGHT: The number and relative concentration of C1s orbitals in the solid poly-epoxy from the stoichiometric ratio 2DGEBA:1EDA. Greyed rows correspond to orbitals which are present in the model dimer, but no longer present in the fully-polymerized solid.

Poly-epoxy (2 DGEBA + 1 EDA)

Orbitals ID	ΔBE(uGTS) (eV)	Functional groups	Number of C1s orbitals	Relative composition
C6	0,00	C_{ph}*-C_{quater}	2	9,1%
C25	0,02	C_{ph}*-C_{quater}	2	
C2	0,08	C_{ph}	2	36,4%
C29	0,08	C_{ph}	2	
C5	0,09	C_{ph}	2	
C30	0,09	C_{ph}	2	
C4	0,12	C_{ph}	2	
C26	0,14	C_{ph}	2	
C3	0,20	C_{ph}	2	
C27	0,21	C_{ph}	2	
C50	0,34	CH_3	2	9,1%
C46	0,35	CH_3	2	
C24	0,84	C_{quater}	2	4,5%
C18	1,12	N-C-C*-N	2*	4,5%
C20	1,30	N(H2)-C*-C-N	0	n/a
C16	1,36	N-C*-C(OH)	4	9,1%
C1	1,73	C_{ph}*-O-C	2	9,1%
C28	1,75	C_{ph}*-O-C	2	
C9	2,13	C-OH	4	9,1%
C8	2.21	C*-O-C_{ph}	4	9,1%
C32	2,53	epoxy-C*-O-C_{ph}	0	n/a
C33	2,64	epoxy	0	n/a
C32	2,67	epoxy	0	n/a

Figure 6 shows the results of the ΔBE (uGTS) with the comparison of the experimental (red full line) and simulated (blue full line) spectra. It helps distinguishing 8 contributions instead of 3 as in the “empirical case”. Again it provides more information than is obtained from the imperfect resolution of the XPS experimental data. In this Figure 6, a Shirley background[40] is subtracted from the experimental spectrum and the simulated spectrum is positioned by applying a rigid shift until the maximum intensity matches the maximum experimental intensity. Intensities are fixed by the relative composition of each bond (as in the final results of HF calculations in Figure 5).

The agreement between the experiment and the theory is very good. The XPS simulation predicts well the shape of the C1s peak; with a main peak centered at 284.5 eV and a shoulder centered at 286.5 eV. The main peak is built from C1s photoelectrons arising from C-C bonds (C atoms in phenyls, in CH_3, and the quaternary C at the center of the DGEBA molecule), whereas the shoulder is formed by C1s electrons of C-O bonds (C-O-C, and C-OH). The intensity between the two main components of the C1s peak comes from C-N contributions. Overall, this decomposition is very close to the one obtained by HF ΔSCF calculations. Chemical shifts are found in the same order. The main difference concerns the position of the high-BE side shoulder: the match is almost perfect with the DFT uGTS better than with the HF ΔSCF calculations. Chemical shifts are spread on a narrower range of BEs, likely because static correlation effects are taken into account here.

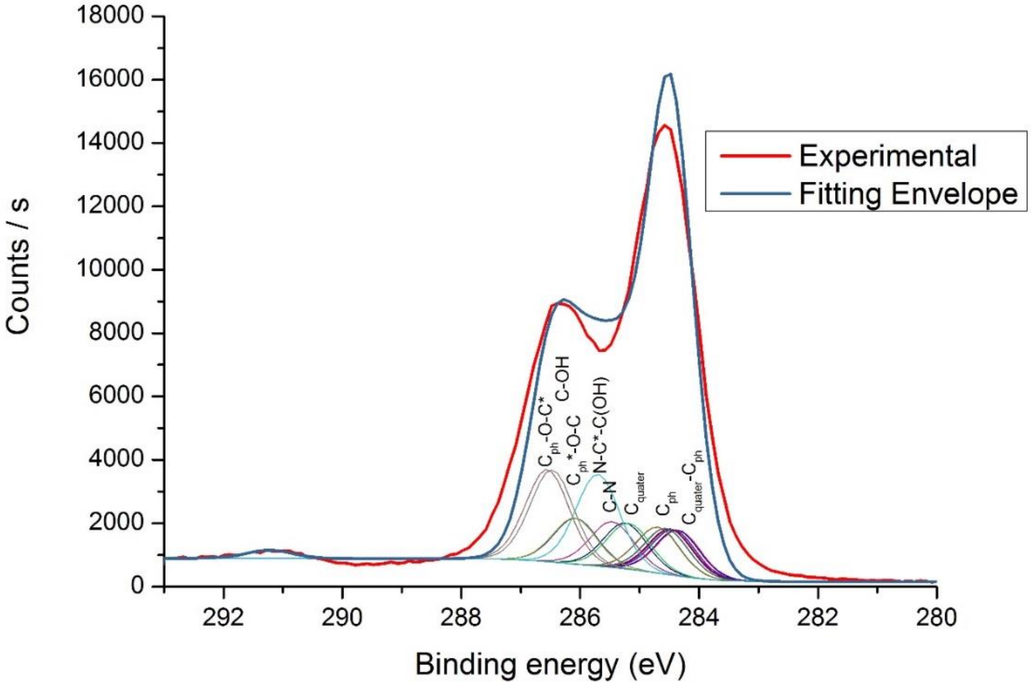

Figure 6. Comparison between experimental and simulated XPS spectra using the uGTS theory. Intensities are fixed by the stoichiometry composition in C1s orbitals.

3.4 Polymer metallized with Cu

3.4.1 Adsorption of Cu atom on the dimer model

To simulate the XPS spectrum for the metallized polymer, we first need to identify the most favorable adsorption site(s) for the Cu atoms on the surface. We perform preliminary computations on the dimer model using the Gaussian09 code[41]. We test several adsorption sites for the copper atom on the dimer molecule with the B3LYP[42,43] and PBE[37] functionals for comparison (6-31G* basis set). The copper atom is initially adsorbed on the chemical groups existing in the polymer (not on a primary amine group or the epoxy ring). The interaction energies between the Cu atom and the polymer are calculated as:

$$E_{int} = E_{Cu/polymer} - \left(E_{Cu\,atom} + E_{polymer}\right) \quad (15)$$

where $E_{Cu/polymer}$ is the total energy of the system with the Cu/dimer interaction. $E_{Cu\,atom}$ and $E_{polymer}$ are the total energies of an isolated Cu atom and the isolated dimer respectively. We call this energetic quantity ‘interaction energy’ because, as it will be demonstrated below, it contains the adsorption energy of the Cu atom but also the dissociation of one bond in the polymer (O-H) in one specific case. We also determine the charge transfer in the system calculating the Mulliken net charges on the atoms. Results are summed up in Table 4.

Table 4. Interaction energies of the Cu atom with the dimer model and charge transfer during the adsorption process. Q_{Cu} is the Mulliken net charge on the Cu atom in the Cu/polymer system.

Adsorption Site	B3LYP/6-31G*	PBE/6-31G*
N17	-1.59 eV (Q_{Cu} = -0.14 e)	-2.59 eV (Q_{Cu} = -0.13 e)
O7	-1.03 eV (Q_{Cu} = +0.01 e)	-2.01 eV (Q_{Cu} = +0.03 e)
C on phenyl ring	-1.43 eV (Q_{Cu} = -0.09 e)	-2.87 eV (Q_{Cu} = -0.08 e)
O10 (in O10-H – case 1)	-1.81 eV (Q_{Cu} =+0.11e)	-3.18 eV (Q_{Cu} = +0.13 e)
O10 (the H is removed – case 2a)	-0.61 eV [a] -5.19 eV[b] (Q_{Cu} = +0.46 e)	-2.07 eV [a] -6.51 eV[b] (Q_{Cu} = +0.45 e)
O10 (the H is removed – case 2b)	+0.50 eV [a] -4.08 eV[b] (Q_{Cu} = +0.39 e)	-0.46 eV [a] -4.89 eV[b] (Q_{Cu} = +0.34 e)

[a] $E_{int} = E_{Cu/polymer} - \left(E_{Cu\,atom} + E_{polymer}\right)$ and [b] $E_{ads} = E_{int} - E_{diss}$

$E_{diss} = \left(E_{polymer/without\,H} + E_H\right) - E_{polymer}$

The three lines at the bottom of Table 3 represent three specific cases that are presented on Figure 7: Case (1) assumes that the copper atom will be adsorbed on the oxygen O10 and the hydrogen will remain connected on this particular oxygen atom as well. Cases (2a) and (2b) on the other hand assume an "interaction" with the oxygen atom O10 and the departure of the hydrogen atom, leading to two stable configurations. For the first case (1), the interaction energy corresponds to the adsorption energy of Cu (-1.81 eV (B3LYP) and -3.18 eV (PBE)). For the latter ones (2a) and (2b), the interaction is weaker even if, for the case (2a), the interaction between the Cu atom and the polymer is stronger (-0.61 eV for B3LYP and -2.07 eV for PBE) than in case (2b)). For the case (2b), the interaction energy is positive for the B3LYP calculation (+0.50 eV) and slightly negative for the PBE computation (-0.46 eV). In fact, the interaction energy is calculated in both cases (2a) and (2b) with the initial system composed of the dimer and the isolated Cu atom, and with the final state composed of the Cu adsorbed on the polymer and the released H atom. Thus the interaction energy in this case includes the dissociation energy of the O-H bond in the polymer and the adsorption energy of Cu on the dehydrogenated polymer (see scheme 1).

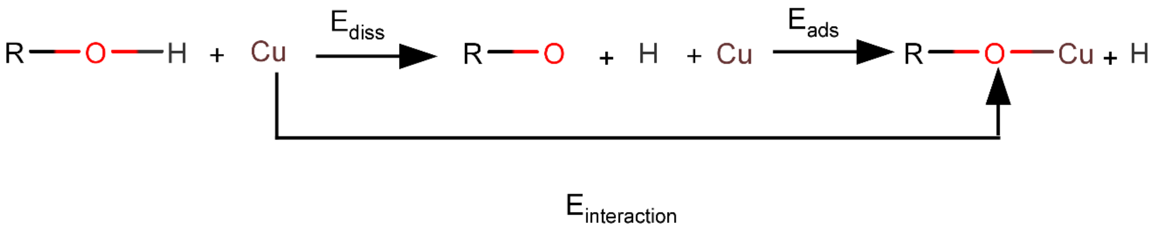

Scheme 1. Interaction of the Cu atom with the polymer – Cases (2a) and (2b).

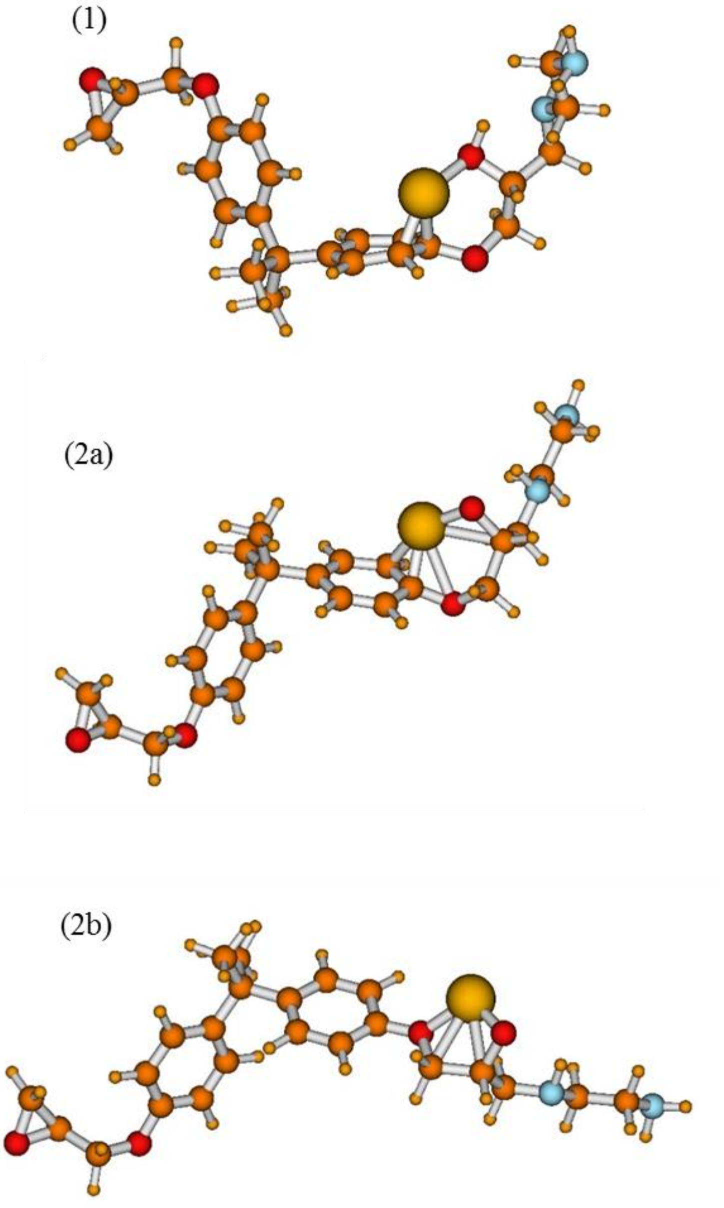

Figure 7. Optimized geometries for cases 1, 2a and 2b. PBE Calculations. We use blue balls for nitrogen atoms, dark orange balls for carbon atoms, red balls for oxygen atoms, yellow balls for copper atoms and light orange balls for hydrogen atoms.

So, to compare with the adsorption energy in the other sites, we subtract the dissociation energy, E_{diss}, of the O-H bond to the interaction energy: $E_{ads} = E_{int} - E_{diss}$

The dissociation energy, 4.58 eV (B3LYP) and 4.43 eV (PBE), is calculated from the total energies of the polymer R-OH, the dehydrogenated polymer RO and the isolated H atom. The adsorption energy for the copper atom on the dehydrogenated polymer is finally -5.19/-4.08 eV (B3LYP, 2a/2b) and -6.51/-4.89 eV (PBE, 2a/2b).

From the adsorption energies of the Cu atom on all the different sites, we can conclude that the adsorption is strong in all cases, but the most favorable adsorption sites is the O10 atom, with the release of the H atom. The Cu atom therefore has a net charge of +0.36/+0.46 e (2a/2b) and is oxidized. Unfortunately, the methodology we use (interface burying, post mortem XPS + ion etching) does not allow the proper experimental monitoring of the CuLMM Auger and Cu2p peaks, where Cu oxidation is usually observed[44,45]. In our case, the proportion of bulk Cu within the 6 nm thickness is largely superior to the interface Cu, hence it is not possible to distinguish Cu-O contributions.

The (2a) configuration corresponds to the strongest adsorption of the copper atom. However both (2a) and (2b) geometries have been used for further simulation of the XPS spectrum of the metallized surface to correlate with the experimental counterpart.

3.4.2 Simulation of the XPS spectrum of the metallized polymer

After identifying the two most favorable adsorption sites for the Cu adsorption using all electron calculations, we simulate the XPS spectrum for these two configurations.

To use the uGTS theory with the demon 2k code, we repeat the several steps described in paragraph 3.3.3. for the pristine surface. We perform pseudopotential (SD pseudopotentials[38]) calculations and we choose the PBE96PBE[37] exchange-correlation functional. The atom of interest is treated all electrons and with the AUG-CC-pVTZ[39] basis set. Table 5 shows the binding energies and the chemical shifts after the uGTS calculation for the two more stable adsorption sites.

Table 5. Binding energies derived from uGTS calculations using pseudopotentials for the two cases of adsorption of the Cu atom on the dimer.

Bond	*Chemical Shift (ΔBE) Away from phenyl*	*Chemical Shift (ΔBE) Interaction with phenyl*
C* phenyl-Cquaternaire	0.00	0.00
C* phenyl-Cquaternaire	0.02	0.01
C phenyl	0.06	0.01
C phenyl	0.07	0.01
C phenyl	0.08	0.08
C phenyl	0.11	0.09
C phenyl	0.11	0.14
C phenyl	0.15	0.15
C phenyl	0.19	0.21
C phenyl	0.19	0.33
CH3	0.34	0.35
CH3	0.34	0.38
COCu-C*-NHC	0.70	0.48
C*H2-NH	0.79	0.57
C quaternaire	0.85	0.82
C*H2-NH	1.27	0.88
C*-O-Cu	1.33	0.91
C* phenyl-O-CH2-COCu	1.71	1.63
C* phenyl-O-CH2-epoxyde	1.73	1.70
phenyl-O-C*-COCu	1.95	2.02
phenyl-O-C*	2.51	2.46
CH2 epoxyde	2.53	
CH epoxyde	2.57	

In Table 5 the second and third columns, chemical shifts (ΔBE) are all obtained from the orbital with the lowest energy, fixed at 0 eV. We can see that between the calculated BEs for the two cases, there is always a 0.1-0.2 eV difference which will play an important role in the deconvolution of the XPS spectra. So these data are used to build the theoretical C1s spectrum with the same FWHM as in the pristine case. The spectrum envelope is the sum of all contributions and is shown in Figure 8.

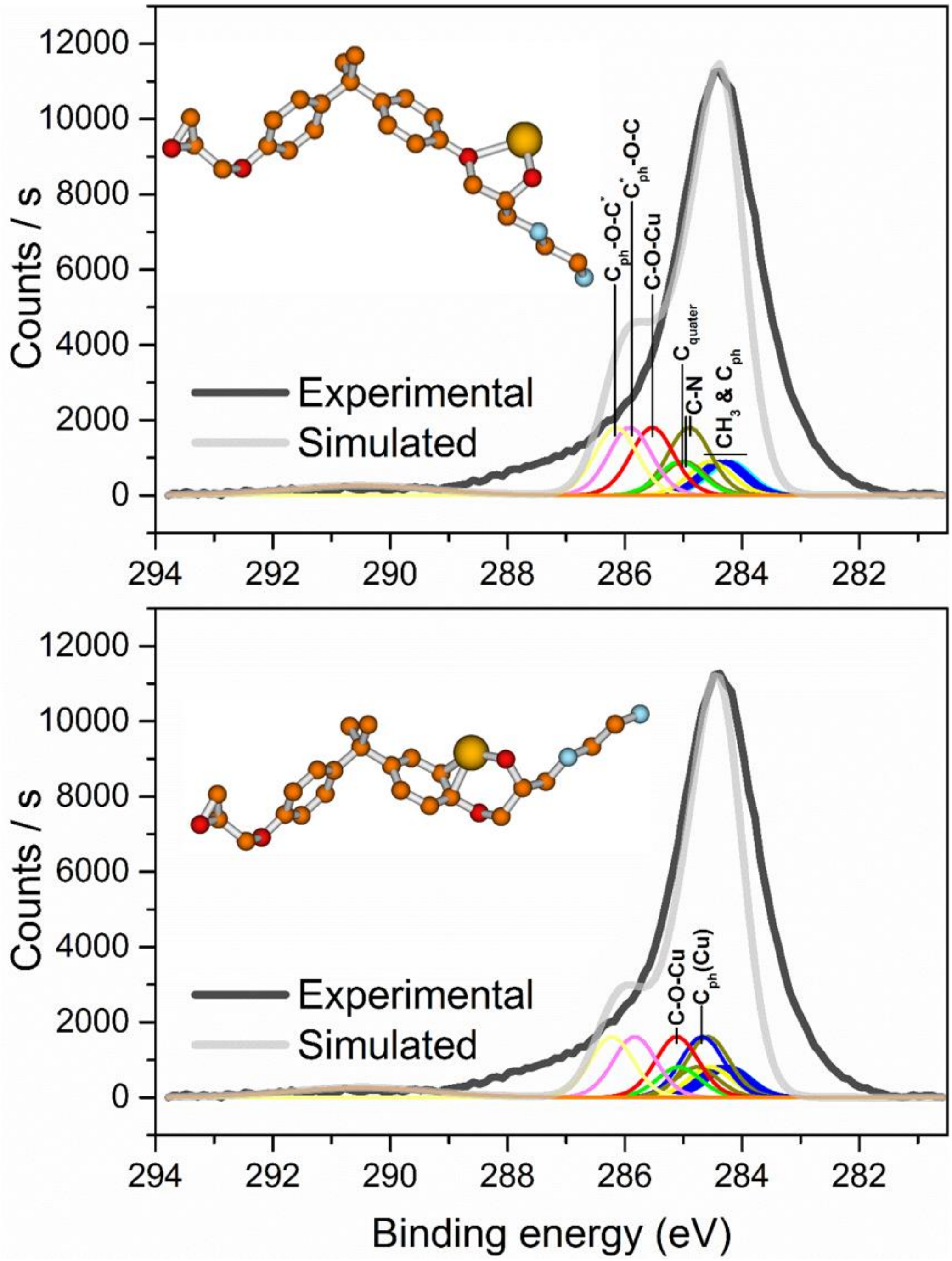

Figure 8. Simulated XPS spectra using uGTS theory. Both corresponds to an oxidative adsorption of the Cu atom on the polymer (case 2). Top: The Cu atom is away from the phenyl (2b). Bottom: The Cu atom is close to the phenyl (2a).

The black line represents the experimental envelope and the grey line represents the simulated spectrum. The XPS spectrum simulated with the Cu atom in interaction with the O10 atom but also with the carbons of the phenyl ring (2b) is closer to the experimental counterpart. The high-BE shoulder is attenuated as compared to the (2a) case. Two differences explain this change of the spectrum shape. First, the C-O-Cu contribution is shifted by ΔBE = 1.33 eV in (2a), whereas it is shifted by ΔBE = 0.91 eV only in 2b, with regard to the reference BE(C*ph-Cquater).

Second, a new contribution noted C_{ph}(Cu) appears in 2b because of the strong interaction between the adsorbed Cu atom and the C atom of the phenyl group. These two shifts of the binding energy are responsible for the concomitant decreasing of the shoulder intensity and increasing of the main peak intensity. However, in both cases, the shoulder is much less intense than on the pristine surface (Figure 6) where the C-OH bonds contribution is strong (ΔBE = 2.13 eV). This shift towards lower binding energies from the initial C-O contribution to the final C-O-M (M = metal) contribution (such as (2a) or (2b)) has already been observed experimentally on a variety of polymers.[45–48] But these works refer to *in situ* and sequential Cu depositions, unlike our case with the buried Cu/poly-epoxy interface. The former methodology permits the monitoring of CuLMM and Cu2p spectra, further confirming the hypothesis for the Cu partial oxidation. When Cu is deposited on the PMDA-ODA polyimide surface,[45,48] the initial C = O contribution to the C1s peak decreases to the benefit of a new contribution at lower BE, and a Cu^+ valence state is identified in the LMM Auger spectrum. The preferential interaction of Cu with the carbonyl groups to form Cu-O=C bonds is further confirmed with a plasma pretreatment of the polyimide surface that increases strongly the concentration of carbonyls and then the concentration of Cu-O=C (and Cu-N) bonds; a consequence being a large increase of the interfacial adherence[47].

Our calculations match perfectly with the scenarios resulting from experiments. Cu atoms interact preferentially with C-OH sites to form Cu-O-C bonds. These bonds are stabilized by a transfer of approximately 0.5 electrons from Cu to O, hence Cu is partially oxidized. This work should be continued with the adsorption of other metals, and with an *in situ* methodology that would allow a more detailed analysis of XPS emissions and Auger transitions.

3.5 Calculation of the charges on the atoms for the DM simulations

For now, the next step of the work will consist in the creation of a larger model using Molecular Dynamics calculations. To perform these numerical simulations, we need to calculate the net charges on the atoms (to be used for the calculation of the electrostatic contribution by the force field). Classical simulations are extremely dependent on these charges and their accurate calculations[49].

For the calculation of atomic charges, several approaches exist, using empirical, semi-empirical or ab initio quantum methods for different molecules. The empirical or semi-empirical approaches are often fast and can be tested easily. The charges generated are often quite accurate when compared to those derived from the more accurate ab initio method, but there are often specific molecules that are poorly handled.[50]

Generating the charges using ab initio methods is quite time expensive. But it can give the most accurate representation of the charge distribution, provided that the atomic basis set that is used is accurate enough. Although the ab initio derived charges demonstrate a heavy fluctuation if a small basis set is used, it has been demonstrated that the electrostatic potential is close to convergent when the basis set is of 6-3lG* quality or more[51]. To derive atomic charges using semi-empirical or ab initio calculations, a methodology consists to fit the charges to reproduce the electrostatic potential (ESP) calculated at a large number of grid points around the molecule. The charges calculated in the ESP method reproduce the quantum mechanically determined multipole moments well and also take into account the intermolecular interactions with nearby molecules. A number of papers[50,52] have shown the advantage of such charges compared to, for example, those derived from Mulliken[53] population analyses. One must not forget that ESP derived charges will, however, be always dependent of the basis set. They are derived from the optimization of the fit of the classical Coulomb formulation for the electrostatic potential and the quantum mechanical electrostatic potential which is evaluated in various points around the molecule. The 6-31G* basis set provides a sufficiently accurate description of the electrostatic properties of polar molecules though not suitable for gas-phases.[50] To even further improve calculations, the above problems have led to the development of a new charge model called RESP charges. It restrains the magnitude of the partial atomic charges that are not so well determined by the electrostatic potential. This is done through a hyperbolic restraint function during the procedure of fitting the partial charges to the electrostatic potential. The tightness of this hyperbola around its minimum and the strength of the weighting of partial charges is controlled by the user and can accurately be calculated to maintain an integral net charge and does not affect the molecular dipole moments. The charges assigned to the molecules using the AMBER force field parameters for instance are derived from fitting the conformational and non-bonded energies using the restrained electrostatic potential (RESP)[50,52] at the HF/6-31G* level.

In the GAFF force field[51], which was used for our MD simulations, this method could be substituted with the AM1-BCC[54,55] charge scheme which is cheaper computationally as it does not involve any ab-initio calculations. The basic idea is to first carry out a semi-empirical AM1 calculation to get Mulliken charges, followed by a bond charge correction (BCC) scheme to obtain results that are compatible to restrained electrostatic potential (RESP)[50,52] at the HF/6-

31G* level charges. AM1 atomic charges are "population" quantities based directly on the occupancies of the atomic orbitals. They are not meant to reproduce directly the ESP or even the multipole moments of the subject molecule, and therefore they perform poorly in condensed-phase simulations vs. ESP-derived charges. Bond charge corrections (BCCs)[55], which have been parameterized using standard least-squares fitting procedures to reproduce the HF/6-31G* ESP of a pre-calculated set of molecules, are then added to emulate the HF/6-31G* ESP.

We used the two methodologies, AM1-BCC[54,55] and RESP[50], to calculate partial charges for the EDA and DGEBA molecules, for a model dimer (1DGEBA:1EDA) and a model trimer (2DGEBA:1EDA). For both dimer and trimer, two different geometries are used to compare the results and to observe the effect that different geometries have on partial atomic charges located in critical positions (such as the reactive centers). Results are detailed in Annex D. We thus choose the RESP charges for the Molecular Dynamic condensed-phase calculations based on existing bibliography[52,56–59].

3.6 Conclusion

With the simple dimer model in which one DGEBA molecule is connected to one EDA molecule, we achieve the simulations of XPS spectra of the pristine poly-epoxy surface, at two level of theory (HF-ΔSCF and DFT-uGTS). With the results of these simulations, we analyze the experimental spectrum more accurately than with the exclusive use of experiments and literature. This dimer model is also used to study the mechanism of the metallization process with Cu by the determination of Cu adsorption energies on the polymer. The most stable adsorption sites are located on the oxygen atom of the O-H group in the polymer. When there is the departure of the H atom simultaneously as the adsorption of the Cu atom, the Cu is oxidized and this leads to the strongest adsorption energy on the polymer. This is in perfect agreement with experimental results of former studies of the adsorption of metals on polyimides, for instance. This allows us to conclude that the first step of the mechanism of metallization of the poly-epoxy surface is the preferential adsorption of Cu on hydroxyls.

Calculations on the dimer need now to be corroborated by calculations on another model, closer to a real polymer. In Chapter 4 we will describe the methodology for creating a bulk polymer with the help of classical Molecular Dynamics.

Bibliography

1. Hüfner, S. *Photoelectron Spectroscopy - Principles and Applications*. (Springer).
2. Lewera, A. *et al.* Core-level binding energy shifts in Pt–Ru nanoparticles: A puzzle resolved. *Chem. Phys. Lett.* **447,** 39–43 (2007).
3. Koopmans, T. Über die Zuordnung von Wellenfunktionen und Eigenwerten zu den Einzelnen Elektronen Eines Atoms. *Physica* **1,** 104–113 (1934).
4. Ziegler, T., Rauk, A. & Baerends, E. J. On the calculation of multiplet energies by the hartree-fock-slater method. *Theor. Chim. Acta* **43,** 261–271 (1977).
5. Williams, A. R., deGroot, R. A. & Sommers, C. B. Generalization of Slater's transition state concept. *J. Chem. Phys.* **63,** 628–631 (1975).
6. Schwartz, M. E. Electron Spectroscopy. in *Applications of Electronic Structure Theory* (ed. III, H. F. S.) 357–380 (Springer US, 1977).
7. Bagus, P. S., Ilton, E. S. & Nelin, C. J. The interpretation of XPS spectra: Insights into materials properties. *Surf. Sci. Rep.* **68,** 273–304 (2013).
8. Bellafont, N. P., Illas, F. & Bagus, P. S. Validation of Koopmans' theorem for density functional theory binding energies. *Phys. Chem. Chem. Phys.* **17,** 4015–4019 (2015).
9. Pueyo Bellafont, N., Bagus, P. S. & Illas, F. Prediction of core level binding energies in density functional theory: Rigorous definition of initial and final state contributions and implications on the physical meaning of Kohn-Sham energies. *J. Chem. Phys.* **142,** 214102 (2015).
10. Pueyo Bellafont, N., Viñes, F. & Illas, F. Performance of the TPSS Functional on Predicting Core Level Binding Energies of Main Group Elements Containing Molecules: A Good Choice for Molecules Adsorbed on Metal Surfaces. *J. Chem. Theory Comput.* **12,** 324–331 (2016).
11. Åberg, T. Theory of X-Ray Satellites. *Phys. Rev.* **156,** 35–41 (1967).
12. Löwdin, P.-O. Quantum Theory of Many-Particle Systems. I. Physical Interpretations by Means of Density Matrices, Natural Spin-Orbitals, and Convergence Problems in the Method of Configurational Interaction. *Phys. Rev.* **97,** 1474–1489 (1955).
13. Slater, J. C. The Theory of Complex Spectra. *Phys. Rev.* **34,** 1293–1322 (1929).
14. Chong, D. P., Hu, C.-H. & Duffy, P. Accurate density-functional calculation of core-electron binding energies with a scaled polarized triple-zeta basis set. Twelve test cases and application to three C2H4O2 isomers. *Chem. Phys. Lett.* **249,** 491–495 (1996).
15. Chong, D. P. Accurate calculation of core-electron binding energies by the density-functional method. *Chem. Phys. Lett.* **232,** 486–490 (1995).
16. Janak, J. F. Proof that θE/θni=εi in density-functional theory. *Phys. Rev. B* **18,** 7165–7168 (1978).
17. Endo, K. *et al.* Theoretical X-ray photoelectron and emission spectra of Si- and S-containing polymers by density-functional theory calculations using model molecules. *J. Mol. Struct.* **561,** 17–28 (2001).
18. Endo, K. *et al.* Valence XPS, IR, and C13 NMR spectral analysis of 6 polymers by quantum chemical calculations. *J. Mol. Struct.* **1027,** 20–30 (2012).
19. Endo, K., Maeda, S. & Aida, M. Simulation of C1s Spectra of C- and O-Containing Polymers in XPS by ab initio MO Calculations Using Model Oligomers. *Polym. J.* **29,** 171–181 (1997).
20. Endo, K., Maeda, S. & Kaneda, Y. Analysis of C1s Spectra of N-, O-, and X-Containing Polymers in X-Ray Photoelectron Spectroscopy by ab initio Molecular Orbital Calculations Using Model Molecules. *Polym. J.* **29,** 255–260 (1997).
21. Schäfer, A., Huber, C. & Ahlrichs, R. Fully optimized contracted Gaussian basis sets of triple zeta valence quality for atoms Li to Kr. *J. Chem. Phys.* **100,** 5829–5835 (1994).
22. Schäfer, A., Horn, H. & Ahlrichs, R. Fully optimized contracted Gaussian basis sets for atoms Li to Kr. *J. Chem. Phys.* **97,** 2571–2577 (1992).
23. Takahashi, O. & Pettersson, L. G. M. Functional dependence of core-excitation energies. *J. Chem. Phys.* **121,** 10339–10345 (2004).

24. Jacobsen, H. & Cavallo, L. Directions for Use of Density Functional Theory: A Short Instruction Manual for Chemists. in *Handbook of Computational Chemistry* (ed. Leszczynski, J.) 95–133 (Springer Netherlands, 2012). doi:10.1007/978-94-007-0711-5_4
25. Krack, M. & Köster, A. M. An adaptive numerical integrator for molecular integrals. *J. Chem. Phys.* **108,** 3226–3234 (1998).
26. Hartree, D. R. The calculation of atomic structures. *Rep. Prog. Phys.* **11,** 113 (1947).
27. Bagus, P. S., Liu, B., McLean, A. D. & Yoshimine, M. *CLIPS is a program system to compute ab initio SCF and correlated wavefunctions for polyatomic systems. It has been developed based on the publicly available programs in the ALCHEMY package from the IBM San Jose Research Laboratory*.
28. Levine, I. N. *Quantum Chemistry*. (Prentice-Hall, 2000).
29. van Duijneveldt, F. B. IBM Research | Technical Paper Search | Gaussian Basis Sets for the Atoms H-Ne for Use in Molecular Calculations. (2016). Available at: http://domino.research.ibm.com/library/cyberdig.nsf/0/3fdb7d4df8e4bca4852579f10056c563?OpenDocument&Highlight=0,gto. (Accessed: 26th July 2017)
30. Pueyo Bellafont, N., Bagus, P. S., Sousa, C. & Illas, F. Assessing the ability of DFT methods to describe static electron correlation effects: CO core level binding energies as a representative case. *J. Chem. Phys.* **147,** 024106 (2017).
31. Jolly, W. L. & Hendrickson, D. N. Thermodynamic interpretation of chemical shifts in core-electron binding energies. *J. Am. Chem. Soc.* **92,** 1863–1871 (1970).
32. Gubner, J. A. A new series for approximating Voigt functions. *J. Phys. Math. Gen.* **27,** L745 (1994).
33. Campbell, J. L. & Papp, T. Widths Of The Atomic K-N7 Levels. *At. Data Nucl. Data Tables* **77,** 1–56 (2001).
34. Campbell, J. L. & Papp, T. Atomic level widths for x-ray spectrometry. *X-Ray Spectrom.* **24,** 307–319 (1995).
35. Seah, M. P., Gilmore, I. S. & Spencer, S. J. Background subtraction: II. General behaviour of REELS and the Tougaard universal cross section in the removal of backgrounds in AES and XPS. *Surf. Sci.* **461,** 1–15 (2000).
36. Endo, K., Kaneda, Y., Okada, H., Chong, D. P. & Duffy, P. Analysis of X-ray Photoelectron Spectra of Eight Polymers by deMon Density-Functional Calculations Using the Model Oligomers. *J. Phys. Chem.* **100,** 19455–19460 (1996).
37. Perdew, J. P., Burke, K. & Ernzerhof, M. Generalized Gradient Approximation Made Simple. *Phys. Rev. Lett.* **77,** 3865–3868 (1996).
38. Institute for Theoretical Chemistry | Institut für Theoretische Chemie | University of Stuttgart. Available at: http://www.uni-stuttgart.de/theochem/. (Accessed: 29th September 2017)
39. Dunning, T. H. Gaussian basis sets for use in correlated molecular calculations. I. The atoms boron through neon and hydrogen. *J. Chem. Phys.* **90,** 1007–1023 (1989).
40. Bagus, P. S., Schrenk, M., Davis, D. W. & Shirley, D. A. Anomalous multiplet-splitting intensity ratios in K-level x-ray photoemission spectra of NO and O2. *Phys. Rev. A* **9,** 1090–1096 (1974).
41. *Gaussian 09, M. J. Frisch, G. W. Trucks, H. B. Schlegel, G. E. Scuseria, M. A. Robb, J. R. Cheeseman, G. Scalmani, V. Barone, G. A. Petersson, H. Nakatsuji, X. Li, M. Caricato, A. Marenich, J. Bloino, B. G. Janesko, R. Gomperts, B. Mennucci, H. P. Hratchian, J. V. Ortiz, A. F. Izmaylov, J. L. Sonnenberg, D. Williams-Young, F. Ding, F. Lipparini, F. Egidi, J. Goings, B. Peng, A. Petrone, T. Henderson, D. Ranasinghe, V. G. Zakrzewski, J. Gao, N. Rega, G. Zheng, W. Liang, M. Hada, M. Ehara, K. Toyota, R. Fukuda, J. Hasegawa, M. Ishida, T. Nakajima, Y. Honda, O. Kitao, H. Nakai, T. Vreven, K. Throssell, J. A. Montgomery, Jr., J. E. Peralta, F. Ogliaro, M. Bearpark, J. J. Heyd, E. Brothers, K. N. Kudin, V. N. Staroverov, T. Keith, R. Kobayashi, J. Normand, K. Raghavachari, A. Rendell, J. C. Burant, S. S. Iyengar, J. Tomasi, M. Cossi, J. M. Millam, M. Klene, C. Adamo, R. Cammi, J. W. Ochterski, R. L. Martin, K. Morokuma, O. Farkas, J. B. Foresman, and D. J. Fox, Gaussian, Inc., Wallingford CT, 2016.*
42. Becke, A. D. Density-functional thermochemistry. III. The role of exact exchange. *J. Chem. Phys.* **98,** 5648–5652 (1993).
43. Lee, C., Yang, W. & Parr, R. G. Development of the Colle-Salvetti correlation-energy formula into a functional of the electron density. *Phys. Rev. B* **37,** 785–789 (1988).

44. Platzman, I., Brener, R., Haick, H. & Tannenbaum, R. Oxidation of Polycrystalline Copper Thin Films at Ambient Conditions. *J. Phys. Chem. C* **112,** 1101–1108 (2008).
45. Pertsin, A. J. & Pashunin, Y. M. An XPS study of the in-situ formation of the polyimide/copper interface. *Appl. Surf. Sci.* **47,** 115–125 (1991).
46. Bébin, P. & Prud'homme, R. E. Comparative XPS Study of Copper, Nickel, and Aluminum Coatings on Polymer Surfaces. *Chem. Mater.* **15,** 965–973 (2003).
47. Wolany, D. *et al.* Combined ToF-SIMS/XPS study of plasma modification and metallization of polyimide. *Surf. Interface Anal.* **27,** 609–617 (1999).
48. Haight, R., White, R. C., Silverman, B. D. & Ho, P. S. Complex formation and growth at the Cr– and Cu–polyimide interface. *J. Vac. Sci. Technol. Vac. Surf. Films* **6,** 2188–2199 (1988).
49. Ramachandran, K. I., Deepa, G. & Namboori, K. *Computational Chemistry and Molecular Modeling: Principles and Applications*. (Springer).
50. Bayly, C. I., Cieplak, P., Cornell, W. & Kollman, P. A. A well-behaved electrostatic potential based method using charge restraints for deriving atomic charges: the RESP model. *J. Phys. Chem.* **97,** 10269–10280 (1993).
51. Wang, J., Wolf, R. M., Caldwell, J. W., Kollman, P. A. & Case, D. A. Development and testing of a general amber force field. *J. Comput. Chem.* **25,** 1157–1174 (2004).
52. Cornell, W. D., Cieplak, P., Bayly, C. I. & Kollmann, P. A. Application of RESP charges to calculate conformational energies, hydrogen bond energies, and free energies of solvation. *J. Am. Chem. Soc.* **115,** 9620–9631 (1993).
53. Segall, M. D., Pickard, C. J., Shah, R. & Payne, M. C. Population analysis in plane wave electronic structure calculations. *Mol. Phys.* **89,** 571–577 (1996).
54. Jakalian, A., Bush, B. L., Jack, D. B. & Bayly, C. I. Fast, efficient generation of high-quality atomic charges. AM1-BCC model: I. Method. *J. Comput. Chem.* **21,** 132–146 (2000).
55. Jakalian, A., Jack, D. B. & Bayly, C. I. Fast, efficient generation of high-quality atomic charges. AM1-BCC model: II. Parameterization and validation. *J. Comput. Chem.* **23,** 1623–1641 (2002).
56. Özpınar, G. A., Peukert, W. & Clark, T. An improved generalized AMBER force field (GAFF) for urea. *J. Mol. Model.* **16,** 1427–1440 (2010).
57. Woods, R. J. & Chappelle, R. Restrained electrostatic potential atomic partial charges for condensed-phase simulations of carbohydrates. *J. Mol. Struct. THEOCHEM* **527,** 149–156 (2000).
58. Cieplak, P., Cornell, W. D., Bayly, C. & Kollman, P. A. Application of the multimolecule and multiconformational RESP methodology to biopolymers: Charge derivation for DNA, RNA, and proteins. *J. Comput. Chem.* **16,** 1357–1377 (1995).
59. Torras, J., Bromley, S., Bertran, O. & Illas, F. Modelling organic molecular crystals by hybrid quantum mechanical/molecular mechanical embedding. *Chem. Phys. Lett.* **457,** 154–158 (2008).

Chapter 4: Molecular Dynamics Simulations

4.1 Introduction

Molecular Dynamics (MD) simulations are a very valuable tool when someone seeks to simulate the properties of polymers and to study their dynamic behavior and evolution with time. With the evolution of modern computers (from personal to supercomputers) the time scales vary from a few femtoseconds (fs) close to several nanoseconds (ns).

In this chapter we use molecular dynamics for (i) simulating and calculating properties of pure liquids of the reactants (DGEBA and EDA) and (ii) to simulate the polymerization process using an "in-situ" multi-step static code.

In the first section, we give information on the state of the art as well as examples from bibliography about the various methods for simulating polymers and their properties. Then, we detail our methodology and the algorithm that lead to the final code, and give a step-by-step explanation of how molecular dynamics calculations are used in conjunction with the static cross-linking code. After these explanations of the theoretical aspects, we introduce results. First, the results for the simulation of the pure liquids of DGEBA and EDA are presented, from which we extract their physical (e.g. density) and structural (e.g. bond lengths distribution) properties. Then, we simulate the melt of the two reactants in stoichiometric analogy (400 DGEBA:200 EDA). The properties of the melt are extracted and compared with the existing literature. Finally, we show how various steps of polymerization change the structural properties of the simulation box, and monitor the polymerization rate. The influence of the initial melt box particles distribution on the final polymerization percentage is also assessed. Finally we extract physical and structural information of the final polymer that compare well with the existing literature; noticeably the glass transition temperature of the DGEBA-EDA poly-epoxy is calculated with a high accuracy.

4.2 Simulation of bulk polymer properties

The first step before the development of a surface model is to obtain a bulk poly-epoxy polymer cross-linked in a simulated chemical process. Molecular simulations at the atomic or molecular scales have proven their ability to achieve thermodynamically accurate models and to simulate thermodynamic and structural properties[1–5]. But only seldom attempts have been made to study the dynamics of cross-linking processes and structure-property relationships of cross-linked polymers. These simulation approaches can be classified in two categories:

(1) Coarse graining of the monomers and cross-linking using the appropriate simulation of the reaction, followed by reverse mapping back to the original atomistic description.
(2) Fully atomistic description of the monomers and then formation of the polymer structure through a cross-linking algorithm.

These two approaches can be used in conjunction with Monte Carlo or Molecular Dynamics computations to simulate the effects of temperature and take time into account. For instance Vogiatzis *et al.*[6] have used the Monte Carlo formalism in conjunction with a coarse grained model to simulate the filling of a polystyrene matrix with tightly cross-linked polystyrene nanoparticles. The local structure of the polymer matrix in the area of the nanoparticles was studied as well as the polymer density profile. Theodorou and Suter[7] developed methods to predict mechanical properties of polymeric glasses. They developed mathematical models for simulating the small deformations of a glassy atactic polypropylene. The microscopic properties were obtained by the arithmetic averages of the responses of each individual microstate to deformation. The internal stress and elastic coefficients were calculated as well as the thermal expansion coefficients through the internal stress tensor.

Doherty *et al.*[1] developed a polymerization molecular dynamics atomistic scheme to construct cross-linked poly(methacrylates) (PMA) networks. This includes reversing the direction of polymerization at various points in the simulation to increase the network formation speed. This reversal technique is employed by stopping polymerization on an end of the network structure and re-initiating on the opposite end of the network so that a chemically conformed structure can be formed. An explicit velocity rescaling methodology is employed to aid in the equilibration of unnatural mechanical stresses. The resulting network is chemically reasonable in terms of bond lengths, angles and overall stereochemical aspects.

By the use of large-scale MD simulations, Tsige and Stevens[8] investigated the mechanical properties of highly cross-linked poly-epoxy polymer networks bonded to a solid surface. The effect of the cross-linker functionality and the number of interfacial bonds on the adhesive to cohesive transition is also shown. Three different cross-linker functionalities (f = 3, 4, or 6) are studied. The correspondence between the stress-strain curve and the sequence of molecular deformations was described in detail. They concluded that the plateau area in the stress-strain curve depends on the functionality of the cross-linker. An increase in f diminishes the strain range of this plateau. Increasing f leads to a higher failure stress and a lower failure strain.

Overall it was shown that the work to failure decreases with an increase in the functionality of the cross-linker.

The cross-linking of poly(vinyl alcohol) with polyol curing agent was studied by Bermegio and Ugarte[9,10]. A method is developed for building fully atomistic models of crosslinked PVA. It combines a dynamic crosslinking approach (the cross-linking takes place while the MD calculation is executed) followed by a high-temperature annealing procedure. The crosslinking procedure allows to control both crosslinking density and the amount of free crosslinking sites. This procedure results in well relaxed chemical networks with different crosslinking densities. They proposed a model that also includes some network defects, such as dangling tails and loops which have been experimentally observed on several polymer networks. Simulations are then carried out to investigate various thermodynamic and structural properties as a function of the cross-linker length. Glass transition temperatures and mechanical properties of pure and crosslinked PVA are successfully simulated; they are very close to experimental values found in the literature.

A great research can be found in the study of poly-epoxy systems of DGEBA cross-linked with diethyltoluenediamine[11–14] (DETDA) and triethylenetetramine[15–18] (TETA) curing agents, because of their wide use in the fields of modern aeronautics, composite materials and nanotechnologies. In these theoretical studies various properties are calculated which are of importance when studying polymers such as the glass transition temperature, the linear thermal expansion coefficients and the Young's modulus. Studies also focus on the structural properties and the formation of the epoxy networks. Jang *et al.*[19] developed algorithms for the cross-linking of a poly(oxypropelene) diamine (POP) and DGEBA. They used two approaches:

(i) A single-step cross-linking method that does not make use of dynamics but generates a fully cured network by assigning cross-link bonds to nearby pairs of a single snapshot of the system and uses a Monte Carlo methodology with a modified Metropolis criterion to assign initial bond partners. The only use of molecular dynamics was to relax the system after polymerization.

(ii) With the use of a multi-step cross-linking method, authors were able to make continuous polymerization steps in combination with molecular dynamics (an approach we use in the present work). An initial cut-off distance is defined and all reactive pairs within that distance are cross-linked. Short MD simulations (NVE and NPT) are performed and the partial charges are adjusted, the extra hydrogens are removed, and a new pair connection within a cut-off radius is initialized. This runs until no reactive pairs longer exist in the cut-off distance. After the final structure is obtained, an annealing allows the structure to attain its final density.

In a similar multi-step fashion Lin and Khare[20] managed to create and study cross-linked epoxy and epoxy-POSS (polyhedral oligomeric silsesquioexane) nanocomposite. In both studies the Radial Distribution Functions (RDF) were studied as well as extraction of various properties such as the coefficient of volume thermal expansion (CVTE). Finally, Arab and Shokufar[21] studied the effect of various force fields in the calculation of properties of various epoxy polymers that they generated using a cross-linking algorithm. After testing the COMPASS, PCFF, UFF and Dreiding force fields they concluded that COMPASS and PCFF force fields can be reliably used for the simulation of cross-linked polymers to calculate various mechanical properties[22].

4.3 Description of the methodology and cross-linking algorithm

In the present work we will use the atomistic approach along with a home-made code to cross-link the poly-epoxy polymer. The polymer is obtained from the epoxy resin, DGEBA, cross linked in the presence of the EDA curing agent. Both reactants are shown in Figure 1.

We have created our own cross-linking procedure based on the works of Jang *et al.*[19] and Sirk *et al.*[23]. Molecular Dynamics simulations are used in order to achieve thermal motion and ensure the maximum percentage of polymerization. We start from a stoichiometric mixture of 2DGEBA:1EDA.

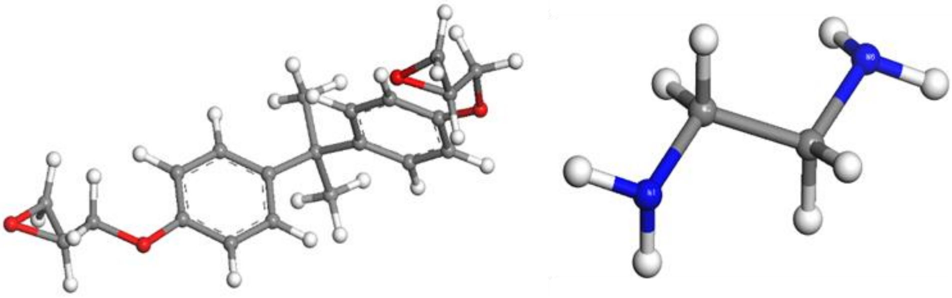

Figure 1. The epoxy resin (DGEBA) molecule (Left) and the amine (EDA) molecule (Right). Red balls correspond to oxygen atoms, blue balls correspond to nitrogen atoms, grey balls correspond to carbon atoms, white balls correspond to hydrogen atoms.

The cross-linking consists in the reaction of the amine groups with the epoxy groups. DGEBA is a bi-functional reactant with two epoxide groups, while EDA has four reactive sites on its two primary amine groups. The epoxy-amine reaction is depicted in Figure 2.

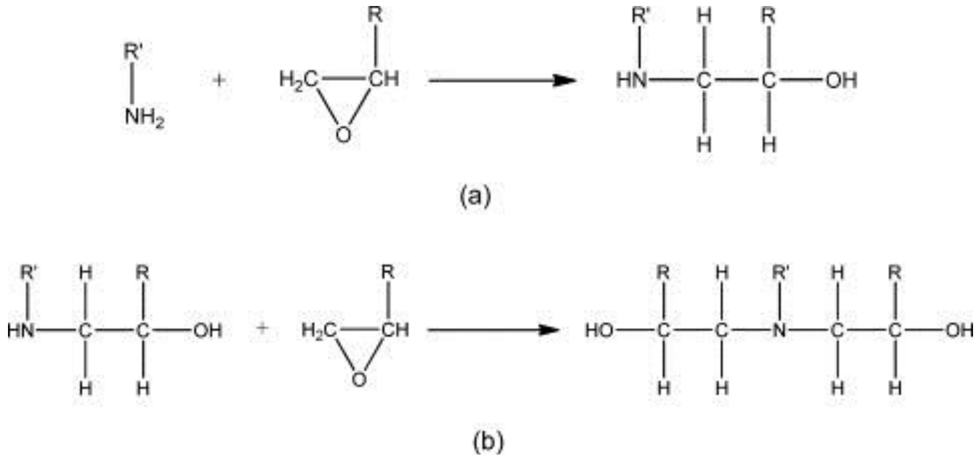

Figure 2. Epoxy-amine reaction (adapted from Ref[24]).

The nitrogen atom reacts with one electrophilic carbon of the epoxide ring that opens. The oxygen atom abstracts a hydrogen atom from the primary amine creating an alcohol group and a secondary amine. This reaction is repeated to grow epoxy chains and to form the crosslinked network. We developed a cross-linking code that mimics this reactional scheme. The global calculations procedure is described step by step on the logigram given in Figure 3.

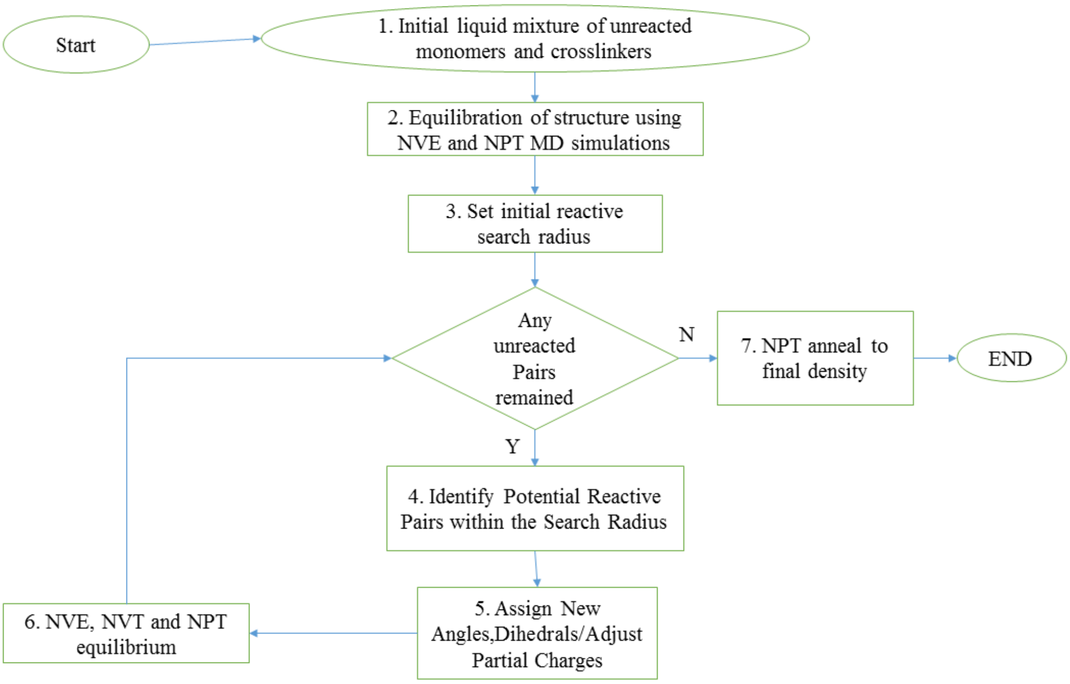

Figure 3. The multi-step cross-linking logigram.

The logigram is composed of numbered blocks of execution. First, the initial structure of the liquid mixture is created (1). This is obtained by the use of an external code[25] that creates a box where the two molecules are in stoichiometric analogy (400 DGEBA:200 EDA) in a given volume. This mixture is equilibrated using MD simulations (2). Then, the cross-linking code initially searches for reactive pairs in a given search radius (3), and, if unreacted pairs remain, they are covalently bonded (4&5). Finally, the structure is equilibrated with MD simulations at each polymerization step. Polymerization/Equilibration cycles continue until the polymerization rate remain constant.

The logigram can be expressed in a number of Steps:

Step 1: Initial simulation boxes construction and minimization of the systems simulation

The first step is to pack the mixed reactants in a box in order to start the equilibration procedure with an initial energy minimization and NVE and NVT MD simulations to relax the systems. To create such boxes, we use the PACKMOL[25] code which is an open source code distributed freely. Detailed instructions on how to produce simulation boxes using the PACKMOL code are given in Annex E. The code produces a random simulation box, containing the required number of molecules. Its density is controlled by regulating the spatial coordinates. In our case we use cubic, simulation boxes and periodic conditions for the simulations. The PACKMOL code can only produce one configuration for a given density and it is based on the concept of packing optimization[25,26]. This is done by minimizing a mathematical function called the merit function[26] which is unique for each set of spatial constraints. Since our simulation boxes are cubic that means for a given density only one box can be created. For simulating different simulation boxes for both the monomers, their stoichiometric mixture and for polymerizing multiple boxes we employ in conjunction with PACKMOL the Materials Studio[27] software suite that has the capability of creating various configurations of cubic simulation boxes that have the same initial density. Its ability to create this variety of cubic simulation boxes comes from the application of Monte Carlo simulations[28] to create random configurations.

For the calculation of the atomic charges using the RESP procedure[29,30], the geometries of the DGEBA and EDA molecules are calculated at the HF/6-31G* level of theory (see Chapter 3) with Gaussian09[31]. RESP[29] atomic charges are calculated for individual molecules, for the dimer model (1 DGEBA-1 EDA) and for the trimer model (2 DGEBA-1 EDA) using the AmberTools code[32]. The Generalized Amber Force Field[33] (GAFF 1.8) is used to describe the intra- and inter-molecular interactions. Any missing force field values were calculated using the AmberTools 16 code[32]. A cutoff distance of 9 Å (with the buffer of 2 Å) is used for the Coulomb and van der Waals interactions. The Particle-Particle-Particle Mesh (PPPM) algorithm[34] is used to handle long range interactions.

In many cases the initial potential energy calculated with GAFF is high due to the presence of atom-atom overlaps. Thus the energy must be minimized by equilibrating interatomic forces and the overlaps must be suppressed. After an energy minimization, the systems are relaxed and are ready to be used as initial configurations for MD. In general, the conditions that have to be satisfied for the minimization of the potential energy led to a highly coupled system of non-linear equations. Solving algorithms are called energy minimization algorithms. In the current study, the HFTN method was employed because of its higher accuracy[35] and its fast convergence to the minimum.

Step 2: Simulation of pure liquids and mixture

This step involves simulations on pure liquids of DGEBA and EDA, and on their stoichiometric mixture. One objective of these MD simulations is to validate the force field on pure monomers for which we know physical and structural properties by experiments and from literature. Another objective is to obtain a liquid that is at an equilibrium before polymerization.

The molecular dynamics calculations and minimizations are carried out using the LAMMPS[36] code. The velocity-Verlet integrator[37] is used to integrate the equations of motion. The time step is 1 fs as we want to observe large motions of atoms. The temperature and pressure are controlled using the Nosé-Hoover thermostat and barostat methods[38,39]. The temperature used in the NVT and NPT ensembles is fixed at 700 K. This high temperature is chosen as an enabler for moving unreacted monomers in the box vigorously and allowing them to diffuse at larger distances, reaching other unreacted monomers and thus connecting a larger number of pairs. The pressure is fixed at 1 atm in NPT in order to avoid any effects of high tensions in the epoxy network that would result in the failure of the simulation and the “destruction” of the simulation box as well as structures that are not structurally consistent with reality.

Steps 3, 4 and 5: Cross-linking algorithm

The code for cross-linking is written in the FORTRAN90 ® programming language as it is a language that has a significant advantage in the execution and resolution of mathematical problems. FORTRAN’s library support for numerical calculations is unmatched by other modern programming languages (e.g. C++) and it is still heavily used in scientific fields. For this reason FORTRAN has some of the best optimizers that exist today in its compilers.

The linking between the N and C atoms and between the O and H atoms is made by updating the identities of the atoms and bonds, the partial charges and the force field parameters in the *lammps#.data* files.

It starts by reading the list of all atoms and finds reactive sites. Then, it searches around a given cutoff radius (in our case 3Å) for any given site to react with. Two bonds are then created: (i) between one H of the $–NH_2$ and the epoxy O atom, (ii) between the N and the epoxy $–\underline{C}(H_2)$ atom. A more detailed procedure on how to fill the input files and execute the code is located in Annex F.

Step 6: NVE, NVT and NPT simulations

After a polymerization step has been completed, we perform the equilibration of the simulation box and the preparation for the next polymerization step. Three successive MD calculations are performed in the NVE, NVT, and NPT ensembles, respectively. NVE simulations relaxes the solid-liquid system by adjusting bond lengths which recover equilibrium values. But the total energy of the system remains constant, thus it is not a physical simulation. The NVT simulation keeps the volume of the box constant while allowing the reacted and unreacted molecules to move fast. The polymerized regions will not accelerate as much as individual molecules, allowing them to reach reactive sites to polymerize further in the next cross-linking step. The NPT simulation simulates physical properties accurately as it is able to describe real conformations. The scripts for the execution of the MD simulations are all given in detail in Annex G.

Steps 3 to 6 are repeated until no more pairs can react. This is confirmed by executing NVT and NPT simulations up to the point where the polymerization percentage is constant in 3 consecutive polymerization steps. The polymerization percentage is calculated by counting the change of identities over the number of initial reactive pairs.

Step 7: Final annealing

When a polymer structure is formed with a constant polymerization rate (above 90%), the final structure is annealed to 700K to reach an equilibrium. The structure is then cooled down to 300K where we can calculate properties of the polymer at ambient temperature.

4.4 Results

4.4.1 MD simulations on pure monomers: validation of the GAFF force field

4.4.1.1 MD calculations on DGEBA

We create a cubic box containing 400 molecules packed at a density of $0.7\ g/cm^3$. In order to predict equilibrium properties of the two reactants in ambient conditions and to have a comparison with their experimental counterpart, a series of NVE and NPT calculations are achieved. The NVE calculations are used to relax the system after the initial minimization while the NPT calculations are used to bring the system to a physically meaningful state. More precisely, 1 ns of NVE molecular dynamics calculations are performed for the equilibration of the system followed by 2 ns of NPT calculations. We use the Nosé-Hoover thermostat and barostat fixed at 300 K and 1 atm, respectively.

An example of the NVE results for one DGEBA monomers box is shown in Figure 4.

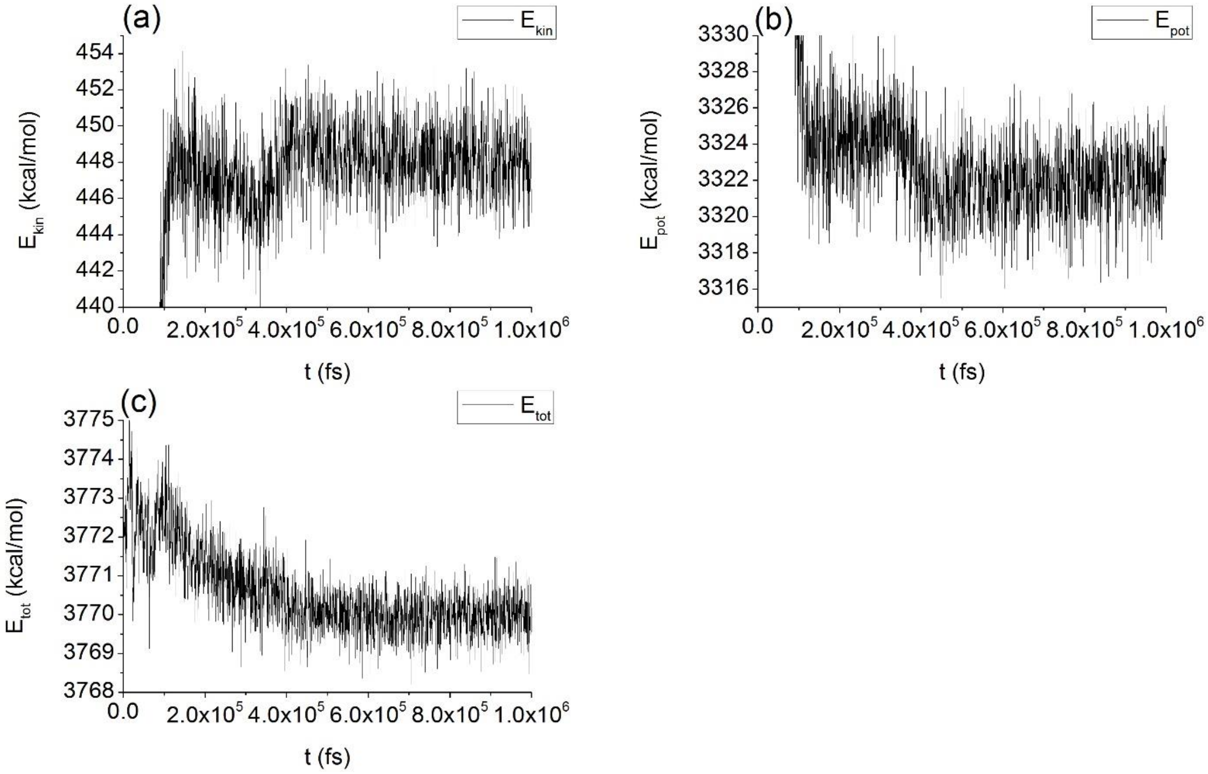

Figure 4. Kinetic (a), Potential (b) and Total (c) Energy evolution during a 1 ns NVE simulation of a 400 DGEBA molecules box at a density of 0.7 g/cm^3.

Figure 4a shows the variation of the kinetic energy of the system as a function of time. We observe that the kinetic energy is well equilibrated after 0.4 ns. The oscillations are limited around a mean value of 449 kcal/mol and the range of variations do not exceed 14 kcal/mol (i.e.

3% of the mean value). Figure 4b shows the variation of the potential energy as function of time. We also observe a plateau after 0.4 ns as with the kinetic energy. Figure 4c shows the variation of the total energy of the system which is the addition of the kinetic and potential energy. A plateau is reached after 0.4 ns that remains until the end of the simulation. We can conclude that the DGEBA liquid is well equilibrated using the GAFF force field and a Molecular Dynamics simulation of 1 ns.

We then perform a 2 ns NPT simulation at 300 K and 1 atm, to reach an equilibrium and further evaluate if the density is close to experimental values. An example of the results of this simulation is presented in Figure 5.

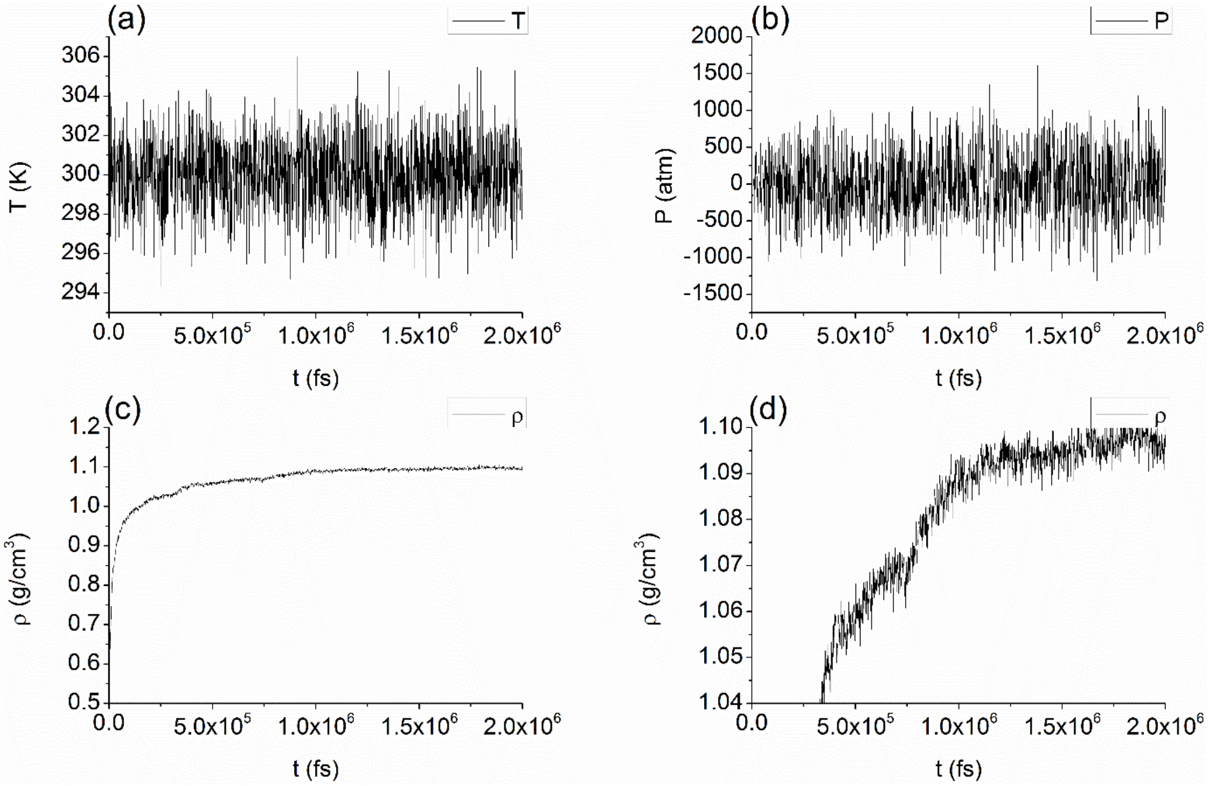

Figure 5. Temperature (a), pressure (b), overall density (c) and custom (zoom) range density (d) evolution during a 2ns NPT simulation of a 400 DGEBA molecules box at 300 K and 1 atm.

Figure 5a presents the variation of the temperature as a function of time. We observe that the temperature is well equilibrated throughout the simulation duration around the value that we have fixed with the thermostat (300 K). The oscillations are in a limited range of ± 6 K. Figure 5b shows the evolution of the pressure as a function of time. Although the mean value regulated by the barostat is 1 atm, we observe large fluctuations of up to 1500 atm. This is typical of MD simulations of condensed phases. Pressure is a macroscopic property of the system and thus should be considered as an average value over long simulations. Pressure fluctuations are large because the pressure-volume isotherm of a liquid has a very steep region. It takes a large pressure change to account for a small volume change and the other way around. The fluctuations in pressure are related to this as shown by Landau and Lifshitz[40]. Figures 5c and 5d give an overview and a closer view of the variation of the DGEBA density as a function of simulation time. We observe a drastic change from 0.5 to 1.05 g/cm^3 from 0 to around 0.3 ns. Then the density increases almost linearly in a monotonous fashion from 0.3 ns to around 1.25 ns where it reaches a plateau. The mean value of the density after the 2 ns simulation is 1.10 g/cm^3 which is in good agreement with the experimental density of the liquid DGEBA at 300K, i.e. 1.16 g/cm^3.[41] That validates the force-field and simulation parameters of DGEBA. A detailed analysis of all the tests performed with various DGEBA boxes exists in Annex H.

4.4.1.2 MD calculations on EDA

The same protocol is followed for the EDA box which contains 500 molecules at an initial density of 0.7 g/cm^3. The NVE results are presented in Figure 6.

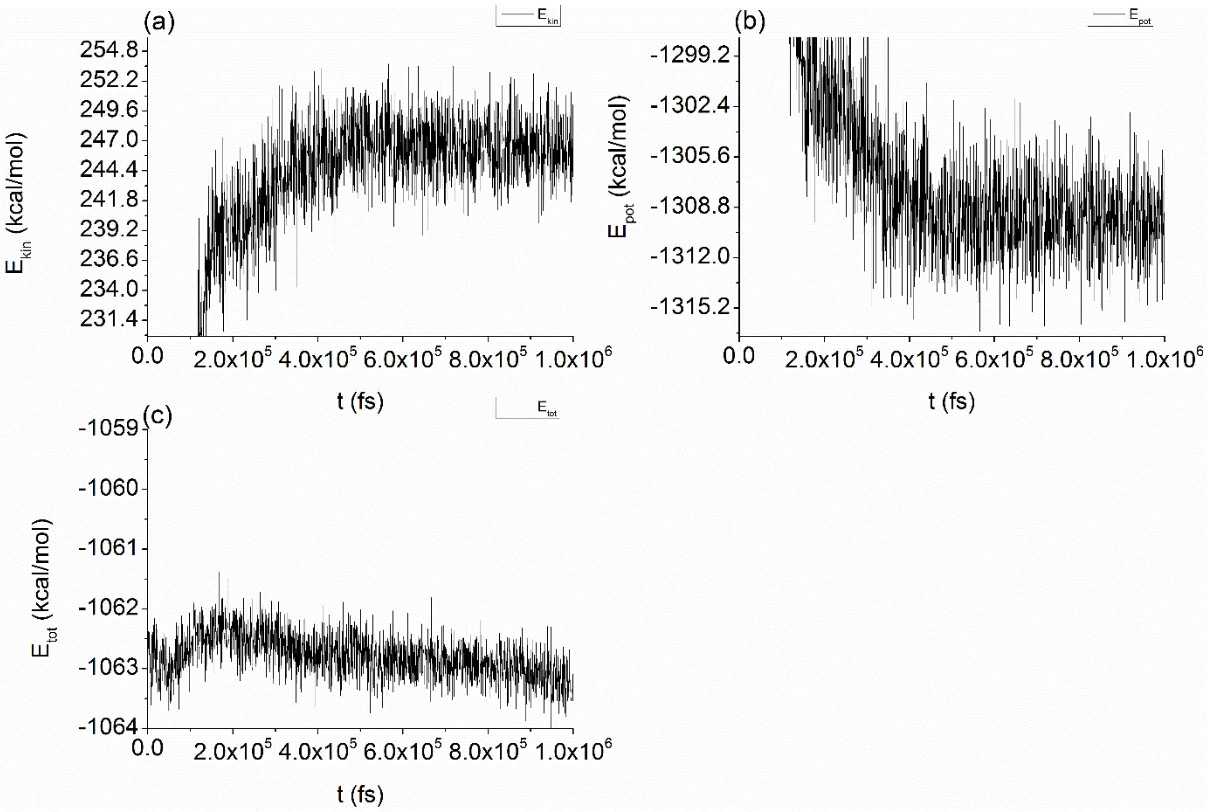

Figure 6. Kinetic (a), Potential (b) and Total (c) Energy evolution during a 1 ns NVE simulation of a 400 DGEBA molecules box at a density of 0.7 g/cm^3.

Figure 6a shows the variation of the kinetic energy of the system as a function of time. We observe that, after 0.4 ns, the kinetic energy is equilibrated at about 247 kcal/mol, and that the variations do not exceed 9 kcal/mol. The variation of the potential energy with time is presented in Figure 6b. We observe a slight decrease up to 0.42 ns where a plateau is reached (-1311 kcal/mol). Figure 6c shows the variation of the total energy of the system which is the addition of the kinetic and potential energy. We assume that the equilibration is reached after 0.4 ns until the end of the simulation.

A NPT simulation of a total duration of 2 ns is performed at 300 K and 1 atm to simulate the ambient conditions that are useful to derive the physical properties of the pure EDA. The results are presented in Figure 7.

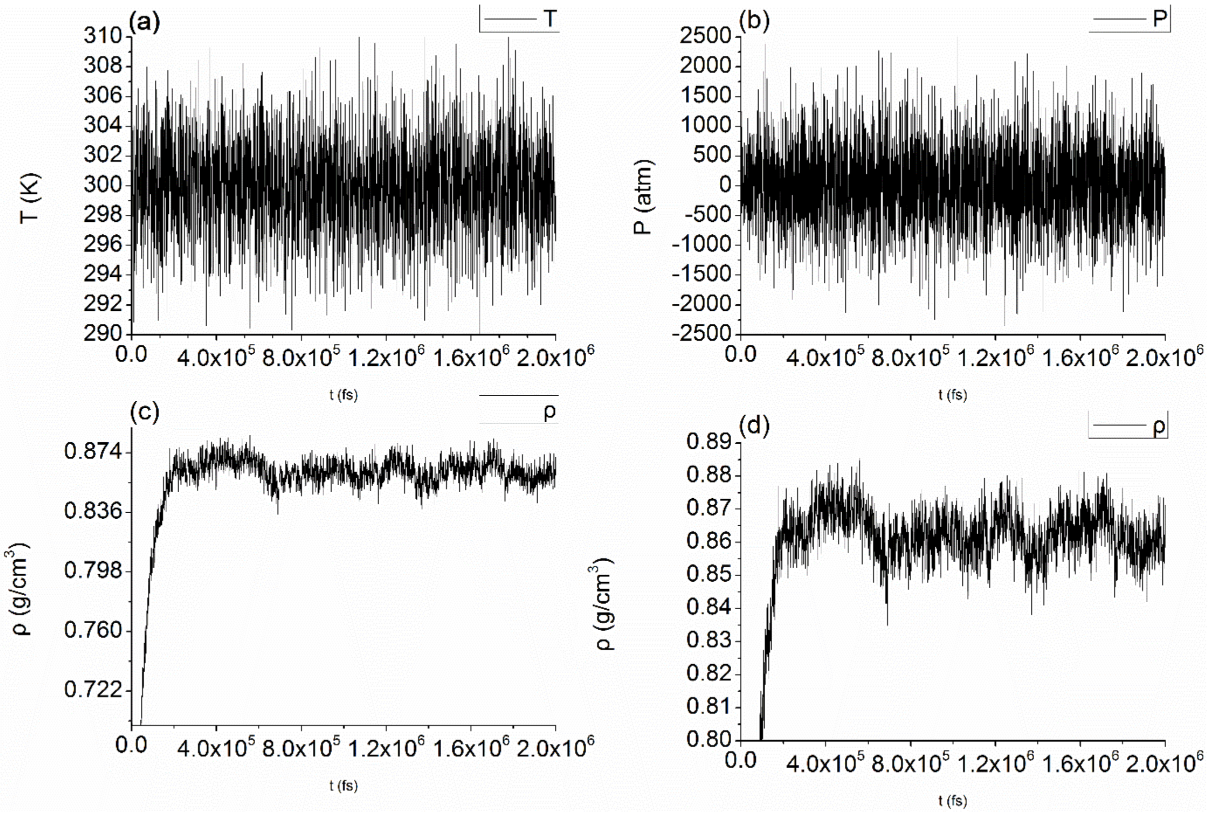

Figure 7. Temperature (a), pressure (b), overall density (c) and custom (zoom) range density (d) evolution during a 2ns NPT simulation of a 500 EDA molecules box at 300 K and 1 atm.

Figure 7a presents the variation of the temperature as a function of time. We observe that the temperature is well equilibrated around the value that we have fixed with the thermostat, which is 300 K. Oscillations are in the range ± 10 K. Figure 7b shows the fluctuation of pressure as a function on time. Although the value fixed in the barostat is 1 atm, we observe fluctuations up to 2500 atm. As mentioned above, this is not a major concern since the mean value equals 1 atm. Figure 7c gives an overview of the variation of the density as a function of time and we can observe a drastic increase from the starting density of 0.70 g/cm^3 at t=0 to 0.86 g/cm^3 at t=0.125 ns, where it reaches a plateau. The mean density value after equilibration of the EDA liquid is approximately 0.87 g/cm^3 which is in a fairly good accordance with the experimental value of 0.90 g/cm^3 at 300K.[42] The series of tests performed on various pure liquid EDA boxes is shown in detail in Annex I.

In conclusion, the series of tests on both reactants indicate that the parameters chosen and the force field used are accurate in reproducing experimental data and thus validate our choices.

4.4.2. MD calculations on the 2DGEBA:1EDA liquid mixture

We have shown that the pure monomers are both well equilibrated and that we are able to reproduce their experimental density. We now move to the next step that is to create an initial mixture in stoichiometric concentration (2DGEBA:1 EDA). An initial mixture of a total of 600 molecules (400 DGEBA + 200 EDA) is selected. This number of molecules is a good compromise between saving computational time and having a large-enough number of molecules relevant to simulate polymer properties accurately.

Figures 8 and 9 show an example of the results of NVE and NPT calculations that are obtained using 5 ns of NVE calculations and 10 ns of NPT calculations fixed at 300 K and 1 atm. These much longer calculations are achieved in order to double check that the initial mixture is well equilibrated before cross-linking.

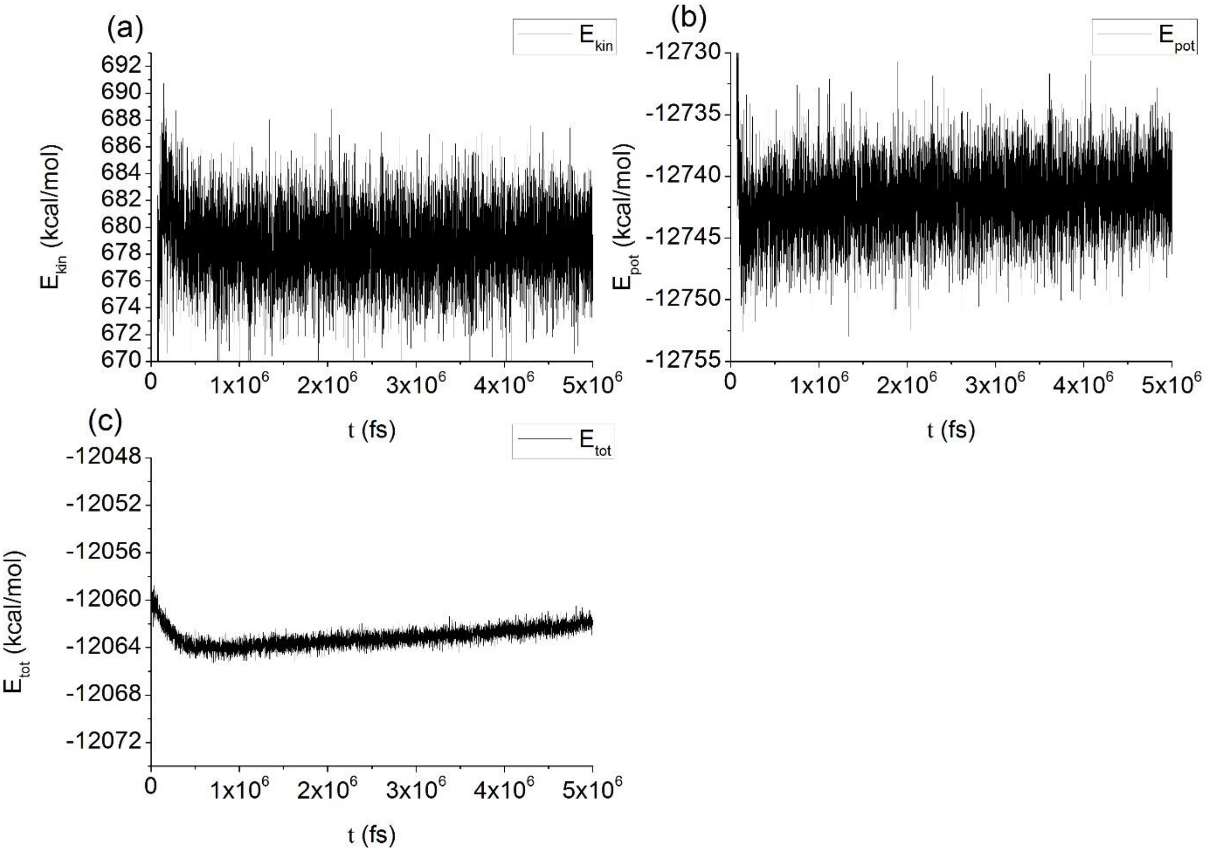

Figure 8. Kinetic (a), Potential (b) and Total (c) Energy evolution during a 1 ns NVE simulation of a 400 DGEBA and 200 EDA molecules box at a density of 0.7 g/cm^3.

Figure 8a shows the variation of the kinetic energy of the system as a function of time. We observe that the kinetic energy is well equilibrated after 0.5 ns and that the fluctuations are limited to 14 kcal/mol. Figure 8b plots the variation of the potential energy as function of time. We observe that a plateau is rapidly reached. Figure 8c shows the variation of the total energy of the system which is the addition of the kinetic and potential energy. The energy stabilizes after 0.5 ns and until the end of the simulation.

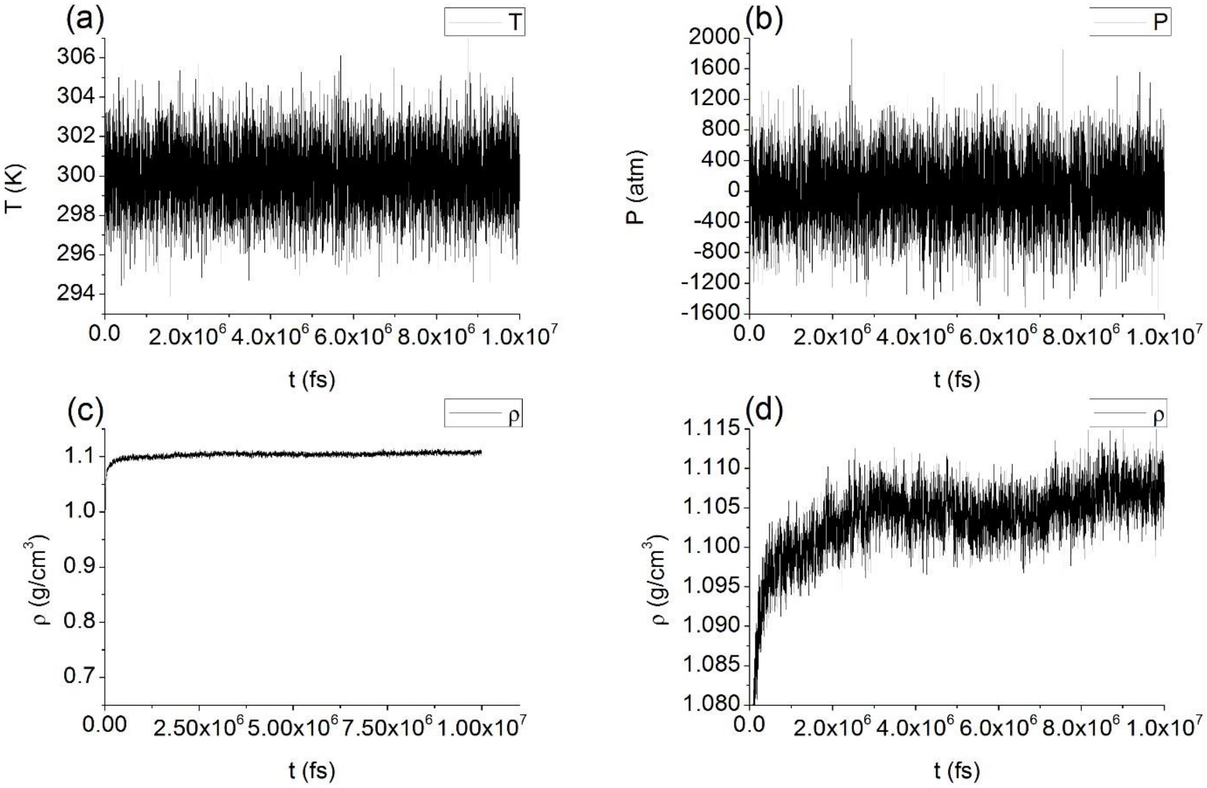

Figure 9. Temperature (a), pressure (b), overall density (c) and custom (zoom) range density (d) evolution during a 10 ns NPT simulation of a 400 DGEBA and 200 EDA molecules box at 300 K and 1 atm.

Figure 9a presents the variation of the temperature as a function of time. We can observe that the temperature is stable around the value that we fixed in the thermostat. The temperature is then 300 ± 6 K. Figure 9b shows the fluctuation of pressure as a function on time. The value regulated by the barostat is 1 atm. We observe fluctuations of up to 2000 atm but the mean value is correct. Figures 9c and 9d give the overview and focused view of the variation of density as a function of time. We observe a drastic change from 0.5 to 1.08 g/cm^3 from 0 to around 0.1 ns. Then the density increases almost linearly in a monotonous fashion from 0.1 ns to around 1.75 ns where it reaches a plateau. The mean density on the plateau is 1.11 g/cm^3.

We have also simulated the mixture at 700K and 900K in the NPT ensemble, for two reasons: (i) to allow a more vigorous movement of molecules, thus increasing the chance of distant molecules to be crosslinked and (ii) to test higher temperatures needed in the protocol for the calculation of the T_g. Results are presented in Annex J.

The Radial Distribution Function (RDF) describes how atoms in a simulation box are packed radially around each other. More generally, the RDF depends on the state of matter. We calculated the inter- and intra- atomic distances RDF to get first conclusions about the distributions of the bond lengths and the homogeneity of the box. The RDFs for the two reactants and their stoichiometric mixture are given in Figure 10.

For the two pure reactants (DGEBA and EDA) and the stoichiometric mixture the RDFs are calculated after the NPT equilibration before moving to the first polymerization step. We do it to make sure that the mixture is a homogeneous liquid.

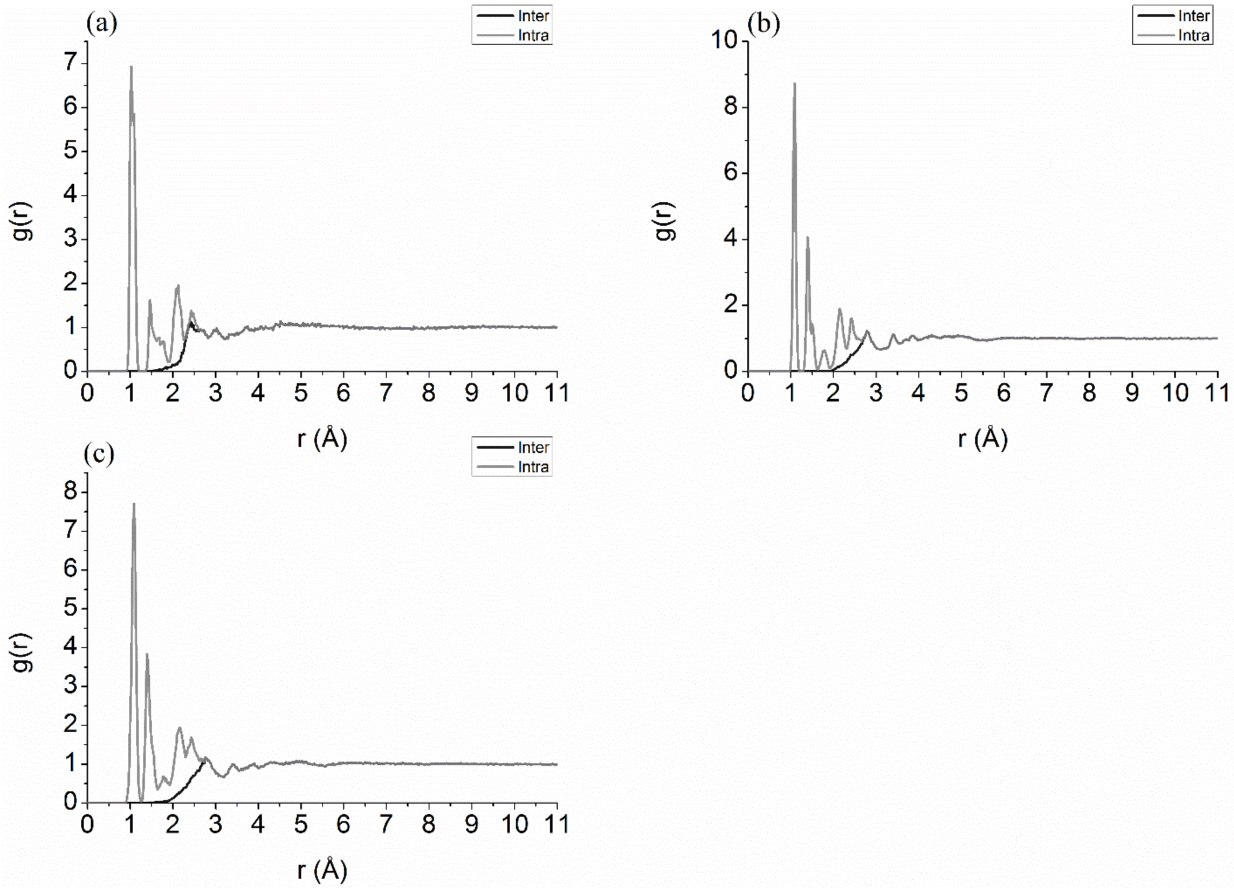

Figure 10. Radial Distribution functions for the inter- and intra- molecular distances for (a) the EDA molecule, (b) the DGEBA molecule and (c) the stoichiometric mixture.

As shown in Figure 10 we calculated the RDFs with two different conditions: (i) by taking into account the intramolecular distances (up to two intermediate bonds) and (ii) by taking into account only the intermolecular distances. The reason behind these two different calculations is to derive conclusions on the potential overlapping of atoms and to distinguish bond lengths.

In all the simulation boxes, the intermolecular RDFs show that there is a minimum distance of 2Å between any set of atoms, which excludes any possible overlaps. The peaks in the intramolecular RDFs do not indicate too large bond lengths. The peaks of both DGEBA and EDA exist in the RDF of the mixture and the N-H (1.01 Å), C-H (1.09 Å), C_{ph}---C_{ph} (1.39 Å), C-O (1.43 Å) and C-C (1.54 Å) bonds are identified. The peaks identified after the bond length limit (1.54 Å for the C-C bond) are distances between second neighbor atoms. After verifying the structure of the simulation boxes we move on to the polymerization of the stoichiometric mixture (2DGEBA:1EDA) boxes.

4.4.3 Polymerization of the 2DGEBA:1EDA system

We create five independent boxes starting from a 600 molecules mixture in stoichiometric composition. These five boxes will help us test our cross-linking code and its reproducibility in creating highly cross-linked configurations. All boxes are equilibrated as described above (NVE and NPT simulations).

In the polymerization code, our initial choice for the cut-off (maximal distance between two reactive atoms) is 3Å. This relatively short distance ensures that after a polymerization step is finished, the resulting structure is easy to re-equilibrate using NVE, NVT and NPT calculations (Step 6).

The conversion rates of the 5 boxes are shown in Figure 11 versus the number of simulation steps.

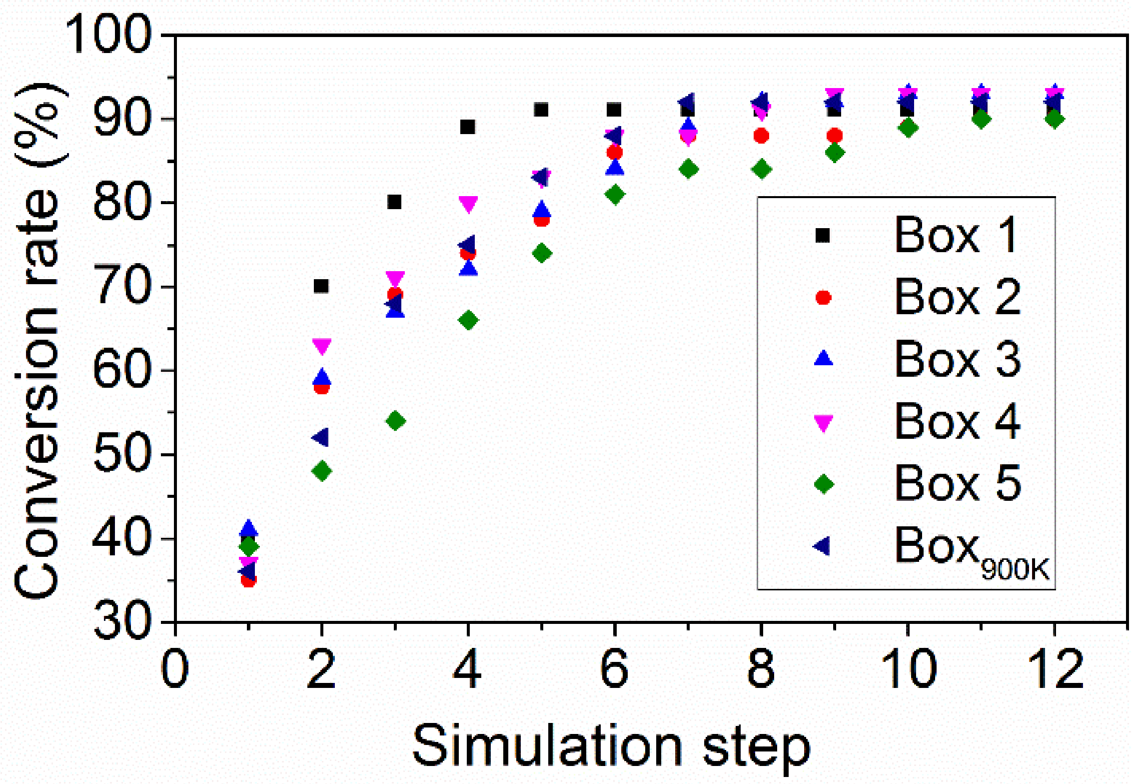

Figure 11. Monitoring of the conversion rate during the multi-step cross-linking process, for 5 different boxes equilibrated at 700K, and 1 box equilibrated at 900K.

We observe that final conversion rates are all above 90% after 11 steps. In the most promising cases we achieve a conversion rate of 93%. Calculations have been attempted up to 12 steps without further polymerization. The mobility of the remaining molecules or the steric availability of the remaining reactive sites is too low at these conversion rates. We also tried to maximize the conversion rate with an additional box equilibrated in NVT and NPT at 900 K without more success (conversion rate = 92%). This tends to show that the 93% limit will be difficult to surpass with our simulation parameters.

In Figure 12 we present the analysis of the distribution of bond lengths after 11 polymerization steps with the NPT and NVT molecular dynamics fixed at 700K. It helps identifying bonds and make sure that these lengths are in agreement with chemical bond length. We identify 3 distinct distributions, centered on 1.10 Å, 1.40 Å, and 1.54 Å. In all this distribution, the bond lengths that belong in this distributions correspond to O-H (0.96 Å), N-H (1.01 Å), C-H (1.09 Å), C_{ph}---C_{ph} (1.39 Å), C-O (1.43 Å) and C-C (1.54 Å) bonds.

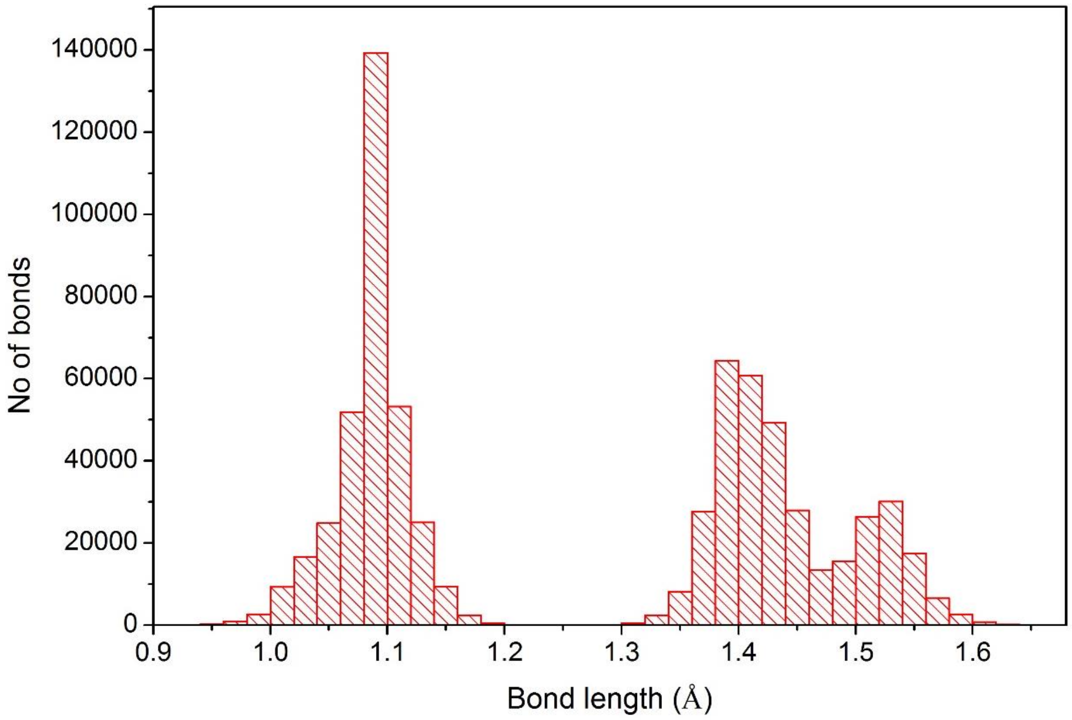

Figure 12. Bond lengths distribution after 2 ns of NPT simulation fixed at 700 K and 1 atm of a polymerized box.

The bond length distribution analysis is also performed as a checking protocol at all polymerization steps (not shown). It never shows bonds over 3 Å throughout the polymerization procedure, validating the operability of the cross-linking cutoff. The intramolecular and intermolecular RDFs calculated for Box#1 is shown in Figure 13.

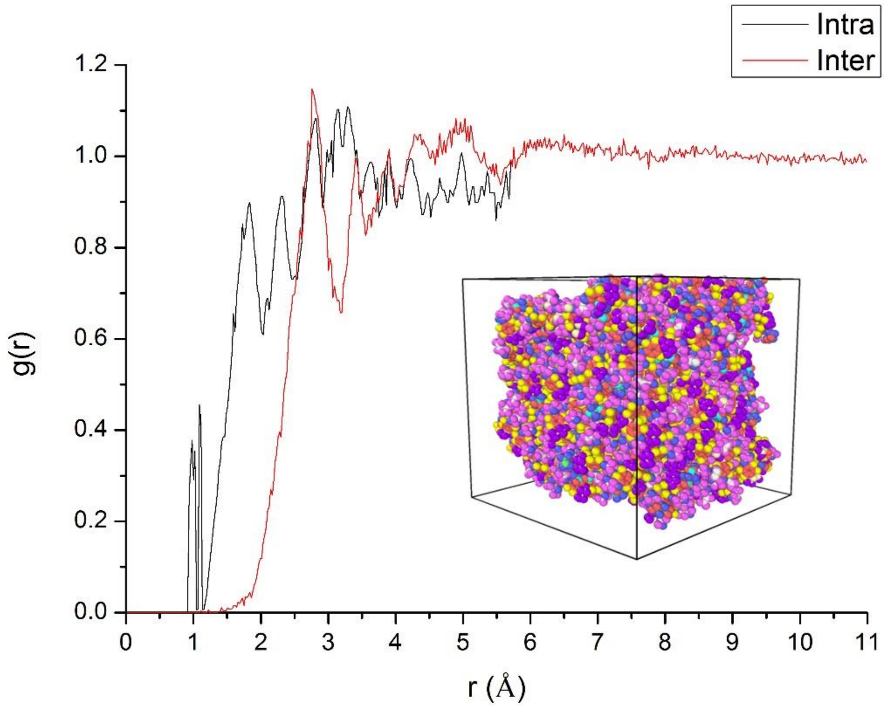

Figure 13. Inter- and intramolecular Radial Distribution Function calculated for the fully polymerized simulation box

The intramolecular RDF shows a significant peak around 1Å corresponding to the O-H bonds (length = 0.9Å). We also conclude that there is no significant overlapping as there is no contribution to the intermolecular RDF before the 2Å point. We proceed with the calculation of the glass transition temperature.

4.4.4 Glass transition temperature of the model polymer

The glass transition is observed in amorphous materials as it is the case for our poly-epoxy polymer. It is the physical transition from a hard "glassy" state into a viscous or rubbery state with the increase of temperature; and it corresponds to the breaking of intermolecular VdW interactions.

To determine the glass transition temperature with MD simulations, a protocol is followed based on the paper of Sirk *et al.*[23] First, the procedure consists in heating the polymer at 700 K for 2 ns and cooling it at a rate of 25 K/ns down to 25 K. Thus we cover a large spectrum of temperatures. Then we plot the specific volume v (the inverse of the calculated density) as a function of temperature. The result for Box #4 is shown in Figure 14.

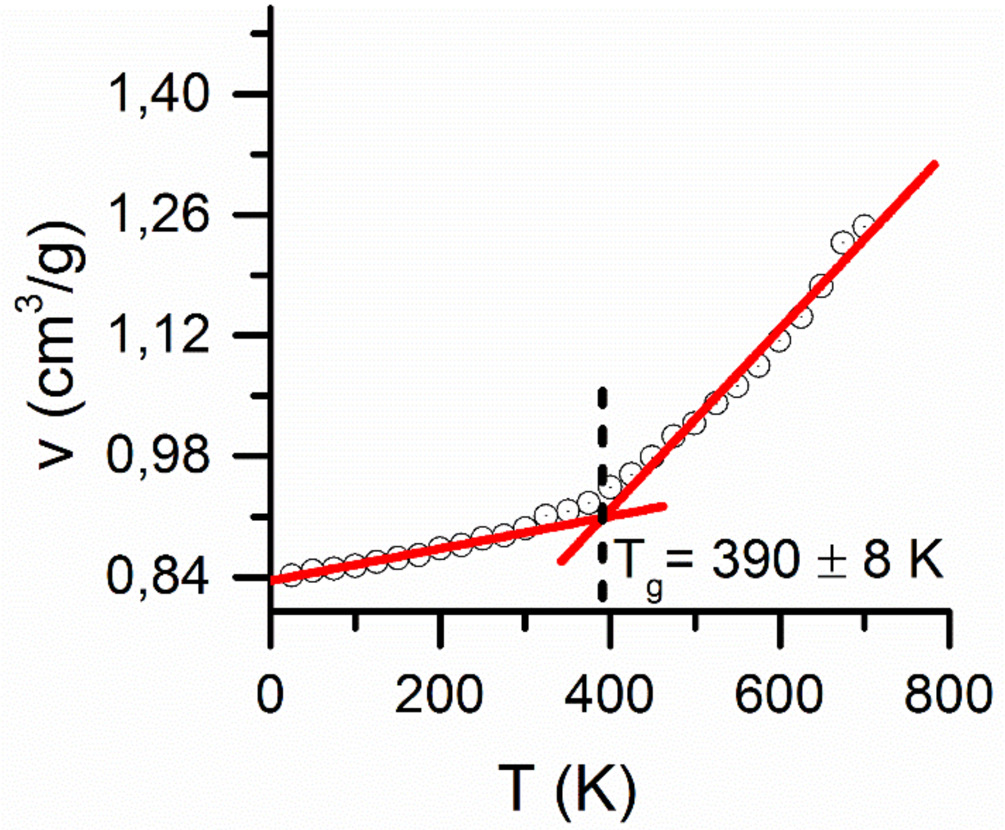

Figure 14. Specific volume as a function of temperature. The intersection of the linear regressions in the glassy and rubbery temperature regions helps estimating the glass transition temperature.

An elegant procedure to analyze the plot in Figure 14 consists in distinguishing the glassy and rubbery temperature domains. Actually, although there is a change in physical properties during the glass transition, it is not considered as a phase transition but rather like a phenomenon that evolves through an undefined range of temperatures. Temperature regions must then be identified to fit the linear regimes properly and to estimate the T_g at the intersection. For that reason we plot the coefficient of thermal volume expansion (CVTE) versus temperature. The coefficient is calculated via Equation 1:

$$CVTE = \left[\left(\frac{1}{v}\right)\left(\frac{\partial v}{\partial T}\right)\right]_P \quad (1)$$

The term, $\left[\left(\frac{\partial v}{\partial T}\right)\right]_P$ is calculated from the v-T diagram as presented in Figure 15 using a finite-difference method in Origin software.

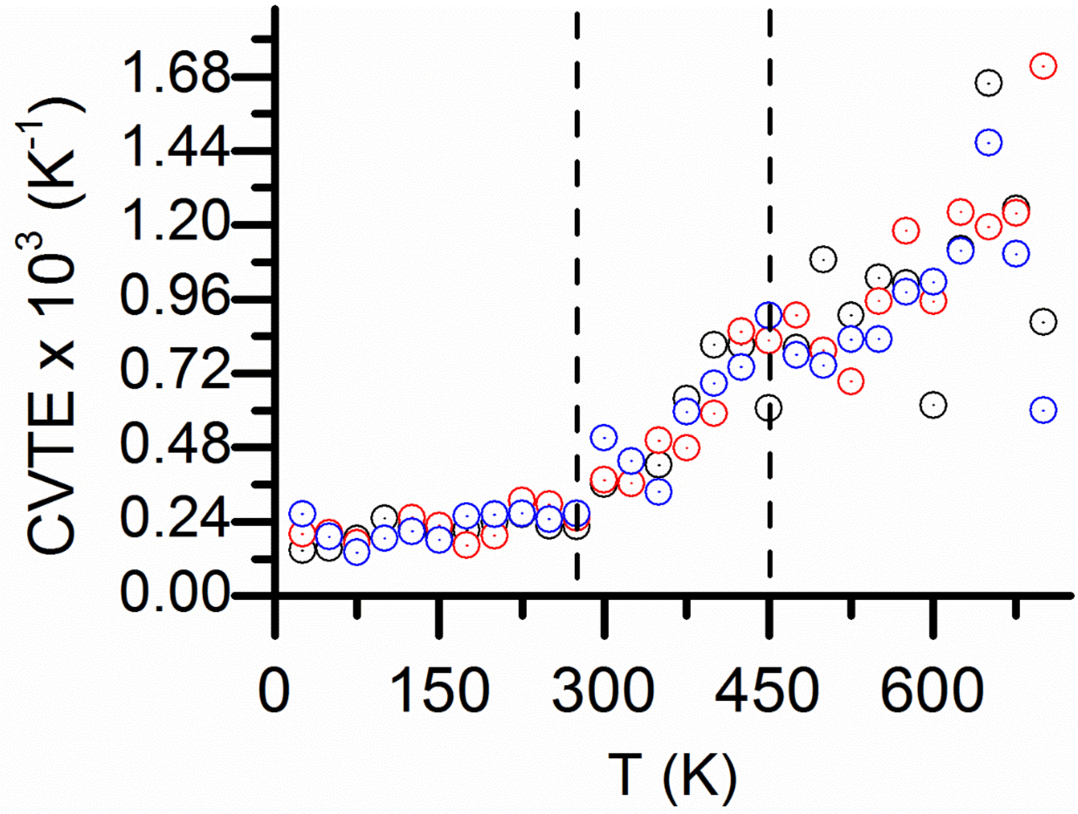

Figure 15. Dependence of the coefficient of thermal volume expansion in relation with temperature for 3 different boxes.

The CVTE is constant at a given state and varies in transition states. In Figure 15, the glassy state region is easily identified up to T = 275 K. At higher temperatures there are no clear regions. Nevertheless we conditionally place a second limit at T = 450 K. By doing so, we assume that all points above 575 K are not valid because they exceed known limits for the CVTE of thermosets in the rubbery region[43], i.e. $4x10^{-4}$-$8x10^{-4}$ K^{-1}. Consequences are that we can fit the plot in Figure 14 with a single linear regression calculated from 25 K to 350 K. Above, there are multiple possibilities for the range of the linear regression. With the regression proposed in Figure 14, we get a result of a computed T_g of 390±8 K which compares very well with the experimental glass transition temperature of 391±1 K measured using DSC. The polymer density is also in very good accordance with bibliography as it was calculated to be 1.115 g/cm^3 at 300 K whereas the value obtained through empirical calculations, is 1.142 g/cm^3.[44] This empirical density is calculated through the relationship $\rho = 350 + 120M(kg \cdot m^{-3})$ where M is the molecular weight of the repeat unit. The value of the M parameter is representative of the poly-epoxy polymer based on the stoichiometry of two molecules of DGEBA and one of amine.

4.5 Conclusion

In this chapter we fulfill the goal of creating a bulk polymer starting from a stoichiometric liquid mixture of the two reactants (DGEBA and EDA). To achieve this task we have developed a home-made cross-linking code that identifies any reactive centers that exist in a distance of less than 3Å and creates covalent bonds. Through a series of molecular dynamics calculations and by the use of parameters from the GAFF 1.8 force field we were able to equilibrate and calculate properties for our pure reactants liquids, the liquid mixtures, as well as for the intermediate semi-polymerized phases and for the final polymer. The cross-linking is based on a multi-step approach based on MD equilibration/cross-linking cycles. The characteristics of the final polymer compare very well with experimental values, in terms of density and T_g. The bulk poly-epoxy model is in good agreement with the experimental counterpart. The validation of the model can be continued through the calculation of mechanical properties such as the Young's modulus. In addition, a model of the surface was not yet extracted at the end of the PhD, something that is of great value for future works.

Bibliography

1. Doherty, D. C., Holmes, B. N., Leung, P. & Ross, R. B. Polymerization molecular dynamics simulations. I. Cross-linked atomistic models for poly(methacrylate) networks. *Comput. Theor. Polym. Sci.* **8,** 169–178 (1998).
2. Deng, M., Tan, V. B. C. & Tay, T. E. Atomistic modeling: interfacial diffusion and adhesion of polycarbonate and silanes. *Polymer* **45,** 6399–6407 (2004).
3. Tzoumanekas, C. & Theodorou, D. N. From atomistic simulations to slip-link models of entangled polymer melts: Hierarchical strategies for the prediction of rheological properties. *Curr. Opin. Solid State Mater. Sci.* **10,** 61–72 (2006).
4. Auhl, R., Everaers, R., Grest, G. S., Kremer, K. & Plimpton, S. J. Equilibration of long chain polymer melts in computer simulations. *J. Chem. Phys.* **119,** 12718–12728 (2003).
5. Pakula, T. & Zhulina, E. B. Computer simulation of polymers in thin layers. II. Structure of polymer melt layers consisting of end-to-wall grafted chains. *J. Chem. Phys.* **95,** 4691–4697 (1991).
6. Vogiatzis, G. G., Voyiatzis, E. & Theodorou, D. N. Monte Carlo simulations of a coarse grained model for an athermal all-polystyrene nanocomposite system. *Eur. Polym. J.* **47,** 699–712 (2011).
7. Theodorou, D. N. & Suter, U. W. Atomistic modeling of mechanical properties of polymeric glasses. *Macromolecules* **19,** 139–154 (1986).
8. Tsige, M. & Stevens, M. J. Effect of Cross-Linker Functionality on the Adhesion of Highly Cross-Linked Polymer Networks: A Molecular Dynamics Study of Epoxies. *Macromolecules* **37,** 630–637 (2004).
9. Bermejo, J. S. & Ugarte, C. M. Chemical Crosslinking of PVA and Prediction of Material Properties by Means of Fully Atomistic MD Simulations. *Macromol. Theory Simul.* **18,** 259–267 (2009).
10. Bermejo, J. S. & Ugarte, C. M. Influence of Cross-Linking Density on the Glass Transition and Structure of Chemically Cross-Linked PVA: A Molecular Dynamics Study. *Macromol. Theory Simul.* **18,** 317–327 (2009).

11. Bandyopadhyay, A., Valavala, P. K., Clancy, T. C., Wise, K. E. & Odegard, G. M. Molecular modeling of crosslinked epoxy polymers: The effect of crosslink density on thermomechanical properties. *Polymer* **52,** 2445–2452 (2011).
12. Li, C. & Strachan, A. Molecular simulations of crosslinking process of thermosetting polymers. *Polymer* **51,** 6058–6070 (2010).
13. Nouri, N. & Ziaei-Rad, S. A Molecular Dynamics Investigation on Mechanical Properties of Cross-Linked Polymer Networks. *Macromolecules* **44,** 5481–5489 (2011).
14. Varshney, V., Patnaik, S. S., Roy, A. K. & Farmer, B. L. A Molecular Dynamics Study of Epoxy-Based Networks: Cross-Linking Procedure and Prediction of Molecular and Material Properties. *Macromolecules* **41,** 6837–6842 (2008).
15. Fan, H. B. & Yuen, M. M. F. Material properties of the cross-linked epoxy resin compound predicted by molecular dynamics simulation. *Polymer* **48,** 2174–2178 (2007).
16. Choi, J., Yu, S., Yang, S. & Cho, M. The glass transition and thermoelastic behavior of epoxy-based nanocomposites: A molecular dynamics study. *Polymer* **52,** 5197–5203 (2011).
17. Yu, S., Yang, S. & Cho, M. Multiscale modeling of cross-linked epoxy nanocomposites to characterize the effect of particle size on thermal conductivity. *J. Appl. Phys.* **110,** 124302 (2011).
18. Zeng, Q. H., Yu, A. B. & Lu, G. Q. Multiscale modeling and simulation of polymer nanocomposites. *Prog. Polym. Sci.* **33,** 191–269 (2008).
19. Jang, C., Sirk, T. W., Andzelm, J. W. & Abrams, C. F. Comparison of Crosslinking Algorithms in Molecular Dynamics Simulation of Thermosetting Polymers. *Macromol. Theory Simul.* **24,** 260–270 (2015).
20. Lin, P.-H. & Khare, R. Molecular Simulation of Cross-Linked Epoxy and Epoxy−POSS Nanocomposite. *Macromolecules* **42,** 4319–4327 (2009).
21. Arab, B. & Shokuhfar, A. Molecular Dynamics Simulation of Cross-Linked Epoxy Polymers: the Effect of Force Field on the Estimation of Properties. *Журнал Нано-Та Електронної Фізики* 01013–1 (2013).
22. Masoumi, S., Arab, B. & Valipour, H. A study of thermo-mechanical properties of the cross-linked epoxy: An atomistic simulation. *Polymer* **70,** 351–360 (2015).
23. Sirk, T. W. *et al.* High strain rate mechanical properties of a cross-linked epoxy across the glass transition. *Polymer* **54,** 7048–7057 (2013).
24. Machavaram, V. R. *et al.* Multi-point monitoring of cross-linking reactions. *J. Appl. Polym. Sci.* **131,** n/a-n/a (2014).
25. Martínez, L., Andrade, R., Birgin, E. G. & Martínez, J. M. PACKMOL: a package for building initial configurations for molecular dynamics simulations. *J. Comput. Chem.* **30,** 2157–2164 (2009).
26. Martínez, J. M. & Martínez, L. Packing optimization for automated generation of complex system's initial configurations for molecular dynamics and docking. *J. Comput. Chem.* **24,** 819–825 (2003).
27. Materials Studio Materials Modeling & Simulation Application | Dassault Systèmes BIOVIA. Available at: http://accelrys.com/products/collaborative-science/biovia-materials-studio/. (Accessed: 3rd October 2017)
28. Akkermans, R. L. C., Spenley, N. A. & Robertson, S. H. Monte Carlo methods in Materials Studio. *Mol. Simul.* **39,** 1153–1164 (2013).
29. Bayly, C. I., Cieplak, P., Cornell, W. & Kollman, P. A. A well-behaved electrostatic potential based method using charge restraints for deriving atomic charges: the RESP model. *J. Phys. Chem.* **97,** 10269–10280 (1993).
30. Cornell, W. D., Cieplak, P., Bayly, C. I. & Kollmann, P. A. Application of RESP charges to calculate conformational energies, hydrogen bond energies, and free energies of solvation. *J. Am. Chem. Soc.* **115,** 9620–9631 (1993).
31. *Gaussian 09, M. J. Frisch, G. W. Trucks, H. B. Schlegel, G. E. Scuseria, M. A. Robb, J. R. Cheeseman, G. Scalmani, V. Barone, G. A. Petersson, H. Nakatsuji, X. Li, M. Caricato, A. Marenich, J. Bloino, B. G. Janesko, R. Gomperts, B. Mennucci, H. P. Hratchian, J. V. Ortiz, A. F. Izmaylov, J. L. Sonnenberg, D. Williams-Young, F. Ding, F. Lipparini, F. Egidi, J. Goings, B. Peng, A. Petrone, T. Henderson, D. Ranasinghe, V. G. Zakrzewski, J. Gao, N. Rega, G. Zheng, W. Liang, M. Hada, M. Ehara, K. Toyota, R. Fukuda, J. Hasegawa, M. Ishida, T. Nakajima, Y.*

Honda, O. Kitao, H. Nakai, T. Vreven, K. Throssell, J. A. Montgomery, Jr., J. E. Peralta, F. Ogliaro, M. Bearpark, J. J. Heyd, E. Brothers, K. N. Kudin, V. N. Staroverov, T. Keith, R. Kobayashi, J. Normand, K. Raghavachari, A. Rendell, J. C. Burant, S. S. Iyengar, J. Tomasi, M. Cossi, J. M. Millam, M. Klene, C. Adamo, R. Cammi, J. W. Ochterski, R. L. Martin, K. Morokuma, O. Farkas, J. B. Foresman, and D. J. Fox, Gaussian, Inc., Wallingford CT, 2016.

32. *D.A. Case, D.S. Cerutti, T.E. Cheatham, III, T.A. Darden, R.E. Duke, T.J. Giese, H. Gohlke, A.W. Goetz, D. Greene, N. Homeyer, S. Izadi, A. Kovalenko, T.S. Lee, S. LeGrand, P. Li, C. Lin, J. Liu, T. Luchko, R. Luo, D. Mermelstein, K.M. Merz, G. Monard, H. Nguyen, I. Omelyan, A. Onufriev, F. Pan, R. Qi, D.R. Roe, A. Roitberg, C. Sagui, C.L. Simmerling, W.M. Botello-Smith, J. Swails, R.C. Walker, J. Wang, R.M. Wolf, X. Wu, L. Xiao, D.M. York and P.A. Kollman (2017), AMBER 2017, University of California, San Francisco.*
33. Wang, J., Wolf, R. M., Caldwell, J. W., Kollman, P. A. & Case, D. A. Development and testing of a general amber force field. *J. Comput. Chem.* **25,** 1157–1174 (2004).
34. Hockney, R. & Eastwood, J. Particle-Particle-Particle-Mesh (P3M) Algorithms. in *Computer simulation using particles* 267–304 (Adam Hilger).
35. Chapelle, O. & Erhan, D. Improved preconditioner for hessian free optimization. in *In NIPS Workshop on Deep Learning and Unsupervised Feature Learning* (2011).
36. Plimpton, S. Fast Parallel Algorithms for Short-Range Molecular Dynamics. *J. Comput. Phys.* **117,** 1–19 (1995).
37. Verlet, L. Computer ‘Experiments’ on Classical Fluids. I. Thermodynamical Properties of Lennard-Jones Molecules. *Phys. Rev.* **159,** 98–103 (1967).
38. Hoover, W. G. & Holian, B. L. Kinetic moments method for the canonical ensemble distribution. *Phys. Lett. A* **211,** 253–257 (1996).
39. Nosé, S. A unified formulation of the constant temperature molecular dynamics methods. *J. Chem. Phys.* **81,** 511–519 (1984).
40. Landau, L. D. & Lifshitz, E. M. *Statistical Physics*. (Pergamon Press).
41. DGEBA Epoxy Resin. Available at: http://polymerdatabase.com/polymers/bisphenol-adiglycidyletherepoxyresin.html. (Accessed: 18th September 2017)
42. Ethylenediamine E26266. *NH2CH2CH2NH2* Available at: http://www.sigmaaldrich.com/catalog/product/sial/e26266. (Accessed: 18th September 2017)
43. Pascault, J. P., Sautereau, H., Verdu, J. & Williams, R. J. J. Glass Transition and Transformation Diagrams. in *Thermosetting Polymers* 121 (Marcel Dekker, Inc.).
44. Garcia, F. G., Soares, B. G., Pita, V. J. R. R., Sánchez, R. & Rieumont, J. Mechanical properties of epoxy networks based on DGEBA and aliphatic amines. *J. Appl. Polym. Sci.* **106,** 2047–2055 (2007).

Conclusions générales et perspectives

Le Chapitre 1 a permis d’introduire les notions générales et les outils théoriques utilisés dans ce travail. Notre choix a porté sur deux techniques de calculs :

- des calculs quantiques statiques (DFT et HF) qui permettent d’obtenir des informations sur les liaisons chimiques et la structure électronique du polymère avec ou sans interaction(s) avec le cuivre.
- des calculs de dynamique moléculaire qui permettent d'équilibrer les liquides purs de réactifs et leur mélange et de calculer diverses propriétés structurales et physiques. En conjonction avec un code de réticulation, ils peuvent aussi conduire à la formation d’un polymère et au calcul de ses propriétés. Un choix important est réalisé dans ce chapitre : le champ de force. Nous avons sélectionné GAFF1.8.

Dans le chapitre 2, nous avons développé l'aspect expérimental de ce travail. Le protocole de synthèse est présenté qui comprend la polymérisation et le post-traitement du polymère dans des conditions inertes (atmosphère d'argon). Les échantillons de polymères sont déposés sur des plaquettes de silicium, et laissés à température ambiante pendant 48 h, avant d’être chauffés à 140 °C pendant 2h pour atteindre un pourcentage de polymérisation élevé. Le pourcentage de polymérisation est surveillée et la température de transition vitreuse est mesurée et comparée à la bibliographie[1]. La rugosité de surface est contrôlée par AFM (autour de 1 nm). Elle est suffisamment faible pour observer la croissance des films de Cu sans interférence[2]. La surface est également caractérisée par XPS et 3 contributions peuvent être placées sous le pic de C1s pour sa décomposition. Les échantillons de polymère sont ensuite métallisés sous ultravide (UHV, $1\text{x}10^{-9}$ mbar) à la température ambiante à l'aide d'un évaporateur de métaux. On forme alors des couches minces de Cu d’épaisseur 5-6 nm. Le dépôt provoque la disparition de l'épaulement C-O (l’une des 3 contributions du pic C1s), nous donnant ainsi une première idée du mécanisme d'adsorption des atomes de Cu.

Dans le Chapitre 3, nous avons montré que les interprétations des résultats XPS du chapitre précédent peuvent être largement améliorées en utilisant les données de sortie de calculs quantiques. Nous avons démontré comment des calculs HF-ΔSCF permettent de simuler le spectre du C1s grâce aux calculs des décalages chimiques[3] (ΔBE) et des intensités relatives des différentes composantes du pic. Cependant, les calculs de type HF ont été réalisés par le Pr. P.S. Bagus, à l'université du North Texas[4], en collaboration. Afin d'internaliser la démarche, nous avons décidé de reproduire ces résultats dans le cadre de la théorie DFT (maitrisée en interne). Le code deMon2k nous a permis d'utiliser la théorie uGTS[5–8] et nous avons simulé de nouveau les spectres XPS avec succès. Les spectres obtenus à partir des deux modes de calculs (HF et uGTS) révèlent 8 contributions, en lieu et place des 3 contributions déterminées expérimentalement. Le travail a été poursuivi avec l'adsorption d'un atome de cuivre dans différentes positions sur le dimère modèle. Au total, 9 sites d'adsorption ont été testés et les géométries optimisées. Les meilleurs résultats sont obtenus lorsque l'atome de Cu est chimisorbé en pont sur un atome d'oxygène et un atome de carbone du phényl adjacent. La simulation du spectre XPS C1s à partir de cette configuration est en bon accord avec l'expérience. La contribution d'origine C-OH qui se trouvait dans l'épaulement aux hautes énergies de liaison sur le spectre de la surface nue, est maintenant remplacée par une contribution C-O-Cu, décalée vers les basses énergies de liaison. L'épaulement est donc très fortement atténué, en adéquation avec les observations expérimentales avant et après dépôt du film nanométrique de Cu.

Le chapitre 4 décrit nos efforts pour extraire les propriétés structurales et physiques des liquides purs de réactifs et de leur mélange, et du polymère final. Le mélange (DGEBA, EDA) est utilisé pour simuler la réticulation. Un algorithme de réticulation maison[9] est appelé en alternance avec la dynamique moléculaire, de la façon suivante : le mélange est d'abord équilibré à 700 K et 1 atm, ce qui assure une agitation vigoureuse des molécules. Puis chaque étape de réticulation est réalisée en statique et consiste à lier les atomes réactifs qui se trouvent à 3Å ou moins l'une de l'autre. A l'issue de ces cycles d'équilibration/réticulation, le pourcentage de polymérisation maximal se stabilise à 93%. Les structures sont validées par le calcul des distributions de distances interatomiques, et par la comparaison entre les densités calculée et expérimentale. Enfin, une méthodologie proposée par Sirk *et al.*[11] est employée pour le calcul de la température de transition vitreuse, T_g. La T_g calculée (390±8 K) est très proche de la T_g expérimentale (391±1 K). Par conséquent, même si ce premier modèle volumique pour le poly-epoxy doit encore être affiné, ces travaux vont permettre l'extraction d'un modèle de surface (slab) pour procéder à des calculs périodiques DFT et à des adsorptions sur une surface poly-époxy « bidimensionnelle ».

Nous avons donc réussi à créer, à la fois expérimentalement et numériquement, une surface poly-époxy adaptée à la métallisation. Nous avons pu étudier le mécanisme d'adsorption de Cu en utilisant des spectres XPS expérimentaux et calculés. Ce n'était qu'une première étape qui permettra d'ouvrir la voie pour des travaux futurs:

- ✓ Le dépôt d'une grande variété de métaux (Al, Ag, Au, Ni, Co, Cr, etc.), dont la réactivité vis-à-vis du polymère diffère, le calcul des spectres XPS et la comparaison avec leurs homologues expérimentaux ;
- ✓ L'obtention des fonctions de distribution (RDF) expérimentalement, par analyse des diagrammes de diffraction des rayons X (DRX) en travaillant sur le facteur de structure totale normalisé S(Q) qui correspond à l'intensité mesurée, corrigée du bruit, de la diffusion Compton, de la diffusion multiple, ainsi que de l'absorption et divers autres facteurs), pour comparer avec les RDF calculées ;
- ✓ La décomposition des spectres O1s et N1s à l'aide de nouveaux calculs (DFT, uGTS) et la comparaison avec la contrepartie expérimentale ;
- ✓ L'extraction d'un échantillon de surface (*slab*) du modèle volumique pour des études DFT périodique et l'adsorption de différents atomes métalliques.

Bibliographie

1. Pascault, J. P., Sautereau, H., Verdu, J. & Williams, R. J. . *Thermosetting Polymers*. (CRC Press, 2002).
2. Duguet, T. *et al.* Toward a computational and experimental model of a poly-epoxy surface. *Appl. Surf. Sci.* **324,** 605–611 (2015).
3. Gavrielides, A., Duguet, T., Esvan, J., Lacaze-Dufaure, C. & Bagus, P. S. A poly-epoxy surface explored by Hartree-Fock ΔSCF simulations of C1s XPS spectra. *J. Chem. Phys.* **145,** 074703 (2016).
4. Bagus, P. S., Liu, B., McLean, A. D. & Yoshimine, M. *CLIPS is a program system to compute ab initio SCF and correlated wavefunctions for polyatomic systems. It has been developed based on the publicly available programs in the ALCHEMY package from the IBM San Jose Research Laboratory*.
5. Endo, K., Kaneda, Y., Okada, H., Chong, D. P. & Duffy, P. Analysis of X-ray Photoelectron Spectra of Eight Polymers by deMon Density-Functional Calculations Using the Model Oligomers. *J. Phys. Chem.* **100,** 19455–19460 (1996).
6. Otsuka, T., Endo, K., Suhara, M. & Chong, D. P. Theoretical X-ray photoelectron spectra of polymers by deMon DFT calculations using the model dimers. *J. Mol. Struct.* **522,** 47–60 (2000).
7. Motozaki, W., Otsuka, T., Endo, K. & Chong, D. P. Electron Binding Energies of Si 2p and S 2p for Si- and S-containing Substances by DFT Calculations Using the Model Molecules. *Polym. J.* **36,** 600–606 (2004).
8. Takaoka, K. *et al.* Analysis of X-ray photoelectron spectra of electrochemically prepared polyaniline by DFT calculations using model molecules. *J. Mol. Struct.* **608,** 175–182 (2002).
9. Jang, C., Sirk, T. W., Andzelm, J. W. & Abrams, C. F. Comparison of Crosslinking Algorithms in Molecular Dynamics Simulation of Thermosetting Polymers. *Macromol. Theory Simul.* **24,** 260–270 (2015).

10. Garcia, F. G., Soares, B. G., Pita, V. J. R. R., Sánchez, R. & Rieumont, J. Mechanical properties of epoxy networks based on DGEBA and aliphatic amines. *J. Appl. Polym. Sci.* **106,** 2047–2055 (2007).
11. Sirk, T. W. *et al.* High strain rate mechanical properties of a cross-linked epoxy across the glass transition. *Polymer* **54,** 7048–7057 (2013).

Annexes

Annex A: Generalized Amber Force Field[1] (GAFF) parameters and atom types

In order to calculate the energetics of the system that is simulated we must choose a suitable set of parameters that will serve as inputs to the equations for the calculation of all the interactions (inter- and intramolecular) we desire to take into account. For our molecules the following parameters were chosen for input in the .data LAMMPS[2] files.

For the EDA molecule we use 4 atom types to describe the molecule (which will be explained below), 4 bond types, 6 angle types and 2 dihedral types (generic types). The parameters are inputted in the beginning of the .data file as such:

```
Masses
  1     14.01 # n3
  2     12.01 # c3
  3     1.008 # hn
  4     1.008 # h1
 Pair Coeffs # lj/charmm/coul/long
  1     0.1700 3.2498 # n3
  2     0.1094 3.3996 # c3
  3     0.0157 1.0690 # hn
  4     0.0157 2.6494 # h1
Bond Coeffs # harmonic
  1      325.9   1.4647   # n3-c3
  2     392.4   1.0190   # n3-hn
  3     300.9   1.5375   # c3-c3
  4     330.6   1.0969   # c3-h1
Angle Coeffs # harmonic
  1     47.42     109.29 # c3-n3-hn
  2     41.40     106.40 # hn-n3-hn
  3     66.02     111.04 # n3-c3-c3
  4     49.53     109.88 # n3-c3-h1
  5     46.39     109.56 # c3-c3-h1
  6     39.24     108.46 # h1-c3-h1
```

```
Dihedral Coeffs # charmm
  1    1.800 3 0 0 # -n3-c3-
  2    1.400 3 0 0 # -c3-c3-
```

For the DGEBA molecule we use 7 atom types to describe the molecule and the parameters for 12 bond types, 23 angle types and 12 generic dihedral types. The parameters are adapted directly from the force field file where available. For the DGEBA molecule some parameters are missing from the original file. To counter this problem the missing parameters can be calculated using the AmberTools[3] software tools that can identify and calculate empirically any parameters missing from a given geometry.

```
Masses
  1  12.01 # ca
  2  16.00 # os
  3  12.01 # c3
  4  12.01 # cx
  5  1.008 # ha
  6  1.008 # h1
  7  1.008 # hc
Pair Coeffs # lj/cut/coul/cut
  1  0.0860  3.3996 # ca
  2  0.1700  3.0000 # os
  3  0.1094  3.3996 # c3
  4  0.0860  3.3996 # cx
  5  0.0150  2.5996 # ha
  6  0.0157  2.4712 # h1
  7  0.0157  2.6494 # hc
Bond Coeffs # harmonic
  1   461.1    1.3984   # ca-ca
  2   376.6    1.3696   # ca-os
  3   345.8    1.0860   # ca-ha
  4   321.0    1.5156   # ca-c3
```

```
  5   308.6    1.4316   # os-c3
  6   330.6    1.0969   # c3-h1
  7   318.3    1.5184   # c3-cx
  8   341.5    1.0890   # cx-h1
  9   332.2    1.5041   # cx-cx
  10   303.6    1.4368   # cx-os
  11   300.9    1.5375   # c3-c3
  12   330.6    1.0969   # c3-hc
Angle Coeffs # harmonic
  1   69.58      119.20  # ca-ca-os
  2   66.62      120.02  # ca-ca-ca
  3   48.18      119.88  # ca-ca-ha
  4   63.53      120.77  # ca-ca-c3
  5   62.52      117.96  # ca-os-c3
  6   50.80      109.78  # os-c3-h1
  7   68.53      107.87  # os-c3-cx
  8   39.24      108.46  # h1-c3-h1
  9   46.89      109.68  # cx-c3-h1
  10   45.76      115.32  # c3-cx-h1
  11   61.62      120.10  # c3-cx-cx
  12   66.07      115.68  # c3-cx-os
  13   45.49      118.70  # cx-cx-h1
  14   49.56      114.93  # os-cx-h1
  15   92.94       59.09  # cx-cx-os
  16   38.31      115.46  # h1-cx-h1
  17   63.15      112.07  # ca-c3-c3
  18   63.56      112.24  # ca-c3-ca
  19   62.86      111.51  # c3-c3-c3
  20   46.34      109.80  # c3-c3-hc
  21   39.40      107.58  # hc-c3-hc
  22   46.34      109.80  # c3-c3-hc
  23   84.30       61.78  # cx-os-cx
```

```
Dihedral Coeffs # fourier

  1   1   14.500     2   180   # X-ca-ca-X
  2   1    1.800     2   180   # X-ca-os-X
  3   1    0.000     2     0   # X-ca-c3-X
  4   1    1.150     3     0   # X-os-c3-X and h1-cx-os-cx
  5   1    1.400     3     0   # X-cx-cx-X
  6   1    1.400     3     0   # X-c3-c3-X and os-c3-cx-cx
  7   2    0.144     3     0       1.175   2       0 # os-c3-cx-os
  8   2    0.000     3     0       0.250   1       0       # os-c3-cx-h1
  9   2    0.383     3     0       0.100   2       180 # c3-cx-os-cx and cx-cx-os-cx
  10  1    0.160     3     0   # h1-c3-cx-cx
  11  2    0.000     3     0       0.250   1       0 # h1-c3-cx-os
  12  1    0.150     3     0   # h1-c3-cx-h1
```

For the stoichiometric mixture one needs to combine the above parameters with the correct numbering and be careful to give the correct identities. Also in the Dihedral Coeffs department we had to convert from the charmm style to fourier style by using the appropriate parameters as to not alter the calculations. The mixture parameters give us a total of 9 atom types, 16 bond types, 29 angle types and 14 dihedral types as such:

```
Masses

  1   12.01 # ca
  2   16.00 # os
  3   12.01 # c3
  4   12.01 # cx
  5   1.008 # ha
  6   1.008 # h1
  7   1.008 # hc
  8   14.01 # n3
  9   12.01 # c3
  10  1.008 # hn
  11  1.008 # h1
```

```
Pair Coeffs # lj/charmm/coul/long
  1   0.0860  3.3996 # ca
  2   0.1700  3.0000 # os
  3   0.1094  3.3996 # c3
  4   0.0860  3.3996 # cx
  5   0.0150  2.5996 # ha
  6   0.0157  2.4712 # h1
  7   0.0157  2.6494 # hc
  8   0.1700  3.2498 # n3
  9   0.1094  3.3996 # c3
  10  0.0157  1.0690 # hn
  11  0.0157  2.4712 # h1
Bond Coeffs # harmonic
  1   461.1    1.3984   # ca-ca
  2   376.6    1.3696   # ca-os
  3   345.8    1.0860   # ca-ha
  4   321.0    1.5156   # ca-c3
  5   308.6    1.4316   # os-c3
  6   330.6    1.0969   # c3-h1
  7   318.3    1.5184   # c3-cx
  8   341.5    1.0890   # cx-h1
  9   332.2    1.5041   # cx-cx
 10   303.6    1.4368   # cx-os
 11   300.9    1.5375   # c3-c3
 12   330.6    1.0969   # c3-hc
 13   325.9    1.4647   # n3-c3
 14   392.4    1.0190   # n3-hn
 15   300.9    1.5375   # c3-c3
 16   330.6    1.0969   # c3-h1
```

```
Angle Coeffs # harmonic

  1   69.58    119.20  # ca-ca-os
  2   66.62    120.02  # ca-ca-ca
  3   48.18    119.88  # ca-ca-ha
  4   63.53    120.77  # ca-ca-c3
  5   62.52    117.96  # ca-os-c3
  6   50.80    109.78  # os-c3-h1
  7   68.53    107.87  # os-c3-cx
  8   39.24    108.46  # h1-c3-h1
  9   46.89    109.68  # cx-c3-h1
 10   45.76    115.32  # c3-cx-h1
 11   61.62    120.10  # c3-cx-cx
 12   66.07    115.68  # c3-cx-os
 13   45.49    118.70  # cx-cx-h1
 14   49.56    114.93  # os-cx-h1
 15   92.94     59.09  # cx-cx-os
 16   38.31    115.46  # h1-cx-h1
 17   63.15    112.07  # ca-c3-c3
 18   63.56    112.24  # ca-c3-ca
 19   62.86    111.51  # c3-c3-c3
 20   46.34    109.80  # c3-c3-hc
 21   39.40    107.58  # hc-c3-hc
 22   46.34    109.80  # c3-c3-hc
 23   84.30     61.78  # cx-os-cx
 24   47.42    109.29  # c3-n3-hn
 25   41.40    106.40  # hn-n3-hn
 26   66.02    111.04  # n3-c3-c3
 27   49.53    109.88  # n3-c3-h1
 28   46.39    109.56  # c3-c3-h1
 29   39.24    108.46  # h1-c3-h1
```

```
Dihedral Coeffs # fourier
  1    1   14.500     2   180   # X-ca-ca-X
  2    1    1.800     2   180   # X-ca-os-X
  3    1    0.000     2     0   # X-ca-c3-X
  4    1    1.150     3     0   # X-os-c3-X and h1-cx-os-cx
  5    1    1.400     3     0   # X-cx-cx-X
  6    1    1.400     3     0   # X-c3-c3-X and os-c3-cx-cx
  7    2    0.144     3     0       1.175   2       0        # os-c3-cx-os
  8    2    0.000     3     0       0.250   1       0        # os-c3-cx-h1
  9    2    0.383     3     0       0.100   2       180 # c3-cx-os-cx and cx-cx-os-cx
  10   1    0.160     3     0   # h1-c3-cx-cx
  11   2    0.000     3     0       0.250   1       0 # h1-c3-cx-os
  12   1    0.150     3     0   # h1-c3-cx-h1
  13   1    1.800     3     0   # -n3-c3-
  14   1    1.400     3     0   # -c3-c3-
```

For simulating the crosslinked box in every cross-linking step and the final annealing we must adjust our coefficients appropriately to include the newly formed bonds which will be automatically updated by our code. This results in 11 atom types, 17 bond types, 30 angle types and 14 dihedral types given below:

```
Masses
  1   12.01 # ca
  2   16.00 # os
  3   12.01 # c3
  4   12.01 # cx
  5   1.008 # ha
  6   1.008 # h1
  7   1.008 # hc
  8   14.01 # n3
  9   12.01 # c3
```

```
  10  1.008 # hn
  11  1.008 # h1
  12  16.00 # oh
  13  1.008 # ho
Pair Coeffs # lj/charmm/coul/long
  1   0.0860  3.3996 # ca
  2   0.1700  3.0000 # os
  3   0.1094  3.3996 # c3
  4   0.0860  3.3996 # cx
  5   0.0150  2.5996 # ha
  6   0.0157  2.4712 # h1
  7   0.0157  2.6494 # hc
  8   0.1700  3.2498 # n3
  9   0.1094  3.3996 # c3
  10  0.0157  1.0690 # hn
  11  0.0157  2.4712 # h1
  12  0.2104  3.0664 # oh
  13  0.0000  0.0000 # ho
Bond Coeffs # harmonic
  1   461.1    1.3984   # ca-ca
  2   376.6    1.3696   # ca-os
  3   345.8    1.0860   # ca-ha
  4   321.0    1.5156   # ca-c3
  5   308.6    1.4316   # os-c3
  6   330.6    1.0969   # c3-h1
  7   318.3    1.5184   # c3-cx
  8   341.5    1.0890   # cx-h1
  9   332.2    1.5041   # cx-cx
 10   303.6    1.4368   # cx-os
```

```
 11   300.9    1.5375   # c3-c3
 12   330.6    1.0969   # c3-hc
 13   325.9    1.4647   # n3-c3
 14   392.4    1.0190   # n3-hn
 15   300.9    1.5375   # c3-c3
 16   330.6    1.0969   # c3-h1
 17   371.4    0.9730   # ho-oh
Angle Coeffs # harmonic
  1   69.58      119.20  # ca-ca-os
  2   66.62      120.02  # ca-ca-ca
  3   48.18      119.88  # ca-ca-ha
  4   63.53      120.77  # ca-ca-c3
  5   62.52      117.96  # ca-os-c3
  6   50.80      109.78  # os-c3-h1
  7   68.53      107.87  # os-c3-cx
  8   39.24      108.46  # h1-c3-h1
  9   46.89      109.68  # cx-c3-h1
 10   45.76      115.32  # c3-cx-h1
 11   61.62      120.10  # c3-cx-cx
 12   66.07      115.68  # c3-cx-os
 13   45.49      118.70  # cx-cx-h1
 14   49.56      114.93  # os-cx-h1
 15   92.94       59.09  # cx-cx-os
 16   38.31      115.46  # h1-cx-h1
 17   63.15      112.07  # ca-c3-c3
 18   63.56      112.24  # ca-c3-ca
 19   62.86      111.51  # c3-c3-c3
 20   46.34      109.80  # c3-c3-hc
 21   39.40      107.58  # hc-c3-hc
```

```
 22   46.34      109.80  # c3-c3-hc
 23   84.30       61.78  # cx-os-cx
 24   47.42      109.29  # c3-n3-hn
 25   41.40      106.40  # hn-n3-hn
 26   66.02      111.04  # n3-c3-c3
 27   49.53      109.88  # n3-c3-h1
 28   46.39      109.56  # c3-c3-h1
 29   39.24      108.46  # h1-c3-h1
 30   47.38      107.26  # c3-oh-ho
Dihedral Coeffs # fourier
  1    1   14.500      2   180   # X-ca-ca-X
  2    1    1.800      2   180   # X-ca-os-X
  3    1    0.000      2     0   # X-ca-c3-X
  4    1    1.150      3     0   # X-os-c3-X and h1-cx-os-cx
  5    1    1.400      3     0   # X-cx-cx-X
  6    1    1.400      3     0   # X-c3-c3-X and os-c3-cx-cx
  7    2    0.144      3     0       1.175   2         0         # os-c3-cx-os
  8    2    0.000      3     0       0.250   1         0         # os-c3-cx-h1
  9    2    0.383      3     0       0.100   2         180 # c3-cx-os-cx and cx-cx-os-cx
  10   1    0.160      3     0   # h1-c3-cx-cx
  11   2    0.000      3     0       0.250   1         0 # h1-c3-cx-os
  12   1    0.150      3     0   # h1-c3-cx-h1
  13   1    1.800      3     0   # -n3-c3-
  14   1    1.400      3     0   # -c3-c3-
```

The atom types given throughout this Annex represent the following atoms:

ca represents an sp^2 aromatic carbon

os represents an sp^3 oxygen in ethers and esters

c3 represents an sp^3 carbon

cx represents an sp^3 carbon in three-membered rings

ha represents a hydrogen on aromatic carbon

h1 represents a hydrogen on aliphatic carbon with 1 electron-withdrawal group

hc represents a hydrogen on aliphatic carbon

n3 represents an sp^3 nitrogen with 3 substitutes

hn represents hydrogen on nitrogen

oh represents sp^3 oxygen in hydroxyl groups

ho represents hydrogen on oxygen

Bibliography

1. Wang, J., Wolf, R. M., Caldwell, J. W., Kollman, P. A. & Case, D. A. Development and testing of a general amber force field. *J. Comput. Chem.* **25,** 1157–1174 (2004).
2. Plimpton, S. Fast Parallel Algorithms for Short-Range Molecular Dynamics. *J. Comput. Phys.* **117,** 1–19 (1995).
3. *D.A. Case, D.S. Cerutti, T.E. Cheatham, III, T.A. Darden, R.E. Duke, T.J. Giese, H. Gohlke, A.W. Goetz, D. Greene, N. Homeyer, S. Izadi, A. Kovalenko, T.S. Lee, S. LeGrand, P. Li, C. Lin, J. Liu, T. Luchko, R. Luo, D. Mermelstein, K.M. Merz, G. Monard, H. Nguyen, I. Omelyan, A. Onufriev, F. Pan, R. Qi, D.R. Roe, A. Roitberg, C. Sagui, C.L. Simmerling, W.M. Botello-Smith, J. Swails, R.C. Walker, J. Wang, R.M. Wolf, X. Wu, L. Xiao, D.M. York and P.A. Kollman (2017), AMBER 2017, University of California, San Francisco.*

Annex B: The velocity Verlet algorithm

Verlet integration[1] is a numerical method that is used for the integration of Newtonian equations of motion. It is commonly used in Molecular Dynamics simulations to calculate the trajectories of the molecules in simulation boxes as they evolve in time. It presents greater stability in comparison with the much simpler Euler method and due to its time-reversibility (the ability to follow the trajectory backwards to the point that it begun) and area preserving (the ability to solve the equations of Newton and represent them on an phase-area preserving map thus being in accordance with Liouville's[2] theorem) properties makes it indispensable for use in our simulations.

In the velocity Verlet algorithm the velocity and position are calculated at the current time step as time evolves. This is not the case for other algorithms such as the Leapfrog algorithm giving an advantage of performing timesteps of various sizes and maintaining stability. The velocity Verlet, as the name suggests utilizes velocity to calculate the first timestep equations presented in the Basic Verlet algorithm:

$$\vec{r}(t+\Delta t) = \vec{r}(t) + \vec{v}(t)\Delta t + \frac{1}{2}\vec{a}(t)\Delta t^2 \ (1)$$

$$\vec{v}(t+\Delta t) = \vec{v}(t) + \frac{\vec{a}(t) + \vec{a}(t+\Delta t)}{2}\Delta t \ (2)$$

The velocity Verlet algorithm does not need to keep track of the velocity at every timestep making it less memory consuming.

The implementation of the algorithm is summed in the following steps:

1. Calculate $\vec{v}\left(t+\frac{1}{2}\Delta t\right) = \vec{v}(t) + \frac{1}{2}\vec{a}(t)\Delta t$
2. Calculate $\vec{r}(t+\Delta t) = \vec{r}(t) + \vec{v}\left(t+\frac{1}{2}\Delta t\right)\Delta t$
3. Derive $\vec{a}(t+\Delta t)$ using $\vec{r}(t+\Delta t)$
4. Calculate $\vec{v}(t+\Delta t) = \vec{v}\left(t+\frac{1}{2}\Delta t\right) + \frac{1}{2}\vec{a}(t+\Delta t)\Delta t$

What needs to be noted is that the acceleration $\vec{a}(t+\Delta t)$ depends ony on the position $\vec{r}(t+\Delta t)$ and not on the velocity.

Bibliography

1. Verlet, L. Computer 'Experiments' on Classical Fluids. I. Thermodynamical Properties of Lennard-Jones Molecules. *Phys. Rev.* **159,** 98–103 (1967).
2. Nelson, E. A proof of Liouville's theorem. *Proc. Am. Math. Soc.* **12,** 995 (1961).

Annex C: Structure comparison of the dimer molecule optimized using different computational conditions

This Annex will provide the optimization results for the optimization of the dimer molecule under different computational conditions (e.g. various exchange-correlation potentials and basis sets) to compare the various structures produced. All of the calculations were executed using the deMon2k code[1]. Table 1 contains the 3 sets of computational parameters that were used for the optimization of the geometry of the dimer molecules and the total energy of the molecule after each optimization.

Table 1. Optimization results for the dimer molecule under various computational conditions.

Structure #	*Basis Set*	*Exchange-Correlation potential*	*SCF tolerance (μHartree)*	*Optimization Tolerance (Å)*	E_{tot} *(Hartree)*
1	DZVP	B88-LYP	$1x10^{-7}$	$1x10^{-4}$	-1305.94
2	TZVP	B88-LYP	$1x10^{-7}$	$1x10^{-4}$	-1306.01
3	TZVP	B88-PW91	$1x10^{-9}$	$1x10^{-4}$	-1306.35

The dimer geometries optimized with the conditions given in Table 1 are shown in Figure 1.

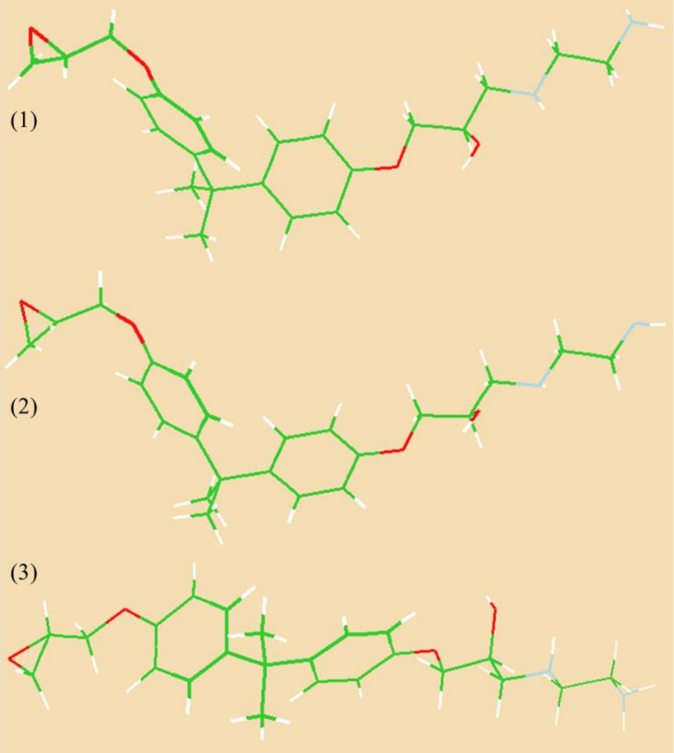

Figure 1. The 3 dimer molecule structures after optimization under different computational parameters (green is used to symbolize C atoms, blue for N atoms, red for O atoms and white for H atoms).

By merely looking at the 3 dimer molecule structures we can see the effect of the change of the computational parameters in the geometry optimization of the dimer molecule. A very good indicator apart from the positions of the hydrogens connected to the nitrogen atoms is the final position of the $–CH_3$ carbons. We further analyze the dimer structures in Table 2 by comparing various bond lengths existing in the dimer molecule.

Table 2. Bond length comparison for the structural analysis of the 3 dimer molecules

Dimer Structure #	*C_{ep}-O_{ep} (Å)*	*C_{ph}-C_{ph} (Å)*	*C-N (Å)*	*N-H (Å)*	*C-H (Å)*	*C-O (Å)*	*C-C (Å)*
1	1.46	1.40	1.47	1.03	1.11	1.45	1.53
2	1.46	1.40	1.48	1.02	1.10	1.45	1.54
3	1.45	1.40	1.48	1.02	1.10	1.44	1.53
Experimental	1.44	1.39	1.47	1.01	1.09	1.43	1.54

We can see that although different geometries and by expansion different atom orientations are produced by changing the computational parameters there is no significant change in the bond lengths. We chose the computational parameters used to optimize the third structure for the XPS initial state calculations by taking into account studies[2,3] on the functional dependence of calculated core energies. It is also worth noting that all the calculated bond lengths are in good accordance with experimental bond lengths in similar molecules[4,5].

Bibliography

1. Kostar, A. M. et al. A.M. Koster, G. Geudtner, P. Calaminici, M.E. Casida, V.D. Dominguez, R. Flores-Moreno, G.U. Gamboa, A. Goursot, T. Heine, A. Ipatov, F. Janetzko, J.M. del Campo, J. U. Reveles, A. Vela, B. Zuniga-Gutierrez, and D.R. Salahub, deMon2k, Version 3.0.6, The deMon developers, Cinvestav, Mexico City (2011). (2014).
2. Takahashi, O. & Pettersson, L. G. M. Functional dependence of core-excitation energies. J. Chem. Phys. **121,** 10339–10345 (2004).
3. Jacobsen, H. & Cavallo, L. Directions for Use of Density Functional Theory: A Short Instruction Manual for Chemists. in Handbook of Computational Chemistry (ed. Leszczynski, J.) 95–133 (Springer Netherlands, 2012). doi:10.1007/978-94-007-0711-5_4
4. Ellis, B. Chemistry and Technology of Epoxy Resins. (Springer-Science+Business Media, 1993).
5. Computational Chemistry Comparison and Benchmark DataBase (CCCBDB). Available at: http://cccbdb.nist.gov/.

Annex D: Comparison between RESP and AM1-BCC methodologies for partial charge calculations of the EDA, DGEBA, dimer and trimer molecules

We compare the two methodologies for the calculations of the charges using the RESP and AM1-BCC protocol as described in chapter 3. Results for the calculated of the EDA molecule using both methodologies are shown in Table 1.

Table 1. EDA net charges (in e) calculated using the RESP and AM1-BCC methodologies.

Atom ID	**RESP**	**AM1-BCC**
N1	-0.9375	-0.9168
C2	0.2930	0.1568
H3	0.3301	0.3493
H4	0.3301	0.3493
C5	0.2811	0.1568
N6	-0.9341	-0.9168
H7	0.3306	0.3493
H8	0.3306	0.3493
H9	-0.0071	0.0307
H10	-0.0070	0.0307
H11	-0.0049	0.0307
H12	-0.0049	0.0307
	0	1.04×10^{-16}

The results for the DGEBA molecule are shown in Table 2.

Table 2. DGEBA net charges (in e) calculated using the RESP and AM1-BCC methodologies

Atom ID	**RESP**	**AM1-BCC**
C1	-0.3833	-0.0861
O1	-0.4339	-0.3244
C2	0.1085	0.1329
C3	0.4647	0.0486
C4	-0.3528	-0.0861
C5	-0.0932	-0.1013
C6	-0.3173	-0.1748
C7	0.4577	0.1116

C8	-0.3866	-0.1748
C9	-0.1300	-0.0955
C10	-0.0606	-0.1013
C11	-0.2248	-0.0955
C12	-0.2469	-0.1748
C13	0.4583	0.1116
C14	-0.3691	-0.1748
C15	-0.1059	-0.0955
O2	-0.4115	-0.3244
C16	0.1038	0.1329
C17	-0.0202	0.0296
O3	-0.3068	-0.4061
C18	-0.1344	0.0549
C19	-0.0078	0.0296
C20	-0.0853	0.0549
O4	-0.3500	-0.4081
H1	0.1084	0.0727
H2	0.0680	0.0727
H3	0.0948	0.0399
H4	0.0724	0.0399
H5	0.0684	0.0399
H6	0.1716	0.1473
H7	0.1823	0.1473
H8	0.1482	0.138
H9	0.1676	0.138
H10	0.1525	0.1473
H11	0.1797	0.1473
H12	0.1466	0.1380
H13	0.0707	0.0727
H14	0.0717	0.0727
H15	0.1527	0.1107
H16	0.1327	0.0800
H17	0.1412	0.07995
H18	0.1508	0.1107
H19	0.1225	0.0800

H20	0.1312	0.0800
C21	-0.1059	-0.0955
H21	0.0820	0.0399
H22	0.0937	0.0399
H23	0.0857	0.0399
H24	0.1382	0.1380
	$-4.0\text{x}10^{-06}$	$2.2\text{x}10^{-16}$

The two methodologies give a total sum of charges close to 0.

Two optimized geometries were found for the model dimer. The hydrogens on the epoxy rings were oriented differently. The results for the partial charges using the two above mentioned methodologies are given in Table 3.

Table 3. Net Charges (in e) calculated using the AM1-BCC and RESP methodologies for a dimer

Atom ID	**Geometry1** **AM1-BCC**	**Geometry1** **RESP**	**Geometry2** **AM1-BCC**	**Geometry2** **RESP**
N1	-0.9158	-1.148009	-0.9158	-1.111729
C1	0.1588	0.400539	0.1588	0.252475
N2	-0.8222	-0.891701	-0.8262	-0.94021
C2	-0.0861	-0.387624	-0.0861	-0.367398
O1	-0.3319	-0.424641	-0.3289	-0.329247
C3	0.1374	0.034038	0.1324	0.139189
C4	0.0466	0.355989	0.0496	0.396596
C5	-0.0861	-0.355284	-0.0861	-0.353608
C6	-0.0863	-0.028703	-0.1033	-0.082021
C7	-0.1545	-0.297769	-0.179	-0.339099
C8	0.0951	0.394829	0.1241	0.381983
C9	-0.1545	-0.281687	-0.179	-0.302073
C10	-0.1075	-0.173573	-0.0925	-0.149044

C11	-0.1063	-0.071127	-0.1053	-0.087543
C12	-0.0915	-0.068835	-0.0925	-0.091543
C13	-0.179	-0.426182	-0.18	-0.374004
C14	0.1251	0.494092	0.1251	0.500323
C15	-0.179	-0.304987	-0.18	-0.364288
C16	-0.0915	-0.154394	-0.0925	-0.12795
O2	-0.3439	-0.38778	-0.3349	-0.472696
C17	0.0894	-0.041275	0.1244	0.067174
C18	0.1361	0.373958	0.1381	0.285328
O3	-0.6048	-0.65015	-0.6048	-0.706632
C19	0.1708	0.190518	0.1338	0.333346
C20	0.0321	0.032959	0.0611	-0.061955
C21	0.0554	-0.07183	0.0544	-0.09444
O4	-0.4036	-0.35832	-0.4036	-0.307381
H1	0.0687	0.123789	0.0562	0.086759
H2	0.0687	0.077204	0.0562	0.03605
H3	0.0402	0.099442	0.039533	0.097501
H4	0.0402	0.086998	0.039533	0.072188
H5	0.0402	0.076035	0.039533	0.079092
H6	0.143	0.169957	0.143	0.172479
H7	0.143	0.172577	0.143	0.136348
H8	0.139	0.154796	0.138	0.15688
H9	0.1385	0.1473	0.1375	0.137441
H10	0.1425	0.189308	0.1435	0.192658
H11	0.1425	0.154282	0.1435	0.163294
H12	0.1385	0.16543	0.1375	0.155477
H13	0.0532	0.056936	0.0552	0.071582

H14	0.0532	0.065258	0.0552	0.075298
H15	0.0647	0.000421	0.0687	0.03379
H16	0.0392	0.013317	0.0467	-0.014048
H17	0.0392	0.003328	0.0467	-0.016827
H18	0.1057	0.135218	0.1157	0.150855
H19	0.0787	0.113553	0.0797	0.128196
H20	0.0787	0.13535	0.0797	0.121256
C22	-0.1075	-0.147022	-0.0925	-0.06987
H21	0.0402	0.079338	0.039533	0.078233
H22	0.0402	0.106901	0.039533	0.081127
H23	0.0402	0.094027	0.039533	0.100816
H24	0.139	0.153723	0.138	0.137257
C23	0.1538	0.380308	0.1538	0.403885
H25	0.3498	0.418118	0.3508	0.406376
H26	0.3498	0.389215	0.3508	0.378086
H27	0.0362	-0.007357	0.0392	0.05444
H28	0.0362	-0.041362	0.0392	-0.01766
H29	0.3728	0.341958	0.3548	0.368608
H30	0.419	0.403164	0.411	0.416552
H31	0.0332	0.010362	0.0312	-0.071587
H32	0.0332	-0.074922	0.0312	0.003912
	-0.004	$1x10^{-06}$	0.001998	$-3x10^{-06}$

The sum of the charges using the RESP[1,2] methodology is in the order of 10^{-6}. On the other hand the AM1-BCC[3,4] gives a sum of approximately 10^{-3}. Therefore, the RESP methodology is more suitable to make sure that the net charge is 0 with the large number of molecules of our system (600 molecules).

Similar results are observed for the two conformations of the trimers. The results of the calculations of the RESP and AM1-BCC charges are given in Table 4.

Table 4. Net Charges (in e) calculated using the AM1-BCC and RESP methodologies for a trimer.

Atom ID	Geometry 1 AM1_BCC	Geometry 1 RESP	Geometry 2 AM1-BCC	Geometry 2 RESP
C1	-0.0861	-0.4332	-0.0861	-0.414391
H1	0.03995	0.108934	0.03995	0.102748
H2	0.03995	0.108934	0.03995	0.102748
H3	0.03995	0.108934	0.03995	0.102748
C2	0.0496	0.353015	0.0496	0.350015
C3	-0.0861	-0.4332	-0.0861	-0.414391
H4	0.03995	0.108934	0.03995	0.102748
H5	0.03995	0.108934	0.03995	0.102748
H6	0.03995	0.108934	0.03995	0.102748
C10	-0.1018	-0.058203	-0.1018	-0.036019
C11	-0.0955	-0.121932	-0.0955	-0.130904
C12	-0.175	-0.339236	-0.175	-0.341668
C13	0.1111	0.46287	0.1111	0.460621
C14	-0.175	-0.339236	-0.175	-0.341668
C15	-0.0955	-0.121932	-0.0955	-0.130904
H14	0.138	0.146588	0.138	0.145354
H13	0.147	0.16774	0.147	0.17788
O3	-0.3244	-0.374525	-0.3244	-0.413891
C19	0.1329	0.040529	0.1329	0.090376
C20	0.0296	0.060653	0.0296	-0.02125
O4	-0.4061	-0.309537	-0.4061	-0.317951
C21	0.0549	-0.152598	0.0549	-0.101877
H23	0.07995	0.136832	0.07995	0.122098
H24	0.07995	0.136832	0.07995	0.122098
H22	0.1107	0.118671	0.1107	0.158378
H20	0.07295	0.078815	0.07295	0.081995
H21	0.07295	0.078815	0.07295	0.081995
H12	0.147	0.16774	0.147	0.17788

H11	0.138	0.146588	0.138	0.145354
C4	-0.1048	-0.052125	-0.1048	-0.044194
C9	-0.09225	-0.108933	-0.09225	-0.10885
C8	-0.17975	-0.36552	-0.17975	-0.375811
H9	0.14325	0.174113	0.14325	0.181992
H10	0.138	0.144508	0.138	0.143788
C5	-0.09225	-0.108933	-0.09225	-0.10885
H7	0.138	0.144508	0.138	0.143788
C6	-0.17975	-0.36552	-0.17975	-0.375811
H8	0.14325	0.174113	0.14325	0.181992
C7	0.1241	0.479457	0.1241	0.490312
O1	-0.3369	-0.397127	-0.3369	-0.439557
C16	0.1254	0.044581	0.1254	0.090049
H15	0.05545	0.060631	0.05545	0.058156
H16	0.05545	0.060631	0.05545	0.058156
C17	0.1381	0.330209	0.1381	0.361923
O2	-0.6113	-0.659974	-0.6113	-0.708317
H56	0.4225	0.3997	0.4225	0.425393
H17	0.0582	0.011692	0.0582	0.005945
C18	0.1418	0.008734	0.1418	-0.125794
H18	0.0562	0.058102	0.0562	0.114422
H19	0.0562	0.058102	0.0562	0.114422
N2	-0.7746	-0.415815	-0.7746	-0.521536
C22	0.1768	-0.19457	0.1768	0.060019
C44	0.1528	0.495311	0.1528	0.432458
N1	-0.9178	-1.105928	-0.9178	-1.117585
H49	0.3503	0.401102	0.3503	0.400068
H50	0.3503	0.401102	0.3503	0.400068
H54	0.0332	-0.057232	0.0332	-0.030174
H55	0.0332	-0.057232	0.0332	-0.030174
H51	0.0422	0.109992	0.0422	0.054656
H52	0.0422	0.109992	0.0422	0.054656
C40	0.1418	0.008734	0.1418	-0.125794
C39	0.1381	0.330209	0.1381	0.361923
C38	0.1254	0.044581	0.1254	0.090049

O6	-0.3369	-0.397127	-0.3369	-0.439557
C35	0.1241	0.479457	0.1241	0.490312
C34	-0.17975	-0.36552	-0.17975	-0.375811
C33	-0.09225	-0.108933	-0.09225	-0.10885
C32	-0.1048	-0.052125	-0.1048	-0.044194
C25	0.0496	0.353015	0.0496	0.350015
C23	-0.0861	-0.4332	-0.0861	-0.414391
H45	0.03995	0.108934	0.03995	0.102748
H46	0.03995	0.108934	0.03995	0.102748
H47	0.03995	0.108934	0.03995	0.102748
C26	-0.0861	-0.4332	-0.0861	-0.414391
H27	0.03995	0.108934	0.03995	0.102748
H28	0.03995	0.108934	0.03995	0.102748
H29	0.03995	0.108934	0.03995	0.102748
C27	-0.1018	-0.058203	-0.1018	-0.036019
C31	-0.0955	-0.121932	-0.0955	-0.130904
C30	-0.175	-0.339236	-0.175	-0.341668
C29	0.1111	0.46287	0.1111	0.460621
O5	-0.3244	-0.374525	-0.3244	-0.413891
C24	0.1329	0.040529	0.1329	0.090376
C41	0.0296	0.060653	0.0296	-0.02125
C42	0.0549	-0.152598	0.0549	-0.101877
O8	-0.4061	-0.309537	-0.4061	-0.317951
H43	0.07995	0.136832	0.07995	0.122098
H44	0.07995	0.136832	0.07995	0.122098
H42	0.1107	0.118671	0.1107	0.158378
H25	0.07295	0.078815	0.07295	0.081995
H26	0.07295	0.078815	0.07295	0.081995
C28	-0.175	-0.339236	-0.175	-0.341668
H30	0.147	0.16774	0.147	0.17788
C43	-0.0955	-0.121932	-0.0955	-0.130904
H48	0.138	0.146588	0.138	0.145354
H31	0.147	0.16774	0.147	0.17788
H32	0.138	0.146588	0.138	0.145354
C37	-0.09225	-0.108933	-0.09225	-0.10885

C36	-0.17975	-0.36552	-0.17975	-0.375811
H35	0.14325	0.174113	0.14325	0.181992
H36	0.138	0.144508	0.138	0.143788
H33	0.138	0.144508	0.138	0.143788
H34	0.14325	0.174113	0.14325	0.181992
H37	0.05545	0.060631	0.05545	0.058156
H38	0.05545	0.060631	0.05545	0.058156
O7	-0.6113	-0.659974	-0.6113	-0.708317
H53	0.4225	0.3997	0.4225	0.425393
H39	0.0582	0.011692	0.0582	0.005945
H40	0.0562	0.058102	0.0562	0.114422
H41	0.0562	0.058102	0.0562	0.114422
Total	0.004	$6x10^{-06}$	0.004	$4.16334x10^{-16}$

There is no need to go beyond the trimer molecule. The aim of using both a dimer and a trimer in our calculations was to calculate the partial charges that will be used in the cross-linking procedure in various intermediate states of connectivity of the active centers that take place in the polymerization procedure. The trimer is used to saturate the amine site with two DGEBA molecules. Considering the number of molecules, the RESP methodology is the best choice.

Bibliography

1. Bayly, C. I., Cieplak, P., Cornell, W. & Kollman, P. A. A well-behaved electrostatic potential based method using charge restraints for deriving atomic charges: the RESP model. *J. Phys. Chem.* **97,** 10269–10280 (1993).
2. Cornell, W. D., Cieplak, P., Bayly, C. I. & Kollmann, P. A. Application of RESP charges to calculate conformational energies, hydrogen bond energies, and free energies of solvation. *J. Am. Chem. Soc.* **115,** 9620–9631 (1993).
3. Jakalian, A., Bush, B. L., Jack, D. B. & Bayly, C. I. Fast, efficient generation of high-quality atomic charges. AM1-BCC model: I. Method. *J. Comput. Chem.* **21,** 132–146 (2000).
4. Jakalian, A., Jack, D. B. & Bayly, C. I. Fast, efficient generation of high-quality atomic charges. AM1-BCC model: II. Parameterization and validation. *J. Comput. Chem.* **23,** 1623–1641 (2002).

Annex E: Step-by-Step Guide to execute a simulation box generation using the PACKMOL code

The first step to create a simulation box using PACKMOL[1,2] is by constructing the execution script (namefile.inp) for the code. An example is given below for the generation of a mixture simulation box:

tolerance 3.0 #This line indicates the minimum distance in Å that atoms between molecules should be separated by another

avoid_overlap yes #This line states that no overlaps between atoms is accepted

filetype pdb #This line indicates that the output file is a .pdb file with the coordinates of the atoms inside the simulation box

output mix_600_85.pdb #This line indicates name of the output file

nloop 1000 #This line indicates the maximum number of loops the program can execute before finding a solution to the packing problem. If it surpasses this number the program stops and a new simulation box must be defined

The section below states the number of molecules of each type we want to insert in the box.

structure dgebaresp0.pdb → This line indicates the name of the file containing the structure of the molecule we want to reproduce

number 400 → This indicates the total number of molecules that are to be placed inside the simulation box

inside cube 0. 0. 0. 85.0 → This command indicates the geometry of the simulation box (cube) and its coordinates (the above command will create a cube of 85Å x 85Å x 85Å with coordinates which will extend from 0.0 to 85Å)

end structure

```
structure EDA_in.pdb
  number 200
  inside cube 0. 0. 0. 85.0
end structure
```

After completing the script it needs to be saved in the same directory as the files containing the structural information of the molecules that are to be placed in the simulation box. In the same directory the executable of PACKMOL must be contained which can be downloaded through the website: *http://www.ime.unicamp.br/~martinez/packmol/download.shtml.* The software is freely distributed under the terms of the MIT license.

After accessing the directory on the Linux Operating System profile on EoS through the use of a software like MobaXterm we execute the software using the command:

```
./packmol < (namefile).inp
```

An example screen after the execution of this command, if the script is correctly written is:

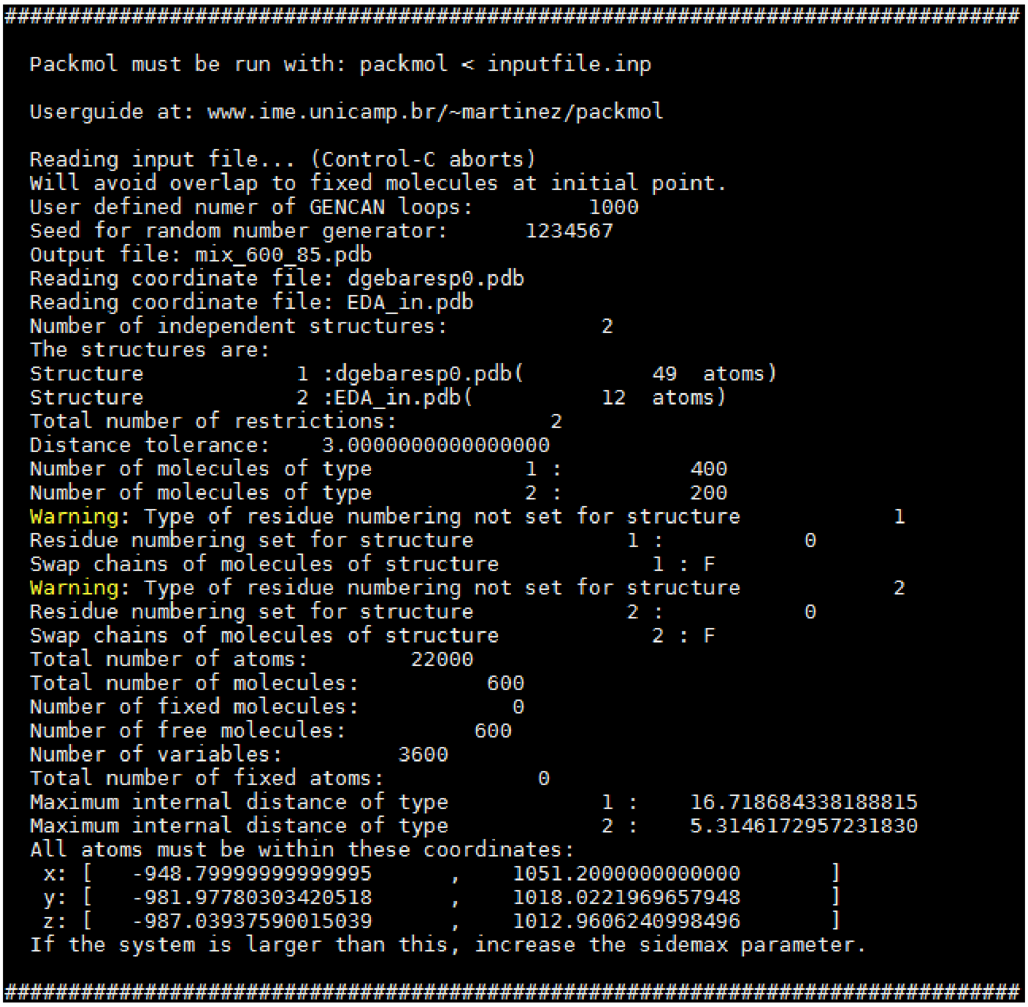

```
################################################################################

  Packmol must be run with: packmol < inputfile.inp

  Userguide at: www.ime.unicamp.br/~martinez/packmol

  Reading input file... (Control-C aborts)
  Will avoid overlap to fixed molecules at initial point.
  User defined numer of GENCAN loops:         1000
  Seed for random number generator:      1234567
  Output file: mix_600_85.pdb
  Reading coordinate file: dgebaresp0.pdb
  Reading coordinate file: EDA_in.pdb
  Number of independent structures:            2
  The structures are:
  Structure            1 :dgebaresp0.pdb(          49  atoms)
  Structure            2 :EDA_in.pdb(          12  atoms)
  Total number of restrictions:            2
  Distance tolerance:    3.0000000000000000
  Number of molecules of type            1 :          400
  Number of molecules of type            2 :          200
  Warning: Type of residue numbering not set for structure            1
  Residue numbering set for structure            1 :           0
  Swap chains of molecules of structure            1 : F
  Warning: Type of residue numbering not set for structure            2
  Residue numbering set for structure            2 :           0
  Swap chains of molecules of structure            2 : F
  Total number of atoms:        22000
  Total number of molecules:          600
  Number of fixed molecules:            0
  Number of free molecules:          600
  Number of variables:         3600
  Total number of fixed atoms:            0
  Maximum internal distance of type            1 :    16.718684338188815
  Maximum internal distance of type            2 :    5.3146172957231830
  All atoms must be within these coordinates:
   x: [   -948.79999999999995      ,    1051.2000000000000       ]
   y: [   -981.97780303420518      ,    1018.0221969657948       ]
   z: [   -987.03937590015039      ,    1012.9606240998496       ]
  If the system is larger than this, increase the sidemax parameter.

################################################################################
```

Figure 1. Initial parameters of choice for the packing algorithm.

This screen aids the user in verifying that the input molecular structural files are in accordance with the needs of the simulation that will be executed. If everything is in accordance and no errors are produced we are then lead to a screen resembling Figure 2.

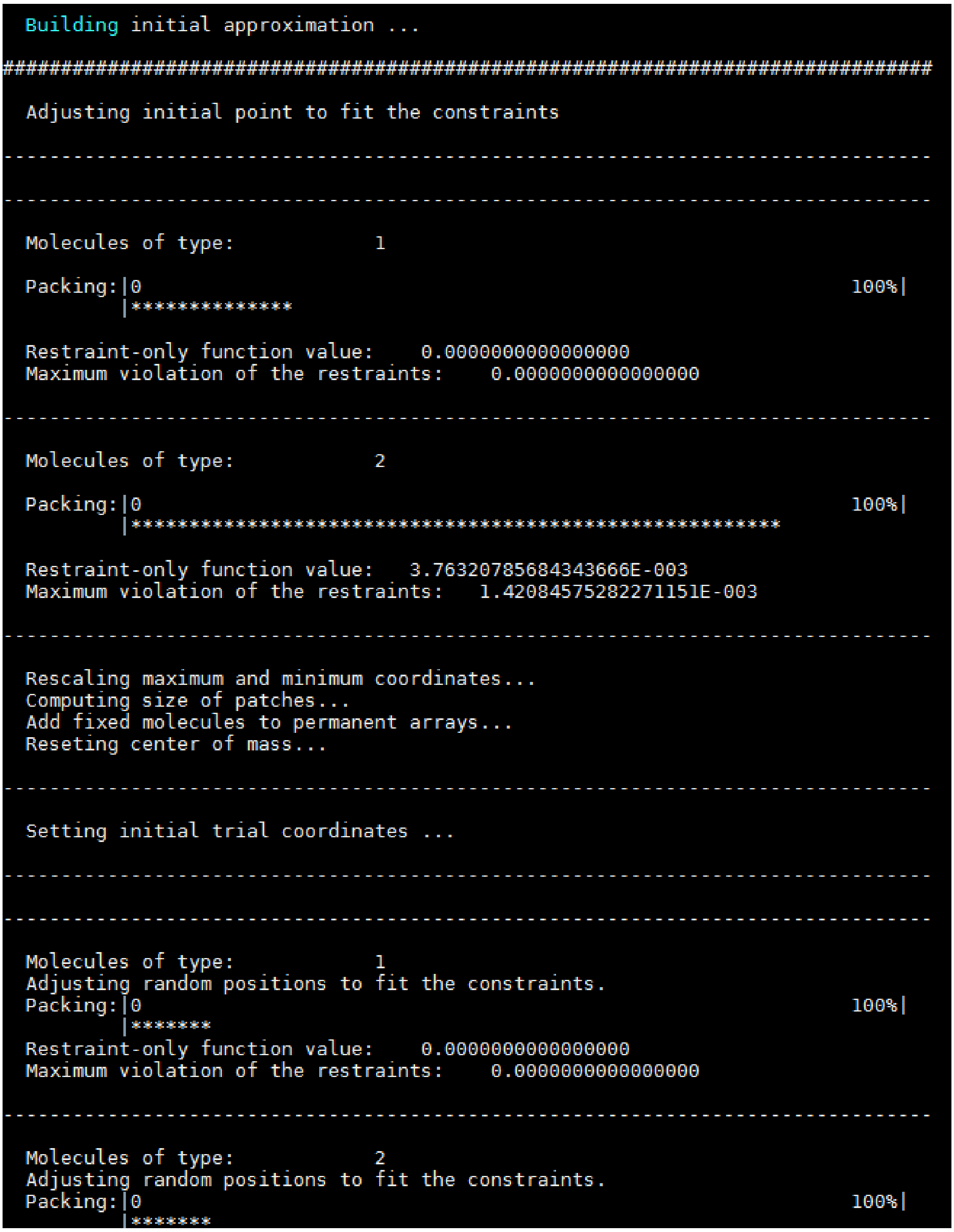

```
  Building initial approximation ...

################################################################################

  Adjusting initial point to fit the constraints

--------------------------------------------------------------------------------

--------------------------------------------------------------------------------

  Molecules of type:           1

  Packing:|0                                                             100%|
          |**************

  Restraint-only function value:    0.0000000000000000
  Maximum violation of the restraints:    0.0000000000000000

--------------------------------------------------------------------------------

  Molecules of type:           2

  Packing:|0                                                             100%|
          |********************************************************

  Restraint-only function value:   3.7632078568434366E-003
  Maximum violation of the restraints:   1.4208457528227115E-003

--------------------------------------------------------------------------------

  Rescaling maximum and minimum coordinates...
  Computing size of patches...
  Add fixed molecules to permanent arrays...
  Reseting center of mass...

--------------------------------------------------------------------------------

  Setting initial trial coordinates ...

--------------------------------------------------------------------------------


--------------------------------------------------------------------------------

  Molecules of type:           1
  Adjusting random positions to fit the constraints.
  Packing:|0                                                             100%|
          |*******
  Restraint-only function value:    0.0000000000000000
  Maximum violation of the restraints:    0.0000000000000000

--------------------------------------------------------------------------------

  Molecules of type:           2
  Adjusting random positions to fit the constraints.
  Packing:|0                                                             100%|
          |*******
```

Figure 2. Initial trials for packing and restraints criteria

An initial packing trial configuration for the 2 types of molecules is tested by the program and is compared to the criteria that we have imposed in the initial script (no. of molecules and size of the periodic box as well as the restraints for overlapping and minimum distances between molecules). The algorithm will then start packing the two types of molecules independently in volume that we specified and then will pack their ensemble for the mixture. If only one molecule type is specified the packing algorithm will produce a solution faster. If the packing solution satisfies all of the criteria we are greeted with the screen in Figure 3.

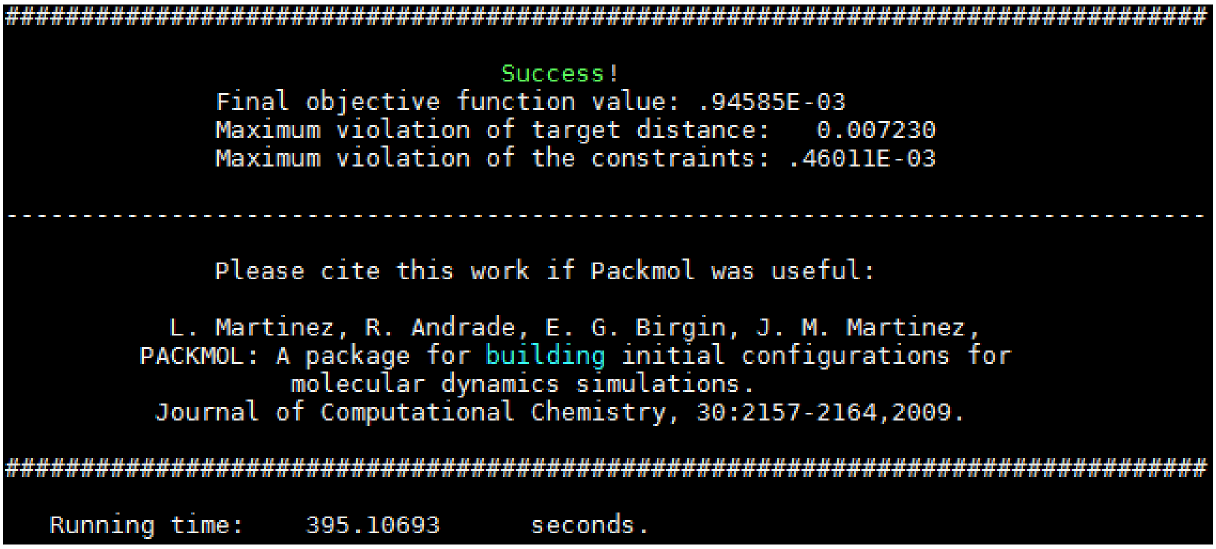

```
################################################################################

                                 Success!
              Final objective function value: .94585E-03
              Maximum violation of target distance:   0.007230
              Maximum violation of the constraints: .46011E-03

--------------------------------------------------------------------------------

              Please cite this work if Packmol was useful:

           L. Martinez, R. Andrade, E. G. Birgin, J. M. Martinez,
         PACKMOL: A package for building initial configurations for
                   molecular dynamics simulations.
          Journal of Computational Chemistry, 30:2157-2164,2009.

################################################################################

   Running time:    395.10693      seconds.
```

Figure 3. Converged solution of the packing algorithm for the configuration desired by the user.

Bibliography

1. Martínez, L., Andrade, R., Birgin, E. G. & Martínez, J. M. PACKMOL: a package for building initial configurations for molecular dynamics simulations. *J. Comput. Chem.* **30,** 2157–2164 (2009).
2. Martínez, J. M. & Martínez, L. Packing optimization for automated generation of complex system's initial configurations for molecular dynamics and docking. *J. Comput. Chem.* **24,** 819–825 (2003).

Annex F: Cross-linking code

As mentioned in Chapter 4 we have developed our “in-house” code to simulate the cross-linking of a stoichiometric mixture of DGEBA and EDA reactants. To use the code one has to have the executable file named *crosslinkpolyepoxy*.

To start the cross-linking procedure one must include in the folder of the executable file the .data file of the simulation box that is used in the LAMMPS[1] code. With this .data file one must in advance (after the 700 K and 1 atm fixed NPT simulation, or any temperature suits the user) give the dump command to produce a dump file containing the x, y and z coordinates, and id numbers of the atoms in the simulation box.

The code will then read these identities and choose a random nitrogen atom that is reactive. After the cross-linking step, the code identifies the atom that has been linked and changes the identity of the specific nitrogen atom one indicating that there is one connection. If the maximum number of connections is reached, the new id of this nitrogen atom will make the code skip it and thus avoid any extra connections.

The dump file must then be converged through LAMMPS into a new .data file where the new atom ids, bond, angles, dihedrals are updated and the .data file has all of its parts updated except from the GAFF parameters and charges. The charges are then substituted manually in accordance with the RESP charges as indicated in Annex F. The manual substitution is necessary as due to problem with code compilation we could not get the code to automatically substitute them without fear of false substitutions.

The process is repeated after every NPT simulation. The cross-linking percentage is calculated by counting the change in identities of the reactive pairs divided by the total number of atoms available for pairing.

Bibliography

1. Plimpton, S. Fast Parallel Algorithms for Short-Range Molecular Dynamics. *J. Comput. Phys.* **117,** 1–19 (1995).

Annex G: LAMMPS MD scripts description

In this Annex we will give a detailed description of the input scripts used for LAMMPS[1] for the various calculations used in this thesis.

Script no.1: NVE and NPT calculations

#Simulation of a 400 DGEBA box → Title of the calculation for the user's reference

units real → Type of units (in our case real means T is in K, P is in atm, density is g/cm^3 and energy is in kcal/mol)

atom_style full → Denotes that fully described molecules will exist in the simulation box

boundary p p p → The box will be satisfy boundary conditions in all spatial expansion

kspace_style pppm[2] 0.0001

pair_style lj/charmm/coul/long 9.0 11.0

Coulombic interactions will be calculated using the PPPM solver

bond_style harmonic

angle_style harmonic

dihedral_style fourier

improper_style none

Define equations that will be used for the calculation of the intramolecular energies → same equations used in GAFF

read_data 400DGEBA700K.data → Define the name of the .data file that will be used for the initialization of the calculation (must be in the same folder as the executable LAMMPS file)

min_style hftn[3] → Choice of the minimization algorithm

minimize 1.0e-9 1.0e-9 10000 100000 → Minimization parameters (first term stopping energy tolerance, second term stopping force tolerance, third term max iterations of the minimizer and fourth term is maximum number of evaluations of the force and energy)

timestep 1.0 → Choice of the time interval for each simulation step (in fs defined by the units parameter)

compute 1 all property/local btype batom1 batom2

compute 2 all bond/local dist

compute 3 all property/local aatom1 aatom2 aatom3 atype

compute 4 all angle/local theta

dump 1 all local 100000 tmp.angle index c_3[1] c_3[2] c_3[3] c_3[4] c_4

dump 2 all local 100000 tmp.bond index c_1[1] c_1[2] c_1[3] c_2

Bond and angle distribution calculation that will be given in the tmp.bond and tmp.angle files `dump 3 all atom 200000 dump.lammpstrj` → Creation of the dump file (the number denotes the time interval between each successive update of the dump file with the current coordinates) named dump.lammpstrj

`fix 1 all nve` → An NVE calculation will be executed

`thermo_style custom step temp press ke pe etotal vol density` → These are the thermodynamic quantities that will be outputted in the log file produced by LAMMPS (log.lammps)

`thermo 500` → Every 500 timesteps the instantaneous thermodynamic quantities that govern the simulation box will be written in the log.lammps file

`run 1000000` → The NVE simulation will be executed for $1x10^6$ timesteps (i.e. 1ns)

`unfix 1` → Stop the NVE simulation

`fix 2 all npt temp 700.0 700.0 100 iso 1.0 1.0 1000` → An NPT simulation fixed at 700 K will be initiated with no ramp and 1 atm (denoted by the units command) pressure with no ramp. (the 100 and 1000 values are for the temperature and pressure damping parameters which should be kept fixed)

```
thermo_style custom step temp press ke pe etotal vol density pxx pyy pzz enthalpy

thermo 1000

run 2000000
```

Script no.2: Radial Distribution function (RDF) calculation

```
units                  real

atom_style  full

boundary      p p p

kspace_style pppm 0.0001

pair_style lj/charmm/coul/long 9.0 11.0

pair_modify mix arithmetic tail no

bond_style harmonic

angle_style harmonic

dihedral_style fourier

improper_style none

read_data 400DGrdf.data

timestep 1.0
```

`read_dump dump.lammpstrj 2000000 x y z box yes replace yes` → Read the coordinates of the dump file at timestep 2000000 to restart a calculation

`compute myRDF all rdf 500` → The RDF will be calculate and spaced out in 500 points across 11Å (the long range intermolecular interaction extend as given by lj/charmm/coul/long)

`fix 1 all ave/time 1 1 1 c_myRDF[*] file tmpDG700K.rdf mode vector` → Launch of a time averaged simulation which will produce the RDF for the first step of the calculation (with no other fixes, it is a frozen image calculation)

```
run 1
```

Script no.3: Glass transition temperature (T_g) calculation

```
#Tg calculation for the final polymer structure
units                   real
atom_style  full
boundary       p p p
kspace_style pppm 0.0001
pair_style lj/charmm/coul/long 9.0 11.0
bond_style harmonic
angle_style harmonic
dihedral_style fourier
improper_style none
read_data polymfinal.data
dump 1 all atom 200000 dump.lammpstrj
fix 1 all nve
thermo_style custom step temp press ke pe etotal vol density
thermo 500
run 1000000
unfix 1
fix 1 all npt temp 700.0 700.0 100 iso 1.0 1.0 1000
thermo_style custom step temp press ke pe etotal vol density pxx pyy pzz enthalpy
thermo 1000
run 2000000
unfix 1
fix 1 all npt temp 700.0 675.0 100 iso 1.0 1.0 1000
```

```
thermo_style custom step temp press ke pe etotal vol density pxx pyy pzz enthalpy
thermo 1000
run 1000000
unfix 1
fix 1 all npt temp 675.0 650.0 100 iso 1.0 1.0 1000
thermo_style custom step temp press ke pe etotal vol density pxx pyy pzz enthalpy
thermo 1000
run 1000000
unfix 1
fix 1 all npt temp 650.0 625.0 100 iso 1.0 1.0 1000
thermo_style custom step temp press ke pe etotal vol density pxx pyy pzz enthalpy
thermo 1000
run 1000000
unfix 1
fix 1 all npt temp 625.0 600.0 100 iso 1.0 1.0 1000
thermo_style custom step temp press ke pe etotal vol density pxx pyy pzz enthalpy
thermo 1000
run 1000000
unfix 1
fix 1 all npt temp 600.0 575.0 100 iso 1.0 1.0 1000
thermo_style custom step temp press ke pe etotal vol density pxx pyy pzz enthalpy
thermo 1000
run 1000000
unfix 1
fix 1 all npt temp 575.0 550.0 100 iso 1.0 1.0 1000
thermo_style custom step temp press ke pe etotal vol density pxx pyy pzz enthalpy
thermo 1000
run 1000000
unfix 1
```

```
fix 1 all npt temp 550.0 525.0 100 iso 1.0 1.0 1000
thermo_style custom step temp press ke pe etotal vol density pxx pyy pzz enthalpy
thermo 1000
run 1000000
unfix 1
fix 1 all npt temp 525.0 500.0 100 iso 1.0 1.0 1000
thermo_style custom step temp press ke pe etotal vol density pxx pyy pzz enthalpy
thermo 1000
run 1000000
unfix 1
fix 1 all npt temp 500.0 475.0 100 iso 1.0 1.0 1000
thermo_style custom step temp press ke pe etotal vol density pxx pyy pzz enthalpy
thermo 1000
run 1000000
unfix 1
fix 1 all npt temp 475.0 450.0 100 iso 1.0 1.0 1000
thermo_style custom step temp press ke pe etotal vol density pxx pyy pzz enthalpy
thermo 1000
run 1000000
unfix 1
fix 1 all npt temp 450.0 425.0 100 iso 1.0 1.0 1000
thermo_style custom step temp press ke pe etotal vol density pxx pyy pzz enthalpy
thermo 1000
run 1000000
unfix 1
fix 1 all npt temp 425.0 400.0 100 iso 1.0 1.0 1000
thermo_style custom step temp press ke pe etotal vol density pxx pyy pzz enthalpy
thermo 1000
run 1000000
unfix 1
```

```
fix 1 all npt temp 400.0 375.0 100 iso 1.0 1.0 1000
thermo_style custom step temp press ke pe etotal vol density pxx pyy pzz enthalpy
thermo 1000
run 1000000
unfix 1
fix 1 all npt temp 375.0 350.0 100 iso 1.0 1.0 1000
thermo_style custom step temp press ke pe etotal vol density pxx pyy pzz enthalpy
thermo 1000
run 1000000
unfix 1
fix 1 all npt temp 350.0 325.0 100 iso 1.0 1.0 1000
thermo_style custom step temp press ke pe etotal vol density pxx pyy pzz enthalpy
thermo 1000
run 1000000
unfix 1
fix 1 all npt temp 325.0 300.0 100 iso 1.0 1.0 1000
thermo_style custom step temp press ke pe etotal vol density pxx pyy pzz enthalpy
thermo 1000
run 1000000
unfix 1
fix 1 all npt temp 300.0 275.0 100 iso 1.0 1.0 1000
thermo_style custom step temp press ke pe etotal vol density pxx pyy pzz enthalpy
thermo 1000
run 1000000
unfix 1
fix 1 all npt temp 275.0 250.0 100 iso 1.0 1.0 1000
thermo_style custom step temp press ke pe etotal vol density pxx pyy pzz enthalpy
thermo 1000
run 1000000
unfix 1
```

```
fix 1 all npt temp 250.0 225.0 100 iso 1.0 1.0 1000

thermo_style custom step temp press ke pe etotal vol density pxx pyy pzz enthalpy

thermo 1000

run 1000000

unfix 1

fix 1 all npt temp 225.0 200.0 100 iso 1.0 1.0 1000

thermo_style custom step temp press ke pe etotal vol density pxx pyy pzz enthalpy

thermo 1000

run 1000000

unfix 1

fix 1 all npt temp 200.0 175.0 100 iso 1.0 1.0 1000

thermo_style custom step temp press ke pe etotal vol density pxx pyy pzz enthalpy

thermo 1000

run 1000000

unfix 1

fix 1 all npt temp 175.0 150.0 100 iso 1.0 1.0 1000

thermo_style custom step temp press ke pe etotal vol density pxx pyy pzz enthalpy

thermo 1000

run 1000000

unfix 1

fix 1 all npt temp 150.0 125.0 100 iso 1.0 1.0 1000

thermo_style custom step temp press ke pe etotal vol density pxx pyy pzz enthalpy

thermo 1000

run 1000000

unfix 1

fix 1 all npt temp 125.0 100.0 100 iso 1.0 1.0 1000

thermo_style custom step temp press ke pe etotal vol density pxx pyy pzz enthalpy

thermo 1000

run 1000000

unfix 1
```

```
fix 1 all npt temp 100.0 75.0 100 iso 1.0 1.0 1000
thermo_style custom step temp press ke pe etotal vol density pxx pyy pzz enthalpy
thermo 1000
run 1000000
unfix 1
fix 1 all npt temp 75.0 50.0 100 iso 1.0 1.0 1000
thermo_style custom step temp press ke pe etotal vol density pxx pyy pzz enthalpy
thermo 1000
run 1000000
unfix 1
fix 1 all npt temp 50.0 25.0 100 iso 1.0 1.0 1000
thermo_style custom step temp press ke pe etotal vol density pxx pyy pzz enthalpy
thermo 1000
run 1000000
```

The above script uses consecutive NPT calculations that will diminish the initial temperature of the NPT calculation (the first number after the `temp` keyword) to the final temperature (the second number after the `temp` keyword) in the span of 1 ns given by the `run` parameter.

Bibliography

1. Plimpton, S. Fast Parallel Algorithms for Short-Range Molecular Dynamics. *J. Comput. Phys.* **117,** 1–19 (1995).
2. Hockney, R. & Eastwood, J. Particle-Particle-Particle-Mesh (P3M) Algorithms. in *Computer simulation using particles* 267–304
3. Chapelle, O. & Erhan, D. Improved preconditioner for hessian free optimization. in *In NIPS Workshop on Deep Learning and Unsupervised Feature Learning* (2011).

Annex H: DGEBA simulation boxes and NPT simulation results for different initial parameters

In this Annex we present results for the NPT simulations of pure DGEBA varying the initial density and the number of molecules as well as the computational parameters. Unless stated otherwise in the column "Other comments" the Particle Particle Particle Mesh (PPPM) algorithm[1] is used to calculate the intermolecular interactions and the GAFF force field[2] is used for the intramolecular parameters. The point charges we use are the ones calculated with the RESP[3,4] methodology.

Table 1. DGEBA NPT simulations under variable density, no. of molecules and computational parameters

Test	*Number of Molecules*	*T (K)*	t_{tot} *(ns)*	$\rho_{initial}$ *(g/cm³)*	ρ_{final} *(g/cm³)*	*Other comments*
1	50	300	1	0.001	1.18	Pair_Style lj/cut/coul/cut Rcut,lj = 5.0 Å, Rcut,coul = 3.0 Å
2	100	300	1	0.001	1.28	Pair_Style lj/cut/coul/cut Rcut,lj = 5.0 Å, Rcut,coul = 3.0 Å
3	256	300	1	0.001	1.25	Pair_Style lj/cut/coul/cut Rcut,lj = 5.0 Å, Rcut,coul = 3.0 Å
4	400	300	2	0.700	1.10	
5	400	300	2	0.560	1.10	
6	400	700	2	0.700	0.85	
7	500	300	2	0.700	1.09	
8	500	300	2	0.700	1.09	
9	500	300	10	0.700	1.09	
10	500	300	2	0.700	1.08	Pair_Style lj/cut/coul/cut Rcut,lj = 9.0 Å, Rcut,coul = 9.0 Å

From Table 1 we can observe that for 400 DGEBA molecules, independent by the total simulation time or the initial density, by using the same computational parameters for NPT simulations at 300 K and 1 atm, the final density has a similar value around 1.09 g/cm^3 which is in good agreement with the experimental density of the liquid DGEBA[5] at 300 K, i.e. 1.16 g/cm^3. This value is lower if the temperature is increased at 700 K which is expected as the volume expands more with an increase in the kinetic energy of the molecules. For 500 DGEBA molecules, using the same computational parameters for an NPT simulation fixed at 300 K and 1 atm, we calculate the same density as the 400 molecules. By changing the pair style to a style that does not take into account the long range intermolecular interactions we have an overestimation of the final density when the initial density is very low.

Bibliography

1. Hockney, R. & Eastwood, J. Particle-Particle-Particle-Mesh (P3M) Algorithms. in *Computer simulation using particles* 267–304
2. Wang, J., Wolf, R. M., Caldwell, J. W., Kollman, P. A. & Case, D. A. Development and testing of a general amber force field. *J. Comput. Chem.* **25,** 1157–1174 (2004).
3. Bayly, C. I., Cieplak, P., Cornell, W. & Kollman, P. A. A well-behaved electrostatic potential based method using charge restraints for deriving atomic charges: the RESP model. *J. Phys. Chem.* **97,** 10269–10280 (1993).
4. Cornell, W. D., Cieplak, P., Bayly, C. I. & Kollmann, P. A. Application of RESP charges to calculate conformational energies, hydrogen bond energies, and free energies of solvation. *J. Am. Chem. Soc.* **115,** 9620–9631 (1993).
5. DGEBA Epoxy Resin. Available at: http://polymerdatabase.com/polymers/bisphenol-adiglycidyletherepoxyresin.html. (Accessed: 18th September 2017)

Annex I: EDA simulation boxes and NPT simulation results for different initial parameters

In this Annex we will present a variety of results using simulation boxes for the NPT simulations pure EDA liquids varying the initial density and the number of molecules as well as the computational parameters. Unless stated otherwise in the column "Other comments" the Particle Particle Particle Mesh (PPPM) algorithm[1] is used to calculate the intermolecular interactions and the GAFF force field[2] is used for the intramolecular parameters. The point charges we use are the ones calculated with the RESP[3,4] methodology.

Table 1. EDA NPT simulations tests under variable density, no. of molecules and computational parameters

Test	*Number of Molecules*	*T (K)*	t_{tot} *(ns)*	$\rho_{initial}$ *(g/cm^3)*	ρ_{final} *(g/cm^3)*	*Other comments*
1	50	300	10	0.001	1.62	Pair_Style lj/cut/coul/cut Rcut,lj = 5.0 Å, Rcut,coul = 3.0 Å
2	50	300	1	0.500	0.53	Pair_Style lj/cut/coul/cut Rcut,lj = 5.0 Å, Rcut,coul = 3.0 Å
3	100	300	10	0.001	0.74	Pair_Style lj/cut/coul/cut Rcut,lj = 5.0 Å, Rcut,coul = 3.0 Å
4	400	300	2	0.700	0.99	
5	400	300	2	0.700	0.99	
6	500	300	2	0.700	0.86	
7	1000	300	1	0.700	0.96	

From Table 1 we can observe that for 400 EDA molecules, for NPT simulations at 300 K and 1 atm, the final density has a value for all simulation boxes around 0.99 g/cm^3 which is in a fairly good accordance with the experimental value of 0.90 g/cm^3 at 300 K[5]. This accordance is improved if we use a 500 EDA molecule simulation box giving us a final density of 0.86 g/cm^3. By changing the pair style to a style that does not take into account the long range intermolecular interactions the final density in various conditions (from very low to higher initial densities) is inconsistent and in the case of a 10 ns simulation is dramatically increased to a value of 1.62 g/cm^3 suggesting that for a longer simulation the box could explode as a very small volume would create very large energies crashing the simulation. . This shows us that a computational method not taking into account long range effects will not yield the desirable results and is abandoned.

Bibliography

1. Hockney, R. & Eastwood, J. Particle-Particle-Particle-Mesh (P3M) Algorithms. in *Computer simulation using particles* 267–304
2. Wang, J., Wolf, R. M., Caldwell, J. W., Kollman, P. A. & Case, D. A. Development and testing of a general amber force field. *J. Comput. Chem.* **25,** 1157–1174 (2004).
3. Bayly, C. I., Cieplak, P., Cornell, W. & Kollman, P. A. A well-behaved electrostatic potential based method using charge restraints for deriving atomic charges: the RESP model. *J. Phys. Chem.* **97,** 10269–10280 (1993).
4. Cornell, W. D., Cieplak, P., Bayly, C. I. & Kollmann, P. A. Application of RESP charges to calculate conformational energies, hydrogen bond energies, and free energies of solvation. *J. Am. Chem. Soc.* **115,** 9620–9631 (1993).
5. Ethylenediamine E26266. *NH2CH2CH2NH2* Available at: http://www.sigmaaldrich.com/catalog/product/sial/e26266. (Accessed: 18th September 2017)

<u>Annex J</u>: Test of several temperatures for NPT simulations of the DGEBA, EDA and stoichiometric mixture simulation boxes

This Annex includes NPT simulations at higher temperatures for the DGEBA and EDA reactants and their stoichiometric mixture. These NPT simulations are used to study the behavior of such simulation boxes at higher temperatures. Higher temperatures allow the vigorous motion of molecules. In the mixture, it allows a better distribution of the molecules inside the simulation box, potentially allowing more reactive centers to be cross-linked. We tested NPT simulations fixed at 700 K and 1 atm for the DGEBA and EDA reactants. For the stoichiometric mixture we tested two fixed temperatures (900 K and 1000 K) and a fixed 1 atm pressure. The results are presented in Figures 1-4. For all the simulation boxes the initial density was fixed at 0.700 g/cm^3.

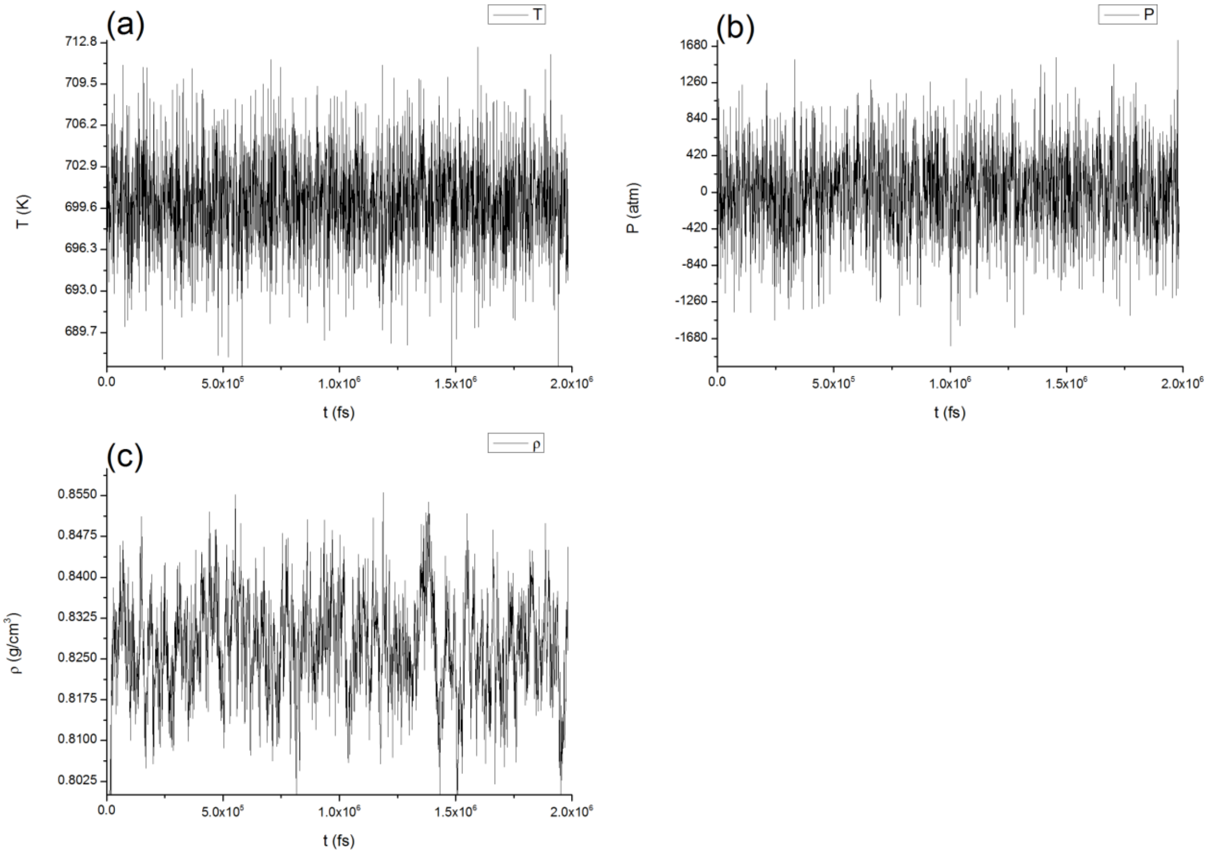

Figure 1. 2ns NPT simulation of the 400 DGEBA monomer box fixed at 700 K and 1 atm.

Figure 1a presents the variation of the temperature as a function of time. We observe that the temperature is well equilibrated throughout the simulation duration around the value that we have fixed with the thermostat (700 K). The oscillations are in a limited range of ± 6 K which matches the results for the simulation boxes fixed at other temperatures. Figure 1b shows the evolution of the pressure as a function of time. Although the mean value regulated by the barostat is 1 atm, we observe large fluctuations of up to 1680 atm. This is typical of MD simulations of large systems. Figure 1c gives an overview of the variation of the DGEBA density as a function of simulation time. We observe that in a few fs a drastic change is observed from 0.700 g/cm^3 (the initial density) to 0.829 g/cm^3. Then the density fluctuates slightly around this point throughout the 2 ns simulation giving a mean value of the density after the 2 ns simulation around that point. This is below the 1.100 g/cm^3 density calculated in the 300 K NPT simulation which is expected.

Figure 2 presents the 700 K and 1 atm NPT simulation for 400 EDA molecules at an initial density of 0.700 g/cm^3.

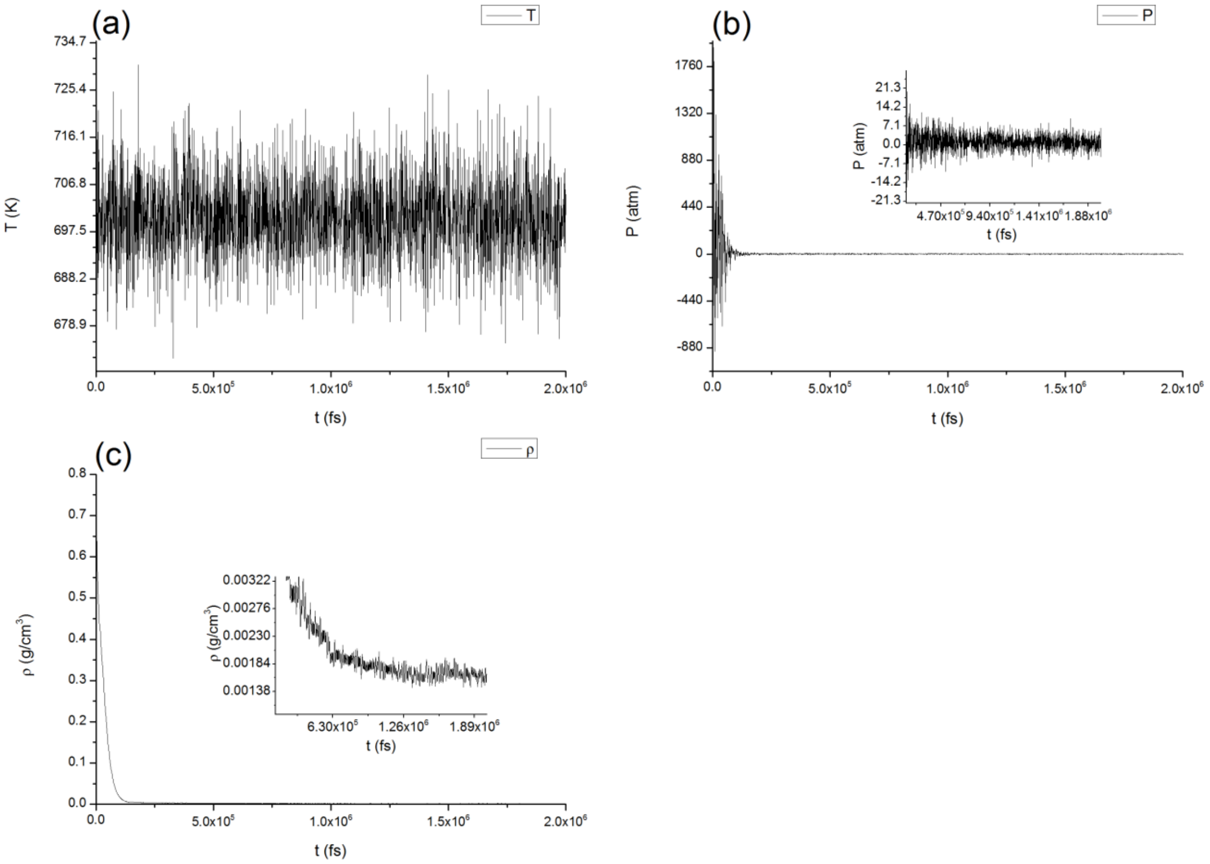

Figure 2. 2ns NPT simulation of the 400 EDA monomer box fixed at 700 K and 1 atm.

Figure 2a presents the variation of the temperature as a function of time. We observe that the temperature is well equilibrated around the value that we have fixed with the thermostat, which is 300 K. Oscillations are in the range ± 20 K. Figure 2b shows the fluctuation of pressure as a function on time. Although the value fixed in the barostat is 1 atm, we observe fluctuations of up to 860 atm for the first 0.1 ns. After the box is given time to equilibrate and the molecules to gain their kinetic energy from the 700 K temperature we observe the fluctuations of the temperature fall to 7.1 atm until the end of the 2 ns simulation. The reason behind that becomes more obvious from figure 2c which gives an overview of the variation of the density as a function of time and we can observe a drastic decrease from the starting density of 0.700 g/cm^3 at t=0 to 0.002 g/cm^3 at t=0.63 ns, where it reaches a plateau. The mean density value after equilibration of the EDA liquid remains 0.002 g/cm^3 which indicates a very big expansion of the simulation box and the development of big distances between the EDA molecules thus reducing significantly the pressure on the boundaries of the box hence the low pressure indicated in Figure 2b.

Figure 3 shows the NPT simulation of the mixture in stoichiometric analogy of the two reactants (400 DGEBA : 200 EDA) fixed at 1000 K and 1 atm.

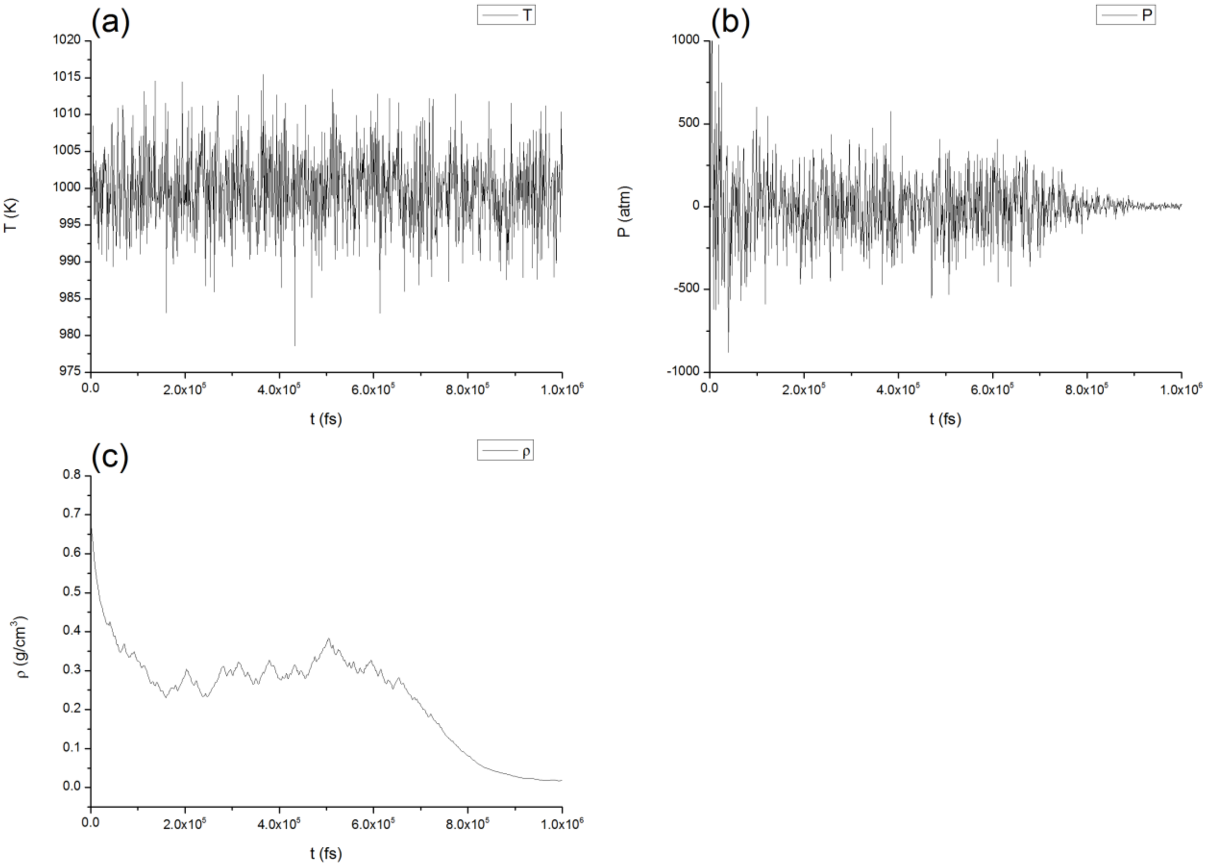

Figure 3. 1 ns NPT simulation of the 600 molecule mixture fixed at 1000 K and 1 atm.

Figure 3a presents the variation of the temperature as a function of time. We observe that the temperature is well equilibrated around the value that we have fixed with the thermostat, which is 1000 K. Oscillations are in the range ± 15 K. Figure 3b shows the fluctuation of pressure as a function on time. Although the value fixed in the barostat is 1 atm, we observe fluctuations of up to 500 atm for the first 0.8 ns. After the box is given time to equilibrate and the molecules to gain their kinetic energy from the 1000 K temperature we observe the fluctuations of the temperature fall to 20 atm until the end of the 1 ns simulation. The reason behind that becomes more obvious from Figure 3c which gives an overview of the variation of the density as a function of time and we can observe a drastic decrease from the starting density of 0.700 g/cm^3 at t=0 to 0.250 g/cm^3 that indicates the rapid movement and thus distancing of the molecules leading to a rapid expansion of the simulation box. This density has oscillations in the range of ±0.1 g/cm^3 until t=0.7ns where it steadily descends at 0.002 g/cm^3 at t=0.80 ns, where it reaches a plateau. The oscillations are a result of the DGEBA molecules not being able to reach a kinetic energy high enough for them to escape their attractive forces. The mean density value after equilibration of the stoichiometric molecular mixture remains 0.002 g/cm^3 which indicates a very big expansion of the simulation box and the development of big distances between the largest (DGEBA) molecules thus reducing significantly the pressure on the boundaries of the box hence the low pressure indicated in Figure 3b.

Figure 4 shows the NPT simulation of the mixture in stoichiometric analogy of the two reactants fixed at 900 K and 1 atm.

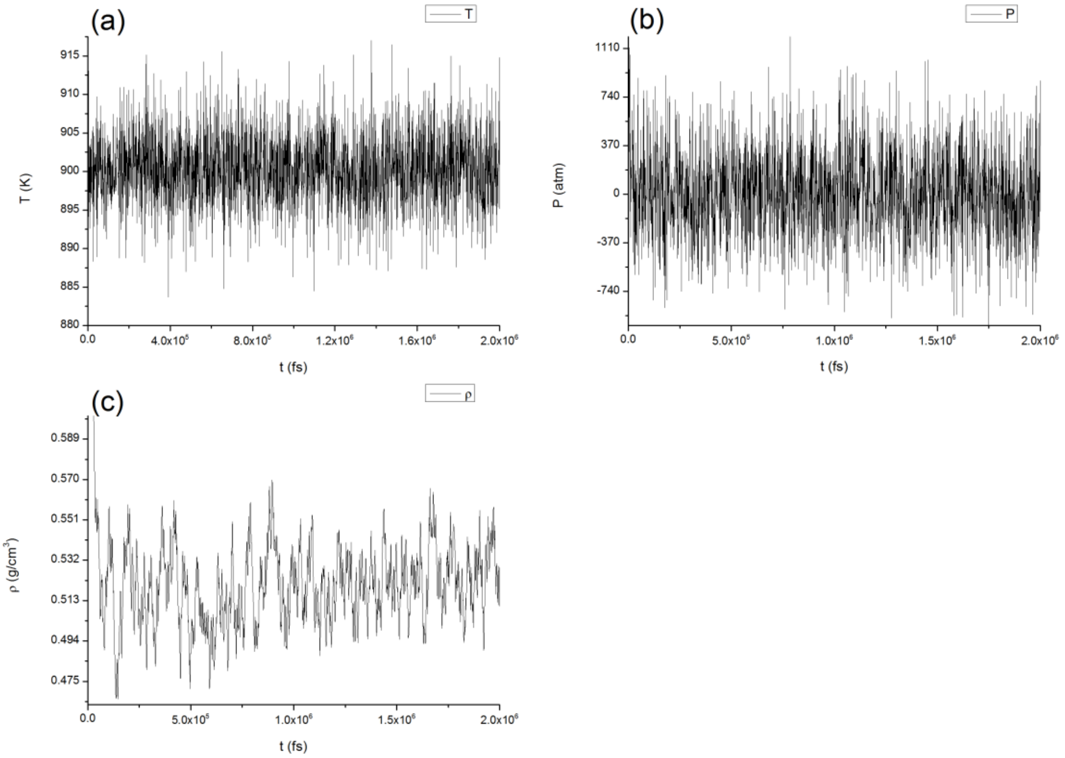

Figure 4. 1 ns NPT simulation of the 600 molecule mixture fixed at 900 K and 1 atm.

Figure 4a presents the variation of the temperature as a function of time. We observe that the temperature is well equilibrated throughout the simulation duration around the value that we have fixed with the thermostat (900 K). The oscillations are again as with the 1000 K NPT simulation in the range of ± 15 K. Figure 4b shows the evolution of the pressure as a function of time. Although the mean value regulated by the barostat is 1 atm, we observe large fluctuations of up to 740 atm throughout the 2ns simulation. Figure 4c gives an overview of the variation of the density as a function of simulation time. We observe that in a few fs a drastic change is observed from 0.700 g/cm^3 to 0.522 g/cm^3. Then the density fluctuates slightly around this point throughout the 2 ns simulation giving a mean value of the density after the 2 ns simulation around that point. We can thus deduce that a 900 K temperature allows the molecules to move in the simulation box vigorously but does not provide too much kinetic energy to escape as it was the case at 1000 K (ρ_{final} ~ 0.002 g/cm^3). Thus we conclude that if a higher temperature is to be tested for the cross-linking algorithm, 900 K or below should be considered.

Bibliography

1. Landau, L. D. & Lifshitz, E. M. *Statistical Physics*. (Pergamon Press).

Résumé vulgarisé en français

Il y a un besoin croissant de substituer certains composants métalliques utilisés dans les industries de l'aérospatiale et du transport, par des matériaux plus légers. Dans cette optique, les polymères (la famille comprenant les plastiques) sont de bons candidats. Mais leurs propriétés physiques et chimiques sont totalement différentes de celles des métaux. Par exemple, certains composants doivent pouvoir conduire l'électricité. Les pièces métalliques le font mais les plastiques sont des isolants électriques. Dans ce cas, une couche de métal peut être déposée sur la surface du composant polymère. De nombreuses techniques ont été développées pour la métallisation des polymères, mais aucune n'est universelle. Par conséquent, il est nécessaire d'élaborer des modèles qui pourraient être utiles à la compréhension de l'élaboration de la majorité des systèmes métal / polymère. Dans cet objectif, nous avons développé une méthodologie scientifique capable d'identifier et d'expliquer les processus responsables de la formation de la couche de métallisation sur la surface du polymère. Ce modèle est basé sur la combinaison de simulations informatiques et de travaux expérimentaux. Afin de comprendre en détails la formation d'une couche de cuivre sur un polymère utilisé dans l'industrie aérospatiale, nous avons construit un modèle numérique de ce polymère qui sera très utile pour d'autres études scientifiques.

Popularized summary in English

There is a growing interest in the substitution of metallic components used in the aerospace and transport industries, by lighter materials. Polymers (the family of plastics) are good candidates in this purpose. But their physical and chemical properties are totally different. For instance, some components need to conduct electricity. Metallic parts do; plastics don’t. In these cases, a metallization layer is requested over the polymer component surface. Many techniques were developed for metallizing polymers, but none is universal. Therefore, there is a need to develop models which could be useful to the understanding of the majority of metal/polymer systems. In this course, we have developed a scientific methodology which is able to identify and explain the processes that are responsible for the formation of the metallization layer on the polymer surface. It is based on the combination of computational simulations and experimental work. At the end, we could explain better the formation of a copper layer on a polymer used in the aerospace industry, and we developed a numerical model of this polymer that will be very useful for further studies.

Titre. *Modélisation du poly-époxy DGEBA-EDA et de sa réactivité vis à vis du cuivre : approche expérimentale et numérique*

Résumé. Grâce à la métallisation de leur surface, des pièces en polymères peuvent substituer certains composants métalliques dans les industries de l'aérospatiale et du transport. Les polymères ont des masses volumiques plus faibles que les métaux et une réactivité chimique limitée, ce qui en fait des candidats idéaux pour les applications spatiales. En combinant techniques expérimentales et simulations numériques, nous avons étudié les mécanismes fondamentaux de la métallisation de surface d'un polymère poly-époxy (DGEBA / EDA). L'objectif de notre étude était de développer un modèle non empirique prenant en compte les mécanismes régissant la nucléation et la croissance des films minces métalliques. Notre groupe a une longue expérience des dépôts chimiques en phase vapeur, CVD. Mais cette technique n'a pas été choisie pour la métallisation de nos surfaces de polymères car les températures requises dans le réacteur étaient trop élevées. Comme alternative, nous avons effectué une évaporation sous ultravide de Cu à température ambiante, conduisant à une diffusion des atomes en phase gazeuse sans énergie cinétique. Les processus d'adsorption et de diffusion sont donc plus proches des conditions thermodynamiques associées aux calculs. Un protocole expérimental a été mis en place afin de créer une surface polymère chimiquement homogène présentant une faible rugosité. Le polymère obtenu a été caractérisé (i) par spectroscopie infrarouge à transformée de Fourier, pour déterminer le taux de polymérisation (supérieur à 90%), (ii) par calorimétrie différentielle à balayage pour obtenir la température de transition vitreuse (Tg) (118,1 °C), (iii) par microscopie à force atomique (AFM) pour estimer la rugosité de la surface ($Ra \approx 1$ nm), et (iv) par spectroscopie de photoélectrons X (XPS) pour caractériser les liaisons chimiques de surface. La surface de polymère a ensuite été métallisée. Grâce à des analyses AFM, l'épaisseur du film mince a été estimée à 6 nm. Nous avons ensuite utilisé l'XPS pour caractériser les liaisons interfaciales Cu / Poly-époxy. Nous avons déduit de l'interprétation des spectres XPS que le Cu est adsorbé préférentiellement sur un atome d'oxygène spécifique du polymère. Pour identifier clairement ces sites d'adsorption de Cu, nous avons ensuite simulé les spectres XPS du polymère non revêtu, par des calculs quantiques, en utilisant un modèle moléculaire (dimère : 1 molécule de DGEBA liée à 1 molécule d'EDA). Les méthodes Hartree-Fock (HF) et de la théorie de la fonctionnelle de la densité (DFT) nous ont permis de simuler des spectres XPS pour la surface nue, en prenant en compte les effets d'état final et initial. Grâce à ces résultats, nous avons pu décomposer le spectre expérimental en 8 contributions, ce qui conduit à des résultats beaucoup plus précis que les résultats habituels obtenus par l'utilisation exclusive des expériences et de la littérature. Nous avons ensuite effectué des simulations de dynamique moléculaire classique (MD) pour passer d'un modèle moléculaire (dimère) à un modèle de polymère amorphe. Nous avons utilisé le champ de force Amber généralisé (GAFF) et nous avons développé un code de réticulation des molécules de monomères. Le système initial était un mélange stœchiométrique de molécules DGEBA et EDA qui a été équilibré à 700K. Lorsque l'équilibre a été atteint, certaines propriétés structurales (par exemple, la distribution des liaisons) ont été extraites des simulations NPT. À partir de ce mélange liquide de monomères, notre code de réticulation a identifié et relié les atomes réactifs (à une distance interatomique prédéfinie < 3 Å). Après chaque étape de polymérisation, le système a été rééquilibré à 700K (simulations NPT). Après plusieurs cycles de réticulation/simulation de dynamique moléculaire, nous avons pu atteindre un taux de polymérisation de 93% et la fonction de distribution radiale (RDF), la masse volumique (1.115 à 300K) et la température de transition vitreuse Tg (115,5 °C) ont été calculées. La Tg est en accord avec la valeur expérimentale de 118,1 °C, validant notre approche numérique pour développer un modèle pour les polymères poly-époxy.

Title. *Modelling the DGEBA-EDA poly-epoxy and its reactivity towards copper: experimental and numerical approach*

Abstract. Metallization of polymer surfaces can lead to the substitution of metallic components. Polymers have lower densities and limited chemical reactivity, making them ideal candidates for the space applications. Through experiments and calculations, we studied the fundamental mechanisms of surface metallization of a poly-epoxy polymer (DGEBA/EDA). The objective of our study was to develop a non-empirical model that could take into account the mechanisms governing the nucleation and growth of thin metal films. Our group has a long experience in chemical vapor deposition, CVD, and metallization of polymer composites. But we did not applied CVD at first because of the high temperatures required in the reactor. We alternatively used ultrahigh vacuum evaporation of Cu at ambient temperature. Therefore, we make sure that atoms diffuse in the gas phase without kinetic energy. Adsorption and diffusion processes are thus closer to thermodynamic conditions that prevails in calculations. An experimental protocol was refined in order to create a chemically homogeneous polymer surface with a low roughness (R_a<1nm). The bulk and the surface of the pristine polymer were characterized (i) by Fourier Transform Infrared Spectroscopy, to determine the polymerization rate (above 90%), (ii) by differential scanning calorimetry in order to obtain the glass transition temperature (T_g) (118.1 °C), (iii) by atomic force microscopy (AFM) to calculate surface roughness ($Ra \approx 1$ nm), and (iv) by X-ray photoelectron spectroscopy (XPS) to characterize surface chemical bonding. The surface was then metallized. Through AFM, the thickness of the thin film was estimated at 6 nm. We then used XPS to characterize the Cu/Poly-epoxy interfacial bonding. We deduced that Cu adsorbed preferentially on a specific oxygen atom of the polymer. To clearly identify this Cu adsorption site, we further simulated the XPS spectra of our clean or metallized polymer by quantum calculations, using a dimer model (1 molecule of DGEBA connected to 1 molecule of EDA). In the Hartree-Fock (HF) and Density Functional Theory (DFT) framework, we first simulated the XPS spectra for the pristine surface taking into account initial and final state effects. Thanks to these results, we were able to analyze the experimental spectrum with 8 contributions, leading to much more accurate results than the usual results obtained by the exclusive use of experiments and literature. We then performed classical Molecular Dynamics (MD) simulations to move from a dimer model to an amorphous polymer model. We used the general Amber force field (GAFF) and we developed a code to mimic the reticulation of monomers molecules. We started from a stoichiometric mixture of DGEBA and EDA molecules. When equilibration was reached, structural properties at 700K (e.g. distribution of bonds) were extracted from the results of the NPT simulations. From this melt of monomers, the homemade reticulation code identified and connected reactive atoms (at a pre-defined inter-atomic distance < 3Å). After each step of polymerization, the system was equilibrated at 700K (NPT simulations). After multiple reticulation/MD cycles we could achieve a polymerization rate of 93% and the Radial Distribution Function (RDF), the density and the glass transition temperature T_g were calculated. The value of the computed density was 1.115 at 300K and the calculated Tg (115.5 °C) was in good agreement with the experimental T_g of 118.1 °C, validating our numerical approach to develop a model for poly-epoxies.